UNIVERSITÀ DEL SALENTO

FACOLTÀ DI SCIENZE MM.FF.NN. - DIPARTIMENTO DI FISICA

DOTTORATO DI RICERCA IN FISICA - XIX CICLO - FIS/05

ROSARIO BRUNETTO

SPACE WEATHERING IN THE SOLAR SYSTEM: FROM LABORATORY TO OBSERVATIONS, THROUGH SPECTRAL MODELS

PhD Thesis

Tutors:
Prof. Vincenzo Orofino
Prof. Giovanni Strazzulla

ANNO ACCADEMICO 2006 - 2007

To Nadia

Contents

List of Figures

List of Tables

Sommario

La gran parte dei corpi del Sistema Solare non possiede atmosfera o campi magnetici; tali corpi sono a volte chiamati "corpi minori", ed includono asteroidi, oggetti Trans-Nettuniani, pianeti nani, comete e satelliti dei pianeti.

Le superfici dei corpi del Sistema Solare non protetti, o debolmente protetti da atmosfere o campi magnetici, sono costantemente sottoposte all'interazione con micro-meteoriti, con particelle del vento solare e con particelle cariche di più alta energia, di provenienza solare, galattica o magnetosferica (ad es. i satelliti di Giove e Saturno). Tale interazione, nota con il nome di "space weathering", è causa di un notevole numero di effetti.

Il bombardamento da parte di micro-impattori causa principalmente: ablazione (con rideposizione di parte del materiale vaporizzato); effetti termici; creazione di micro-crateri. L'irraggiamento da parte di ioni veloci (impiantazione) causa: variazioni della struttura del bersaglio (ad es. amorfizzazione); variazione della composizione; erosione della superficie.

I processi di space weathering portano quindi anche alla variazione delle proprietà ottiche dei materiali che compongono la superficie dell'oggetto. Essa si riflette in una variazione delle proprietà spettrali, che possono essere studiate mediante l'osservazione della luce solare riflessa da tali superfici. Di conseguenza, per interpretare gli spettri di riflettanza acquisiti mediante osservazioni, è necessario comprendere i meccanismi e i processi che governano l'evoluzione di tali superfici.

Un contributo importante viene da esperimenti di laboratorio, che permettono la simulazione dei processi di space weathering e delle variazioni spettrali associate. Questi studi vengono condotti su materiali che sono dei buoni analoghi dei materiali

che compongono le superfici dei corpi minori. Si tratta principalmente di silicati, ghiacci e materiali carboniosi refrattari. Un caso particolare viene dalle meteoriti; si tratta di uno dei pochi casi in cui è possibile studiare direttamente in laboratorio i materiali che compongono i corpi minori.

Lo scopo principale di questa tesi è di contribuire ad una migliore conoscenza dei fenomeni di space weathering, per comprendere come tali processi energetici possano aver influenzato la formazione ed evoluzione dei corpi minori del Sistema Solare. L'approccio è principalmente di tipo sperimentale, con la caratterizzazione dei materiali in laboratorio mediante spettroscopia in trasmissione e in riflessione nell'intervallo UV-Vis-IR, spettroscopia Raman e Micro-Raman, e in misura minore analisi molecolare ed elementale.

Per simulare lo space weathering, i materiali studiati sono stati sottoposti a varie alterazioni, in particolare: irraggiamento ed ablazione con laser UV a nano-impulsi (per simulare gli impatti micro-meteoritici); irraggiamento con ioni energetici a diverse temperature (per simulare l'irraggiamento degli ioni cosmici). Lo scopo è la comprensione dei meccanismi fisici di tali processi e la valutazione dei corrispondenti tempi scala astrofisici.

Per gli esperimenti, ho utilizzato la strumentazione del Laboratorio di Astrofisica del Dipartimento di Fisica dell'Università del Salento (ex Università di Lecce) e del Laboratorio di Astrofisica Sperimentale dell'INAF, Osservatorio Astrofisico di Catania, nell'ambito di un progetto di collaborazione. La complementarità dei due apparati permette di studiare con completezza il processo energetico di alterazione e le variazioni spettrali indotte su silicati, ghiacci e carboni.

In relazione alla crescente quantità di informazioni ottenute grazie ai telescopi di nuova generazione ed alle più recenti missioni spaziali, il supporto dei dati di laboratorio si rivela sempre più importante. Tuttavia, un confronto diretto tra dati di laboratorio e osservativi non sempre è possibile; sono necessari opportuni modelli teorici. Ecco perchè in questa tesi ho affiancato all'aspetto sperimentale un lavoro teorico che, partendo dalla stima delle costanti ottiche dei materiali alterati, è in grado di modellare gli spettri in riflettanza dei corpi minori per ricavarne la composizione superficiale.

A tal fine, ho portato avanti collaborazioni con ricercatori di diversi istituti, italiani ed esteri; questo mi ha permesso di lavorare in diversi centri di ricerca, in particolare al Laboratoire d'Etudes Spatiales et d'Instrumentation en Astrophysique, Osservatorio di Parigi-Meudon (Francia), all'Isaac Newton Group of Telescopes & Instituto de Astrofísica de Canarias, Santa Cruz de la Palma (Spagna), e al Dipartimento di Astronomia e Osservatorio Astronomico di Padova. Inoltre, un Protocollo d'Intesa stipulato per l'occasione tra la NASA e il Dipartimento di Fisica dell'Università di Lecce, mi ha permesso di trascorrere circa 4 mesi al NASA - Ames Research Center, CA (USA), dove ho sviluppato alcuni modelli per il calcolo delle costanti ottiche dei materiali irraggiati con ioni e radiazione laser.

I principali risultati sperimentali presentati in questa tesi sono i seguenti:

1. l'alterazione con laser o con ioni di un vasto numero di campioni (terrestri e meteoritici) ricchi di silicati causa una forte riduzione della riflettanza spettrale (oscuramento) maggiormente nel UV-Vis che nel vicino IR (arrossamento); questo processo, altamente efficiente, è probabilmente connesso alla formazione di nano-inclusioni di ferro metallico sulla superficie dei grani;

2. l'irraggiamento ionico di ghiacci ricchi di carbonio (come CH_3OH, CH_4, o C_6H_6) produce una notevole variazione nella composizione chimica; ciò causa un forte arrossamento e un progressivo oscuramento degli spettri correlato alla distruzione delle molecole originarie e alla conseguente produzione di un residuo carbonioso stabile, anche in presenza di miscele con H_2O;

3. sono state determinate le costanti ottiche di alcuni di questi materiali processati in laboratorio, per usarle nei modelli.

Dal confronto tra dati di laboratorio e osservazioni dei corpi minori è stato possibile ottenere i seguenti risultati:

4. l'arrossamento degli spettri dei silicati è in grado di riprodurre le pendenze spettrali osservate negli asteroidi prossimi all'orbita terrestre (Near Earth Objects) e in quelli di fascia principale (Main Belt Asteroids); è possibile quindi spiegare la discrepanza tra gli spettri delle meteoriti più abbondanti (condriti ordinarie) e quelli degli asteroidi di tipo S (ricchi di silicati), da cui si ritiene provengano tali meteoriti;

5. il tempo scala, nello spazio compreso tra l'orbita terrestre e la fascia principale

degli asteroidi, per l'arrossamento degli asteroidi di tipo S è stato stimato in circa 10^5-10^6 anni; ciò suggerisce anche un'efficienza relativamente alta dei processi di ringiovanimento (ad es. impatti) che si oppongono all'arrossamento degli spettri;

6. gli spettri dei residui prodotti da irraggiamento di ghiacci spiegano la varietà spettrale dei corpi minori del Sistema Solare esterno (centauri, oggetti di Kuiper o Trans-Nettuniani, comete) e indicano la presenza di un mantello superficiale di materiale organico refrattario sulla gran parte di essi;

Per alcuni oggetti specifici, inoltre, ho potuto effettuare un'analisi più dettagliata nell'ambito delle collaborazioni sopra elencate, ottenendo i seguenti risultati:

7. ho sviluppato un modello di space weathering che, facendo uso delle costanti ottiche dei silicati, permette di ricavare la composizione superficiale degli asteroidi e il loro grado di alterazione; l'applicazione di questo modello all'asteroide 832 Karin ha mostrato come i tempi-scala di irraggiamento stimati per questo oggetto siano in accordo con l'età dell'impatto che ne ha ringiovanito la superficie circa 5.8×10^6 anni fa;

8. ho applicato i modelli di space weathering a due oggetti peculiari, l'asteroide 1951 Lick e il centauro 5145 Pholus, dimostrando che i risultati sperimentali simulano correttamente l'arrossamento dei silicati sia in presenza di saturazione che di miscele con ghiacci e materiali organici.

Va sottolineato infine che questa tesi fornisce anche utili strumenti di laboratorio e di modellistica a supporto delle nuove e continue osservazioni effettuate da moderni telescopi e missioni spaziali, che ci aiutano a comprendere la genesi ed evoluzione del Sistema Solare.

Abstract

The majority of Solar System bodies does not have atmosphere or magnetic field; these bodies are sometimes called "minor bodies", and include asteroids, Trans-Neptunian objects, dwarf planets, comets, and satellites of planets.

The surface of Solar System minor bodies not (or weakly) protected by atmosphere or magnetic field, are continuously affected by the interaction with micro-meteorites, solar wind particles, and high energy particles, coming from the Sun, the Galaxy, or local magnetospheres (e.g. satellites of Jupiter and Saturn). This interaction, known as "space weathering", causes several effects.

Micro-meteorite bombardment chiefly induces: ablation (with partial re-deposition of the vapor); thermal effects, formation of micro-craters. Irradiation by fast ions (implantation) induces: modification of the target structure (e.g. amorphization); compositional variations; surface sputtering.

Thus, space weathering processes also cause variations in the optical properties of the surface materials of a body. This is revealed by the variations of the spectral properties, that can be studied observing the solar light reflected from the surface. Therefore, interpretation of the observed reflectance spectra requires the knowledge of the mechanisms and processes determining the surface evolution.

An important role is played by laboratory experiments, that simulate the space weathering processes and the corresponding spectral variations. Such analysis is performed on materials that are good analogues of the minor bodies surface components, mainly: silicates, ices, refractory carbonaceous materials. Analysis of meteorites is a particular and important case, being one of the few chances to study in the laboratory materials coming from minor bodies.

The main goal of this thesis is to investigate the space weathering processes, to better understand how such energetic processing may have influenced the formation and evolution of Solar System minor bodies. The approach is mainly experimental, to characterize solid materials in the laboratory using transmission and reflection spectroscopy in the UV-Vis-IR range, Raman and micro-Raman spectroscopy, and in some case molecular and elemental analysis.

To simulate space weathering, I have used various techniques, in particular: nano-pulsed UV laser irradiation and ablation (to simulate micro-meteorite impacts); fast ion irradiation at different temperatures (to simulate cosmic ion irradiation). The aim is to understand the physical mechanisms and evaluate the corresponding astrophysical timescales.

During the experiments, I have used the setup at the Laboratorio di Astrofisica (Dipartimento di Fisica, Università del Salento - ex Università di Lecce, Italy) and at the Laboratorio di Astrofisica Sperimentale (INAF, Osservatorio Astrofisico di Catania, Italy), in a collaboration project. The two laboratories are complemental, allowing a detailed analysis of the energetic processing and spectral variations induced on silicates, ices, and carbons.

Laboratory data give invaluable support to interpret the large number of information obtained by new generation telescopes and ongoing space missions. However, a direct comparison between laboratory measurements and observations is not always possible, since theoretical models are necessary. Consequently, in this thesis I have also included theoretical efforts to model the reflectance spectra of minor bodies, starting from the estimation of the optical constants of the "weathered" materials. This allows to estimate the surface composition.

To this aim, I have collaborated with researchers from different institutes, in Italy and abroad; this allowed me to work in several research centers, in particular at Laboratoire d'Etudes Spatiales et d'Instrumentation en Astrophysique, Observatory of Paris-Meudon (France), at Isaac Newton Group of Telescopes & Instituto de Astrofísica de Canarias, Santa Cruz de la Palma (Spain), and at Dipartimento di Astronomia and Osservatorio Astronomico di Padova. Furthermore, a specific Agreement between NASA and Dipartimento di Fisica (Lecce), allowed me to spend

about 4 months at NASA - Ames Research Center, CA (USA), where I developed some models to calculate the optical constants of materials after ion and laser irradiation.

The main experimental results presented in this thesis are the following:

1. laser and ion processing of a large number of silicate-rich samples (terrestrial and meteoritic) induces a substantial decrease of the spectral reflectance (darkening), mainly in the UV-Vis range (reddening); this process is highly efficient, and is probably caused by the formation of nanophase metallic iron inclusions in the surface grains;

2. ion irradiation of carbon-rich ices (such as CH_3OH, CH_4, C_6H_6) causes a strong variation of the chemical composition; this induces spectral reddening and darkening, related to the destruction of the original molecules and consequent production of a stable carbonaceous residue, even when mixed with H_2O;

3. optical constants of some of these processed materials have been estimated, to use them in the models.

From the comparison between laboratory data and observations of minor bodies, the following results have been obtained:

4. the spectral reddening of silicates is able to reproduce the observed spectral slopes for Near-Earth and Main Belt asteroids; consequently, it is possible to explain the spectral mismatch between the most abundant meteorites (ordinary chondrites) and their presumed parent bodies (S-type asteroids);

5. the astrophysical timescales (between the Earth orbit and the Main Belt) for the reddening of S-type asteroids has been estimated to be about 10^5-10^6 years; this also suggests a relatively high efficiency for the rejuvenating processes (e.g. impacts) that oppose to the spectral reddening;

6. the spectra of residues (produced after irradiation of ices) explain the spectral variety of minor bodies in the outer Solar System (centaurs, Kuiper Belt or Trans-Neptunian objects, comets) and indicate the presence of a surface mantle composed of organic refractory materials in the majority of these bodies;

In addition, for some peculiar bodies I have performed a more detailed analysis (thanks to the collaborations mentioned above), with the following results:

7. I have developed a space weathering model that, using the optical constants of silicates, allow to estimate the surface composition of asteroids and their weathering level; application of this model to asteroid 832 Karin showed that the irradiation timescales that we estimate for this body are in agreement with the age of the impact that rejuvenated the surface about 5.8×10^6 years ago.

8. I have applied the space weathering models to two peculiar objects, i.e. asteroid 1951 Lick and centaur 5145 Pholus, showing that the experimental results correctly simulate the reddening of silicates, even in a saturation regime or when silicates are mixed with ices and organic materials.

Finally, it must be stressed that this thesis provides useful laboratory and theoretical tools as a support for the new observations collected with modern telescopes and space missions, that help us to understand the origin and evolution of the Solar System.

Acknowledgments

I am gratefully and deeply indebted to all the people who have helped, supported, and guided me during these last three years, but unfortunately there is no room here to list them all individually. First and foremost I wish to thank my supervisors Vincenzo Orofino and Giovanni Strazzulla, especially for their positive and constructive criticism and discussions. I consider myself very lucky to have been guided by these two scientists, who always provided invaluable personal and scientific support.

I warmly thank the groups of experimental Astrophysics in Lecce and in Catania. From the continuos interaction with all these bright people, inside and outside the laboratory, I received expertise, help, and a lot of encouragement. I am also grateful to the technicians and researchers at the Department of Physics in Lecce and at the Catania Observatory, who helped me several times in many ways during my PhD courses and during the experiments. A special thank goes to the students that shared with me the everyday struggle to get a job!

As a PhD student I have been allowed to travel (more than 100,000 km!) to attend congresses and to work in foreign institutes. This has been an extraordinary opportunity to improve my skills and knowledge, but also to enlarge my vision meeting people from very different cultures. I thank the individuals and institutions who gave financial support, in particular the groups in Lecce and Catania.

I wish to thank my colleagues and collaborators in Paris, Padova, Canary Islands, and in the USA, especially Ted Roush at NASA ARC, for all the things I have experienced and all I have learned from them. In particular, I am thankful to my American and Spanish colleagues and friends, for teaching me also their wonderful languages.

I owe much to my Italian and international friends, especially to those who hosted and guided me during my stays and journeys. I have an exceptional thank to give to the "scattered ones", for the great moments we had.

I thank my close friends in Catania. During these three years, I have realized how their powerful presence in my life has been absolutely fundamental to the realization of this thesis, step by step, following our common ideals.

I am overwhelmed with gratitude and love to my family. From my parents and my brother I received a constant and very important help in so many ways that it is hard to describe.

Last but of course not least, I wish to thank Nadia, the person who gives meaning to all my words and thoughts, since we share the same struggle and contradictory love for science, knowledge, freedom, democracy, and all the other little things of our everyday life. Through joy and pain, there is no way to measure the support and love I received from her during the last three years.

Rosario Brunetto
April, 2007
Università del Salento, Italy

Introduction

Immagina le stelle, scoprirai che sorridono sempre.
Immagina intensamente e vedrai dove gli altri pensano che non ci sia niente.
(Cristina Donà, Dove sei tu - 2003)

This thesis focuses on the space weathering processes in the Solar System, using mainly laboratory results, and applying them to observations through spectral models.

In the first part I will introduce the space weathering issue related to the alteration of surface composition, chemistry, and physics of minor bodies in the Solar System. I will also review the present knowledge of the subject and the previous experimental results obtained in different laboratories. Then I will describe the laboratory setup I have used: the main experimental facilities are the ones in Lecce (Italy) at the Laboratorio di Astrofisica, Dipartimento di Fisica, Università del Salento, and in Catania (Italy) at the Laboratorio di Astrofisica Sperimentale, Osservatorio Astrofisico di Catania (INAF).

In the second part I will discuss the main experimental results that I have obtained after laser ablation and ion irradiation of silicates, ices, and meteorites. The spectral modifications will be carefully analyzed and results will be compared with previous experiments; a first glance to the astrophysical implications will be given.

The third part includes the application of the experiments to the observed surface spectra of minor bodies, using various approaches. In some cases, optical characterization of laboratory samples is performed to produce optical constants that are input parameters for the spectral models. The case of a few peculiar objects is also

discussed. This also allows to connect space weathering results to dynamical analysis, and to link surface properties to internal structure and physical properties of asteroids.

The results described in this thesis are obtained through several collaborations with various researchers and colleagues in Italy, France, Spain, USA, and Germany. Most of the work has been published in peer reviewed journals (listed below).

Since English is not my native language, I wish to apologize for any mistake and incorrect use of the language that the reader could find in this thesis.

Journal publications related to this thesis:

1. R. Brunetto, T.L. Roush, A.C. Marra, V. Orofino, 2007. *Optical characterization of laser ablated silicates.* Icarus, submitted.

2. P. Vernazza, M. Birlan, A. Rossi, E. Dotto, D. Nesvorny, R. Brunetto, S. Fornasier, M. Fulchignoni, S. Renner, 2006. *Physical characterization of the Karin family.* Astronomy and Astrophysics 460, 945-951.

3. R. Brunetto, P. Vernazza, S. Marchi, M. Birlan, M. Fulchignoni, V. Orofino, G. Strazzulla, 2006. *Modeling asteroid surfaces from observations and irradiation experiments: The case of 832 Karin.* Icarus 184, 327-337.

4. M. Lazzarin, S. Marchi, L.V. Moroz, R. Brunetto, S. Magrin, P. Paolicchi, G. Strazzulla, 2006. *Space Weathering in the Main Asteroid Belt: The Big Picture.* The Astrophysical Journal Letters 647, L179-L182.

5. R. Brunetto, M.A. Barucci, E. Dotto, G. Strazzulla, 2006. *Ion irradiation of frozen methanol, methane, and benzene: linking to the colors of Centaurs and Trans-Neptunian objects.* The Astrophysical Journal 644, 646-650.

6. P. Vernazza, R. Brunetto, G. Strazzulla, M. Fulchignoni, P. Rochette, N. Meyer-Vernet, I. Zouganelis, 2006. *Asteroid colors: a novel tool for magnetic field detection? The case of Vesta.* Astronomy and Astrophysics Letters 451, L43-L46.

7. R. Brunetto, F. Romano, A. Blanco, S. Fonti, M. Martino, V. Orofino, C. Verrienti, 2006. *Space weathering of silicates simulated by nanosecond pulse UV excimer laser.* Icarus 180, 546-554.

8. R. Brunetto, G. Strazzulla, 2005. *Elastic collisions in ion irradiation experiments: A mechanism for space weathering of silicates.* Icarus 179, 265-273.

9. S. Marchi, R. Brunetto, S. Magrin, M. Lazzarin, D. Gandolfi, 2005. *Space weathering of near-Earth and main belt silicate-rich asteroids: observations and ion irradiation experiments.* Astronomy and Astrophysics 443, 769-775.

10. R. Brunetto, G.A. Baratta, M. Domingo, G. Strazzulla, 2005. *Reflectance and transmittance spectra (2.2-2.4 μm) of ion irradiated frozen methanol.* Icarus 175, 226-232.

11. G. Strazzulla, E. Dotto, R. Binzel, R. Brunetto, M.A. Barucci, A. Blanco, V. Orofino, 2005. *Spectral alteration of the meteorite Epinal (H5) induced by heavy ion irradiation: a simulation of space weathering effects on Near Earth Asteroids.* Icarus 174, 31-35.

12. R. Brunetto, G.A. Baratta, G. Strazzulla, 2005. *Amorphization of diamond by ion irradiation: a Raman study.* Journal of Physics: Conference Series, Vol. 6, Issue 1, 120-125.

Part I

The surface of minor bodies

Chapter 1

Surface composition and processing

Our knowledge of the Solar System is evolving rapidly after the discovery of several new bodies in the last decades.

On 24 August 2006, the International Astronomical Union (IAU) has voted a resolution (IAU Resolution 5, 2006) that gives a new definition of what a planet is:

1. it is a celestial body in orbit around the Sun,

2. it has sufficient mass for its self-gravity to overcome rigid body forces so that it assumes a hydrostatic equilibrium (nearly round) shape, and

3. has cleared the neighborhood around its orbit.

According to this new definition, there are currently eight planets in the Solar System. The IAU also resolved that bodies in the Solar System (except satellites) must be divided into three distinct categories: planets, dwarf planets, and small Solar System bodies. In particular, a non-satellite body fulfilling only the first two of these criteria is classified as a dwarf planet; a non-satellite body fulfilling only the first criterion is classified as small Solar System body.

The IAU has officially identified three celestial bodies that have immediately received the dwarf planet classification: Eris (see below), Ceres (the largest Main-Belt asteroid), and Pluto, which has lost its status of planet. Other bodies might be added to the list once it has been determined whether they are in hydrostatic equilibrium or not. Consequently, all other objects, except satellites, orbiting the

Sun are now referred to collectively as small Solar System bodies. These currently include the classical asteroids (except for Ceres), most Trans-Neptunian Objects (TNOs), the centaurs, all comets, and other small bodies.

When I began my Ph.D. courses in May 2004, the discovery of 2003 UB_{313} (later named Eris, the largest TNO and dwarf planet) was still to be announced, and Pluto was still considered a planet[1]. I started my research in the space weathering area, assuming that my experiments would be applied to a large number of "minor bodies", including asteroids, comets, TNOs, etc.

Now that we have new definitions for planets, dwarf planets, and small Solar System bodies, the use of the term "minor body" may sound confusing. However, in this thesis I will keep using it, with the following warning: I call "minor body" a body not (or weakly) protected by an atmosphere or a magnetic field, so that its surface is exposed to the bombardment by micro-meteorites and solar wind ions. This is to specify that the space weathering experiments that I will describe in the following sections apply to any body that has its surface exposed to significant amount of dose by weathering agents. Consequently, the objects that I am primarily interested in include not only the small Solar System bodies, but also the dwarf planets, many satellites[2] and even one planet, i.e. Mercury.

Generally speaking, the surfaces of minor bodies are rich in silicates, ices, and carbons[3]. Bodies in the inner Solar System are usually enriched in silicates, while ices become dominant in the surface of outer objects.

Irradiation by cosmic and solar wind ions and bombardment by interplanetary dust (micrometeorites) are processes believed to induce space weathering (see Fig. 1.1), i.e., time-related processes able to change progressively the solar reflectance spectra of airless planetary surfaces. These two processing mechanisms are believed

[1]It is probable that the definition of planet will change again in the future, and it is possible that new categories will need to be introduced, especially when a more detailed comprehension of extra-solar systems and solid bodies formation and evolution will be achieved. Luckily, definitions change with time, as this witnesses that our knowledge continues evolving.

[2]Some satellites have physical and compositional characteristics very close to those of asteroids or TNOs. For a few objects, the possibility of a gravitational capture by the planets has been explored.

[3]In this thesis I will not deal with dynamical properties and classifications of minor bodies. The main topic will be the surface composition.

to be active, with different intensity and effects, on a large distance scale, from Mercury (Killen et al., 2001) to the Kuiper Belt (Doressoundiram et al., 2002).

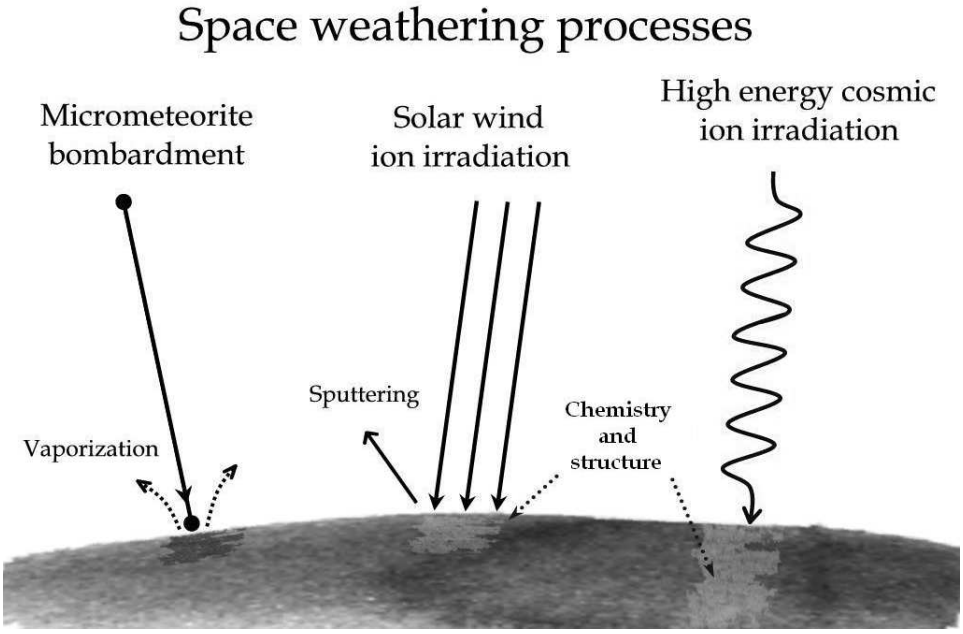

Figure 1.1: A scheme of the space weathering processes studied in this thesis.

The effects of space weathering change progressively the solar reflectance spectra of airless bodies (in the UV-vis-NIR range), and include spectral darkening, reddening and subdued absorption bands (Hapke, 2001).

In this chapter I will briefly review the present knowledge of the surface processing of minor bodies; in particular I will focus on the state of the art of laboratory experiments.

1.1 Tools: observations and models

1.1.1 UV-Vis-IR spectroscopy

Ultraviolet, visible, and near-infrared (UV-Vis-NIR) reflectance spectroscopy is a widely used tool to determine minor bodies' composition since it gives direct indications on their surface composition.

The solar incident flux reaching an airless body surface is split in two contributions: the reflected and the absorbed part, whose ratio depends on the surface albedo, which is a complex function of the optical properties, grain size, and other scattering parameters. The observer receives both the light reflected from the surface and the black-body emission, that is function of its temperature. Generally speaking, reflected sunlight dominates the spectrum in the Vis-NIR range, while the contribution of thermal emission becomes more important at longer wavelength.

Luckily, many diagnostic features that come from electronic and vibrational transitions within minerals or molecules are detectable in the 0.25-2.50 μm spectral range. Thanks to laboratory calibrations, it is possible from the observed features to establish the presence of specific minerals or species on the surface, and in some instances to get information about important parameters, like temperature, density, solid state structure, etc.

The possibility of revealing a feature depends of course on the abundance of the particular species and on the strength of the feature itself (sometimes called absorbance). Thanks to new generation telescopes, a large number of species are being detected (see discussion below). Starting from high quality spectra of a given mixtures, the average composition and relative abundances can be also determined my means of scattering models (see below). Hence, it is clear that it is possible to get a huge amount of compositional data on minor bodies' surface materials through reflectance spectroscopy.

1.1.2 Hapke and Shkuratov theories

Minor bodies' surfaces are composed of several to many different minerals. Deconvolving a reflectance spectrum to mineral abundance in an unambiguous way is difficult, because the spectra are complex nonlinear functions of grain size, abundance, and material opacity (Poulet et al., 2002).

Multiple scattering models can provide approximate solutions to the radiative transfer in a particulate medium. The optical constants of the considered materials are important input parameters for those models, and must be carefully measured

in the laboratory. They serve as the basis for the calculation of the necessary absorption and scattering efficiencies for different size and shape distributions of the dust particles.

In the literature, the two mainly used scattering theories (based on the equivalent slab model) are the Hapke theory (Hapke, 1981) and the Shkuratov theory (Shkuratov et al., 1999). A detailed and interesting comparison between these two models has been performed by Poulet et al. (2002). I will use both theories in the third part of the thesis.

The Hapke theory was one of the first to derive the single scattering albedo for a grain of given size and refractive index and to provide this critical element in a simple and straightforward way. Because of this simplicity, this has become the dominant theory used in the planetary community. Shkuratov et al. (1999) applied a similar form of statistical approach to calculate the albedo of a typical grain, but the approach after that point is different. Poulet et al. (2002) found that their main difference is the role of the phase function of individual particles of regolith, which is predicted (and generally forward directed) in the case of the Shkuratov model instead of being a free parameter as formulated in the Hapke model.

It is interesting to note that both models are invertible. In particular, Hapke and Wells (1981) and Clark and Roush (1984) describe an approach to determination of the absorption coefficient, α, of a given material starting from its measured reflectance spectra. Since α is related to k via the dispersion relation, $\alpha = 4\pi k/\lambda$, this approach, that relies upon Hapke's description of radiative transfer within particulate surfaces (see Hapke (1981), Hapke (1986), and Hapke (1993), and references therein), provides a useful mechanism of determining k. An example of this will be given in the last part of this thesis.

1.1.3 Results from space missions

Space missions are a powerful tool to study minor bodies in the Solar System. Once a spacecraft arrives in the proximity of a body, it usually collects an incredibly huge amount of data through the several instruments onboard.

In this thesis I will not deal with space mission results. However, it is mandatory to stress that results described in this work can be useful when interpreting data from spacecrafts (especially spectroscopical data). Laboratory experiments and ground-based observations give invaluable support to scientists working on space mission data. In particular, I would like to number the main space missions currently in flight, or ready to be launched, that can have strong scientific connection with the work of this thesis:

1. Cassini-Huygens, a joint NASA/ESA/ASI space mission intended to study Saturn and its moons, that is already sending us extraordinary results about the saturnian satellites.

2. Rosetta, a ESA-led space mission, launched in 2004, intended to study the comet 67P/Churyumov-Gerasimenko; Rosetta will also fly-by two asteroids (2867 Steins and 21 Lutetia).

3. New Horizons, a NASA mission to Pluto and its moons (and eventually one or more other TNOs), successfully launched on January 19, 2006; it is expected to arrive at Pluto in July 2015.

4. Dawn, a NASA space mission ready to be launched; it is an orbiting space probe that will visit and study the two most massive members of the asteroid belt, the dwarf planet Ceres and the asteroid Vesta.

Other missions that may be related to this work are several missions to the Moon, or missions that successfully visited asteroids (e.g. NEAR Shoemaker that studied the near-Earth asteroid Eros, or Hayabusa that visited the near-Earth asteroid Itokawa). It is also worth to mention BepiColombo (currently under development), a joint ESA/JAXA mission planned to reach Mercury.

1.2 Space weathering of silicates

The first zone of the Solar System, known as the inner Solar System, includes the four terrestrial planets, the main asteroid belt, and the Near-Earth Asteroids

(NEAs). There are hundreds of thousands of currently known asteroids in the main belt between Mars and Jupiter [4]. Asteroids are rocky objects of different dimensions and irregular shape (except for a few of them that might have reached the hydrostatic equilibrium), thought to be remnants of the planetesimals that formed at the origin of the Solar System.

When an asteroid collisional fragment enters the terrestrial atmosphere, the friction heats it up, and it is partially disrupted; the possible rock debris that reaches the ground is called "meteorite". Thus, a powerful tool to study asteroids is the laboratory analysis of meteorites.

The spectra of many asteroids are dominated by silicate features. The main species observed are olivine, clinopyroxene and orthopyroxene, spinel, feldspar and hydrated phyllosilicates. Iron-Nickel metals can also be present. In a certain number of bodies, a contribution from organic compounds can be observed, producing a featureless spectrum and a relatively low albedo. Several asteroids are composed of mixture of these minerals.

As I discussed above, studying the surface spectra, in most cases we can detect mineralogical signatures characteristic of a particular species. Since the spectral parameters of the different absorption features (i.e. band peak position, band areas) are related to a specific composition of the considered mineral, information on elemental abundance can often be obtained, such as the Mg/Fe ratio or the Ca content.

However, the spectra of asteroids are also influenced by the effects of the space environment, that alters the optical properties of airless bodies' surfaces. A number of physical processes have been proposed as relevant in this context (e.g. micrometeoroid impacts, solar wind bombardment, etc.). The result of all these effects on airless bodies is known as "space weathering".

Space weathering was initially studied on lunar soils (Pieters et al., 1993), since lunar soils returned from Apollo missions have optical properties that differ significantly from those of pristine lunar rocks (Conel and Nash, 1970). Cassidy and Hapke

[4] Again, definitions vary in space and time, so asteroids are sometimes called "planetoids". Near-Earth Objects with diameter lower than 50 m are called "meteoroids".

(1975) suggested the presence of metallic iron particle coatings on lunar soils; these coatings should be produced by deposition of atoms sputtered by solar wind particles and deposition of gaseous species produced by micrometeoritic impacts. Pieters et al. (2000) analyzed the products of space weathering of lunar soils, and demonstrated that nanophase reduced iron is produced on the surface of grains by a combination of vapor deposition and irradiation effects [5].

Space weathering was proposed also by Chapman (1996) to explain the surface variations of asteroid 243 Ida measured by the Galileo spacecraft. According to this description, space weathering is a progressive change in the surface color of an atmosphere-less body which becomes darker and darker in time, while its reflectance spectrum becomes redder.

Furthermore it has been suggested that space weathering can be responsible for the puzzling and significant mismatch (see Fig. 1.2) between the spectra of the most populous class of meteorites (ordinary chondrites, OC) and the surface spectra of S-type NEOs (Near Earth Objects) and MBAs (Main Belt Asteroids), their presumed asteroidal parent bodies (Jedicke et al., 2004; Lazzarin et al., 2004).

In fact, space weathering processes have been often invoked to explain the spectral diversity among objects of the same population, e.g., main-belt asteroids belonging to dynamical families, near-Earth objects (NEOs), trans-neptunian objects (TNOs) and centaurs. Several authors (Doressoundiram et al., 1998; Florczak et al., 1998; Lazzaro et al., 1999) pointed out that the spectra of MBAs belonging to a single dynamical family show a continuous spread of spectral slopes, and the lower part of the variation range is consistent with the spectra of ordinary chondrite meteorites. This can be due to a compositional effect, or it can be interpreted as due to different space weathering alteration states of the surfaces and as an indication that collisions may have rejuvenated part of the family.

Ordinary chondrites have spectral properties that are at the lowest part (least red sloped) of the range of variation of the spectral properties of NEOs, while the upper

[5] In a recent paper, Moretti et al. (2005) suggest an alternative process for surface alteration of airless bodies, through a shock-induced phase transformation of Fe-Ni alloys. This process will not be investigated in this thesis.

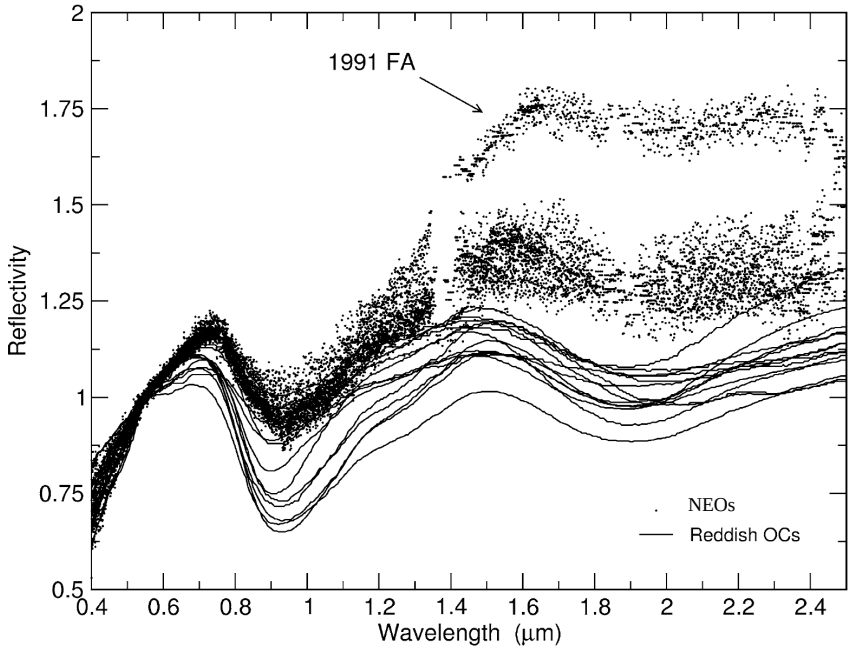

Figure 1.2: The OC paradox. Dots: S-type NEOs, overplotted in order to show their spread. Lines: fourteen ordinary chondrite meteorites chosen among the reddest ones. Clearly apparent is the "gap" between the S-type NEOs and the ordinary chondrites. Adapted from Lazzarin et al. (2004).

region better represents the spectra of the S-type main-belt asteroids (Binzel et al., 1996, 2004a).

The diversity in the spectra of NEOs and S-type asteroids could be trivial due to different mineralogies, and/or due to different regolith particle sizes. It is however largely believed that they are due to time dependent surface weathering processes. In this scenario, NEOs with spectra similar to those of S-type main-belt asteroids would be those with older surfaces, while objects most closely resembling ordinary chondrite meteorites would have the youngest surfaces probably rejuvenated by collisions.

The direct relationship between meteorites and the objects in the lower part of the spectral distribution may come out since breakup events, which are supposed to be at the origin of asteroid dynamical families, can possibly put fragments into chaotic regions. Over relatively short time-scales (10^5- 10^6 yr), these fragments can

become NEOs or meteorites.

1.2.1 Solar wind and cosmic ions

The importance of simulating solar wind irradiation in studying the changes of the optical properties of airless body surfaces has been known since a long time (Cassidy and Hapke, 1975). Yet a limited number of laboratory experiments have been performed to simulate space weathering effects on silicate materials.

A number of laboratory experimentalists have tried to simulate the effects of space weathering on asteroid material analogues.

Ion irradiation of silicate samples has been performed using mainly H^+ and He^+ ions at keV energies (Hapke, 2001). Dukes et al. (1999) irradiated olivines: they did not find any significant spectral change and interpreted this as due to the re-oxidation of iron once removed from the vacuum chamber. Yamada et al. (1999) performed high energy (MeV) proton implantation, producing only small changes in the spectra.

It is known that the presence of reduced iron increases the spectral slope and decreases the depth of the 1 μm band of a mafic material spectrum (see Shkuratov et al. (1999)). Thus a principal factor in producing spectral changes is thought to be the sputtering of iron from iron-bearing silicates due to ion irradiation and the deposition of nanophase neutral Fe on adjacent grains (Hapke, 2001).

1.2.2 Micrometeorites bombardment

Laboratory simulations have been performed on asteroid-like materials simulating solar wind and cosmic ion irradiation by keV-MeV ion irradiation, and assuming that micrometeorite bombardment can be simulated by pulsed laser irradiation.

Ion irradiation experiments can be considered a direct reproduction of solar wind irradiation effects; on the contrary, laser irradiation is assumed to simulate micrometeoroid impacts, but the confidence of this assumption is somewhat unclear. The most important point for a correct simulation by laser irradiation is the use of nanosecond pulses, in order to reproduce the duration of the vaporization process

induced by micrometeorite impacts.

Laser irradiation effects are known to vary widely, depending on the wavelength of the incident laser beam, on the energy fluence (J/cm^2) of the single pulse, on the pulse duration, on the repetition rate, on properties of the target, etc. (Chrisey and Hubler, 2004). In particular varying the laser fluence, it is possible to distinguish two main regions: at low fluence, laser irradiation induces mainly thermal and chemical effects, on the contrary ablation occurs when the laser-light intensity is high enough to induce significant material vaporization so that a dense vapor plume is formed. The threshold fluence value to achieve ablation strongly depends on the properties of the target and on the laser parameters: with inorganic insulators and strong-to-medium absorption, threshold fluence is typically between 0.5 and 2 J/cm^2 per pulse (Bauerle, 2000), valid for nanosecond pulsed laser. Indeed, the threshold value is not independent on the pulse duration.

Furthermore, achieving the congruent ablation regime depends not only on experimenting above the threshold, but also on letting the laser radiation being absorbed in the very upper layers (few tens of nanometers) of the material, to avoid the uncontrolled heating of the surrounding target.

Actually, the first experiments to simulate space weathering of OCs (Moroz et al., 1996) were performed using microsecond pulsed laser irradiation. The effect was to redden and darken reflectance spectra and also to produce a shift in the peak position of the 1 μm absorption band. Nevertheless, the laser pulse duration was much longer than the reasonable timescale of micrometeorite (1-10 μm size) impacts, and, according to Sasaki et al. (2001), the resultant spectral changes should be ascribed to glass formation. A shorter pulse duration (6-8 ns) was consequently used in a number of experiments described by Yamada et al. (1999), Sasaki et al. (2001), and Hiroi and Sasaki (2001). They used a nanosecond pulsed Nd-YAG laser (1064 nm) on pellets of pressed silicate powder, inducing vaporization and redeposition processes. This was supposed to well simulate dust impact, also because of the comparable duration of the pulse (6-8 ns).

Such experiments showed progressive (increasing the shot number) darkening and reddening of the UV-vis-NIR silicate spectra, whose comparison with asteroid

spectra led to a time-scale for this process (in the near-Earth space) of about 10^8 yr. They attributed the observed spectral weathering to formation of coating enriched in vapor-deposited nanophase iron (Sasaki et al., 2001).

It is well know that the characteristic of the ablation process strongly depends on laser parameters, and target properties. The interaction between radiation and matter (as ruled by the considered regime) depends on the particular balance of optical properties, laser fluence, duration of the pulse, wavelength of the laser, etc.

In particular, when an infrared Nd:YAG laser (1064 nm) is considered, like in the experiments of Yamada et al. (1999) and Sasaki et al. (2001), pulsed laser ablation can simply be treated as a thermal process: infrared laser light excites vibrations (related to defects, impurities or the solid surface itself) and the thermalization of the excitation energy is so fast that the laser can simply be considered as a heat source.

With these sources at high laser light intensities ($> 10^8\ W/cm^2$), the interaction between the laser light and the induced plasma is dominant. The excitation energy is instantaneously transformed into heat, and the resulting increase of temperature changes the optical properties of the material, and the amount of absorbed laser power. In this regime, the irradiated material becomes absorbing at any wavelength due to surface breakdown and plasma formation. The temperature rise can result in thermal ablation.

A typical problem with infrared lasers is a surface damage due to uncontrolled melting or ablation of the target; moreover the temperature rise induces stresses which can also affect the optical properties of the surrounding materials. With ultraviolet laser radiation the situation can be quite different. If the photon energy is high enough, laser light excitation can result in a direct bond breaking: as a consequence, single atoms, molecule clusters, and/or fragments desorb from the surface. Furthermore, high photon energies (i.e. short wavelength) allow spatially well defined and stoichiometric ablation (congruent ablation), rapid heating and cooling rates with low damage of the surrounding materials.

1.3 Ices: chemistry and colors

Ices are thought to be dominant on the surface of objects in the outer Solar System. The Vis-NIR spectra of some centaurs and TNOs (or Kuiper Belt objects, KBOs) indicate that their surfaces are rich with simple molecules such as H_2O, N_2, CO_2, CH_4 , and CH_3OH.

Water ice and methane ice have been easily detected due to their relatively strong spectral features. For instance, water ice has been observed on the centaurs Pholus (Cruikshank et al., 1998) and Chiron (Luu et al., 2000), and on KBOs Quaoar (Jewitt and Luu, 2004) and Orcus (Fornasier et al., 2004; de Bergh et al., 2005). Methane (CH_4) is present on Pluto (Owen et al., 1993), on TNO 2005 FY_9 (Licandro et al., 2006), and probably on the TNO Sedna (Barucci et al., 2005).

Other species and interesting ice mixtures have been observed on TNOs, Pluto, Eris, and other objects such as short-period comets, centaurs, and Triton. Methanol (CH_3OH) bands have been possibly identified on Pholus (Cruikshank et al., 1998), as discussed below. For some objects, there are indications of an inhomogeneous surface (see, e.g., Licandro and Pinilla-Alonso (2005)). Benzene (C_6H_6) has not been observed on TNOs or centaurs; in this thesis, it is used as a template for aromatic compounds.

1.3.1 Chemistry of mixtures

Many comets [6] have very elliptical closed orbits, and spend most of time very far from the Sun. Comets have a composition, measured in the gas phase from sublimating molecules, to some extent similar to that observed on icy grains mantles in dense molecular clouds. They are water-rich with significant contribution of CO_2,

[6]The distinction between comets and asteroids is controversial; originally comets were identified because of their activity. A comet is a small body that, due to the effects of solar radiation upon the nucleus, exhibits a coma and/or a tail. The nucleus is a minor body composed of rock, dust, and ices. Thus, comet surfaces should be composed also by volatile materials, besides the same rocks as the asteroids. For this reason, the word comet is often associated with the outer Solar System, while the word asteroid is associated with the inner Solar System. However, there are objects that show asteroidal characteristics during a long time, and comet-like activity for limited amount of time. Thus, from the point of view of the processing (i.e. the subject of this thesis), a more important distinction should be made between silicate-rich and ice-rich objects.

CO, methanol and other hydrocarbons. Comets appear to be nitrogen poor.

On the other hand the surface of Pluto and Triton are nitrogen rich although, locally, ice segragation could have formed surface spot rich in different molecules. In addition to the dominant solid nitrogen and solid methane, CO and CO_2 have been detected on Triton's surface. Pluto has some CO and no CO_2.

The spectrum of the centaur Pholus has been matched with five components among which are 15% of water ice and 15% of methanol ice (Cruikshank et al., 1998), as shown in Fig. 1.3. Thus in addition to silicates and carbons, the icy materials that are of particular interest for outer bodies are mixtures dominated by water and/or hydrocarbons and/or nitrogen, with noteworthy amount of CO and/or CO_2.

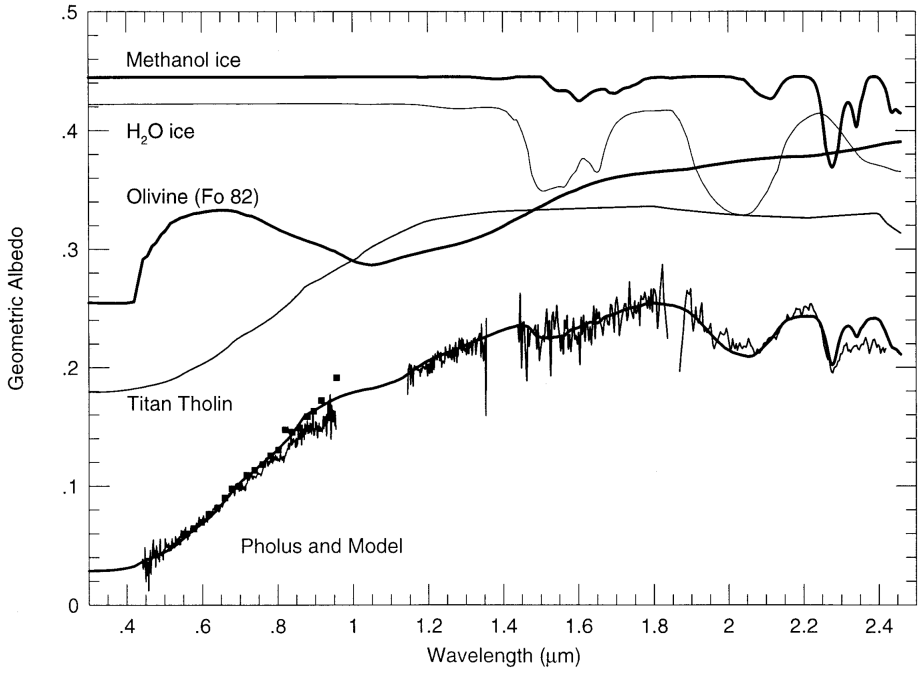

Figure 1.3: The spectrum of Pholus with the model by Cruikshank et al. (1998), showing the spectral contributions of each of the four principal components. The spectra of methanol ice, water ice, olivine, and Titan tholin are computed from their complex refractive indicies (n, k) with the Hapke scattering model, but they are shown here with various scalings (of the ordinate) to fit them conveniently on the figure. Not shown is the neutral and featureless spectrum of amorphous carbon.

Therefore ion irradiation experiments can be performed on relevant mixtures, to predict the presence of still undetected species. For instance, irradiation of H_2O:N_2 mixtures leads to the formation of N_2O, NO and NO_2 (Strazzulla et al., 2003a). Although nitrogen and water are likely to be rapidly spatially segregated, because of their very different thermodynamic properties, it is possible that, due to seasonal sublimation and re-condensation observed for example on Pluto and Triton, the highly volatile nitrogen is deposited on the entire surface of the objects, i.e. including the water-rich spots. It has been shown that N_2 condensed on amorphous water ice diffuses in at temperatures of about 30 K thus realising an H_2O:N_2 mixture. This is demonstrated by the appearance of a sharp water feature in the IR spectra at about 1.88 μm that is easily distinguishable from the broad one of polymeric water centered at about 2 μm (Palumbo and Strazzulla, 2003).

Irradiation of H_2O:CH_4:N_2 mixtures leads to the formation of several species among which carbon dioxide, carbon monoxide, HCN, HNCO, N_2O and CN bearing species (Palumbo et al., 2004). The formation of several new species among which carbon dioxide and suboxides, nitrogen oxides, and a number of CN bearing species have been also observed in irradiated CO:N_2, CH_4:N_2 and CO:CH_4:N_2 mixtures (Moore et al., 2003; Palumbo et al., 2004). Laboratory experiments have also shown that carbonic acid (H_2CO_3) can be expected on objects with surface areas rich in H_2O:CO_2 mixtures (Brucato et al., 1997).

1.3.2 C-rich species

In this thesis I will report the results of new irradiation experiments on C-rich ices. These species play a very important role in determining the spectral behavior of interstellar grains as well as of outer Solar System objects.

Solid methanol (CH_3OH) is thought to be present both in frozen mantles on interstellar grains and on some objects in the outer Solar System. Icy mantles on interstellar dust particles, inside dense molecular clouds (T $\sim$ 10-20 K), and particularly in the circumstellar region around forming massive stars, contain CH_3OH among other simple molecules, such as H_2O, CO, and CO_2. Different absorption

features, assigned to solid methanol after comparison with laboratory spectra, have been identified along several lines of sight of obscured IR sources (Dartois et al. (1999); Keane et al. (2001), and references therein).

Methanol, or some other simple molecule exhibiting C-H stretching, deformation and combination modes, has also been suggested to be present in some objects in the outer Solar System, such as comets (Mumma et al., 1993) and centaur 5145 Pholus (Cruikshank et al., 1998). Methanol has been observed in the coma of comets as gas phase species most likely directly sublimated from the nucleus. Its abundance has been estimated to be on the order of few percent with respect to the dominant water ice (Mumma et al., 1993), and varies among different comets, some appearing to be CH_3OH rich.

Methanol has been tentatively identified on Pholus (Fig. 1.3): Cruikshank et al. (1998) observed the methanol band around 2.27 μm, although the band around 2.34 μm has not been observed, and modeled near-IR spectra with a multicomponent ensemble containing both refractories (silicates and carbons) and ices (water and methanol). More recently Cruikshank et al. (2003)) used the scattering theories of Hapke and Shkuratov to model the reflectance spectra and colors of Kuiper belt and centaur objects.

Both theories yielded good models of the reflectance spectrum of the centaur Pholus using five components, although the derived abundances differed widely. The abundance of methanol would be comparable to that of water ice (between 30 and 100% with respect to water). Presumably this can be true only for surface layers (not the whole object). This implies that, if the identification is correct, thermal processing has occurred and the analyzed surface layers are strongly enriched in methanol.

Both in the case of comets and of Pholus, methanol could be directly aggregated from the ices in the pre-solar nebula and, in any case, could be subjected to ion bombardment from different cosmic ion populations in the various stages of evolution (pre-solar dust in the interstellar medium, pre-solar nebula, comet or solid object in the outer Solar System; e.g., Strazzulla (1997)). Several studies on the effects of energetic processing (ions and UV photons) of solid methanol and mixtures

with other species have been done (Baratta et al. (2002); Hudson and Moore (2000); Palumbo et al. (1999), and references therein). Palumbo et al. (1999) showed that the profile of the CH_3OH bands varies with increasing ion fluence and, in particular, their relative intensities change strongly. IR transmittance spectroscopy has however mostly been conducted in a spectral range (2.7- 25 μm) where bands due to the fundamental vibrations are detectable (more interesting for application to interstellar ices).

Acethylene (C_2H_2), ethane (C_2H_6), and methane (CH_4), have been observed on several comets (Mumma et al., 1996, 2000, 2001). Ethane and acetylene are possibly present as condensates in Titan's stratosphere (Coustenis et al., 1999), and, perhaps mixed with dominant frozen nitrogen, on Triton and Pluto (Bohn et al., 1994).

Methane is present in dense molecular clouds (Lacy et al., 1991; Boogert et al., 1996, 1997), and on several objects in the outer Solar System. Owen et al. (1993) confirmed the presence of solid CH_4 on Pluto, while Douté et al. (1999) showed that the best model requires a fine grained segregated CH_4 layer covering a compact polycrystalline substrate dominated by N_2 with small amount of CO (0.1-0.2%) and CH_4 (0.5%). Also the NIR spectrum of Triton indicates the presence of CO, CO_2, and CH_4 together with the dominant nitrogen ice (Cruikshank et al., 1993). Saturated hydrocarbons, although not yet detected, could be formed on interstellar grains by hydrogen addition (Mumma et al., 1996) or by energetic processing such as UV and ion irradiation. Cometary ices could however be re-processed by ion bombardment in the Solar System before, during and after the formation of comets themselves (Moore, 1999; Strazzulla, 1997; Strazzulla and Johnson, 1991).

1.3.3 A wide spread of colors

Minor bodies in the outer Solar System show a great variety of spectral colors (Doressoundiram et al., 2002; Peixinho et al., 2004). In particular, some centaurs and trans-Neptunian objects (TNOs) are very red (higher reflectance at higher wavelength), because of what has been labeled "ultrared matter" (Jewitt, 2002).

The wide range of visible and near-infrared spectral behaviors observed can be

only partially explained by a different composition. A number of processes are active in the Solar System that could alter the surface properties of atmosphereless bodies. Consequently, it is widely believed that a competition between aging (e.g., cosmic ion irradiation) and rejuvenating (e.g., impacts with space debris, cryovolcanism, etc.) processes produces the observed color distribution (Luu and Jewitt, 1996).

Some laboratory experiments on species considered to be good analogs of minor bodies surface materials have attempted to simulate the space weathering processes. In particular, ion irradiation experiments have demonstrated that solar wind and cosmic ion irradiation can be very efficient mechanisms in reddening Vis-NIR reflectance spectra of silicates (Strazzulla et al., 2005; Marchi et al., 2005). However, when starting from a red material, such as a bitumen (asphaltite, kerite), the weathering trend is inverted: ion irradiation tends to flatten the spectrum in the Vis-NIR range (Moroz et al., 2004a).

In ion irradiation of both silicates and bitumens, an important role is also played by elastic (nuclear) collisions between ions and target nuclei (Brunetto and Strazzulla, 2005; Moroz et al., 2004a).

1.4 Bitumens and other organics

1.4.1 The organic crust

As simulated by laboratory experiments, simple molecules are destroyed by energetic particles and by UV photons, with consequent decrease of their band intensities (Brunetto et al., 2005a) and formation of other molecules (Palumbo et al., 1999; Moore et al., 2003). Furthermore, when carbon is present, an organic residue is synthesized that may produce a crust of refractory material, as in the case of comets in the Oort cloud (Strazzulla and Johnson, 1991; Strazzulla, 1997; Strazzulla et al., 1991, 2001).

These laboratory experiments revealed that when the carbon content is significant, ion irradiation leads to the formation of an organic residue that is left over the substrate after warm up to room temperature. The results indicate that whatever the initial hydrocarbon is, it is converted to a refractory insoluble residue.

Based on these experimental results, it has been suggested that a comet exposed to background particle irradiation develops an outer web of non-volatile material (Johnson et al., 1987) which will lead to the formation of an organic crust, when it is warmed entering in the inner Solar System. However, in situ Raman spectroscopy of carbon-containing ice mixtures has revealed that the organic crust is already forming during irradiation at low temperature and its formation does not require the warming of the sample (Strazzulla et al., 1991; Palumbo et al., 2004; Ferini et al., 2004). This gives support to the hypothesis that an organic crust could be already formed during the TNOs long residence far from the Sun.

In particular, it has been suggested that, due to irradiation processing, TNOs could have a crust even thicker and/or developed much rapidly than previously estimated for comets in the Oort cloud (Strazzulla et al., 2003b).

1.4.2 Tholins

To match the red spectral slope observed on many TNOs or centaurs, it is sometimes necessary to include a material rich in carbon compounds in the scattering models.

A widely used material is the so called "tholin"; tholins are organics produced by plasma irradiation of organic-rich gases. Cruikshank et al. (1998) for instance (Fig. 1.3) used the optical constants published by Khare et al. (1984a) for "Titan" tholin. Such material is the involatile product of plasma irradiation of a gas mixture of N_2 + CH_4 = 0.9 + 0.1, corresponding approximately to the bulk composition of Titan's lower atmosphere (Khare et al., 1984b). Titan tholin consists of a variety of compounds, such as hydrocarbons and nitriles.

In both the Hapke and Shkuratov models, small quantity of tholins are usually included, sometimes as inclusions in water ice. The role of the tholins is to provide the strong absorption observed in many outer bodies, from about 1 μm toward the UV. Also, tholins have relatively high reflectance in the 3.2 μm region, and they therefore quench the very strong absorption of water ice in this spectral region. This effect of tholin has been used to match the spectra of some of the Saturn's

large satellites (Cruikshank et al., 2005).

It should be noted that the tholins used in the models are considered representative of a very broad class of complex organic solids produced by energy deposition in gases and ices having compositions of planetary relevance (Cruikshank et al., 2005). For this reason, experiments described in this thesis will give more detailed information on processed ices and their spectral properties in the Vis-NIR. The by-products of these experiments are expected to well reproduce the organic materials present on outer Solar System objects.

1.4.3 Bitumens

Natural solid oil bitumens (asphaltites, kerites, anthraxolites) appear to be useful spectral analogs for cometary and asteroid refractory organics. They show color similarities to the surfaces of dark asteroids and cometary nuclei, as well as compositional and structural resemblances to organic components of carbonaceous chondrites. These dark solids are composed of a variety of organic compounds, most of which are aromatic and aliphatic hydrocarbons (Moroz et al., 1998).

These materials are very dark in the visible and have red-sloped spectra in the visible and near-infrared. They may be comparable in composition and structure to refractory organic solids on the surfaces of primitive outer Solar System objects (Moroz et al., 2004a).

Ion irradiation experiments recently performed at the Catania laboratory by Moroz et al. (2004a) showed that irradiation-induced carbonization gradually flattens the spectral slopes of these red organic solids, indicating an unusual space weathering trend (see Fig. 1.4). It was found that such spectral alteration increased with increasing contribution of nuclear versus electronic energy loss. This implies that nuclear (elastic) energy deposition plays an important role in changing the optical properties of irradiated refractory complex hydrocarbon materials.

The observed rise of reflectance in the visible range and its drop in the near-infrared have been interpreted as an increase of the absorption coefficients. The increase in overall absorption is probably due to modification of the chemical struc-

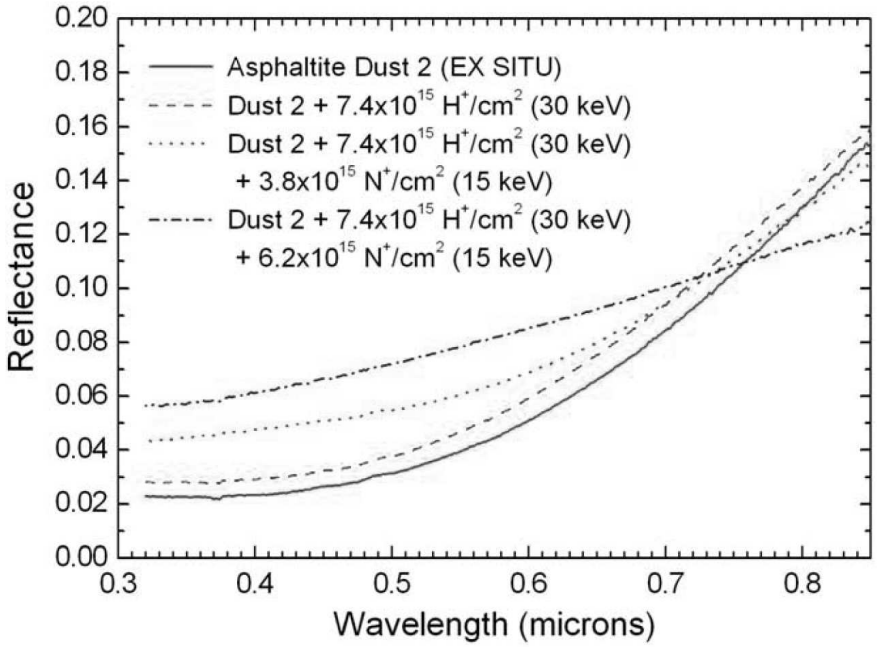

Figure 1.4: Absolute reflectance spectra of asphaltite dust sample before and after irradiation with 30 keV H^+ and 15 keV N^+ ions. Adapted from Moroz et al. (2004a).

ture of complex organics under ion irradiation. Such modification has been demonstrated by the fact that the asphaltite samples, which were completely soluble in chloroform, became insoluble after irradiation.

Interestingly, the Moroz et al. (2004a) experiments indicated that irradiation of these complex hydrocarbon solids at different temperatures (from 40 K to room temperature) produces similar spectral modifications.

Chapter 2

Experimental approach

In this chapter I will describe the laboratory setup I have used to simulate space weathering processes. The main experimental facilities used are the ones in Lecce (Italy) at the Laboratorio di Astrofisica, Dipartimento di Fisica, Università del Salento, and in Catania (Italy) at the Laboratorio di Astrofisica Sperimentale, Osservatorio Astrofisico di Catania (INAF).

2.1 Ion irradiation experiments

Ion irradiation experiments described in this thesis are performed in the Catania Laboratory. The experimental apparatus consists of a stainless steel vacuum chamber (P<10^{-7} mbar) faced to a FTIR spectrophotometer (Bruker Equinox 55) through KBr windows. A scheme of the chamber is shown in Fig. 2.1.

At the center of the chamber there is a cold finger, placed in thermal contact with the tail section of a closed-cycle helium cryostat (10-300 K). An optically rough (diffusing) gold substrate is put in contact with the cold finger for the reflectance measurements and it is used as standard in the 0.7-2.7 μm spectral range, while transmittance studies are performed using a silicon substrate.

In the case of ices, gaseous samples are prepared in a pre-chamber and admitted by a gas inlet, through a needle valve, into the vacuum chamber, where they accrete onto the cold substrate.

The substrate is surrounded by a cold trap; inside the trap the pressure is lower

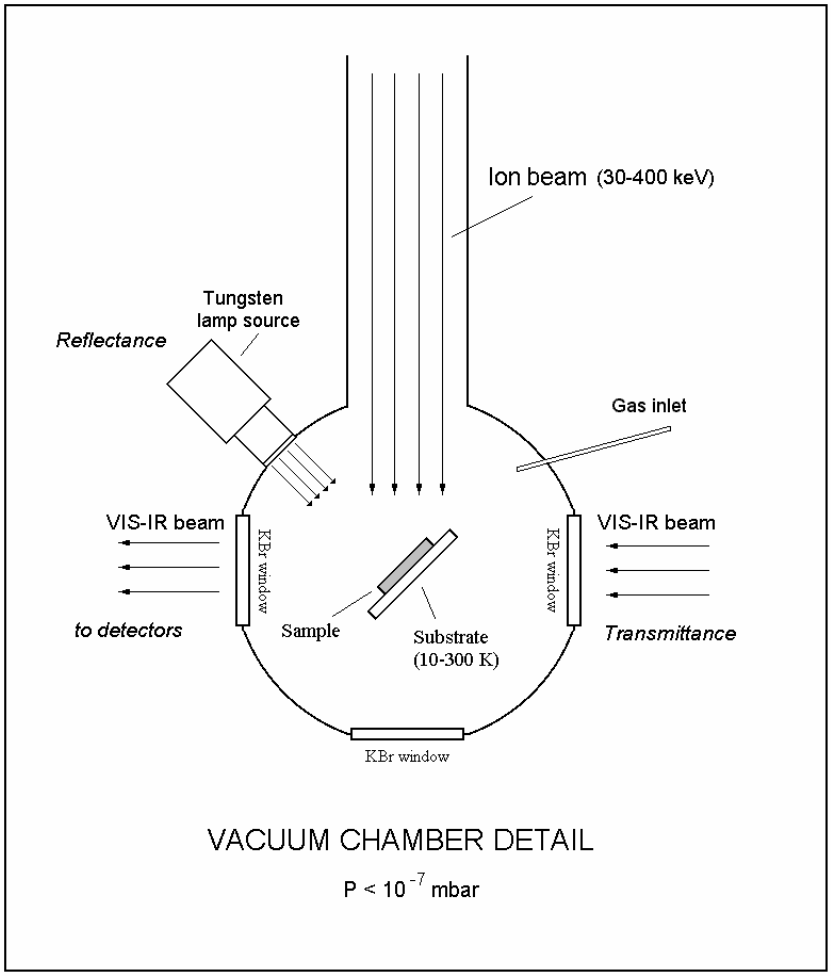

Figure 2.1: A scheme of the vacuum chamber: samples are in contact with the cold finger; the chamber is interfaced to an ion implanter (200 kV); bi-directional reflectance spectra are acquired using a tungsten lamp source, put perpendicularly to the sample surface; in situ spectra can be obtained before, during and after irradiation, without tilting the sample.

by at least an order of magnitude (less than 10^{-8} mbar). The deposition rates depend on the molecule and on the temperature, and can be fixed, within limits, by the experimenter: we commonly use values between 0.5 and 2 nm/s. Bulk samples (e.g. silicates, carbons, etc.) are simply in contact with the finger, held up in place by a metal corona ring.

The vacuum chamber is interfaced to an ion implanter (Danfysik 1080-200) from which ions with energy from 30 up to 200 keV (400 keV for double ionization) can

be obtained; the ion beam produces a uniform spot on the target that is greater than the spot of the vis-IR beam, and currents are usually below 1 μA/cm^2 to avoid macroscopic heating of the sample.

In the case of ices, the currents are typically from 100 to 400 nA/cm^2; the irradiation at the lowest doses is done at the lowest ion currents, the fresh ice being more sensitive to possible temperature increases. If the irradiated sample becomes more refractory, then the ion current is increased to speed up the experiment and avoid as much contamination as possible. The ion current is continuously monitored during irradiation. The ion beam is in fact passing through a sweeping system, producing an area of about 4 cm^2; then it passes through a metallic circular corona having a circular hole of about 1.5 cm^2. Ions that pass through the hole hit the sample; the area of the metallic circular corona around the hole is equal (about 1.5 cm^2) to that of the hole. In this way, we continuously read the ion current.

In the last 10 years, a large number of calibration experiments have been performed at the Catania laboratory to measure the quantity of contaminants (mostly H_2O) deposited during the experiments. Under our present standard conditions the background water deposition is less than 0.25 Å/minute (see, e.g., a detailed discussion in Leto and Baratta (2003)). Each of the current experiments lasts, at most, a couple of hours, so a maximum contamination of 30 Å is expected, i.e., 0.3% of a typical thickness for the originally deposited ice film (see the following chapters). However, the same bombarding ions cause sputtering from the surface of the sample. Thus, the amount of contaminant is negligible. This is also supported by the finding that no molecules containing oxygen (or nitrogen) are formed during irradiation of pure hydrocarbons. In fact, if even small amounts of contaminants (of the order of 1%) such as water are intentionally added, ion irradiation easily forms CO bonds.

Fast ions penetrating solids deposit energy in the target by elastic interactions with target nuclei and by inelastic collisions causing ionizations and excitations. Thus bonds are broken along the path of the incoming ion producing physico-chemical modifications and the erosion of material from the target (sputtering). The sputtering process and the related astrophysical applications will not be discussed here (see e.g. Johnson (1998)). Chemical modifications induce the formation

of molecules originally not present in the target.

The ion mean penetration depth (R_p), the stopping power (energy deposited per unit path length), and the amount of elastic versus inelastic energy loss are functions of the ion energy and mass (see Fig. 2.2) and of the properties of the target. When ion irradiation experiments are performed to simulate solar wind and cosmic ion irradiation, the corresponding type of ion can be easily obtained in laboratory, though it is more difficult to reproduce the energy distribution of these ions. Therefore, the laboratory results can be used for astrophysical application only when we find out which is the physical mechanism that is causing the observed effects, i.e. when we can extrapolate the laboratory data to a wider range of ion masses and energies.

To compare the elastic vs. inelastic collisions, we often use H^+ 200 keV vs. Ar^+ 200 keV or Ar^{++} 400 keV ions. Because protons are the most abundant ions in space, H is used as a case study for light ions, while Ar, even if not abundant in space, is used as a case for heavy ions. The energy loss of 200 keV protons is essentially due to ionizations and excitations (electronic energy loss); 200 and 400 keV Ar ions lose an important fraction of their energy through elastic collisions with the target nuclei (see Fig. 2.2). The use of these projectiles is then the best we can do to mimic the irradiation of the several ion populations (not just the 1 keV/amu solar wind ions; see Strazzulla et al. (2003b)) that irradiate minor bodies in the Solar System.

Bi-directional reflectance spectra are acquired using a tungsten lamp source, put perpendicularly to the sample surface; the scattered light is collected by the spectrometer at an angle of 45° with respect to the incident radiation. Furthermore, since the ion beam forms an angle of 45° with the target plane and of 90° with the collected vis-IR radiation, spectra can be obtained before, during and after irradiation, without tilting the sample. Transmittance spectra can also be collected in the case of low absorbing samples, with the vis-IR radiation traversing the sample through a hole in the cold finger. Spectra are always rationed to the background spectrum which includes the substrate.

With our experimental setup we can measure in situ bidirectional reflectance spectra in two distinct and partially overlapping ranges (0.7-1.1 and 0.9-2.7 μm, al-

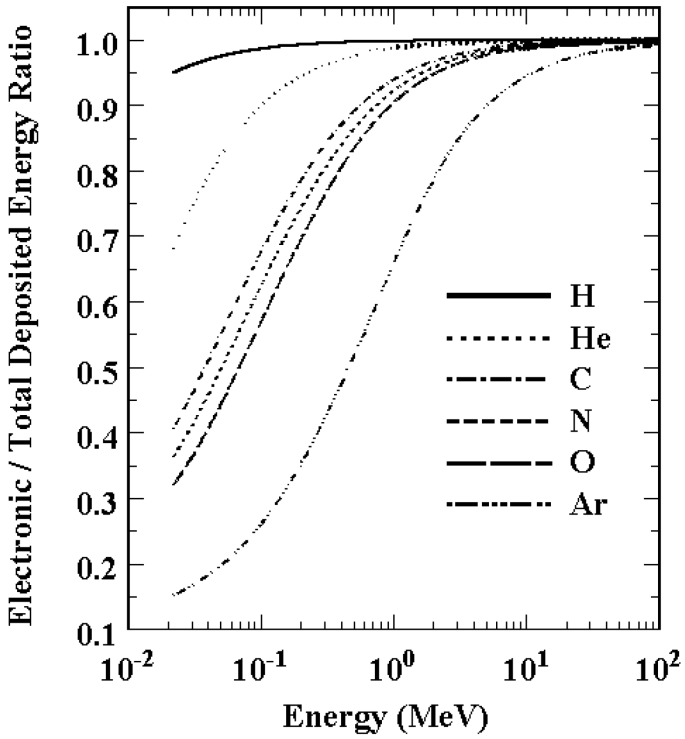

Figure 2.2: Ratio of electronic to total energy loss as a function of incident energy for various ions colliding on water ice target. Computed from the Stopping and Range of Ions in Matter (SRIM) code of Ziegler et al. (1985) at http://www.SRIM.org/. After Strazzulla et al. (2003b).

together covering the 0.7-2.7 μm spectral range), without removing the sample from the vacuum chamber; we can also collect hemispherical reflectance spectra ex situ, in the range 0.25-2.5 μm, using $BaSO_4$ as reference material. In situ measurements avoid atmospheric contamination.

In the case of irradiated ices, we express the amount of energy released to the sample (dose) in eV per small molecule (16 amu), because it is a convenient way to characterize chemical changes, and to have a comparison with other experiments with different samples. The errors in the dose are less than 20% of the calculated values.

Because the unprocessed ices are transparent in the studied range, their spectra show a typical interference pattern (related to the thickness of the film itself) of

two beams: the first reflected at the sample-gold interface and the second at the sample-vacuum interface. We usually subtract the interference pattern in the case of the virgin spectra; if the target is a C-bearing species, such interference is usually destroyed once the film is damaged by the ions.

Raman spectra are collected using a Raman spectrometer equipped with a continuous Ar ion laser beam (514.5 nm) as exciting radiation and a CCD detector in the 0.4-1.0 μm spectral range. We can collect both ex situ micro-Raman spectra (spot of 1-5 μm in size), and in situ macro-Raman spectra (spot of 100 μm). Details of the in situ Raman technique can be found in Brunetto et al. (2004).

2.2 Laser ablation experiments

Laser irradiation and ablation experiments described in this thesis have been performed in the Lecce Laboratory. The experimental setup used to irradiate and ablate the samples consisted of a multigas pulsed excimer laser (Lambda Physics LPX 305i), a multitarget stainless steel chamber and a pumping system.

Irradiations below the ablation threshold (hereinafter BAT irradiation) have been performed with a KrF excimer laser, working at a wavelength of 248 nm with pulse duration of about 20 ns. The laser beam was homogenized by a fly's eye beam homogenizer optimized to work at 248 nm (Microlas), and directed perpendicularly to the sample. The homogenized laser spot on the sample surface was of 0.9 $\times$ 0.9 cm^2, while the energy per pulse of the laser beam was varied in the range 43-105 mJ, obtaining fluences in the range 0.05-0.13 J/cm^2. The number of laser pulses have been changed from 1000 to 20,000.

Ablation of the samples has been performed by an ArF excimer laser operating at 193 nm with pulse duration of 20 ns. In this case the laser beam was focused by a lens and then directed onto the target at an angle of 45° to have a spot of about 1.5 mm^2, so that the laser fluence is about 2 J/cm^2. The targets were mounted vertically on a holder, which can support up to three different targets. Two different types of motions (spinning and spanning) are possible for the targets, in order to irradiate a given area of the samples, and ablate it uniformly. Therefore, a certain number

of pulses is needed to cover a single cycle of motion; further pulses correspond to further passages and ablation on the same area.

The duration of our laser pulse (about 20 ns), typical for an UV excimer laser, is longer than the 7 ns duration used by Yamada et al. (1999). However, only a change of orders of magnitude (regime of picoseconds, or femtoseconds, etc.) would cause strong differences in the physical process. For instance, lengthening the duration to microseconds one would get effects similar to those described in the paper by Moroz et al. (1996). So, the difference between 20 and 7 ns should have little influence on the results.

The total dose (measured in J/cm^2), in the case of BAT irradiation is given by: dose = fluence $\times$ number of pulses; while in case of ablation it is given by: dose = laser energy $\times$ number of pulses/ablated area. Note that, at a given fluence, a large number of pulses may correspond to the lower dose in an increased ablated area, i.e. to about a single complete cycle of motion (spinning and spanning) of the target. In case of ablation, a silicon substrate was positioned parallel to the targets in order to collect the ablated material (film deposition); the distance from target to the substrate was 50 mm. Both BAT (below ablation threshold) irradiation and ablation were performed in a vacuum chamber, evacuated down to 5×10^{-5} Pa, with a frequency of pulses of 10 Hz.

It has to be stressed that, differently from the case of Yamada et al. (1999) and Sasaki et al. (2001) where the samples were placed horizontally, with our experimental setup the targets can be mounted only vertically; this leads to a diverse profile of the plume and a minor amount of re-deposited material. This difference has to be kept in mind when comparing the spectral modifications.

Directional-hemispherical reflectance spectra are collected using a Perkin-Elmer Lambda 900 spectrophotometer in the UV-vis-NIR spectral range (0.25-2.5 μm), equipped with a Labsphere integrating sphere of 150 mm diameter in Spectralon. The error in the reflectance spectra is of about 5%. The laser irradiation covers homogeneously areas of about 0.5-0.8 cm^2, while the beam spot size in the reflectance measurements is about 0.1 cm^2, so that the reflectance measurements after irradiation refer only to the irradiated area.

In addition, XPS measurements are performed at SuperLab (Laboratory of Surfaces and Interfaces), Consorzio Catania Ricerche, University of Catania (Department of Chemical Sciences); XPS analyses are performed with an XPS spectrometer KRATOS ES 300 (180° hemispherical electrostatic analyzer) and MgKα excitation (1253.6 eV) at 15 kV $\times$ 15 mA power. The pressure in the chamber is less than 10^{-7} Pa. The binding energy scale is calibrated by using several known lines.

2.3 How to extrapolate laboratory results

As discussed in the first part of this thesis, real planetary surfaces are composed of several to many different minerals. Deconvolving a reflectance spectrum to mineral abundance in an unambiguous way is difficult, because the spectra are complex nonlinear functions of grain size, abundance, and material opacity. Multiple scattering models can provide approximate solutions to the radiative transfer in a particulate medium (Poulet et al., 2002). The optical constants of the considered materials are important input parameters for those models, and must be carefully measured in the laboratory.

Unfortunately, the estimation of the optical constants is not a simple task; different methods may produce different results, and several assumptions are usually required. In the case of altered or treated samples (i.e. the cases studied in this thesis), the situation is even more complex, since the resulting material usually retains part of the starting material characteristics, and thus it cannot be easily qualified as a specific and self-consistent species. An example will be given in the third part of this thesis.

Important information about minor bodies composition and processing may come from simpler spectral comparison, that would focus on specific features (e.g. spectral slopes, band peak positions, band areas, etc.) without passing through a complex model. In this case it is possible to compare in an easier way laboratory and observational data.

In any case, an additional obstacle when we want to extrapolate laboratory processing experiments to the Solar System comes from the fact that airless surfaces

Irradiated material	D_A (eV/amu)	Mechanism
Water ice	0.095±0.02	total dose
Forsterite	0.45±0.05	elastic dose
Graphite	0.55±0.05	elastic dose
Diamond	1.29±0.04	elastic dose

Table 2.1: The doses D_A needed to reach about 80% of amorphous material as derived from four different ion irradiation experiments.

are exposed to a huge population of ions and dust, in terms of both mass and energy.

Let us focus on the effects of cosmic ions. Laboratory results obtained after ion irradiation experiments can be extrapolated to the astrophysical environment if we understand the physical mechanism which causes the observed effect. Solid state effects as those studied in this thesis are caused by particles with high L.E.T. (Linear Energy Transfer) i.e. having energies in the keV-MeV range. The energies of cosmic ray and stellar wind particles span a range much larger than that used in laboratory experiments.

As an example, let us consider the amorphization process after ion irradiation, and its application to Astrophysics. It is known that amorphization of irradiated diamond depends on the energy released by elastic collisions, whatever is the colliding ion (Brunetto et al., 2004). Thus a comparison of laboratory results is possible if cosmic particle fluxes are known and the energy fraction lost by elastic collision is estimated.

A comparison can be made between the amorphization doses of four different solid material relevant to Astrophysics: water ice, forsterite, graphite, and diamond. Using the experimental data reported elsewhere (Baratta et al., 2004; Brucato et al., 2004; Brunetto et al., 2004; Leto and Baratta, 2003) I have calculated the doses D_A needed to reach about 80% of amorphous material, in the four cases (Brunetto et al., 2005b). Those values are reported in Table 2.1.

The amorphization mechanisms are different: diamond, graphite, and forsterite amorphize under the effects of the elastic dose released by the ions to the sample, while water ice is amorphized by the effects of the total dose, i.e. both the contribution of the elastic and inelastic energy loss. Among these four materials, diamond

is the hardest to be amorphized.

The experimental values of Table 2.1 are plotted versus the values of the displacement energy for the considered materials. For water ice I used the value of the O-H bonding energy. The resulting plot is given in Fig. 2.3, with a linear fit of the data: $D_A(eV/amu) = a + mE_D(eV)$, where $a = -0.03 \pm 0.05$ and $m = 0.022 \pm 0.003$. The fit is good ($r = 0.98$), confirming that the mechanisms of amorphization for these four materials have been rightly understood. Furthermore, since the linear trend shown in Fig. 2.3 is valid for such different materials (ices, silicates, carbons), it may also act as a prediction for other species and compounds.

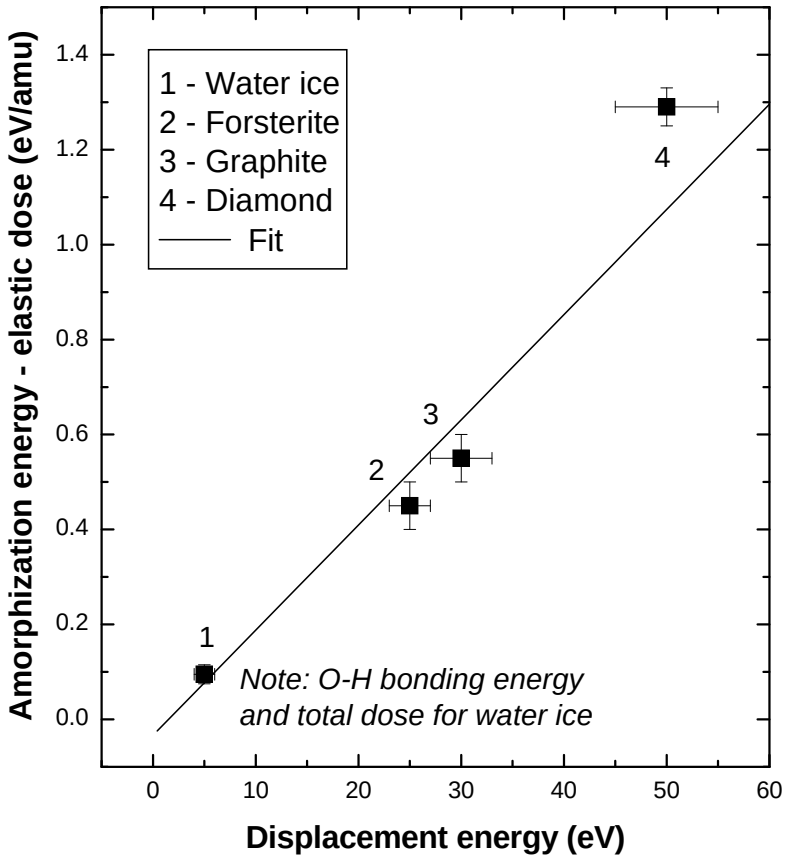

Figure 2.3: The dose D_A needed to reach 80% of amorphous versus the displacement energy, for the four given material. For water ice the value of the O-H bonding energy and the total dose have been used. A linear fit is also shown.

Thus it is clear that a first step in comparing laboratory and observational data is to understand the physical mechanism which causes the observed effect. Then, the knowledge of cosmic particle fluxes and the fraction of energy lost by elastic or inelastic collision is the second important step.

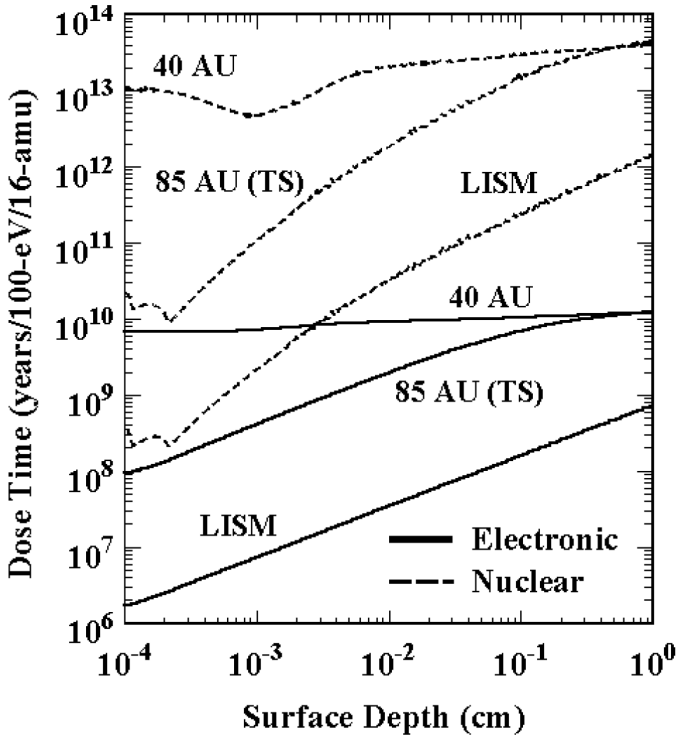

Figure 2.4: Times in years at 40 AU, 85 AU (termination shock), and in the LISM (Local Interstellar Medium) necessary to accumulate chemically significant dosages of 100 eV per 16-amu as functions of target depth for H_2O ice at unit density. The solid and dashed curves are respectively for the electronic ionization and elastic nuclear collision components of ion energy loss. Ion incident angles are 47 degree to approximate isotropic omnidirectional incidence onto a flat surface. After Strazzulla et al. (2003b).

As an example, let us consider the case of ices in the outer Solar System objects. Figure 2.4 gives the times in years at 40 AU, 85 AU (termination shock), and in the LISM (Local Interstellar Medium) to accumulate chemically significant dosages of 100 eV per 16-amu as functions of target depth for H_2O ice at unit density.

Figure 2.4 allows one to evaluate if a particular effect observed in the laboratory is at work on a given astronomical object and to what depths it is relevant. An

important example will be given in the third part of this thesis, about the formation of an organic crust on TNOs.

Part II

New experimental results

Chapter 3

Irradiation and ablation of silicates

As discussed in the first part of this thesis, the effects of space weathering are to change progressively the solar reflectance spectra of airless bodies (in the UV-vis-NIR range), and include spectral darkening, reddening, and subdued absorption bands (Hapke, 2001); such effects would tend to convert spectra of ordinary chondrites, i.e., virgin or fresh materials, to have the spectral traits of S-type asteroids (Chapman, 1996).

In this chapter I report new ion irradiation experiments, performed in the Catania Laboratory, and laser irradiation and ablation experiments, performed in the Lecce Laboratory.

The changes and modifications induced by colliding ions or by laser beam inside the target have been monitored using in situ and ex situ reflectance spectroscopy (0.25-2.7 μm) and Raman spectroscopy. Analogous experiments have been performed in our laboratory on carbonaceous materials and C-rich ices to simulate space weathering by cosmic ions on bodies of the outer Solar System (see next chapter).

3.1 Ordinary Chondrites: Epinal meteorite

Based on the paper: Strazzulla, G., Dotto, E., Binzel, R., Brunetto, R., Barucci, M. A., Blanco, A., Orofino, V. 2005. Spectral alteration of the

Meteorite Epinal (H5) induced by heavy ion irradiation: a simulation of space weathering effects on near-Earth asteroids. Icarus 174, 31-35.

Here I present results obtained by ion-irradiaton of Epinal, an ordinary chondrite meteorite, provided by the Specola Vaticana Observatory. Epinal is an H5 ordinary chondrite meteorite, which shows an unusually high cosmic ray exposure age, with a lower limit of 34-35 Myr (Gilabert and Lavielle, 2001, 2002).

3.1.1 Irradiation and spectroscopy

Micro-Raman spectroscopy

The first step was to perform micro-Raman spectroscopy of Epinal; Fig. 3.1 shows the micro-Raman spectra of two olivine and two pyroxene crystals. The Raman microscope technique allows the analysis of micro-sized structures (3-5 μm) in the meteorite matrices. Many silicate micro-crystals, mainly (Mg, Fe, Ca)SiO_3 pyroxenes (right panel in Fig. 3.1) and (Mg, Fe)$_2SiO_4$ olivines (left panel in Fig. 3.1) are easily identified.

Pyroxenes are characterized by the Si-O stretching modes above 800 cm^{-1}, the Si-O-Si and O-Si-O bending modes between 500 and 760 cm^{-1} and SiO_4 rotation and metal-oxygen translation modes below 500 cm^{-1}. It has been shown (Huang et al., 2000) that, for a constant Ca content, frequencies of the Raman modes in the enstatite-ferrosilite and diopside-hedenbergite series generally decrease with an increase in Fe content. According to the frequencies observed in Epinal (1025, 1009, 681, 662, 400, 340 cm^{-1}) in comparison with the peaks measured in natural and synthetic pyroxenes (Huang et al., 2000), we identify the Epinal pyroxenes with low Fe and Ca content enstatite, that is Mg* = Mg/(Mg + Fe) = 0.8-0.9.

Peak positions of olivines allow the identification of their Fe and Mg content. It is known that in the forsterite-fayalite series of the olivine phase, the Raman shift frequencies of the strongest doublet at $\sim$ 850 and $\sim$ 820 cm^{-1} (tetrahedral stretching bands) decrease with increasing Fe content (Guyot et al., 1986). In Epinal, olivines have band positions at 918, 855, and 825 cm^{-1} implying that the Fe content is lower than 6%. Values lower than 10% are typical for forsterite crystals.

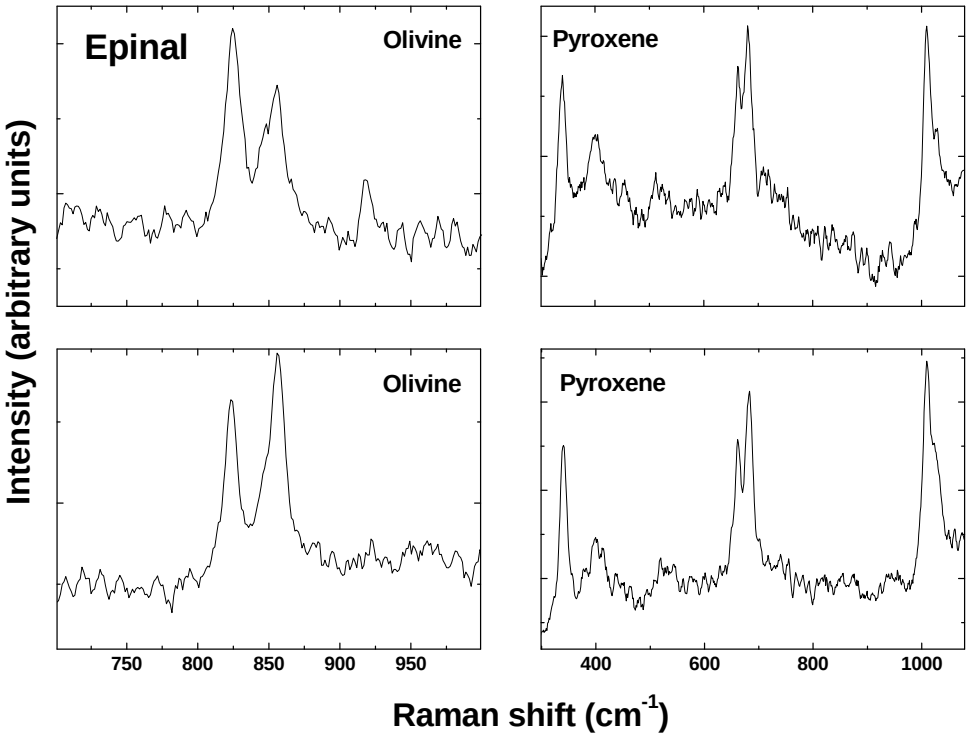

Figure 3.1: Laser (514.5 nm) micro-Raman spectra (spectral resolution 2 cm^{-1}) of two olivine (left panels) and two pyroxene (right panels) micro-crystals in the Epinal meteorite.

Ion irradiation and reflectance spectroscopy

Bulk samples (surface area of about 2 cm^2) of the Epinal meteorite were irradiated with heavy ions, namely 60 keV Ar^{++}, simulating solar wind heavy particle irradiation. Experiments were performed at room temperature, by means of the apparatus previously described. As discussed above, with this experimental setup one can measure in situ bi-directional reflectance spectra in two distinct ranges (0.7-1.11 and 1.1-2.67 μm), before, during, and after irradiation, without removing or tilting the sample; spectra were also collected ex situ, in the range 0.3-0.85 μm, of a virgin sample (i.e., before irradiation) and of the sample irradiated at the maximum dose. Spectra taken at increasing ion fluences are shown in Fig. 3.2. The spectra collected with different spectrometers in the 0.8 μm region seem to match quite well. However it has been found (Dukes et al., 1999) that spectral changes, due to Fe oxidation, may occur because of exposure to the atmosphere. So, the 0.7-2.67 μm range is

more reliable.

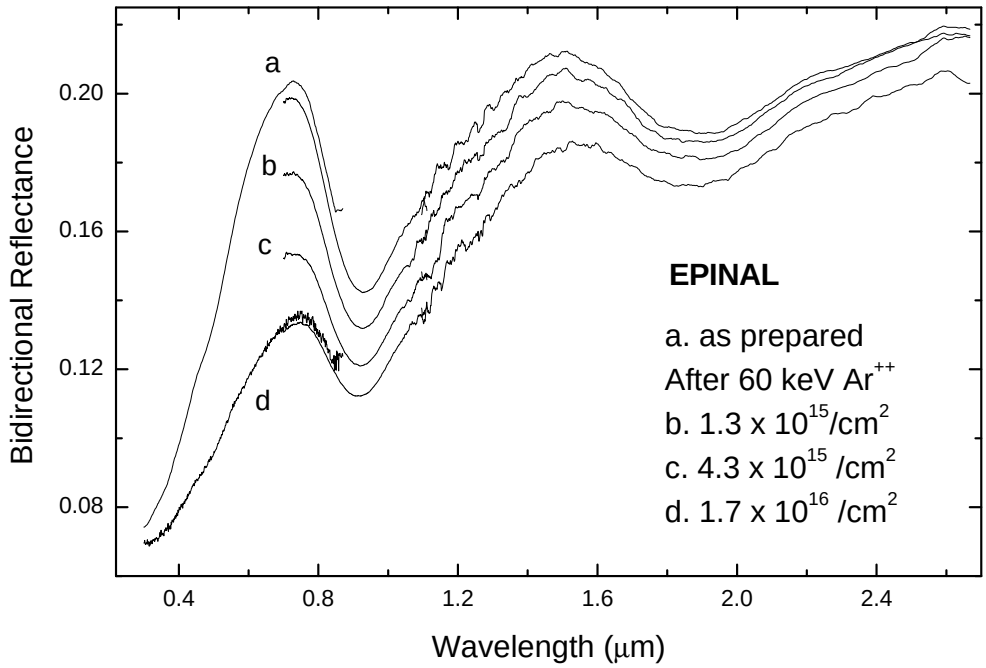

Figure 3.2: UV-Vis-NIR (0.3-2.67 μm) reflectance spectra of the ordinary chondrite meteorite Epinal before irradiation and after three different ion fluences (60 keV Ar^{++}). Spectra in the range 0.7-1.11 and 1.1-2.67 μm have been collected in situ (high vacuum). Spectra in the range 0.3-0.85 μm have been collected ex situ (at atmospheric pressure).

The spectrum of Epinal exhibits the two bands at 1 (band I) and 2 (band II) microns which are typical of ordinary chondrites. The band at 1 μm is due to the presence of ferrous iron in both olivines and pyroxenes. The band at about 2 μm is attributed to pyroxenes (Adams, 1975; Burns et al., 1993; Moroz et al., 2000). Irradiation of the external layers (the penetration depth of 60 keV Ar^{++} ions in the meteorite sample is about 500 angstroms) of Epinal produces a progressive darkening and changes in the slope of the spectra. The spectral slope across band I increases dramatically, while the depths of both band I and band II become weaker. Figure 3.3 reports the ratios between the spectra of the irradiated samples and that of the virgin one.

A few tests with H^+ ions (30 keV) produced modest differences in the spectra. 30 keV protons deposit their energy in the target mainly through ionizations and

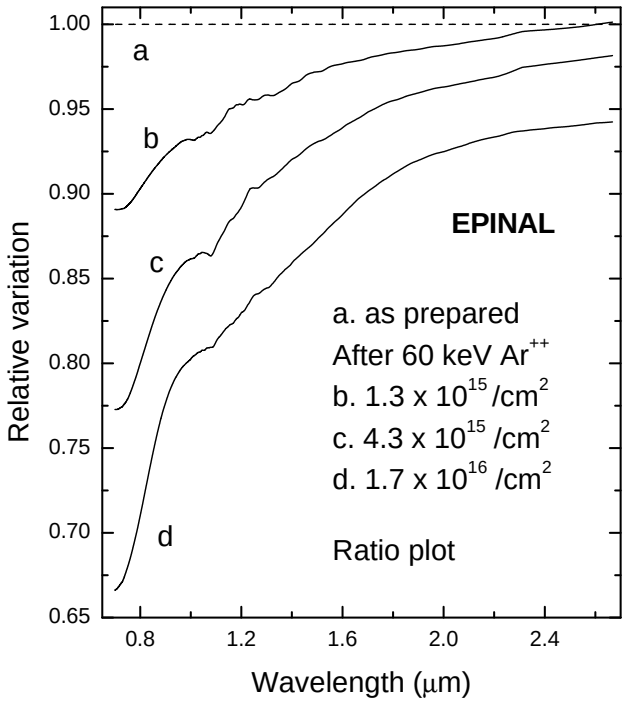

Figure 3.3: Ratio of the irradiated Epinal spectra to the virgin (unweathered) Epinal spectrum.

excitations (inelastic scattering). 60 keV Ar^{++} ions mainly interact with target nuclei through elastic collisions. Thus, results suggest that spectral alteration is produced because the displacements of the nuclei of the target. The key role that displacements play in amorphizing crystalline forsterite has been already demonstrated (Demyk et al., 2001; Jäger et al., 2003; Brucato et al., 2004). Nevertheless it is not possible, at this time, to clearly state if amorphization of the target minerals is causing the observed spectral changes. Further experimental tests are necessary.

3.1.2 Comparison with NEOs and timescale

A first comparison with a few NEOs

In Fig. 3.4 the initial spectrum of Epinal and that obtained at the highest ion fluence are shown normalized to unity at 0.7 μm. Figure 3.4 shows also a comparison between laboratory spectra of Epinal and those of three S-type NEOs: 25143 Itokawa (1998 SF_{36}), 1916 Boreas (1953 RA), and 19356 (1997 GH_3). All spectra

are normalized at 0.7 μm.

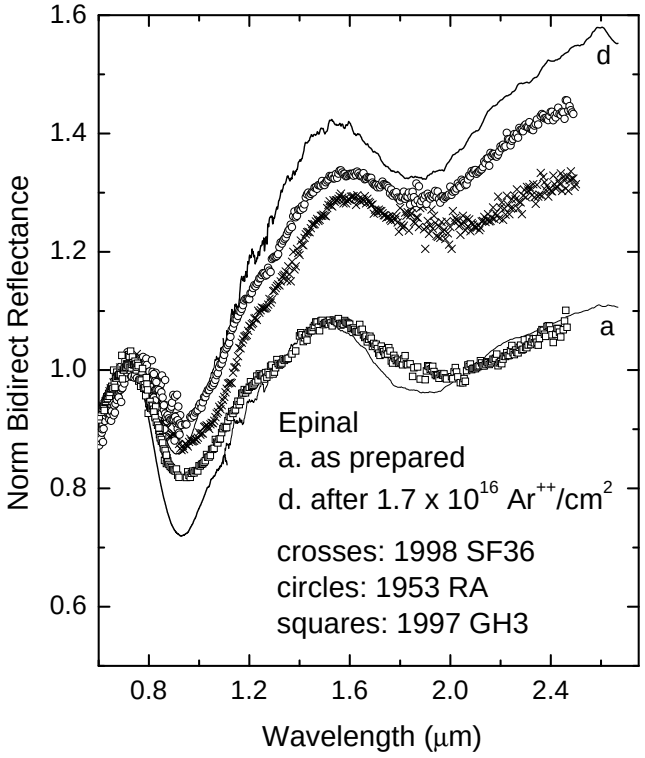

Figure 3.4: The initial reflectance spectrum of Epinal and that obtained at the highest ion fluence are shown normalized to 1 at 0.7 μm. The normalized observed spectra of three NEOs are also shown for comparison.

The three asteroids have been chosen, among those available, because their spectra cover the whole observed spectral variations. Asteroid 1997 GH_3 exhibits the flattest spectrum, i.e., it is representative of less altered objects (or of a surface rejuvenated by a recent collision). Its spectrum is close to that of unprocessed Epinal, but as evidenced by the less intense band I, the asteroid has a lower content of olivine with respect to the meteorite. Asteroids 1916 Boreas and 25143 Itokawa have altered surfaces but their spectra are within the range of variations observed in the laboratory after ion irradiation of Epinal.

From the normalized spectra of Epinal and of 13 NEOs (10 Amors and 3 Apollos) the spectral slopes have been calculated between 0.7 and 1.55 μm as the slope of a linear continuum across band I; the ratio of the areas of band II to band I and

the depth of band I have also been calculated, following the procedure described by Hiroi and Sasaki (2001), and by (Moroz et al., 1996).

Results are plotted in Fig. 3.5, showing that Epinal has a greater band I depth with respect to that of NEOs. Band II to band I area ratios are similar to that of some NEOs, i.e., they should have similar olivine to pyroxene abundance ratio (Gaffey et al., 1993). As a consequence of ion irradiation, the spectral slope between 0.7 and 1.55 μm increases by a factor of six, while the depth of band I becomes weaker by about 25%. Furthermore the band II to band I area ratio in Epinal increases, i.e., the olivine to pyroxene abundance ratio decreases from about 2.3 to about 2.0 (calculated using the calibration reported in Gaffey et al. (1989)); this behavior is the opposite of that reported by Moroz et al. (1996) in impulse laser experiments on the L5 ordinary chondrite, Elenovka.

From both of the plots in Fig. 3.5 it is clearly demonstrated that, though showing a different depth for band I, the points for irradiated Epinal well reproduce the whole spread of spectral slopes observed for S-type NEOs.

The aim of this section is not to obtain a good fit between Epinal and any of NEOs. (See, e.g., Hiroi and Sasaki (2001) for a successful fit of asteroidal spectra with a mix of altered and unaltered silicates.) The purpose is to study a physical process that could be responsible for the dispersion of the observed spectral slopes. Further ion irradiation experiments on materials having different initial mineral compositions are described in the following sections.

A quick estimation of the timescale

Solar wind particles dominate the ion population in the near-Earth region. Solar wind ions have an energy of about 1 keV/amu (amu = atomic mass unit). The flux of Ar ions (36 keV) in the solar wind has been measured to be 4×10^2 ions $cm^{-2}sec^{-1}$ (Jull et al., 1980) at 1 AU (AU= Astronomical Unit, i.e., the average Sun-Earth distance) and decreases as the square of the distance from the Sun. The maximum fluence of Ar^{++} ions we used in the experiments is 1.7×10^{16} ions cm^{-2}. This, in the near-Earth region, corresponds to an irradiation time of about 1.3×10^6 yr.

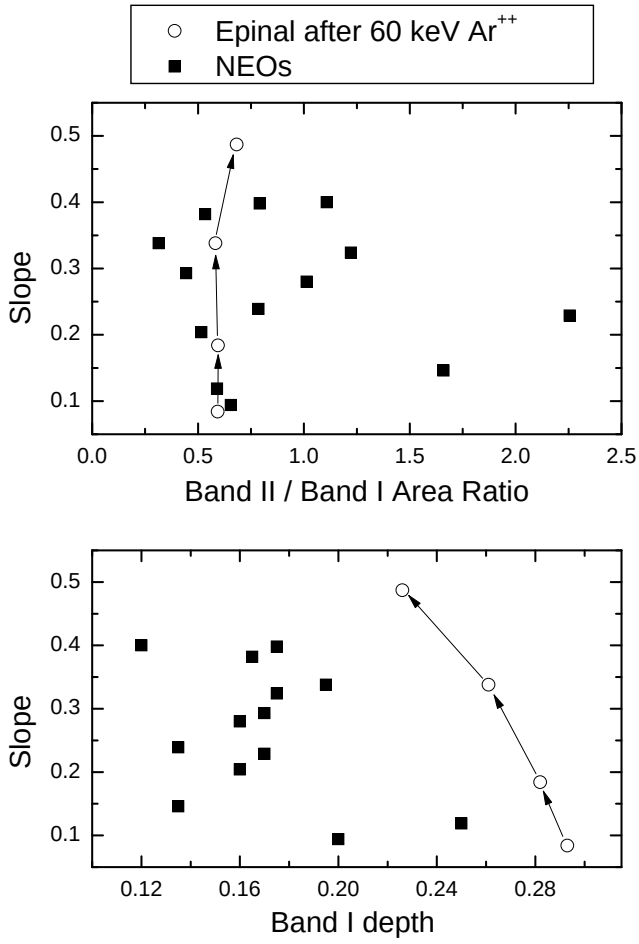

Figure 3.5: Plot of spectral parameters of Epinal and NEOs. (Upper panel) spectral slope (0.7-1.55 μm) vs. band II to band I area ratio for Epinal and 13 NEOs. (Lower panel) spectral slope (0.7-1.55 μm) vs. band I depth for Epinal and 13 NEOs. Arrows indicate points relative to Epinal irradiated at increasing ion fluences.

This time is however a lower limit because a wide range of the solar wind ions may contribute as well to alter the surfaces. 1 keV protons, although by far the most abundant, penetrate only the very thin skin and their effects are probably due to sputtering of surface material and redeposition on a rough surface (Hapke, 2001) and should affect the optical properties mainly in the UV-visible spectral region. Other heavy ions, however, have effects similar to that of argon. Thus, the timescale for the weathering of NEOs surfaces is estimated to be on the order of 10^4-10^6 yr. This is by far more efficient than the effect due to the micrometeoritic impact simulated in

the laboratory by pulsed laser irradiation (Yamada et al., 1999; Sasaki et al., 2001).

Thus ion irradiation may be able to alter the surfaces of NEOs and reproduce the whole range of observed spectra on short time scales. This implies that either the surfaces exhibiting the flattest (least reddened) spectra belong to objects recently injected in the near Earth orbit or they have been recently rejuvenated "fresh" surfaces.

One mystery regarding solar wind as a primary space weathering agent remains why nearly all NEOs are not more weathered than the main-belt asteroids. Binzel et al. (2004b) find that NEOs greater than 5 km across are most similar to main-belt asteroids, while those <5 km tend to have the best spectral matches to ordinary chondrites. In this scenario, either the smaller NEOs are younger with fresher surfaces or perhaps they do not have sufficient age or gravity to have developed a sufficient regolith to be susceptible to the types of irradiation effects explored here.

Acknowledgments

Vatican Observatory is warmly acknowledged for providing us with a fragment of meteorite Epinal. Italian Ministero dell'Istruzione, Università e Ricerca has supported this research.

3.2 Ion irradiation: the role of elastic collisions

Based on the paper: Brunetto, R., Strazzulla, G. 2005. Elastic collisions in ion irradiation experiments: A mechanism for space weathering of silicates. Icarus 179, 265-273.

As I showed in the previous section, ion irradiation of ordinary chondrite Epinal (H5) with Ar^{2+} 60 keV, produces darkening and reddening of the vis-NIR spectra.

In this section I report results of ion irradiation experiments performed on bulk samples of silicate rich terrestrial rocks with a variety of ions (H^+, He^+, Ar^+, Ar^{2+}) and energies (60-400 keV), and a comparison with a previous study of Epinal and

NEOs (Strazzulla et al., 2005). In these experiments, I have used bulk samples because primarily interested in a comparison with our previous experiments with the Epinal meteorite, which was a bulk sample too. The case of powdered samples is discussed in the third part of this thesis.

Changing the ion energy and mass one can change the ion energy loss per unit of path length and the ratio between the amount of energy lost by elastic and inelastic (excitations and ionizations) collisions between ions and target nuclei. In this way it is possible to investigate the physical mechanism that is responsible for the modifications observed in the spectra.

3.2.1 Characterization of the samples

I have irradiated several samples of bulk silicate-rich rocks (surface area of about 4 cm^2), supplied by the Jackson Co., North Carolina, USA. Samples come from igneous rock fragments: ultramafic, coarse grained peridotite. Freshly cut samples from rock fragments are used, with a surface roughness of about 100 μm.

Micro-Raman analysis was performed to characterize the samples. Raman spectroscopy is a useful technique in providing information about structural properties and chemical composition; in particular the Raman microscope technique allows the analysis of micro-sized structures (3-5 μm) in the sample matrices. Many silicate micro-crystals can be identified in the sample surface; as an example, Fig. 3.6 shows two micro-Raman spectra of (Mg, Fe)$_2$SiO$_4$ olivine (upper panel) and (Mg, Fe, Ca)SiO$_3$ low-Ca pyroxene (lower panel) observed among Jackson silicates. Luminescence continuum is absent here because the structures (3-5 μm) considered in Fig. 3.6 are from pure silicate crystals, with no defects or impurities.

Raman spectra of pyroxene are characterized by the Si-O stretching modes above 800 cm^{-1}, the Si-O-Si and O-Si-O bending modes between 500 and 760 cm^{-1}, and SiO_4 rotation and metal-oxygen translation modes below 500 cm^{-1}. It is well known (Huang et al., 2000) that, for a constant Ca content, frequencies of the Raman modes in the enstatite- ferrosilite and diopside-hedenbergite series decrease with an increase in Fe content. Also the peak positions of olivine allow the identification of Fe and

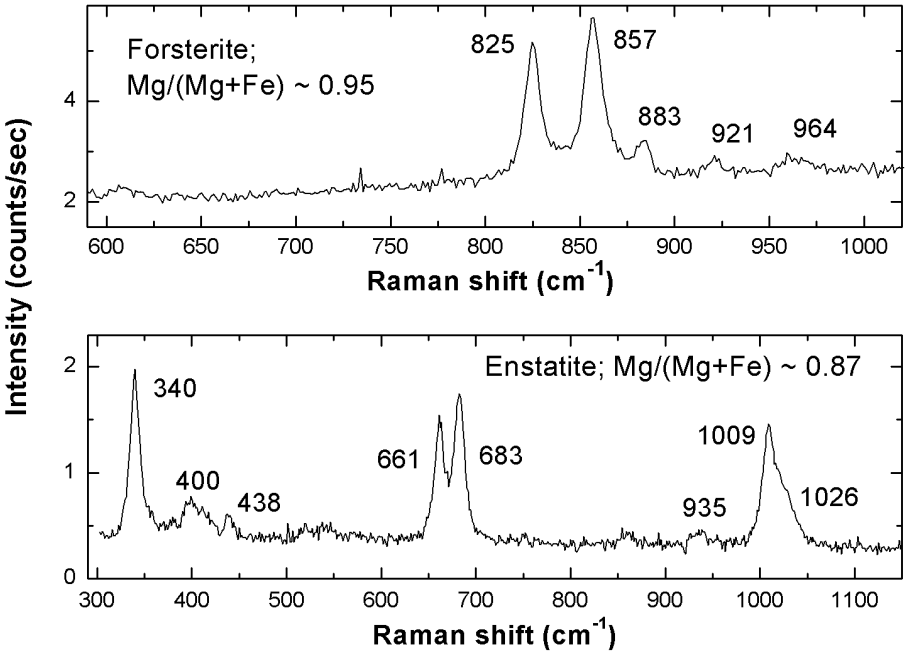

Figure 3.6: Micro-Raman spectra of (Mg, Fe)$_2$SiO$_4$ olivine (upper panel) and (Mg, Fe, Ca)SiO$_3$ low-Ca pyroxene (lower panel) observed in our Jackson silicates. Peak positions of the bands are given; both micro-crystals have low-iron content (forsterite and enstatite).

Mg content. It has been shown (Guyot et al., 1986) that in the forsterite-fayalite series of the olivine phase, the Raman shift frequencies of the strongest doublet at ~ 850 and ~ 820 cm^{-1} (tetrahedral stretching bands) decrease with increasing iron content.

From the Raman shift of the observed peaks (see Fig. 3.6) one can consequently evaluate the relative amount of Mg and Fe in the analyzed micro-crystals; I find that the samples are Mg-rich and Fe-poor (about 5-15% in relative iron content), i.e., mainly low-iron olivine (forsterite), and low-iron and low-calcium pyroxene (enstatite).

The presence of both forsterite and enstatite in these samples is confirmed by spectroscopic analysis. In Fig. 3.7 the ex-situ reflectance spectrum of one of the Jackson silicates is plotted, along with three spectra of pure enstatite, forsterite, and serpentine powders, from the USGS Digital Spectral Library (Clark et al., 2003). A

qualitative comparison hints at the presence of those three different silicate components in the samples. It is important to underline that this is a qualitative comparison, not quantitative, since the USGS spectra are for powder, while here we deal with bulk samples. Serpentine features were not found in the Raman spectra maybe because of both minor content and lower Raman scattering efficiency.

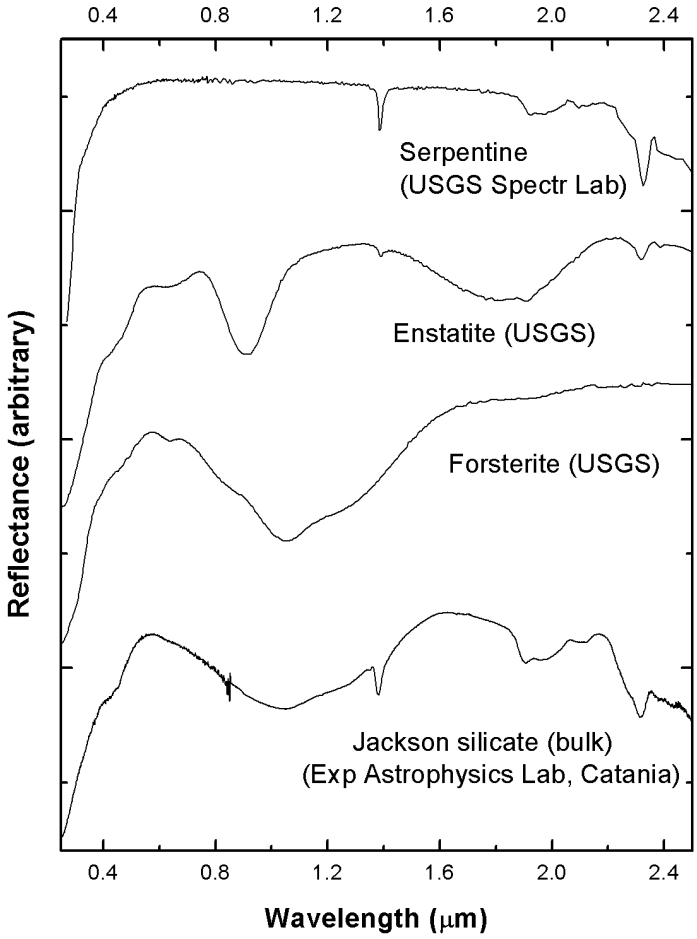

Figure 3.7: Ex situ reflectance spectrum of one of the Jackson silicates, along with three spectra of pure enstatite, forsterite, and serpentine powders, from the USGS Digital Spectral Library (Clark et al., 2003).

The spectrum of unirradiated Jackson sample (Fig. 3.7) exhibits a very strong and broad band at about 1 μm (band I), which is due to the presence of ferrous

Sample irradiation	Ion (E in keV)	Maximum fluence (10^{16} ions/cm^2)	Penetration depth R_p (nm)	Displacements per ion
A	H^+ (200)	1.5	1100	20
B	He^+ (200)	1.5	720	180
C	Ar^{2+} (60)	0.5	50	800
D	Ar^+ (200)	6.8	140	2000
E	Ar^+ (200)	6.0	140	2000
F	Ar^{2+} (400)	4.2	280	3100
G	Ar^{2+} (400)	4.2	280	3100

Table 3.1: The ions used in these experiments, with the energy, maximum fluence, number of displacements per ion, and mean penetration depth in the silicate targets. Note that irradiations A and F refer to the same sample, irradiated first with H^+ ions and then with Ar^{2+} ions.

iron Fe^{2+} in both olivine and pyroxene. It is also observed a contribution of the broad 2 μm band (band II), attributed to pyroxene; the peak position of both band I and band II is known to shift to longer wavelengths with increasing Fe^{2+} and Ca^{2+} contents (Adams, 1975; Moroz et al., 2000). Shallower and weaker features at about 1.38, 1.95, and 2.32 μm are attributed to O-H vibrations in (Mg, Fe)$_3$Si$_2$O$_5$(OH)$_4$ serpentine (phyllosilicate subclass), and a certain amount of trapped water.

The relative amount of olivine, pyroxene, and serpentine in the samples may slightly vary; one can spectrally derive an upper limit of heterogeneity, i.e., deviation from the mean composition, of about 5%: this implies that homogeneity is high enough to discuss the effects of irradiation by different ions.

3.2.2 Mechanisms of ion energy loss and damaging

The aim of this section is to investigate the physical mechanism responsible for weathering of silicates; hence different irradiation experiments have been performed changing the ion mass and energy. I have realized seven different irradiations (A-G) of Jackson rocks with ions and maximum fluence given in Table 3.1 along with the ion mean penetration depth in our configuration (45° angle between the incident beam direction and the sample surface). The ion mean penetration depth (R_p) is a function of the ion energy, ion mass, and of the properties of the target; R_p has been calculated using the SRIM simulation code (at http://www.SRIM.org/).

The stopping power (energy deposited per unit path length) is also a function of the ion energy and mass; ions release energy to the target atoms by elastic and inelastic collisions. The amount of elastic versus inelastic energy loss is as well a function of ion energy and mass, and slightly depends on the target material.

The energy lost by the colliding ions is redistributed among the species present in the target, so that three main effects occur: (1) dislodgment of atoms from their lattice position (vacancies and replacements), (2) ionization processes, and (3) creation of phonons. The atoms of the recoils loose also energy and in turns cause the same three effects.

By using the SRIM code, I have evaluated two parameters to compare the effects of different ions and energies on silicate samples: (1) J_{VAC}, the energy per unit surface (keV cm^{-2}) released by the ions to the target in vacancy formation processes; (2) J_{ION}, the energy per unit surface (keV cm^{-2}) released by the ions to the target in ionization processes:

$$J_{VAC} = EFf_{VAC} \tag{3.1}$$

$$J_{ION} = EFf_{ION} \tag{3.2}$$

where E is the energy of the colliding ions (in keV), F is the ion fluence (ions/cm^2), and f_{VAC} and f_{ION} are the fraction of the energy (per ion) released by a single ion in vacancy formation processes and ionization processes, respectively (calculated by the SRIM code). The contribution of recoils is also included both in J_{VAC} and J_{ION}. The fraction of energy released by a single ion in creation of phonons is f_{PHON}, where:

$$f_{VAC} + f_{ION} + f_{PHON} = 1. \tag{3.3}$$

However, phonons do not contribute to the permanent damage of the target.

For given ion mass and energy, the J_{VAC} value is strongly related to the elastic collisions between ions and target nuclei, while the J_{ION} value is related to the inelastic collisions. For instance, in the case of 200 keV H^+ ions, about 99.6% of the

energy of the colliding ion is released in ionization processes (inelastic collisions), while in the case of 60 keV Ar^{2+} ions this f_{ION} value drops down to about 54%. On the contrary, the f_{VAC} value (elastic collisions) is about 0.02% in the case of 200 keV H^+ ions, while it grows by more than a factor of 100, up to about 2.3%, in the case of 60 keV Ar^{2+} ions.

I have also evaluated the parameter d =number of displacements per cm^2, i.e., d =(displ. per ion)×(ions cm^{-2}); the number of displacements is given by the sum of the vacancies, i.e., atoms removed from their lattice positions, and the replacements, i.e., moving atoms replacing removed atoms of the same species. Actually, in the present case replacement collisions are about 10% of the total, and the number of vacancies is proportional to the number of displacements. All the species get displaced. The d values also are sensitive to the elastic collisions between ions and target nuclei; indeed d is about proportional to J_{VAC}, and they are connected with a progressive amorphization process of the irradiated layer.

The number of displacements per ion can be evaluated by using the SRIM code; their values are also given in Table 3.1; as an example, moving from H^+ to Ar^+ ions (200 keV) the displacement collision events increase by a factor of 100. SRIM simulation has however some limitations, e.g., it does not consider annealing, defect diffusion, or accumulated damage.

3.2.3 Spectral modifications

All the samples listed in Table 3.1 have been studied with ex situ reflectance spectroscopy before and after irradiation. Six of them (from A to F) have been studied also with in situ reflectance spectroscopy, while the last one (sample G) has been also monitored by in situ Raman spectroscopy. Irradiations A and F refer to the same sample.

In Fig. 3.8 results are shown for irradiation of sample G with 400 keV Ar^{2+} ions; the intensity of the two characteristic Raman bands of forsterite decreases with respect to the luminescence continuum, whose value increases with increasing ion fluence (upper panel). In the lower panel of Fig. 3.8 the total area of the

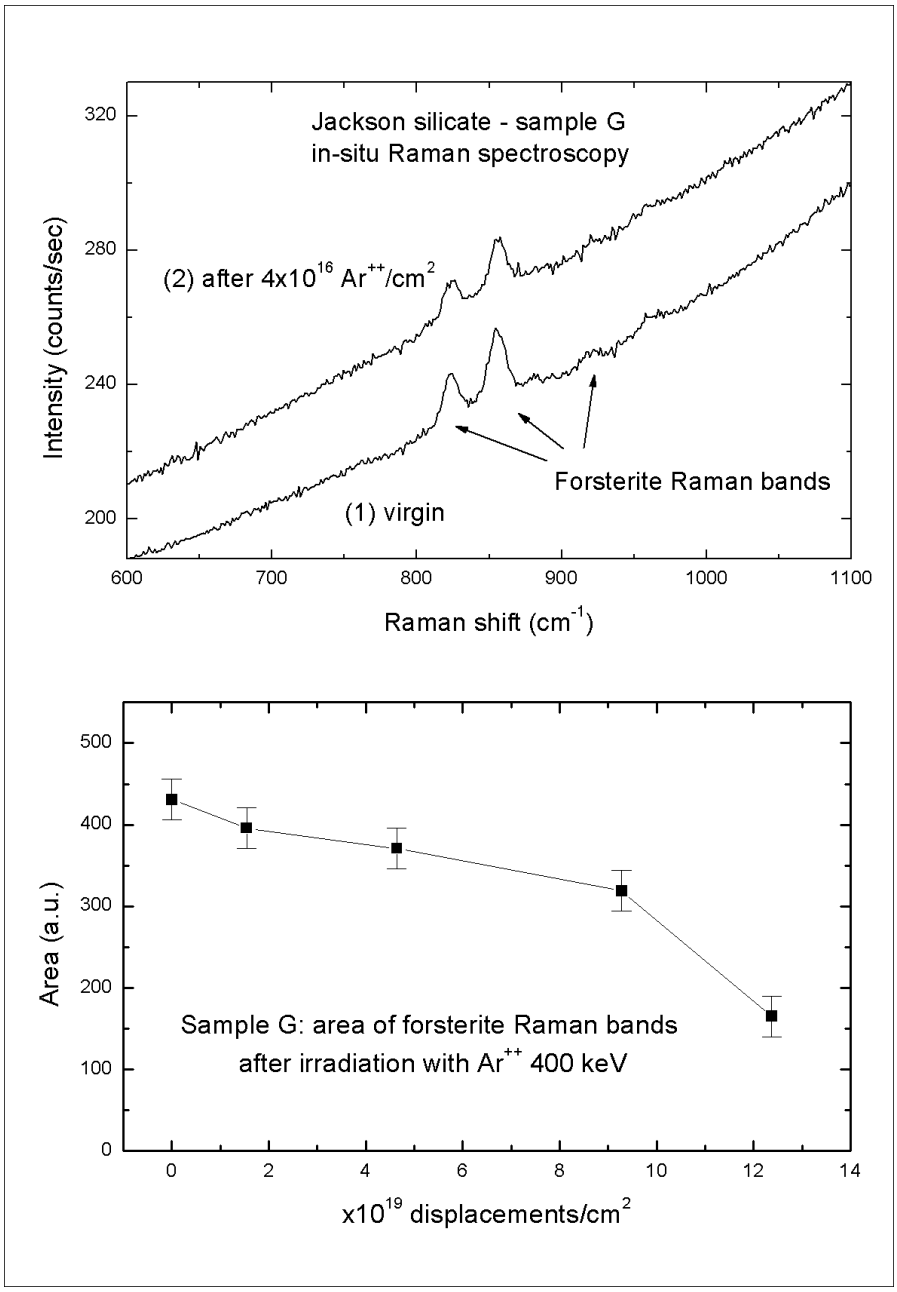

Figure 3.8: Upper panel: in situ Raman spectra of irradiation G (see Table 3.1) with 400 keV Ar^{2+} ions. Lower panel: area of the forsterite Raman bands versus the parameter d; the areas are evaluated after subtracting the continuum.

forsterite Raman bands is plotted versus the parameter d; the areas are evaluated after subtracting the continuum.

Luminescence signal is known to be associated with defects and impurities (Kachurin et al., 1997; Khomenkova et al., 2002). In this case (in situ macro-Raman) the spot of the laser is of about 100 μm and the luminescence signal is high. The Raman spectra shown previously (Fig. 3.6) are ex situ micro-Raman (1-5 μm) spectra and do not exhibit a significant continuum.

The increase of the continuum and decrease of the band areas can be interpreted as an effect of a change in the optical properties of the upper layers of the target, due to ion irradiation.

Indeed, while crystalline unirradiated silicates are transparent to the exciting laser radiation (514.5 nm), in the irradiated samples the laser radiation is absorbed in the very upper layers of the target ($R_p < 1$ μm), after progressive ion fluence; this implies that a fraction of the signal in upper panel of Fig. 3.8 comes from the unmodified target (below R_p) and its contribution decreases following the curve in lower panel of Fig. 3.8.

Reflectance spectra of samples B and G are plotted in Fig. 3.9, collected ex situ before and after irradiation. Strong darkening and reddening of both samples is apparent. Furthermore, these spectral modifications are stronger in the case of sample G than sample B. The area of band I is reduced as the slope of the continuum across band I increases; this spectral reddening agrees with previous experiments of ion irradiation of the Epinal meteorite (Strazzulla et al., 2005) and laser irradiation of silicates (Sasaki et al., 2001). Similar results are obtained for the remaining samples (A, C, D, E, F).

Reddening and darkening are observed also in situ, as it is shown in Fig. 3.10, where spectra from the irradiations A and F (same sample) are plotted. Irradiation with 400 keV Ar^{2+} has been performed after irradiation with 200 keV H^+.

In Fig. 3.10, once again, ions having lower elastic stopping power (H^+), induce spectral modifications less pronounced than ions having higher elastic stopping power (Ar^{2+}), i.e., heavier ions redden and darken UV-vis-NIR spectra more efficiently than lighter ions. In the lower panel of Fig. 3.10 the same spectra are shown normalized to 1 at 0.7 μm.

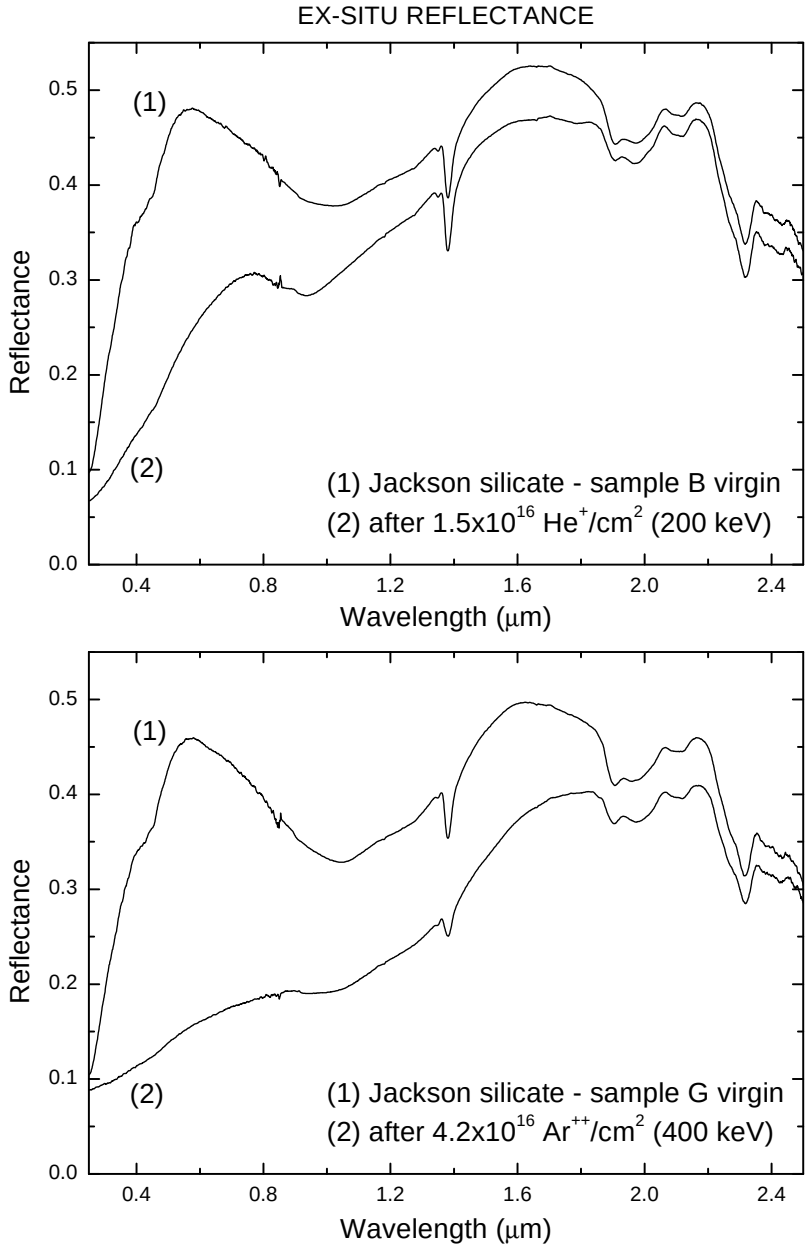

Figure 3.9: Ex situ reflectance spectra of sample B (200 keV He^+, upper panel) and G (400 keV Ar^{2+}, lower panel), before and after irradiation. Darkening and reddening are stronger in the case of sample G than sample B.

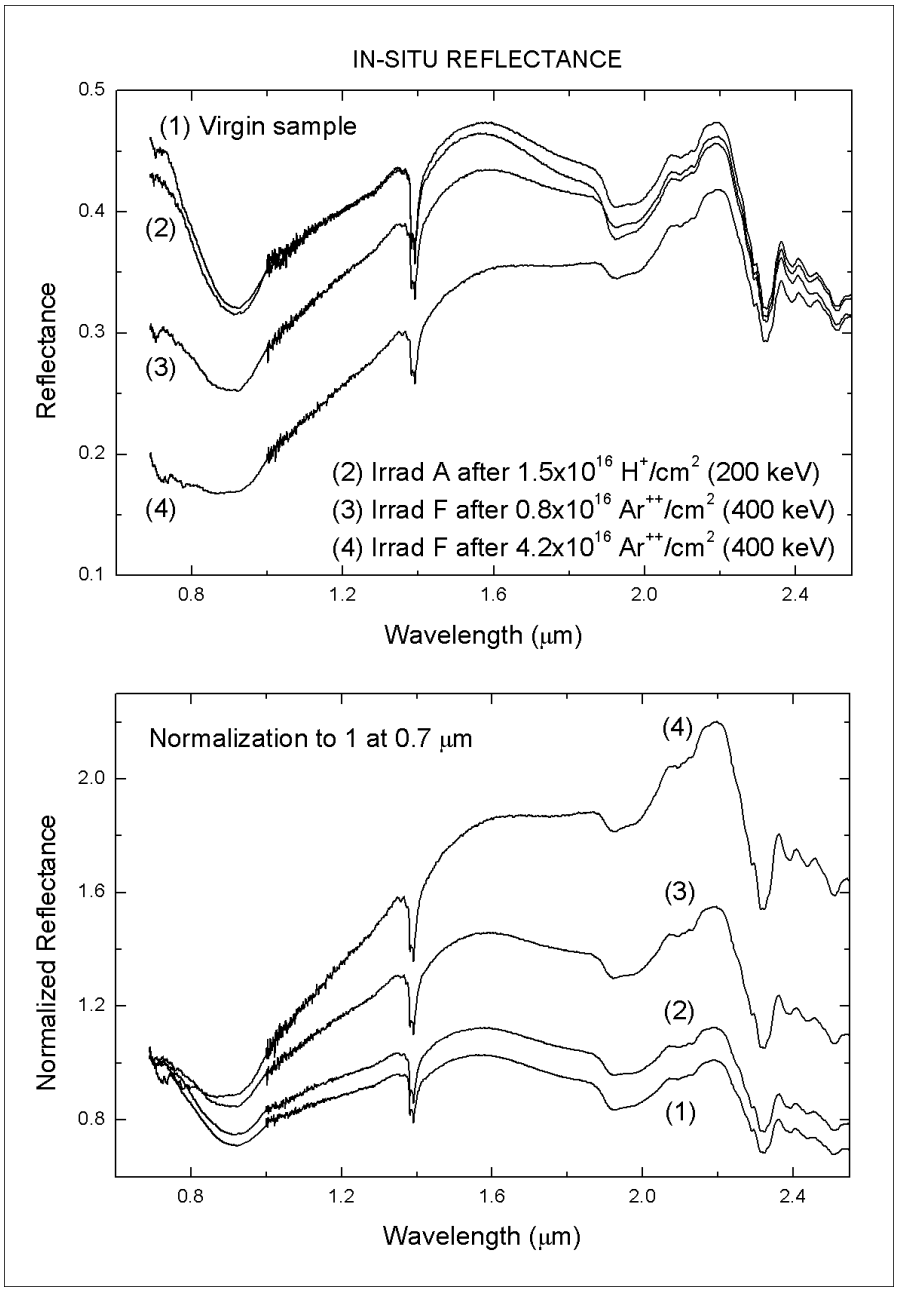

Figure 3.10: Upper panel: in situ reflectance spectra of the irradiations A and F (same sample); irradiation with 400 keV Ar^{2+} has been performed after irradiation with 200 keV H^+. Lower panel: same spectra normalized to 1 at 0.7 μm.

3.2.4 Spectral slopes and elastic collisions

The effects of different ions and energies can be quantified by measuring the spectral slope S (μm^{-1}) of the vis-NIR spectra, following the same procedure de-

scribed by Strazzulla et al. (2005), i.e., the slope of a linear continuum above band I (from about $\lambda_a \sim 0.7$ μm to $\lambda_b \sim 1.6$ μm), after normalization of the spectra at 0.7 μm.

Spectra collected in situ allow us to follow the reddening process with gradually increasing damage value. This procedure differs from that described by other authors (e.g., Hiroi and Sasaki (2001), because normalization here is not at 0.55 μm but at 0.7 μm; this leads to slightly lower values of slopes. One limitation of this procedure is that the slope values may in some case (at the lower fluence) differ from those measured ex situ, i.e., when the left shoulder of band I peaks at wavelength lower than 0.7 μm. In such cases an overestimation of about 0.08 μm^{-1} is present; the S values have been consequently corrected. In Fig. 3.11 the obtained spectral slopes are plotted versus the parameter d, including all the points from the seven experiments listed in Table 3.1, and the spectral slopes obtained after irradiation of the Epinal meteorite (see above). The upper x-axis gives a rough estimate of the astrophysical time-scale (at about 1 AU) necessary to induce the observed spectral reddening on an asteroid surface (see above).

Several results can be drawn from Fig. 3.11:

1. the spectral slopes S measured from different ion irradiation experiments, i.e., different ions and energies, exhibit the same trend when plotted vs the number of displacements per cm^2;

2. the curve determined by data points is characterized by a rapid growth, which tends to alleviate at about 2×10^{19} displacements cm^{-2} (logarithmic-like curve);

3. different samples have different starting slopes ($d = 0$); this is both due to small heterogeneity (about 5%) in the relative content of olivine, pyroxene, and serpentine, and to slightly different surface roughness properties; nevertheless the slopes of all the samples converge to the same curve as the ion damage increases;

4. even the points from irradiated Epinal meteorite follow the same curve, implying that these effects can be observed both in terrestrial and extraterrestrial

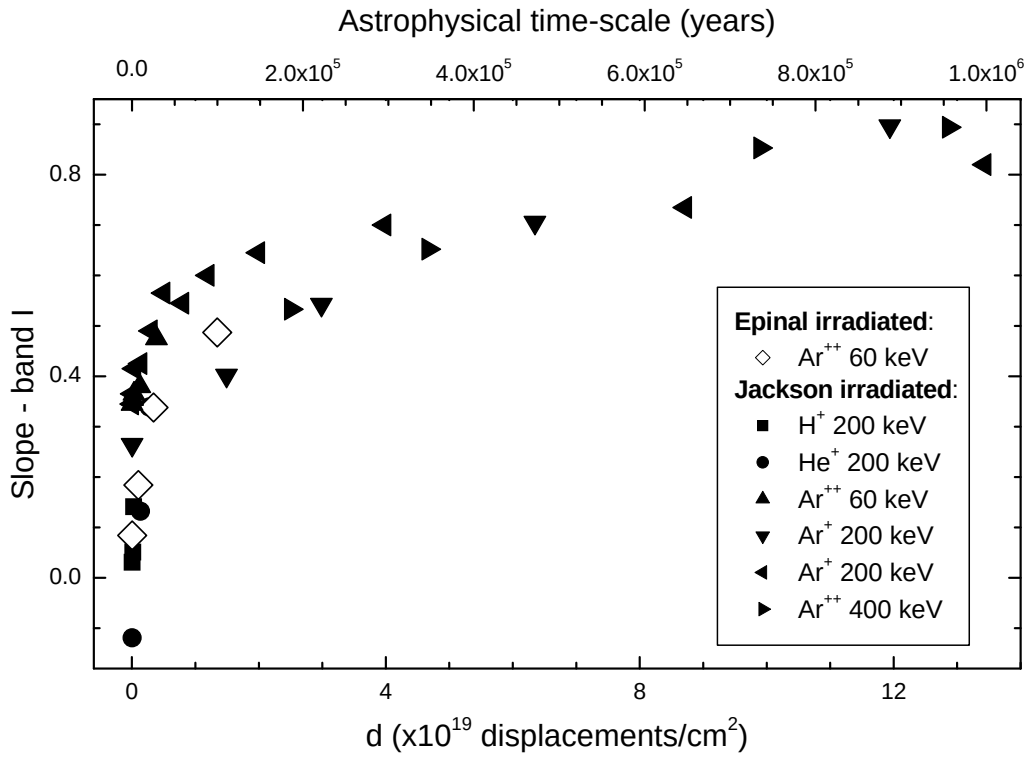

Figure 3.11: The spectral slope S versus the parameter d: all the irradiations discussed in Table 3.1 have been included, and also the spectral slopes of irradiation of the Epinal meteorite; in the upper x-axis an estimate of the astrophysical time-scale at about 1 AU is given, as derived by the data of Strazzulla et al. (2005).

samples;

5. ion irradiated samples reach spectral slopes redder than those observed in a number of NEOs (see above), corresponding to time-scales lower than 10^6 years at 1 AU: this confirms that ion irradiation by solar wind ions can be a very efficient process in weathering the asteroid surfaces (Hapke, 2001).

In order to give further evidence of the role of elastic collisions in reddening silicate samples, in Fig. 3.12 the effects of J_{VAC} (energy per unit surface (keV cm^{-2}) released by the ions to the target in vacancy formation processes) and those of J_{ION} (energy per unit surface (keV cm^{-2}) released by the ions to the target in ionization processes) are compared.

As expected, the behavior of J_{VAC} in Fig. 3.12 (upper panel) is very similar

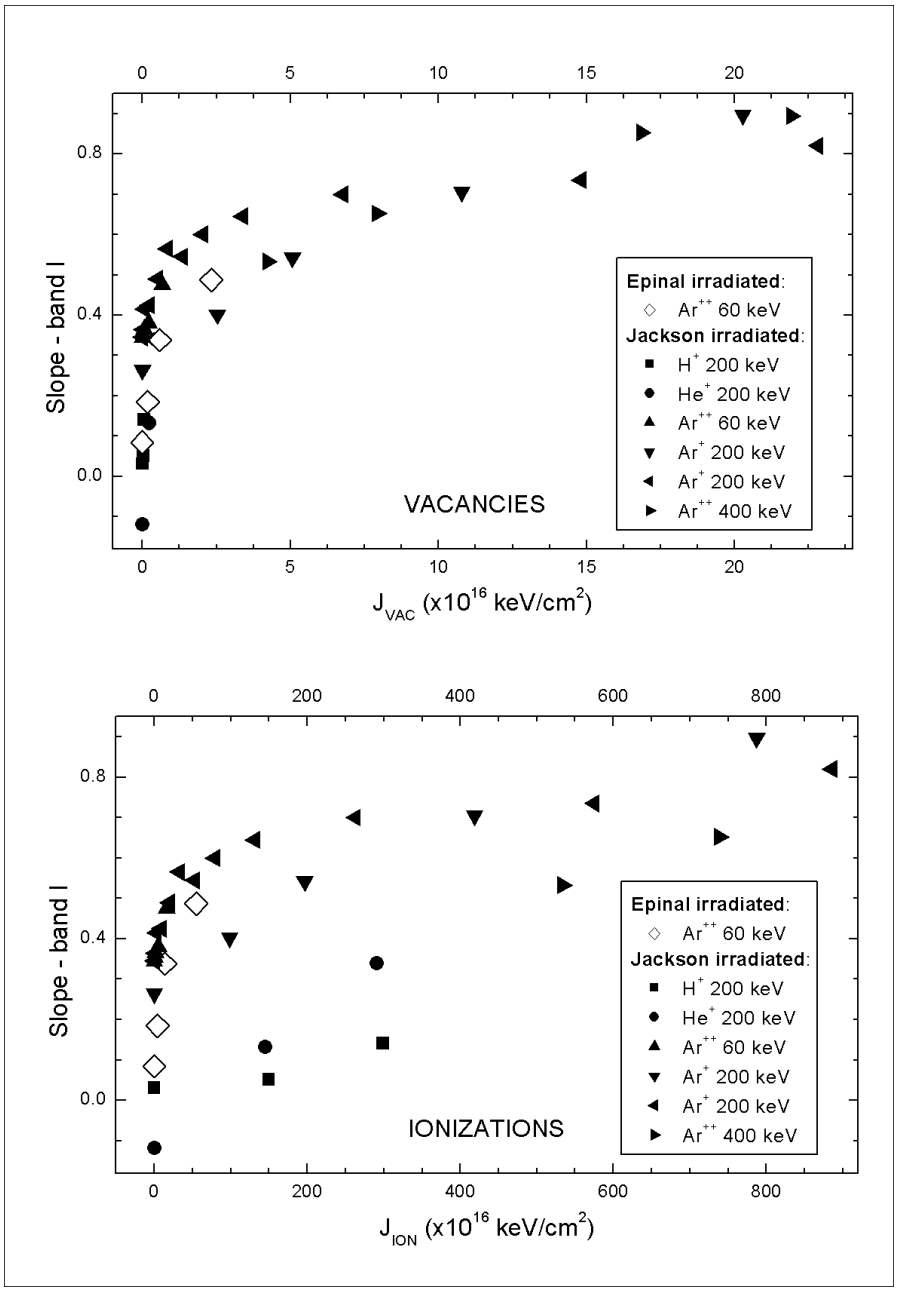

Figure 3.12: Upper panel: the spectral slope S versus the parameter J_{VAC} (elastic collisions, high correlation between different experiments). Lower panel: the spectral slope S versus the parameter J_{ION} (inelastic collisions, low correlation between different experiments).

to that shown in Fig. 3.11, i.e., high correlation between different experiments, being both related with elastic collisions. On the contrary, when the parameter

J_{ION} is considered (lower panel), correlation between the experiments gets lost: in particular the points relative to irradiation with lighter ions (H^+, He^+), i.e., lower elastic stopping power, move apart from that of heavier ions (Ar^+), i.e., higher elastic stopping power. Hence it is demonstrated that ion irradiation induces a reddening of the reflectance spectrum of bulk silicates, which is strongly related with the energy lost by elastic collisions with the target nuclei: heavier ions redden and darken UV-vis-NIR spectra more efficiently than lighter ions.

Conclusions

Ion irradiation experiments of bulk silicates, rich of olivine, pyroxene, and serpentine, have been performed using different ions (H^+, He^+, Ar^+, Ar^{2+}) having different energies (from 60 to 400 keV) to weather the samples, simulating the effects of space weathering induced on asteroids by solar wind ions.

UV-vis-NIR reflectance spectra have shown reddening and darkening in the 0.25-2.7 μm spectral range. The increase of the band I spectral slope is strongly related with the number of displacements caused by colliding ions inside the sample, or the energy per unit surface released by the ions in vacancy formation processes, i.e., the elastic collisions with the target nuclei.

Thus, reddening and darkening can be attributed both to amorphization of the very upper layers ($R_p < 1$ μm) of the samples, and to sputtering of iron from silicates and the deposition of nanophase neutral Fe on adjacent grains (Hapke, 2001), since the two processes can correlate with the nuclear stopping power.

Since the studied samples can be considered bulk mixtures of silicates, further experiments are needed to study whether silicate samples having pure chemical composition (the so called end-members) suffer of spectral modifications analogous to those described in this section. Moreover it is important to study ion irradiation effects on powdered silicates, since it is well known that spectral properties of silicate powder change with grain size, and this can be also a measure of aqueous alteration (Orofino et al., 2006). Those results are described in the third part of the thesis.

Acknowledgments

We are grateful to V. Orofino for supporting and providing useful suggestions. We also thank G.A. Baratta and F. Spinella for help in performing the experiments. This research was supported by the Italian Ministero dell'Istruzione, Università e Ricerca (MIUR).

3.3 Laser irradiation below and above the ablation threshold

Based on the paper: Brunetto, R., Romano, F., Blanco, A., Fonti, S., Martino, M., Orofino, V., Verrienti, C. 2006. Space weathering of silicates simulated by nanosecond pulse UV excimer laser. Icarus 180, 546-554.

In this section I present the results of laser irradiation experiments performed on pellets of powdered silicates, having different composition (orthopyroxene, clinopyroxene, olivine); a nanosecond pulse UV excimer laser is used, at two different wavelength, 193 and 248 nm, to simulate the effects of space weathering induced on minor bodies of the Solar System by micrometeorite bombardment.

These experiments are aimed to extend the previous results, by considering a larger number of experimental situations. Indeed, different fluences, from 0.05 to 2 J/cm^2, are used to weather the samples, experimenting below and above the ablation threshold. In fact, at the present time nobody knows which regime is the closest simulation to space-weathering process. For instance, uncontrolled melting could be a part of the phenomenon occurring in micrometeorite impacts onto airless bodies.

The irradiated and ablated targets are studied by modifications of their UV-vis-NIR reflectance spectra and XPS (X-ray Photoelectron Spectroscopy) analysis.

3.3.1 Spectral modifications

Irradiated samples are pellets of pressed (about 8 t for 60 s) silicate powders having average grain size of a few μm, in particular $(Mg,Fe)_2SiO_4$ olivine,

(Mg,Fe,Ca)SiO_3 orthopyroxene and clinopyroxene, which are supposed to be the most relevant minerals for S-type asteroids (Gaffey et al., 1993). Olivine comes from San Carlos, Arizona (USA), while pyroxenes come from Bamble (Norway).

The UV-vis-NIR reflectance spectra of samples (as prepared) are shown in Fig. 3.13, Fig. 3.14, and Fig. 3.15, for clinopyroxene, olivine, and orthopyroxene, respectively.

The spectrum of olivine before, laser treatment (labeled (1) in Fig.Fig. 3.14) exhibits a very strong and broad band at about 1 μm (band I); this band I is also present in pyroxene (see Figs. 3.13 and 3.15), along with a broad band (band II), characteristic of pyroxene but not olivine, whose peak position is at about 1.85 μm in the case of orthopyroxene, and at about 2.3 μm in the case of clinopyroxene. Consequently, the ratio of band II area to band I area (BII/BI area) is sensitive to the relative amount of pyroxene to olivine in the samples; peak position of band I is known to shift towards lower wavelengths moving from olivine to orthopyroxene (Gaffey et al., 1993). Minor absorption features are observed in the spectra at about 1.4 and 1.9 μm, due to OH absorptions that are present in the samples, and vary in intensity, depending on the pellet preparation conditions.

The clinopyroxene samples have been irradiated both below (Fig. 3.13, upper panel) and above (Fig. 3.13, central and lower panels) ablation threshold.

In the case of BAT irradiation, we have varied both the fluence of the single laser pulse, and the number of pulses. Reddening (lower reflectance at lower wavelengths) and darkening of the clinopyroxene reflectance spectra are evident; these effects increase in intensity with increasing fluence and number of pulses, i.e. with increasing dose = fluence $\times$ number of pulses.

The frequency of pulses is 10 Hz, so the time interval between pulses is 0.1 s. This is long enough (with respect to the duration of the pulse) to assure the independency of the effect of each pulse, which should avoid heat accumulation; we have also verified that varying the frequency to 1 Hz, the spectral changes are the same. Thus, in this frequency range, the reddening is independent on the frequency itself.

Also in the case of ablation, the reflectance spectra of clinopyroxene show pronounced darkening and reddening in the UV-vis-NIR range, even stronger than in

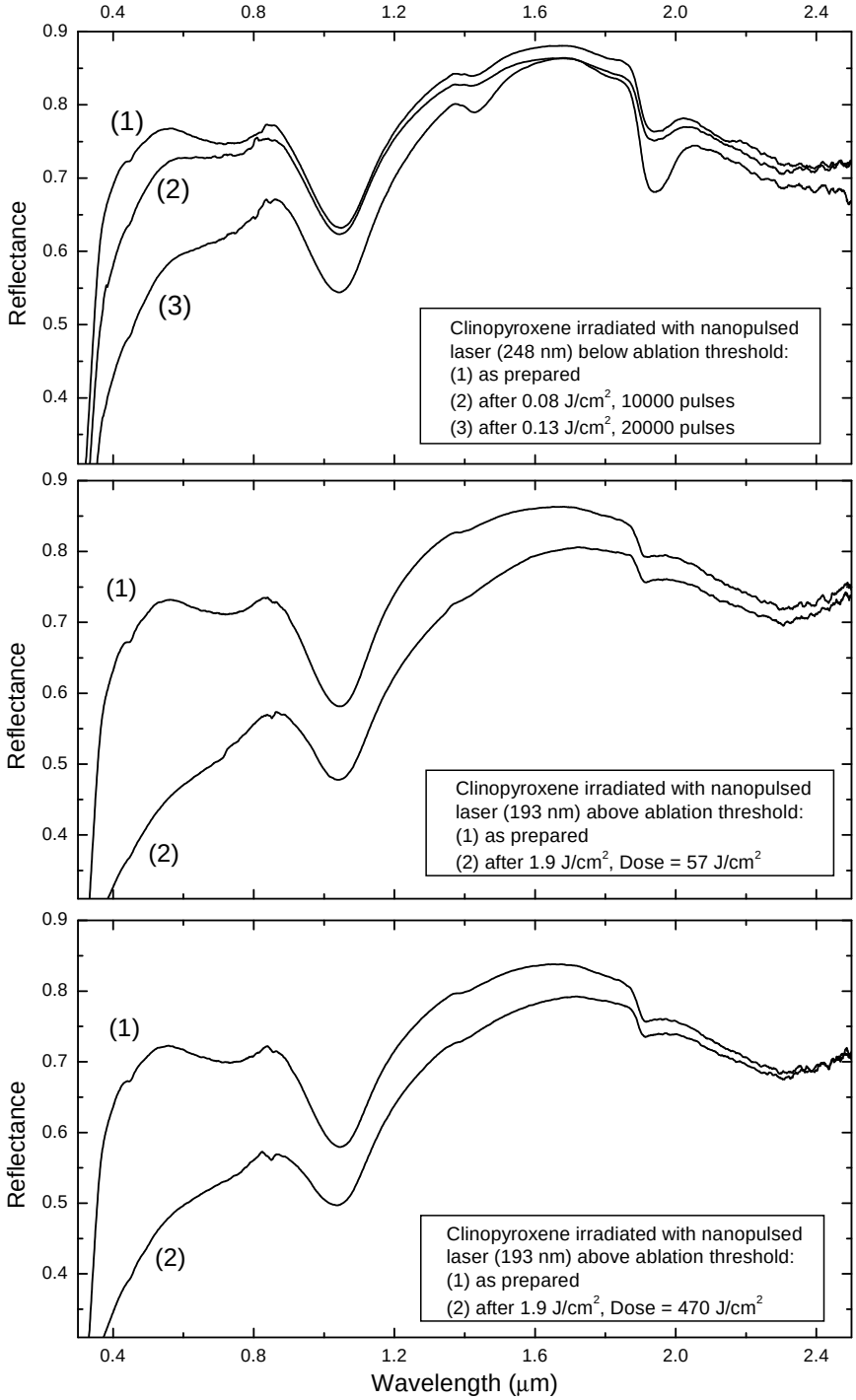

Figure 3.13: Reflectance spectra of clinopyroxene samples before and after irradiation; samples have been irradiated both below (BAT, upper panel) and above (central and lower panels) ablation threshold. Darkening and reddening are stronger in the case of ablation. Spectra in the upper panel have stronger OH features, depending on the pellet preparation conditions.

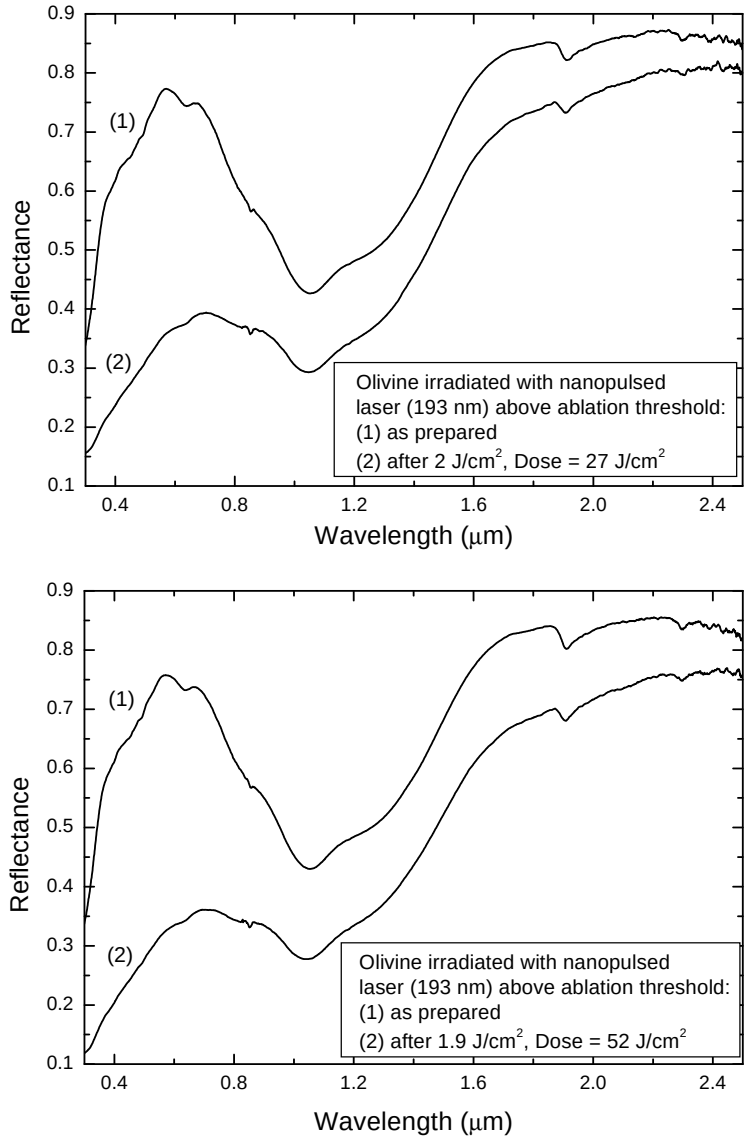

Figure 3.14: Reflectance spectra of olivine samples before and after ablation; samples have been irradiated above ablation threshold, with two different doses.

the BAT irradiation case. Furthermore, in the ablated target, the weathering effects are independent on the total dose released by the laser. (Remember that in the case of ablated samples, the total dose is given by: dose = laser energy × number of pulses/ablated area.) Similar results are obtained in the case of ablated olivine (Fig. 3.14) and ablated orthopyroxene (Fig. 3.15). In all of the ablated samples, an intense plume of ejected material was observed, and deposition of those vaporized material was realized on silicon substrates resulting in the production of amorphous

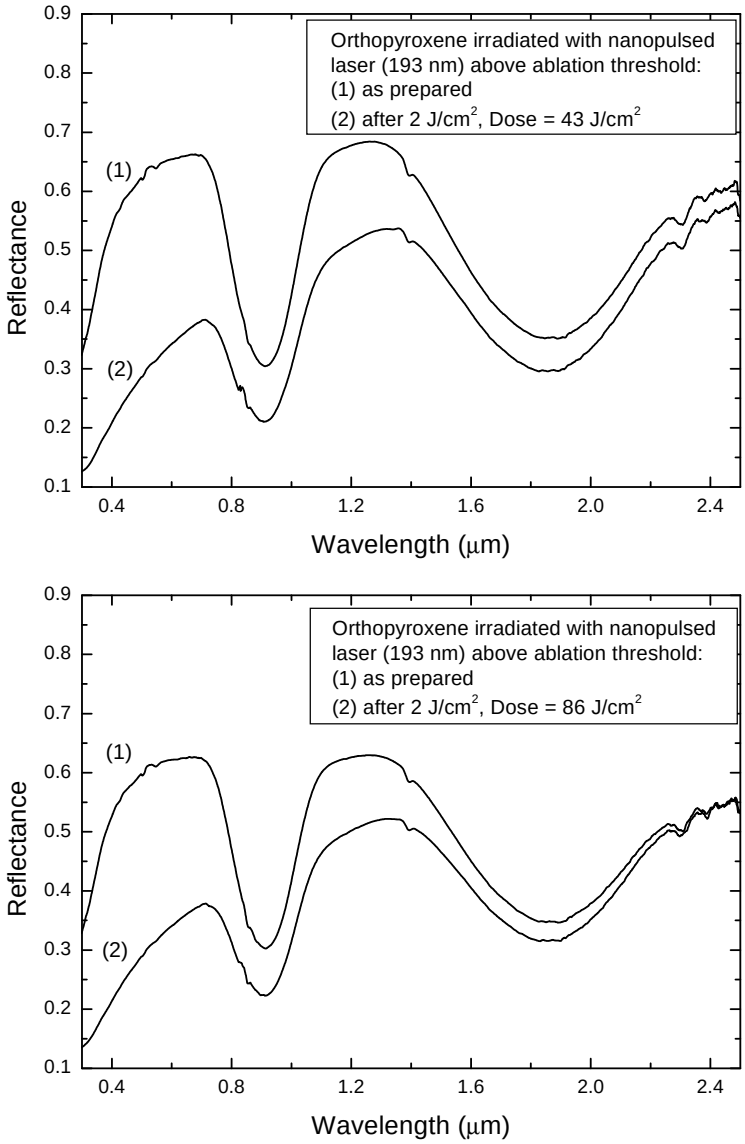

Figure 3.15: Same as Fig. 3.14, but for orthopyroxene samples.

silicate films. Analysis of these deposits, by means of a Scanning Electron Microscope, is planned in forthcoming experiments.

Note that in the case of olivine, a dose of 27 J/cm^2 is able to induce strong darkening and reddening; in these experimental conditions, this dose value corresponds to about a single complete cycle of motion (spinning and spanning) of the target. This means that, in UV ablating conditions, a single passage of the laser on the sample surface is sufficient to induce the observed weathering effects, whose

intensity does not change with further repeated ablation cycles.

In order to quantify the produced weathering effects, and to compare them with those observed in asteroids and previous laser irradiation experiments (Yamada et al., 1999), the reflectance spectra have been scaled to 1 at 0.55 μm, to consequently evaluate the spectral slope, as the slope of a linear continuum across band I (as described by Gaffey et al. (1993), or by Hiroi and Sasaki (2001)). The scaled spectra are plotted in Fig. 3.16; different samples of the same end-member silicate may slightly differ in the initial spectral slope. From Fig. 3.16, it is apparent that ablated clinopyroxene reaches spectral slopes higher than BAT irradiated clinopyroxene, implying that weathering effects are more efficient for ablation than for BAT irradiation.

Moreover, Fig. 3.16 shows that ablated olivine reaches the highest slope observed in this work; this is in agreement with what reported by Hiroi and Sasaki (2001), who found that olivine is weathered at higher level than pyroxene.

3.3.2 Discussion

Since the spectral slope is a good parameter to describe the weathering of silicates, we have analyzed the slope value as a function of fluence and number of pulses, for clinopyroxene. Results are plotted in Fig. 3.17: in the left panel the fluence is fixed, while in the right panel the number of pulses is fixed. Below the ablation threshold, the spectral slope increases linearly with both increasing fluence or number of pulses.

The left panel of Fig. 3.17 includes also the points of ablated clinopyroxene. The point at about 1000 number of pulses corresponds to about two complete cycles of the motion of the target; this comparison shows that ablation is much more efficient, and that the first cycles are enough to reach the highest slope.

The difference between the two regimes has to be ascribed mainly to the different effects of the interaction of the laser with the target surface. Irradiation of a solid with a laser fluence below the ablation threshold, induces changes in the morphology and microstructure of the surface, generation of defects and depletion of one or several components of the target. Even for very low fluences, laser-induced

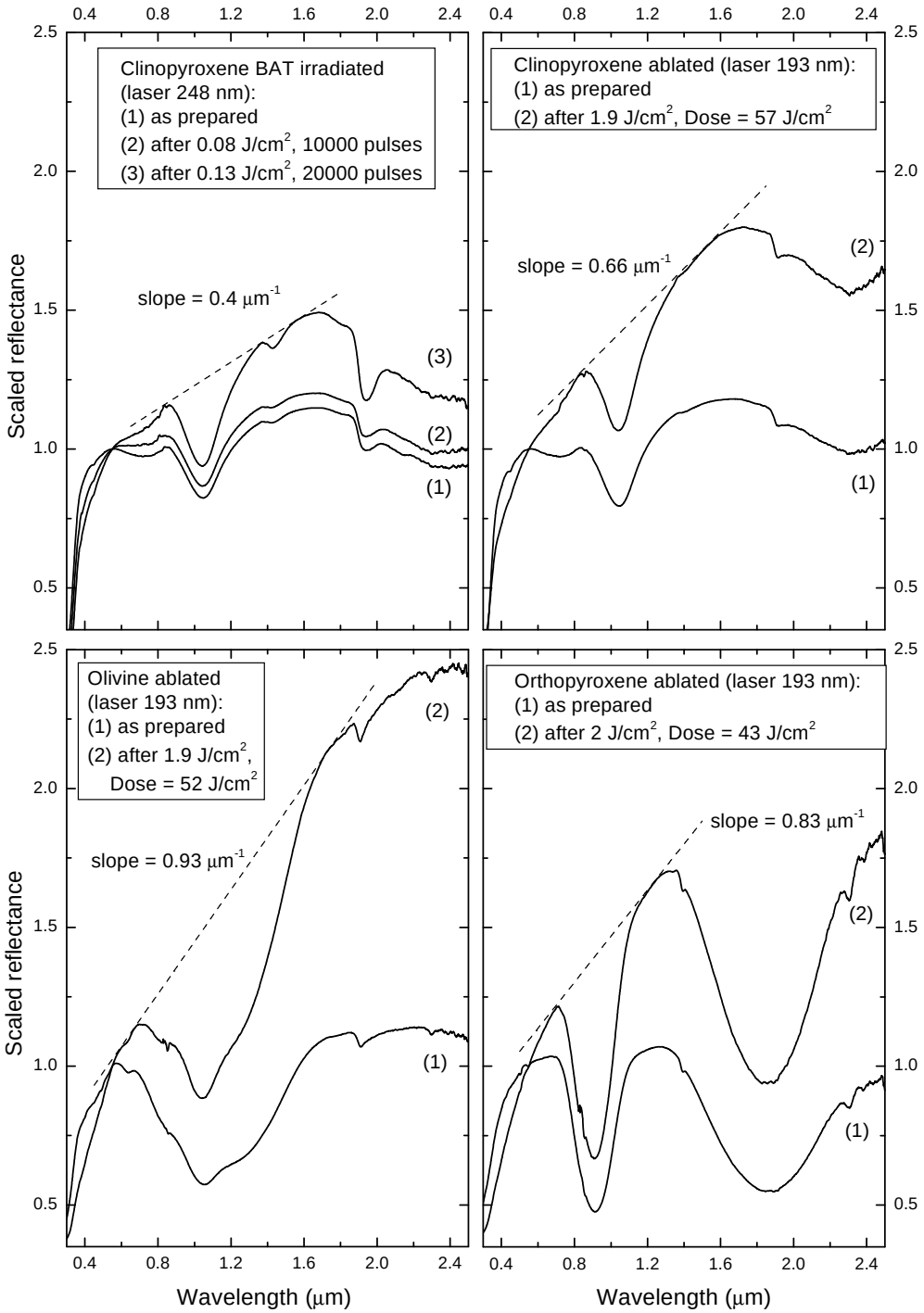

Figure 3.16: Scaled reflectance spectra of clinopyroxene, orthopyroxene, and olivine, before and after irradiation, below and above ablation threshold. The values of the final spectral slopes are reported, showing that ablated olivine reaches the highest slope.

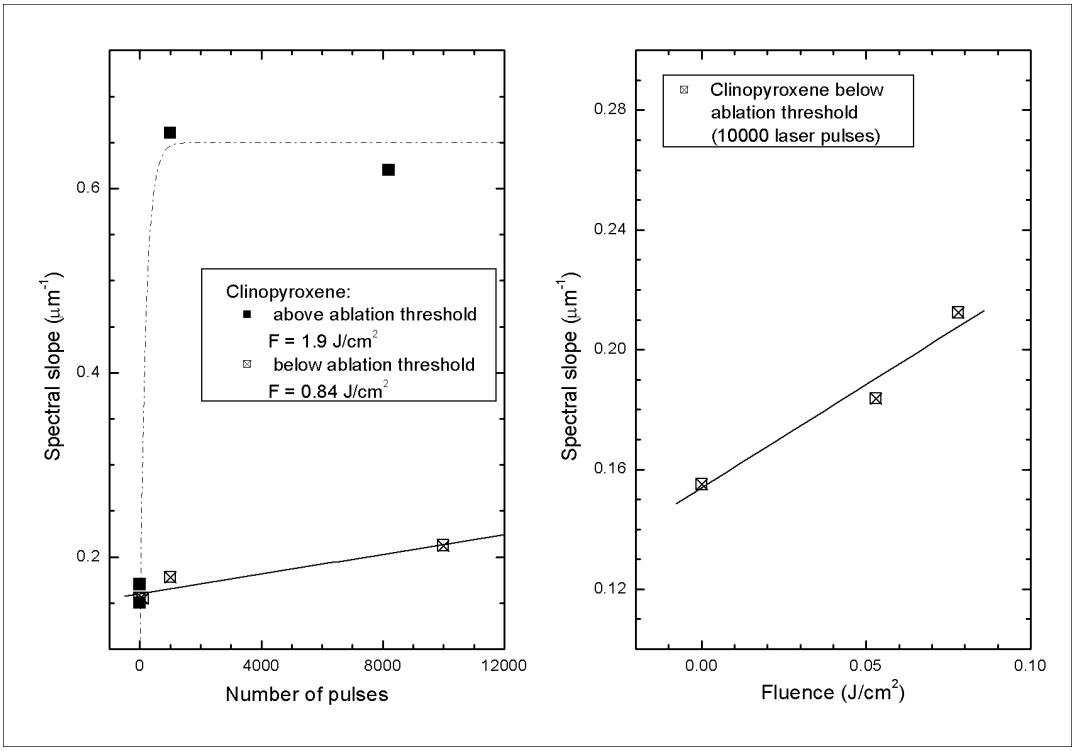

Figure 3.17: Left panel: spectral slope of clinopyroxene vs the number of pulses, below and above ablation threshold. Right panel: spectral slope of clinopyroxene vs the laser fluence, in case of BAT irradiation.

desorption of a single or few monolayers, or the depletion of a single species take place.

On one hand (left panel of Fig. 3.17), increasing the number of pulses the effects of the interaction become more marked; on the other hand (right panel of Fig. 3.17), also increasing the laser fluence causes an increasingly spectral reddening, because the depletion of one particular material component is known to increase with fluence. It is important also to note that the laser fluence corresponding to different degrees of surface damage and depletion depends on the particular material and laser parameters.

On the contrary, let us consider the experiments with fluence higher than ablation threshold: in the present conditions (high laser power densities, short pulses and short laser wavelength) the ablation mechanism takes place on a time-scale short enough to suppress the dissipation of the excitation energy beyond the volume

ablated during the pulse; consequently, the segregation of the remaining target into different components can be largely avoided. In this regime of interaction, the relative concentration of species within the plasma plume remains almost unchanged for successive laser pulses and equal to those of the target, resulting in congruent ablation. In this regime heat loading of the target and material segregation remain small.

This scenario can give an explanation of the different spectral behavior; in case of ablation the highest slope is almost immediately reached. The effect is then saturated: a further increase in the number of laser pulses has only the effect of ablating material of the same composition of the starting target, i.e. the grains fly away from the pellet.

The linear increase of spectral slope, shown in Fig. 3.17 for clinopyroxene below ablation threshold, implies that the slope value of BAT irradiated samples increases linearly with increasing laser dose. This is also shown in Fig. 3.18, where the spectral slope is plotted vs. the dose: it includes the points from our samples (BAT irradiated and ablated), and the values for olivine and orthopyroxene as derived by the published data of Hiroi and Sasaki (2001); in their experiments, both laser energy and number of pulses were varied, so that it is possible to plot their spectral slopes vs. the total dose; in particular they ablated olivine and orthopyroxene using an IR laser, up to a dose of 24 and 480 J/cm^2, respectively.

Also the points from Hiroi and Sasaki (2001) follow a linear trend with increasing dose. Nevertheless, their experimental values seem to be somehow in between results of this thesis obtained in BAT irradiation and ablation regimes. Indeed, Fig. 3.18 reveals that there are some differences between our ablation experiments and those of Hiroi and Sasaki (2001): while they had to increase the dose to reach the highest slopes, in the ablation experiments described here the slope is not influenced by the dose, i.e. the strongest reddening is already observed at the first dose; furthermore, the slopes values obtained for both ablated olivine and ablated orthopyroxene are about 50% higher than those of Hiroi and Sasaki (2001).

The comparison between UV and IR is referred to the total dose, and scaled to the power of the laser, so that the difference between the two regimes is intrinsically

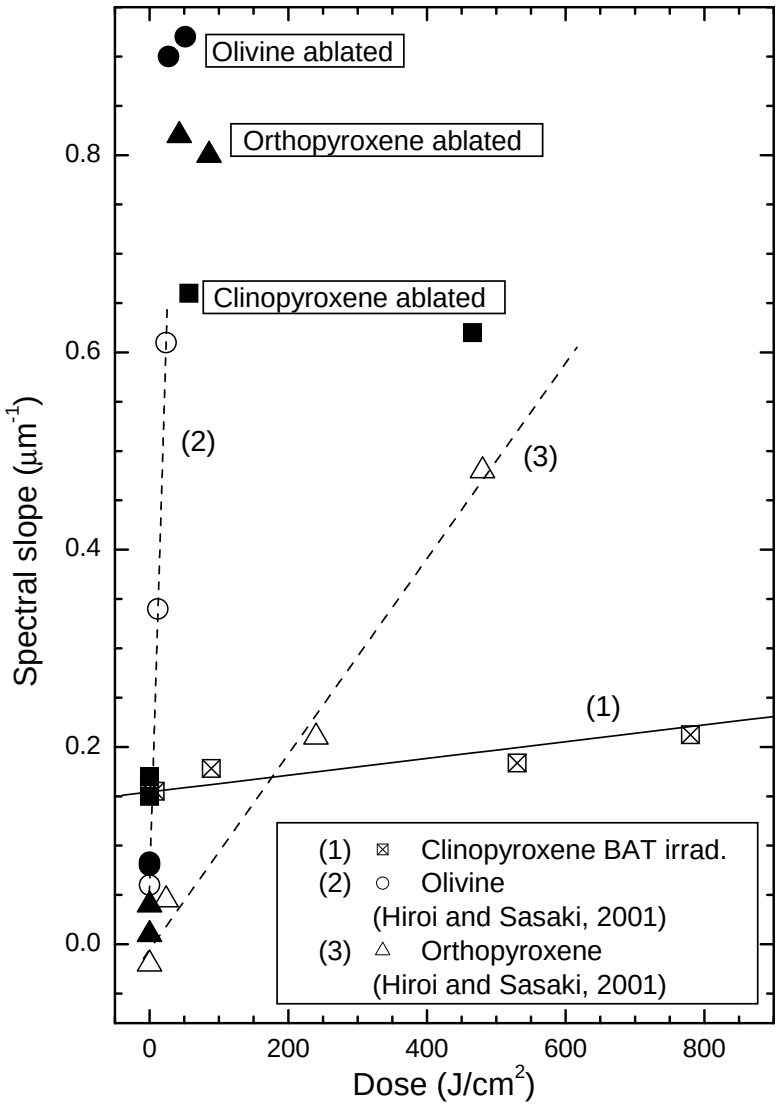

Figure 3.18: Spectral slope vs the total dose, for our experiments below (crossed points) and above (full points) ablation threshold, on clinopyroxene (squares), orthopyroxene (triangles), and olivine (circles). Also the values for orthopyroxene and olivine (open triangles and circles) from Hiroi and Sasaki (2001) and Yamada et al. (1999) are included.

connected with the different mechanism: such discrepancies can be explained by the fact that a UV laser is used in this thesis.

In the case of UV laser a strong absorption of laser light is guaranteed by the very short wavelength. In this case it is possible to limit thermal effects onto the

target and consequently a regime of congruent ablation occurs. On the contrary, with IR laser sources it is necessary to take into account the heat loading of the target, and the consequent damage occurring in the surrounding material.

Nevertheless, since also uncontrolled melting could be a consequence of a micrometeorite impact, it is not easy to say which is the closest simulation to space weathering process. Consequently, Fig. 3.18 has to be seen as an extension of the previous results by Hiroi and Sasaki (2001); however, Fig. 3.18 clearly shows that congruent laser ablation is the most efficient condition to redden silicate spectra[1].

As a proof that we have been experimenting in conditions of congruent ablation, we have performed XPS analyses of the olivine sample before and after UV laser ablation. These analyses have shown that there are no considerable variations of the chemical composition of the weathered target, whose atomic percentage values are: O, 56.6%; Si, 13.2%; and Mg, 30.2%, which lie within a 1% deviation from the measured initial composition: O, 56.9%; Si, 13.9%; and Mg, 29.2%. These values are close to those of pure forsterite (iron poor olivine); indeed in the olivine target the Fe content is undetectable by XPS measurements, i.e. it is in the order of 1-2%. This implies that spectral reddening can be observed also in iron poor silicates.

Magnetic analyses of the ablated samples, like those described by Bentley et al. (2005), are described in the last chapter of this thesis.

3.3.3 Astrophysical implications

The spectra of irradiated silicates should be able to explain the spectral mismatch between meteorites and asteroids. To test whether our BAT irradiation and ablation experiments can explain this space weathering effect, we have calculated the ratio of band II area to band I area (BII/BI area) as described by Gaffey et al. (1993), and then compared the spectral slope and the BII/BI area of laser experiments with those of near- Earth and Main-Belt silicate rich asteroids reported by Marchi et al. (2005). In their slope vs BII/BI area plot, it has been revealed the presence of a

[1]It should be noted that, differently from the case of Yamada et al. (1999), in my experiments the targets are mounted vertically, so that in the present case a minor amount of material is probably redeposited.

rectangle zone occupied by OC meteorites (defined as zero damage zone), and a triangle shaped distribution for asteroids; these two regions overlap only partially, and this is believed to be due to space weathering.

Figure 3.19 plots the spectral slope vs the BII/BI area ratio of our experimental data along with the meteorite and asteroid zones. It is clear that all the slopes observed in the case of asteroids can be reproduced by the laser experiments, whatever is the composition, i.e. pyroxene to olivine ratio, of the target.

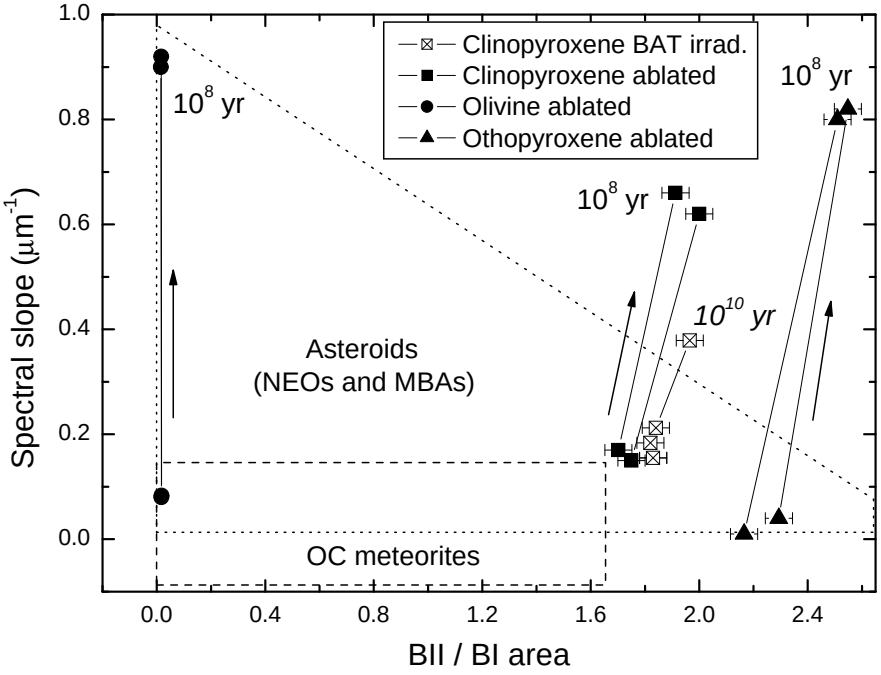

Figure 3.19: Spectral slope vs the BII/BI area ratio, for experiments below (crossed points) and above (full points) ablation threshold, on clinopyroxene (squares), orthopyroxene (triangles), and olivine (circles). The asteroid and meteorite regions are displayed, as derived by the data of Marchi et al. (2005). The arrows mark the direction towards which space weathering by micrometeorite impacts should act. The astrophysical time-scales are given, as derived in the text.

Note that space weathering mainly acts on the slope, but that in the case of pyroxene it also causes an increase of the BII/BI area ratio; this is in agreement with what found by Ueda et al. (2002a).

In order to get an astrophysical time-scale for the process, let us follow Sasaki et al. (2001) who calculated a time-scale of about 10^8 yr in space at about 1 AU: they reported that, considering an impact rate of few 10^{-4} m^{-2} s^{-1} for dust particles

of about 10^{-12} g (1 μm in diameter), and assuming an impact velocity of 20 km s^{-1} for vaporization, the energy release rate by dust impacts is about 10^{-3} J m^{-2} yr^{-1}. The dose provided here to redden olivine samples is 27 J cm^{-2}: this leads to a timescale of about 10^8 yr at 1 AU (similar results are obtained for ablated clinopyroxene and orthopyroxene); it should be stressed that on a comparable time-scale we get higher spectral slopes than Sasaki et al. (2001), by a factor of about 50%, once again implying that UV excimer laser is more efficient than infrared laser in reddening silicate samples.

The same calculation as before have been repeated in the case of BAT clinopyroxene (irradiated below ablation threshold), finding a time-scale of about 10^{10} yr at 1 AU, i.e. longer by a factor of 100 with respect to the ablated targets. As stated above, laser irradiation experiments simulate micrometeorite impacts whereas ion irradiation simulates solar wind irradiation. However, a direct comparison between the two cases is not easy, because the two processes are very different. In terms of energy, it is likely that the two effects have comparable efficiency in reddening silicate spectra; however, in terms of astrophysical timescale, solar wind irradiation seems to be faster (about 10^6 yr). Nevertheless, since the ion fluxes and the micrometeoroid fluxes in space are only partially know, and they vary moving within the Solar System, the relative efficiency of the two processes may strongly change when considering different objects.

In conclusion, this work has confirmed and extended the results of Sasaki et al. (2001); we have found that, in order to simulate micrometeorite bombardment, the most efficient experimental conditions to darken and redden the reflectance spectra are obtained performing congruent laser ablation, i.e. to use an UV laser with fluence higher than ablation threshold.

Furthermore, it seems that congruent ablation reproduces quite well the micrometeorite bombardment, because it minimizes the thermal effects, causes a high transfer of momentum, and reproduces the astrophysical weathering in reasonable time-scales (10^8 yr at 1 AU). On the contrary, irradiation below ablation threshold, even if inducing similar spectral modifications, would correspond to astrophysical time-scales longer than the age of the Solar System.

However, it is possible that, in a micrometeorite impact, uncontrolled melting can occur; the amount of this melting will vary depending on the parameters of the impact (energy, velocity, angle, etc.): varying the laser fluence, all the possible variations of these thermal effects have been investigated, demonstrating that the strongest reddening is obtained when thermal effects are minimized.

Acknowledgments

We are grateful to G. Compagnini and G. Strazzulla for help in the XPS analysis and for other useful suggestions. We thank Takahiro Hiroi and an anonymous reviewer for their helpful comments. This research was supported by the Italian Ministero dell'Istruzione, Università e Ricerca (MIUR).

Chapter 4

Irradiation of ices

Fast ions passing through a molecular solid release energy to the target material. Energetic ions produce surface, chemical, and physical changes when they collide with solid materials.

As a consequence many molecular bonds are broken along the ion-track and, in a very short time (one picosec or less), the molecular fragments recombine giving rise to a rearrangement of the chemical structure.

Original and newly produced molecules can be ejected (sputtered) or remain in the target (chemical alteration) and the structure of the target be changed.

Thus, in addition to the alteration of the chemical and lattice structure of the target material, new molecular species (not present before irradiation) are formed. If the material is originally volatile less volatile species can be formed which can survive at higher temperature.

In this chapter I will describe a few irradiation experiments on C-rich ices; these experiments are a case for the space weathering of outer Solar System objects, and provide important information about the surface composition and processing of those icy and distant bodies.

4.1 Chemistry: the case of methanol

Based on the paper: Brunetto, R., Baratta, G. A., Domingo, M., Strazzulla, G. 2005. Reflectance and transmittance spectra (2.2-2.4 μm)

of ion irradiated frozen methanol. Icarus 175, 226-232.

Here I present a study of the effects induced by ion irradiation on frozen methanol and mixtures water-methanol. In particular I have studied the profile (shape, width and peak position) of methanol bands and the formation of new species at two different temperatures. I show, for the first time, a strong decrease of the 2.34 μm band with respect to the 2.27 μm one.

The technique used for the analysis is in-situ infrared spectroscopy in the 2.2-2.4 μm range, both in reflectance (for the first time) and transmittance. This range is different from that studied previously for methanol (Hudson and Moore, 2000; Palumbo et al., 1999), and it is more appropriate to get information on processes taking place on planetary objects, where spectral properties, in the studied range, are due to the scattering of the solar light from their surface layers.

Transmittance spectra of other simple hydrocarbons (CH_4, C_2H_2, C_2H_4, C_2H_6) and CO have been also obtained both to help in the identification of the new molecules formed after ion irradiation of methanol-rich ices, and to get insight into the question of the presence of simple frozen hydrocarbons on the surface of some objects in the outer Solar System.

4.1.1 Experimental results

Fig. 4.1 presents NIR transmittance spectra (2.2- 2.4 μm) of some frozen (16 K) hydrocarbons (methanol, acethylene, ethylene, ethane, methane) and of carbon monoxide. Different samples have different thickness (1-3 μm); spectra are normalized to the most intense peak of each species, in the exhibited spectral region, and are offset for clarity. Methanol samples have been irradiated with 30 keV He^+ ions. The transmittance spectrum of an irradiated sample (28 eV/16 amu) is also shown in Fig. 4.1.

In Table 4.1 the peak positions and the FWHM of the NIR bands (2.2-2.4 μm) of the studied species are given, as calculated from Fig. 4.1.

CO exhibits a single band at about 2.35 μm attributed to the overtone 2ν of the fundamental vibration at about 4.67 μm. Ethane and ethylene have bands due

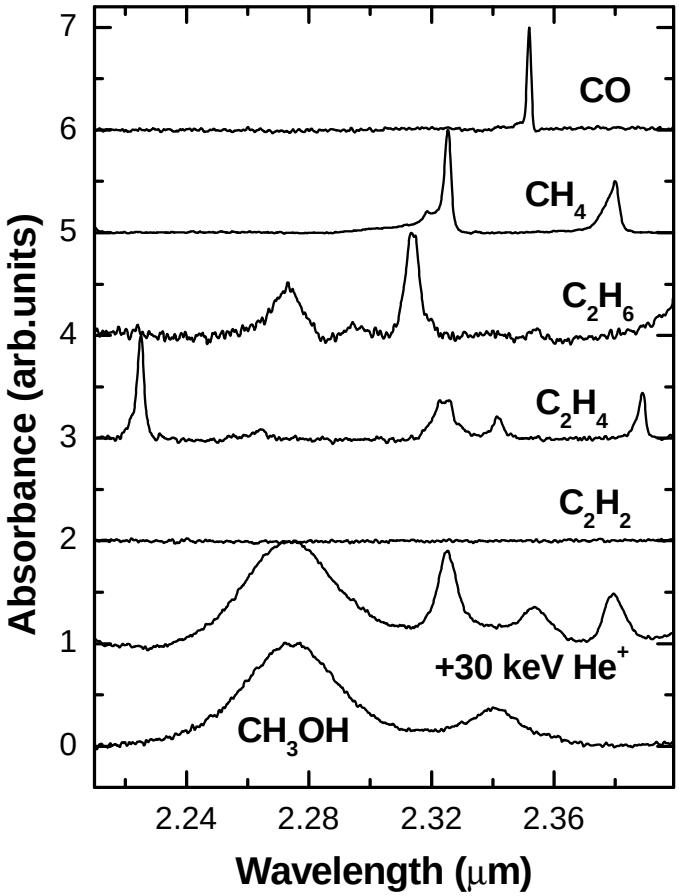

Figure 4.1: NIR transmittance spectra (2.2-2.4 μm) of frozen (16 K) samples of (from bottom to top): methanol, methanol after irradiation with 30 keV He^+ ions at 28 eV/16 amu, acethylene, ethylene, ethane, methane, and carbon monoxide. The samples are 1-3 μm thick; spectra are normalized to the most intense peak of each species, in the exhibited spectral region, and are offset for clarity.

to combinations of C-H stretching and deformation modes. Acethylene does not exhibit any feature in this spectral range. Methane has two bands at 2.33 and 2.38 μm, attributed respectively to combination of the stretching and deformation modes $\nu_3 + \nu_4$ and combination of the symmetric stretching and deformation modes $\nu_1 + \nu_4$ (Quirico and Schmitt, 1997). Methanol is a simple alcohol and its spectrum, in the studied spectral range, exhibits two bands at 2.27 and 2.34 μm attributed to the combinations of the C-H asymmetric stretching and deformation modes and to the

Observed bands (cm^{-1})	(μm)	Responsible species	FWHM (cm^{-1})	(μm)
4252	2.35	CO	2.7	0.0015
4201	2.38	CH_4	8.8	0.0050
4300	2.33		4.8	0.0026
4323	2.31	C_2H_6	9.7	0.0052
4399	2.27		19	0.010
4186	2.39	C_2H_4	4.7	0.0027
4271	2.34		7.1	0.0039
4299	2.33		13	0.0071
4494	2.23		5.2	0.0026
4278	2.34	CH_3OH	44	0.024
4401	2.27		71	0.037
Irradiated CH_3OH:				
4203	2.38	CH_4	19	0.011
4249	2.35	CO	35	0.020
4301	2.33	CH_4	17	0.0091
4395	2.27	CH_3OH	76	0.039

Table 4.1: Peak position and FWHM at T = 16 K of the NIR bands (2.2-2.4 μm) of the molecules relevant for this study (see Fig. 4.1)

combinations of the C-H symmetric stretching and deformation modes respectively (Cruikshank et al., 1998).

After irradiation the spectrum of methanol changes dramatically. New bands appear at 2.33, 2.35, and 2.38 μm that, after a look at Fig. 4.1, we attribute to CH_4, CO, and CH_4, respectively. The amount of newly formed CO and CH_4, at the investigated dose, is estimated to be about 10% with respect to methanol abundance. Moreover the intensity of the CH_3OH band at 2.34 μm decreases more strongly than that of the 2.27 μm feature.

In Fig. 4.2 we report the reflectance spectra of virgin and irradiated CH_3OH at T = 16 K. Three irradiation steps with 200 keV H^+ ions are shown, up to a fluence of 5×10^{14} H^+ cm^{-2} (11 eV/16 amu).

The thickness of the film was about 1 μm, so that the ion beam irradiated the whole sample thickness: the penetration depth of 200 keV H^+ ions in a CH_3OH film is indeed about 2.2 μm, as estimated using the SRIM code (at http://www.SRIM.org/,

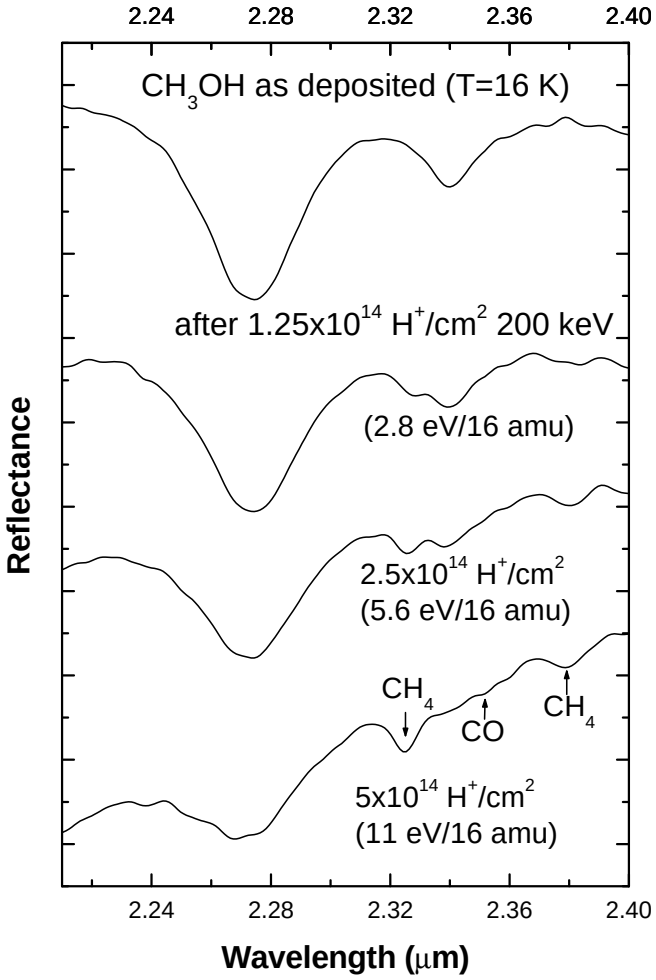

Figure 4.2: NIR reflectance spectra (2.2-2.4 μm) of irradiated methanol at T = 16 K, offset for clarity. The methanol bands decrease, in particular that at 2.34 μm; bands appear from newly formed CO and CH_4. The spectrum gets redder as the ion fluence increases.

Ziegler et al. (1985)) in our 45° configuration. Once again, the CO and CH_4 bands appear, while the methanol bands decrease in intensity. In particular, the band at 2.34 μm almost disappears. An analogous experiment was performed at T = 77 K and spectra are shown in Fig. 4.3. The results are qualitatively the same as at T = 16 K. In both of the experiments it is also apparent a reddening of the spectra, together with a (not shown) darkening.

For ion fluences higher than 10^{15} H^+ cm^{-2} the newly formed molecules are in

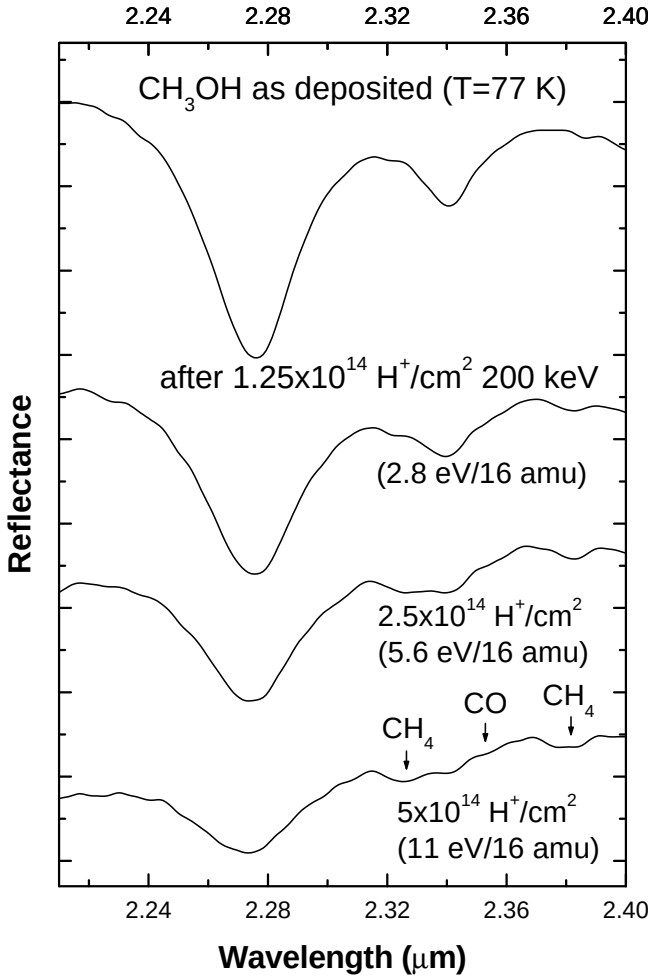

Figure 4.3: NIR reflectance spectra (2.2-2.4 μm) of irradiated methanol at T = 77 K, offset for clarity. The methanol bands decrease, in particular that at 2.34 μm; bands appear from newly formed CO and CH_4. The spectrum gets redder as the ion fluence increases.

turn destroyed; ion irradiation induces a progressive carbonization of the target, and the irradiated icy sample evolves towards a complex carbonaceous refractory structure. This organic residue, that we refer to as IPHAC (Ion Produced Hydrogenated Amorphous Carbon), is stable upon thermal annealing to room temperature. The formation of such a residue has been observed in a large number of ion irradiation experiments of hydrocarbons, organics, and carbon-rich samples (Strazzulla and Johnson, 1991; Strazzulla, 1997).

We have also verified that the results here presented are still valid when mixtures water-methanol are considered. In Fig. 4.4 we show NIR transmittance spectra (2.2-2.4 μm) of a frozen (T = 16 K) mixture water:methanol (1:1) before (full line) and after irradiation with 30 keV He^+ ions at 27 eV/16 amu (dashed line). Also in this case the spectrum changes dramatically because of irradiation: new bands appear at 2.33 (CH_4), 2.35 (CO), and 2.38 (CH_4) and the intensity of the CH_3OH band at 2.34 μm strongly decreases.

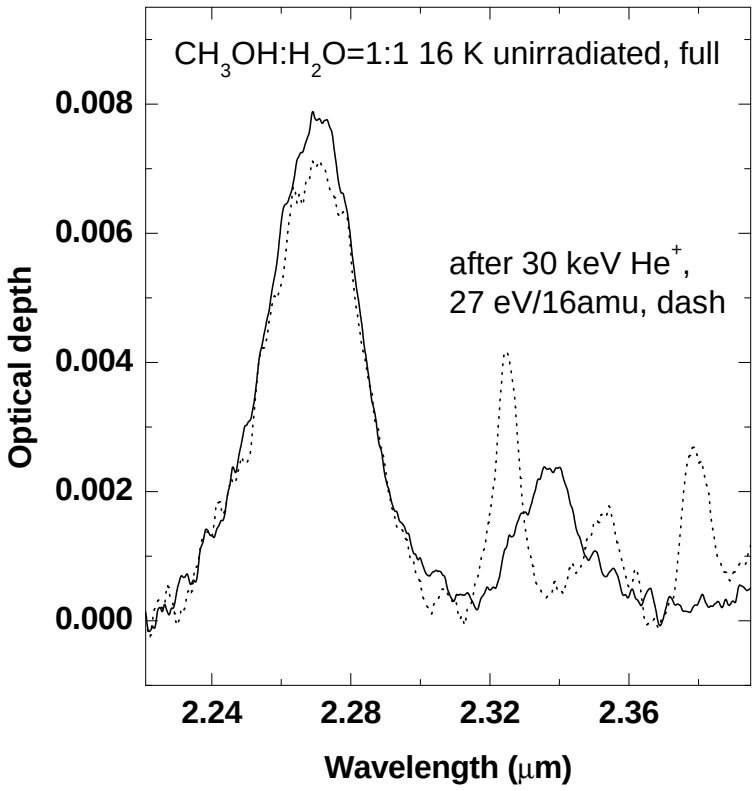

Figure 4.4: NIR transmittance spectra (2.2-2.4 μm) of a frozen (16 K) mixture water:methanol (1:1) before (full line) and after irradiation with 30 keV He^+ ions at 27 eV/16 amu (dashed line).

By means of a multi-Lorentzian fit we evaluated the areas of the methanol bands in the case of reflectance experiments, and in Fig. 4.5 we can see how the normalized areas decrease with increasing ion fluence, at both T = 16 K and T = 77 K. The behavior is that of an exponential decrease added to a constant that we fit by

$Area = A_\infty + kexp(-\sigma\phi)$, where ϕ is the ion fluence, σ is the cross section, A_∞ is the asymptotic value of the normalized area, and k is a coefficient whose value is fixed by the normalization condition $A_\infty + k = 1$. The results are given in Table 4.2.

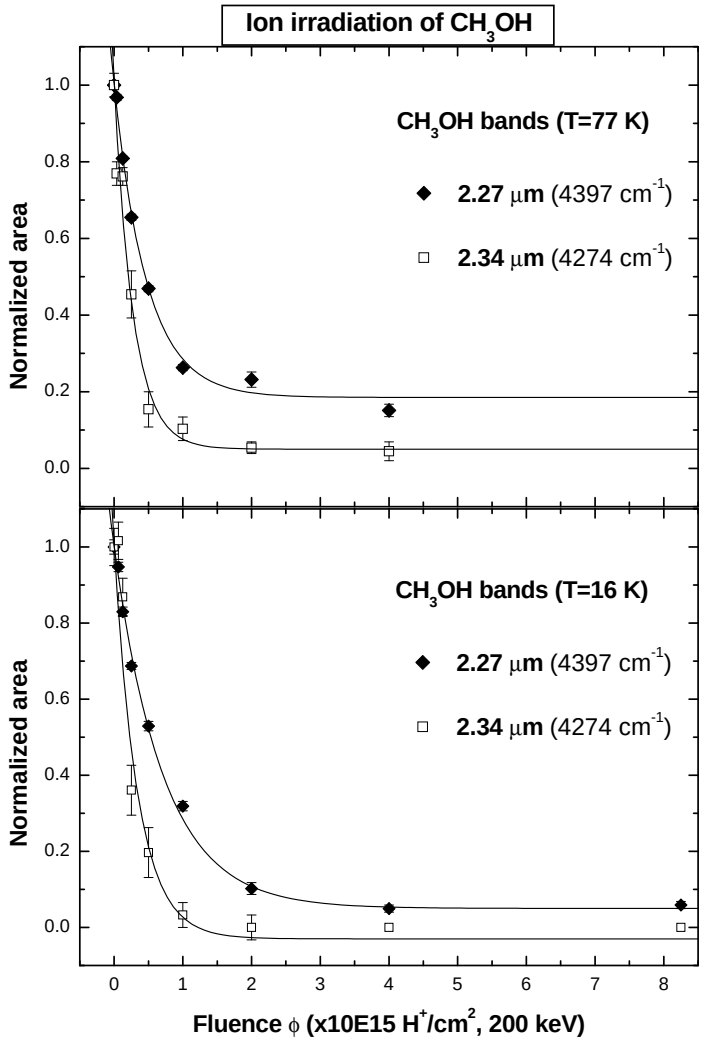

Figure 4.5: Decrease of the CH_3OH bands area after ion irradiation with 200 keV H^+ ions, at T = 77 K (top) and T = 16 K (bottom), as calculated from the reflectance spectra by means of a multi-Lorentzian fit. Exponential fits are shown and the cross sections and asymptotic areas are given in Table 4.2. At both temperatures, the 2.34 μm band is destroyed more efficiently than the band at 2.27 μm.

The value of σ for the 2.34 μm band is, within the errors, essentially the same

Peak position (μm)	Temperature (K)	Cross section σ (10^{-15} cm^2)	Asymptotic area A_∞ (normalized)
2.27	16	1.4 ± 0.1	0.05 ± 0.01
2.34	16	2.9 ± 0.8	-0.03 ± 0.1
2.27	77	2.1 ± 0.2	0.18 ± 0.02
2.34	77	3.6 ± 0.6	0.04 ± 0.05

Table 4.2: Cross sections σ and asymptotic areas A_∞ for the bands at 2.34 and 2.27 μm of irradiated CH_3OH, at T = 77 K and T = 16 K.

for the two temperatures, while the σ value for the 2.27 μm band is higher at T = 77 K than at T = 16 K. Furthermore, the σ values for the 2.34 μm band are always higher than those of the 2.27 μm band. The asymptotic values A_∞ are essentially zero in the case of the 2.34 μm band, while they significantly differ from zero for the 2.27 μm band. We conclude that both of the experiments show a more efficient decrease of the 2.34 μm band with respect to the 2.27 μm one, so that there is a wide range of ion fluences where the 2.27 μm band can be observed even if the 2.34 μm band is not.

4.1.2 Discussion

The knowledge of the physico-chemical properties of the surfaces of the small objects in the outer Solar System is scarce. Key objectives are to understand what materials and processing mechanisms produce the observed colors and/or spectra. Composition could reflect, at least partially, that of pre-existing interstellar grains. These latter could be reprocessed in the solar nebula; so we have to investigate to which extent energetic processing (UV and/or energetic particle irradiation) modifies pre-existing grains, and/or grains that are reformed in the solar nebula and accrete to form larger bodies, and/or the whole object once stored in different regions as the Kuiper belt or Oort cloud (see Strazzulla et al. (2003b); Strazzulla and Johnson (1991)).

Ions colliding with molecular solids cause the rupture of chemical bonds. The recombination of fragments produces newly synthesized molecules as well as an alteration of the structure of the sample (radiation damage and/or amorphization).

Because both the profile and the intensity of the IR bands depend on the chemical composition of the bulk matrix and on its structure, it is not surprising that the relative intensities of different bands of the same species vary. In particular, as observed in the present case for the CH_3OH bands, the symmetric modes are weakened with respect to the asymmetric modes. Further experiments made by depositing mixtures of methanol with CO and/or CH_4, and irradiating them with energetic ions, are programmed in our laboratory in order to clarify the relative relevance of compositional effects (e.g., CO/CH_3OH ratio) into respect to energetic processing in changing the intensities of the methanol bands.

It could be argued that a contribution to the 2.27 μm band in irradiated methanol comes from the synthesis of new species, such as ethylene glycol whose formation has been evidenced, after some controversy, by a study in the mid-IR spectral region (Hudson and Moore, 2000). However such a contribution, if any, would be very small. In fact, if ethylene glycol gave a contribution in the here studied spectral region, typical of overtones and combination modes, its abundance would be such to exhibit some (not observed) very intense features in the mid-IR region.

The results here described corroborate the formation of CH_4 and CO along with other species after irradiation of frozen methanol; similar results were obtained in other studies (e.g., Baratta et al. (2002); Hudson and Moore (2000); Palumbo et al. (1999), and references therein) in a different spectral range (2.6-17 μm).

The results presented here can be also a case for some small bodies in the outer Solar System, such as Pholus: its surface could in fact have been exposed for a long time to ion irradiation at the various stages of its evolution. Let us consider, as an example, only the post accretion irradiation by galactic cosmic rays. Cruikshank et al. (1998) quote that the upper 10 m of the surface (depending on density) accumulated a dose of 1.3×10^{12} ergs cm^{-3} that, for a mean molecular weight of 16 and a density of 0.5 g cm^{-3}, corresponds to about 40 eV/16 amu, i.e., on the order of magnitude that we used in our experiments.

The temperature of Pholus surface is estimated to vary between 40 and 90 K. Our experiments indicate that for different ions (H^+, He^+), in a wide range of energy of the incoming ions (30-200 keV), and temperature (16-77 K), the intensity of the

methanol band at 2.34 μm strongly decreases with respect to the one at 2.27 μm.

Methanol, if present on Pholus, could be mixed with water ice also identified in its spectrum (Cruikshank et al., 1998), and we have verified that the results here presented are still valid when mixtures water-methanol are considered. Pholus surface could then be rich of processed materials, and the fact that the band at 2.34 μm was not observed could be indicative of ion irradiation processes.

Laboratory experiments on methanol are also valuable to simulate variations in the slopes of the UV-VIS spectra that are observed to occur in the small bodies of the outer Solar System. Indeed, the existing observational data of these colors (spectral slopes) show a continuous spread of objects with colors from very red (as it is the case for Pholus) to essentially dark (e.g., Barucci et al. (2001), and references therein).

Laboratory results indicate that whatever is the irradiated hydrocarbon, it is converted to a refractory, insoluble residue (e.g., Strazzulla and Johnson (1991); Strazzulla (1997)). The slope of the reflectance spectra of such a residue changes with ion fluence. First extracted residues (at moderate doses) show red spectra becoming flatter and flatter under further ion irradiation (Andronico et al., 1987).

It is known that natural solid bitumens are possible analogs for cometary and asteroid organics (Moroz et al., 1998); laboratory experiments (Moroz et al., 2004a) show that ion irradiation of bitumens neutralizes the spectral slopes (0.3-2.5 μm) of these red organic solids. On the other hand, in the experiments here reported (2.2-2.4 μm), the reflectance spectrum of methanol, which is flat and bright at the beginning, gets redder after ion irradiation (see Figs. 4.2 and 4.3).

In the following section I will provide a detailed analysis, by in-situ reflectance spectroscopy, of the ion induced evolution in the colors of different ices relevant to the surface properties of distant objects in the Solar System.

Acknowledgments

This research was supported by the Italian Ministero dell'Istruzione, Università e Ricerca (MIUR), and the Spanish Ministerio de Ciencia y Tecnologia (MCyT).

4.2 CH_3OH, CH_4, and C_6H_6: the organic residue

Based on the paper: Brunetto, R., Barucci, M. A., Dotto, E., Strazzulla, G. 2006. Ion Irradiation of Frozen Methanol, Methane, and Benzene: Linking to the Colors of Centaurs and Trans-Neptunian Objects. Astrophysical Journal 644, 646-650.

In this section, I present new ion irradiation experiments of frozen (16-80 K) CH_3OH, CH_4 , and C_6H_6 , conducted with 200-400 keV ions, monitored by Vis-NIR (0.65-2.7 μm) reflectance spectroscopy, to compare the induced color variations with the observed spectra of some centaurs and TNOs.

We irradiated methanol, methane, and benzene with the ions given in Table 4.3. The dose has been varied up to the highest value reported in Table 4.3, and spectra have been collected at several intermediate steps. The thickness of the films and the temperature are also reported in Table 4.3 (the error in the film thickness is <0.2 μm).

In the case of irradiation with 200 keV H^+ ions, the mean penetration depth is between 1.8 and 2.4 μm (depending on the ice density) in our 45° experimental setup, and it is higher than the thickness of the samples (see Table 4.3). In the case of Ar, the penetration depth can be of the same order of magnitude or lower than the sample thickness; in this case the average doses that we use refer to the surface and intermediate layers (the first 70%- 80% of the ion track, where Ar ions lose 80%-90% of their energy), where the total (elastic plus inelastic) stopping power changes by not more than 10%. These layers are the ones that are actually producing the reflectance spectra.

The reflectance spectra of unprocessed and then progressively irradiated methanol, methane, and benzene are reported in Fig. 4.6 (for the sake of clarity, only some of the irradiation steps are shown).

Overtone and/or combination bands of the considered molecules are visible in Fig. 4.6. Those bands are progressively destroyed as the dosage released by the ions increases, and newly synthesized species (CO, CO_2, CH_4 , etc.) are identified.

Species	Film thickness (μm)	Temperature (K)	Ions and energies (keV)	Maximum dose (eV/16amu)
Methanol	1.0	16, 77	H^+ 200, Ar^{++} 400	350
Methane	1.4	16	Ar^{++} 400, Ar^+ 200	310
Benzene	1.0	80	H^+ 200, Ar^{++} 400	320

Table 4.3: Ions, energies, maximum dose, film thickness, and temperature of the irradiation experiments of methanol, methane, and benzene. The reflectance spectra have been collected at several intermediate irradiation steps. The error in the film thickness is lower than 0.2 microns. The errors in the dose are lower than 20% of the calculated values.

Here we do not describe the formation of such molecules nor the change of the band profiles (see, e.g., Foti et al. (1984); Strazzulla and Baratta (1991); Palumbo et al. (1999); Brunetto et al. (2005a) for such detailed analyses). We focus on color variations.

It is clear from Fig. 4.6 that the spectrum of the frozen species, which is initially flat and bright, becomes darker and redder with increasing dose.We also note that the reddening is much stronger in the range 0.65-1.25 μm than in the range 1.25-2.7 μm. At a high dose, the formation of a refractory organic residue was observed in all three cases.

We have calculated, for our experimental and data, the normalized reflectivity gradient, or spectral slope, S' (% per 1000 Å), as defined by Jewitt (2002). We have decided to consider two spectral ranges, 0.68-1.25 μm (which we refer to as J-R slope) and 1.25-2.20 μm (which we refer to as K-J slope).

Figure 4.7 illustrates the increasing (reddening) of the J-R slope for methane and benzene (top panel) and for methanol at the two different temperatures (bottom panel). Asymptotic exponential growth fits [slope $= A(1 - e^{-Bdose})$] are also shown, where B can be regarded as a reddening efficiency. The fit values are included in Fig. 4.7. Some points should be noted:

1. The reddening of irradiated methane and benzene is very rapid up to a dosage of about 50 eV per 16 amu for methane and about 80 eV per 16 amu for benzene, after which an asymptotic value is reached (higher for benzene than for methane).

2. The behavior of methanol is slightly different, characterized by less efficient reddening (10 times less efficient than methane), with a saturation probably reached

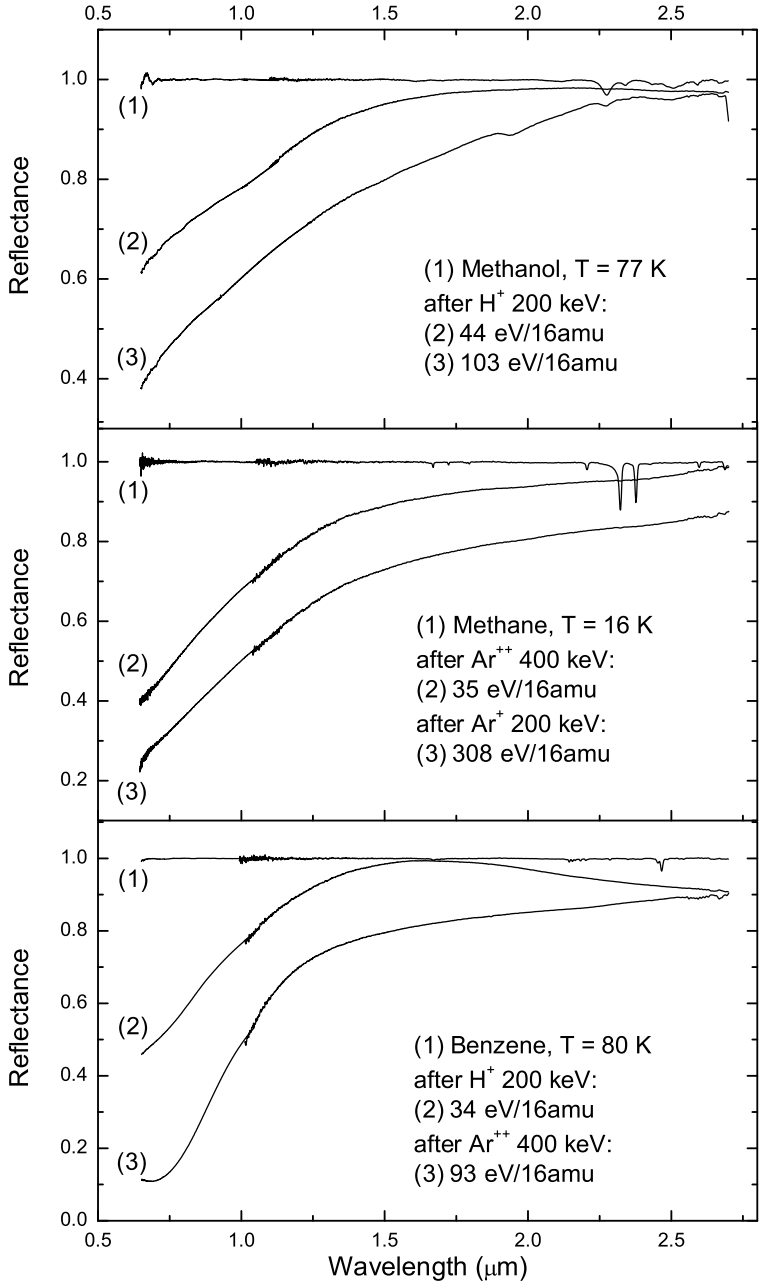

Figure 4.6: Absolute reflectance of as-deposited and then ion-irradiated methanol at 77 K (similar results are obtained at 16 K), methane at 16 K, and benzene at 80 K. For the sake of clarity, only a few irradiation steps are shown.

only at a very high doses (above 300 eV per 16 amu); the increasing of the spectral

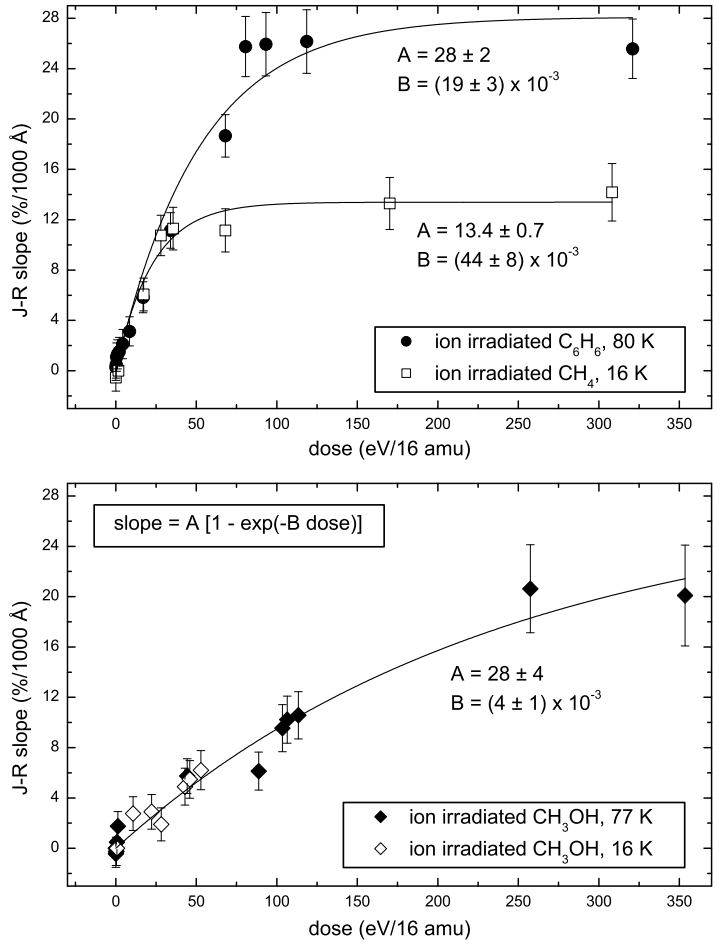

Figure 4.7: J-R slope as a function of the dose, for irradiated methane and benzene (top), and for irradiated methanol (bottom). The fit curves are also shown, with the corresponding values.

color is similar at 16 and 77 K.

3. For the three molecules considered, irradiated with different ions and energies, the total dose (elastic plus inelastic) is the parameter that plays the main role in the reddening process, unlike what we observed for silicates and bitumens (see above).

In the case of the K-J slope, a limited reddening is reached, so the K-J slope is always lower than the J-R slope, i.e., the spectra tend to flatten at higher wavelengths. It is possible to derive a sort of color-color relationship between the K-J and the J-R slopes, to be compared with observations of TNOs and centaurs, as it will be shown in the third part of this thesis.

Acknowledgments

We are grateful to G. A. Baratta and M. E. Palumbo for their helpful suggestions. We thank F. Spinella for precious technical assistance, and an anonymous referee who helped us improve the paper. This research has been supported by MIUR and INAF.

Part III

Space weathering in the Solar System

Chapter 5

Spectral comparisons

I have shown in the previous chapters that the spectral slope is a useful tool in characterizing space weathering effects on silicates, ices, and carbons. In this chapter I will discuss the results of several spectral comparisons between laboratory experiments and a large data-set of observed objects, from asteroids in the near-Earth region to bodies in the Kuiper Belt.

5.1 The spectral slope of Near Earth and Main Belt Asteroids

Based on the paper: Marchi, S., Brunetto, R., Magrin, S., Lazzarin, M., Gandolfi, D. 2005. Space weathering of near-Earth and main belt silicate-rich asteroids: observations and ion irradiation experiments. Astronomy and Astrophysics 443, 769-775.

In this section I report the results of a comparison between ion irradiation experiments on silicates, a large data set of silicate-rich asteroid, and meteorites spectra.

5.1.1 Spectra of NEAs and MBAs

The observational data used in this work consist of a large set of visible and near-infrared spectra of silicate-rich (generally indicated by S-type) asteroids. The vast majority of these objects are in the main belt (MB). However a significant number

of S-types have also been detected in near-Earth space thanks to recent surveys, like SINEO (Lazzarin et al., 2004, 2005). This latter source of S-types is also of greater interest because of its direct connection with meteorites and because, owing to their closeness, it permits study of smaller bodies.

In the present work, we consider only objects for which the whole 0.4-2.4 μm range is available, to perform a detailed analysis of the diagnostic 1 μm and 2 μm absorption bands due to olivine and pyroxene.

Moreover, asteroid data are compared with a large number of meteorite spectra from RELAB (http://www.planetary.brown.edu/relab/).

Main Belt asteroids. The NIR spectra of MBAs have been retrieved from the 52-color survey (Bell et al., 1985) and SMASSIR (Burbine, 2000). As they cover the range 0.9-2.4 μm, we extended them in the visible by using the data from SMASSI (Xu, 1994) and SMASSII (Bus, 1999). Spectra have been joined by minimizing the RMS of the differences in the overlapping region. Notice that for some asteroids the range 0.9-1.6 μm was present in both the 52-color and SMASSIR. In this case we privileged the spectral data instead of the photometric ones. A detailed description of the data used is provided in Table 5.1.

Number	Reference	Spectral range	Slope	λ_{BI}	BII/BI
3	s2+sIR+52c	0.44-2.46	0.164	0.940	0.512
5	s2+sIR+52c	0.44-2.46	0.256	0.910	0.568
6	s2+sIR+52c	0.44-2.51	0.248	0.930	0.475
7	s2+sIR+52c	0.44-2.56	0.332	0.940	0.268
11	s2+sIR+52c	0.44-2.56	0.262	0.980	0.385
12	s2+sIR+52c	0.44-2.46	0.274	1.140	0.196
15	s2+sIR+52c	0.44-2.41	0.227	1.000	0.137
18	s2+sIR+52c	0.44-2.56	0.309	0.900	0.340
20	s2+sIR+52c	0.44-2.51	0.164	0.920	0.967
25	s2+sIR+52c	0.44-2.56	0.513	0.952	0.294
26	s2+sIR+52c	0.44-2.46	0.209	0.974	0.226
27	s2+52c	0.44-2.51	0.237	0.960	0.473
29	s2+sIR+52c	0.44-2.56	0.216	0.980	0.623
32	s2+sIR+52c	0.44-2.41	0.206	0.910	0.263

Continued on next page

Table 5.1 – continued from previous page

Number	Reference	Spectral range	Slope	λ_{BI}	BII/BI
33	s2+sIR+52c	0.44-2.56	0.164	0.910	0.674
37	s2+sIR+52c	0.44-2.51	0.400	0.910	0.947
39	s2+sIR+52c	0.44-2.46	0.147	1.050	0.345
40	s2+sIR+52c	0.44-2.56	0.148	0.930	0.401
42	s2+sIR+52c	0.44-2.56	0.241	1.060	0.009
43	s2+sIR+52c	0.44-2.56	0.324	0.980	0.291
57	s2+sIR+52c	0.44-2.51	0.342	0.920	0.892
63	s2+sIR+52c	0.44-2.51	0.539	0.930	0.376
67	s2+52c	0.44-2.46	0.176	0.930	0.574
68	s1+sIR+52c	0.47-2.56	0.263	1.040	0.209
80	s2+sIR+52c	0.44-2.51	0.410	0.940	0.231
82	s2+sIR+52c	0.44-2.46	0.027	0.910	1.108
89	s2+52c	0.44-2.46	0.274	1.030	0.364
101	s2+52c	0.44-2.51	0.181	0.930	0.748
103	s2+52c	0.44-2.51	0.167	0.930	0.433
113	s2+sIR+52c	0.44-2.46	0.256	1.020	0.026
115	s2+52c	0.44-2.56	0.254	0.950	0.393
116	s2+52c	0.44-2.56	0.185	0.890	0.657
138	s1+52c	0.49-2.51	0.209	1.010	0.090
152	s2+52c	0.44-2.51	0.279	0.920	0.934
218	s1+52c	0.47-2.56	0.249	0.980	0.908
246	s2+sIR+52c	0.44-2.56	0.555	1.100	0.247
258	s2+52c	0.44-2.46	0.165	0.910	0.709
264	s2+52c	0.44-2.51	0.181	0.930	0.374
289	s2+sIR+52c	0.44-2.46	0.882	1.100	0.007
346	s2+sIR+52c	0.44-2.56	0.346	0.950	0.327
349	s2+sIR+52c	0.44-2.51	0.472	0.940	0.696
354	s2+sIR+52c	0.44-2.46	0.594	1.080	0.033
376	s2+52c	0.44-2.46	0.349	0.960	0.468
387	s2+52c	0.44-2.51	0.179	1.050	3.992
389	s2+sIR+52c	0.44-2.41	0.219	0.900	0.619
446	s2+sIR+52c	0.44-2.41	0.826	1.090	0.055
532	s2+52c	0.44-2.41	0.265	0.960	0.158
584	s2+sIR+52c	0.44-2.51	0.571	0.970	0.433
653	s2+sIR+52c	0.44-2.46	-0.082	1.060	0.825
674	s2+52c	0.44-2.41	0.177	0.910	0.830
863	s2+sIR+52c	0.44-2.41	1.118	1.090	0.060
980	s2+sIR+52c	0.44-2.51	0.109	1.000	0.389

Continued on next page

Table 5.1 – continued from previous page

Number	Reference	Spectral range	Slope	λ_{BI}	BII/BI

Table 5.1: List of Main Belt asteroids considered in this section. Column 2 indicates the origin of data used to obtain spectra in the entire range until 2.4 μm. s1: SMASSI data; s2: SMASSII data; sIR: SMASSIR data; 52c: 52-color data (see text for details).

Near-Earth objects. Most parts of these data come from the SINEO survey, as it is the only existing NEO survey up to 2.5 μm available so far. It consists of more than 100 spectra, 24 of which belong to the S-complex and have the full 0.4-2.5 μm coverage. Only few spectra come from Binzel et al. (2004a) and from Rivkin et al. (2004). Another 3 spectra were obtained joining data from Binzel et al. (2004b) and from the 52-color survey. A list containing all NEOs considered in this section can be found in Table 5.2.

Number	Name	Reference	Spectral range	Slope	λ_{BI}	BII/BI
719	Albert	sineo	0.40-2.45	0.320	0.951	0.276
3102	Krok	sineo	0.40-2.45	0.213	0.961	0.152
3753	Cruithne	sineo	0.40-2.54	0.219	0.950	0.264
4587	Rees	sineo	0.50-2.48	0.213	0.909	0.455
6489	Golevka	sineo	0.40-2.54	0.252	0.956	0.403
7341	1991 VK	sineo	0.40-2.51	0.268	0.969	0.428
8013	Gordonmoore	sineo	0.49-2.45	0.013	0.975	0.073
11054	1991 FA	sineo	0.40-2.50	0.667	0.961	0.079
35107	1991 VH	sineo	0.50-2.50	0.361	0.985	0.698
35396	1997 XF_{11}	sineo	0.50-2.49	0.418	0.958	0.048
52340	1992 SY	sineo	0.50-2.50	0.072	1.021	1.020
54071	2000 GQ_{146}	sineo	0.40-2.50	0.390	0.999	0.264
66251	1999 GJ_2	sineo	0.50-2.49	0.603	0.949	0.364
68346	2001 KZ_{66}	sineo	0.50-2.46	0.245	0.974	0.100
88710	2001 SL_9	sineo	0.40-2.48	0.317	0.918	1.786
98943	2001 CC_{21}	sineo	0.50-2.50	0.445	0.956	0.089
	2000 EZ_{148}	sineo	0.40-2.48	0.026	0.963	0.340

Continued on next page

Table 5.2 – continued from previous page

Number	Name	Reference	Spectral range	Slope	λ_{BI}	BII/BI
	2002 AL_{14}	sineo	0.50-2.47	0.705	0.971	0.504
	2002 QE_{15}	sineo	0.50-2.49	0.601	0.968	0.336
	2002 TD_{60}	sineo	0.50-2.50	0.527	0.937	0.235
	2002 TP_{69}	sineo	0.50-2.49	0.235	0.950	1.252
	2002 VP_{69}	sineo	0.40-2.50	0.267	0.991	0.252
	2002 YB_{12}	sineo	0.50-2.49	0.187	0.938	0.097
	2003 KR_{18}	sineo	0.50-2.47	0.306	0.969	0.214
433	Eros	sm9	0.44-2.49	0.333	0.970	0.318
1036	Ganymed	sm8+52c	0.44-2.51	0.344	0.920	0.737
1627	Ivar	sm8+52c	0.44-2.56	0.254	0.950	0.174
1685	Toro	sm6	0.44-2.43	0.202	0.970	0.441
1866	Sisyphus	sm8+52c	0.44-2.46	0.197	0.950	0.243
1943	Anteros	sm6	0.36-2.43	0.561	0.960	0.457
19356	1997 GH_3	sm9	0.44-2.41	0.100	0.960	0.541

Table 5.2: List of Near Earth asteroids considered. Column 2 indicates the source of data. sineo: SINEO project; sm6, sm8, and sm9: NEOs within SMASS survey (respectively: Binzel et al. (2004a,b); Rivkin et al. (2004)); 52c: 52-color data (see text for details).

Meteorites. A large number of meteorites spectra were retrieved from RELAB. Details of the materials used are provided in Table 5.3. All the meteorites selected belong to the ordinary chondrite group, because OCs have been suggested as representing the best analogues of S-type asteroids by several authors (see for example Gaffey et al. (1993). As this work deals with space weathering, we considered only those meteorites for whose no trace of alteration was reported. For this reason all the spectra indicating some natural alteration process (in the headers or in the description file) were discarded. Also those altered in laboratory (e.g. laser irradiated, washed etc.) were not considered.

All the spectra were analyzed in terms of the spectral parametrization developed by Gaffey et al. (1993). For each spectrum, we computed the slope of continuum

PI code	PI full name	Spectra used
CMP	Carl M. Pieters	85
DTB	Dan Britt	12
FPF	Fraser P. Fanale	25
JFB	Jeffery F. Bell	4
LAM	Lucy Ann McFadden	5
MJG	Michael J. Gaffey	39
TXH	Takahiro Hiroi	14
Total		184

Table 5.3: Spectra acquired by different investigators with the NASA RELAB facility at Brown University. This table lists the number of RELAB OC meteorites used from different Principal Investigators.

across the 1 μm absorption band, the 1 μm band (BI) and 2 μm band (BII) area, and BI depth and peak position. The slope thus defined is representative of spectral reddening.

It must be pointed out that by this analysis the BII/BI area ratio and the BI peak position are representative of the composition and that the slope is highly representative of space weathering alteration (see Strazzulla et al. (2005); Hiroi and Sasaki (2001)). However, one should keep in mind that this analysis is not able to constrain the presence of featureless compounds, like metals and glasses. Nevertheless, it remains a good way to describe the silicate-rich bodies which are thought to be mostly made of olivine and pyroxene.

Laboratory spectra Ion irradiation experiments were performed in the Catania Laboratory (see above), using different ions (N^+, Ar^+, Ar^{++}) and energies. The outcomes were monitored by means of reflectance spectroscopy (0.3-2.5 μm). Here I present new experiments simulating space weathering by solar wind ions by ion irradiation experiments (200 keV) of Fe-poor olivine (from Bamble, Norway) and of Fe-poor orthopyroxene (from San Carlos, Arizona, USA), and irradiation of bulk silicate-rich rocks (Eifel silicate, from Germany).

Pellets of olivine and orhopyroxene were obtained by pressing their powders with grain sizes of about 100-200 μm. The Eifel silicates consisted of freshly cut

samples from rock fragments, with a surface roughness of about 100 μm. For better comparison with asteroid spectra I also considered irradiation of Epinal meteorite and of other bulk silicate-rich rocks (Jackson silicate), which have already been presented in Strazzulla et al. (2005) and Brunetto and Strazzulla (2005).

Bulk Eifel silicate rocks are rich in olivine, and have a small content of pyroxene, as can be seen in Fig. 5.1 (upper panel). Indeed, the spectrum of unirradiated Eifel sample exhibits a very strong and broad band at about 1 μm (BI), which is due to the presence of ferrous iron Fe^{2+} in olivine crystals but is also present in pyroxene. It is also evident a less intense broad 2 μm band (BII) that is characteristic of pyroxene but not olivine.

The spectrum of irradiated Eifel (upper panel of Fig. 5.1) shows strong darkening and reddening, and weathering effects are strong in the whole observed spectral range. The area of BI is reduced as the slope of the continuum across BI increases, and a similar effect is observed for BII.

The reflectance spectra of San Carlos olivine and Bamble orthopyroxene are plotted in Fig. 5.1 (middle and lower panel). Also in these cases, darkening and reddening of reflectance spectra are apparent.

This spectral reddening agrees with the results of previous experiments of ion irradiation of the OC Epinal meteorite (Strazzulla et al., 2005) and of Jackson silicates (Brunetto and Strazzulla, 2005). Furthermore, we note that the weathering process is active both on bulk samples and pressed powder samples.

5.1.2 A global view on space weathering of silicate-rich asteroids

The thickness of the damaged region at these energies is lower than 1 μm; i.e. the reddening and darkening process of reflectance spectra is due to displacements in the very upper layers of the target. A similar effect of upper layer alteration should be present in asteroids, which would cause the mismatch between the slope of asteroids and that of OCs.

In this respect, one result concerns the well-known lack of OCs analogues (which

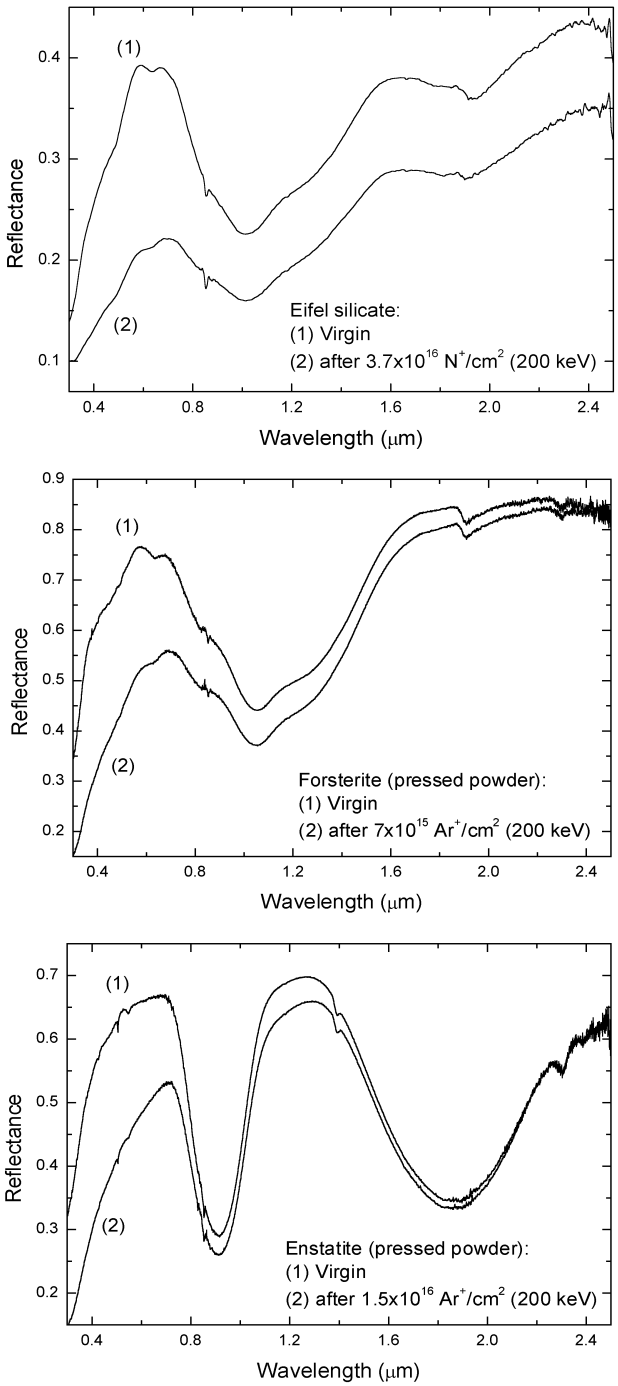

Figure 5.1: Reflectance spectra of virgin and irradiated Eifel (upper panel), San Carlos olivine (middle panel), and Bamble orthopyroxene (lower panel).

represent the largest number of falls on Earth) among minor bodies. The situation is shown in Fig. 5.2, where the slope distributions of OCs, NEOs, and MBAs are very different. Some authors (e.g. see Lazzarin et al. (1997); Binzel et al. (1996)) report the occurrence of OC-like bodies among small asteroids (and in particular among NEOs). Indeed the blue tail of MBAs and NEOs distributions overlap the OCs distribution. However, in terms of numbers, these findings still represent only some exceptions.

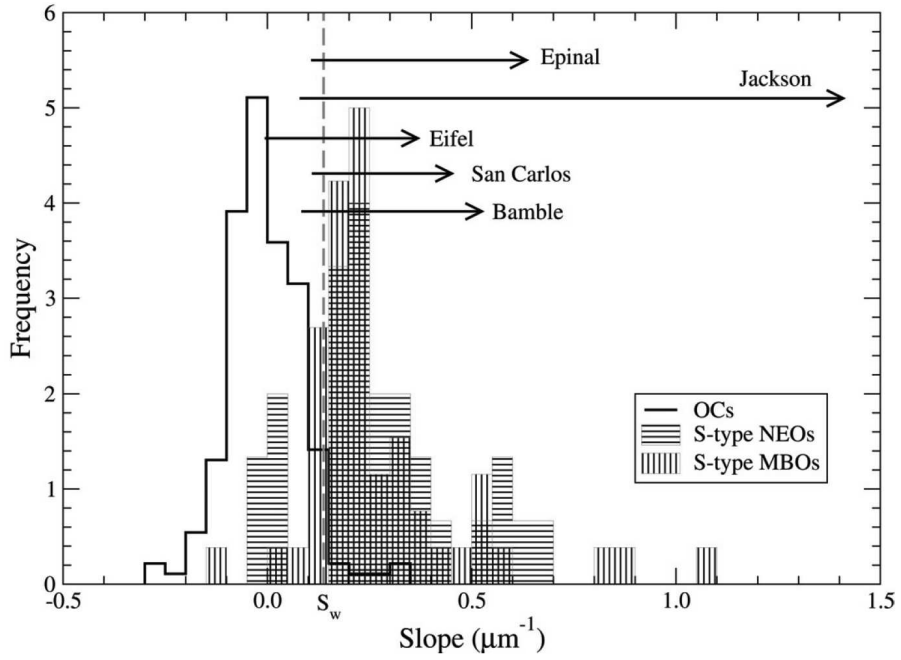

Figure 5.2: Spectral slope distributions of OCs, NEOs, and MBAs. Each distribution has been normalized (area= 1). The vertical dashed line marks the 95% OCs limit (corresponding to a slope of $S_w = 0.138\ \mu\mathrm{m}^{-1}$). Horizontal arrows mark the reddening measured for irradiated Epinal, Jackson (from Strazzulla et al. (2005); Brunetto and Strazzulla (2005)), Eifel, San Carlos, and Bamble.

Nevertheless, OCs distribution (representative of pristine materials) peaks at slope ∼0, and is by far less red than the NEOs and MBAs distributions. On the contrary, the two latter distributions are basically indistinguishable. The striking feature is that, if one defines the limiting slope below which 95% of the OCs lie

(corresponding to a slope of $S_w = 0.138\ \mu\mathrm{m}^{-1}$), we find that 83% of the NEOs and 94% of the MBAs are redder than S_w. Thus only 17% of NEOs and 6% of MBAs are compatible with OCs spectra. Although these percentages can be affected by low number statistic, the NEO population seems to contain a higher percentage of OC-like objects. In this respect, the S_w value can be regarded as an indicator of space weathering: objects redder than S_w may be considered - with high confidence - as weathered, while, in terms of slope, objects below S_w are fully compatible with OCs.

It should be noted that, in spite of the wide size-range involved, NEOs and MBAs span a similar interval of slopes and that the asteroid slope distributions have a broader FWHM with respect to that of OCs (of roughly a factor of 3). A possible explanation for the different FWHM between the asteroid and OCs slope distributions could be that asteroids spend different exposure times in weathering environment, also suffering resurfacing processes. Figure 5.2 also reports the results for ion irradiation experiments. Epinal shows the trend for a typical OC, while Jackson is representative of the maximum reddening attained in laboratory experiments, which largely overcome asteroid slopes. Therefore the shift between OCs and asteroids distributions can be explained by ion irradiation experiments.

Figure 5.3 shows the BI peak position as a function of the BII/BI area ratio. From this plot it is possible to get information about the mineralogy of the analyzed bodies. Gaffey et al. (1993) used a similar plot to separate the S-type asteroids into seven classes (from SI to SVII), where the SIV class had been defined from the corresponding mineralogy of OCs. We enlarged the statistic of both asteroids and OCs, so that from Fig. 5.3 one can deduce that the SIV class is indeed much wider than that defined by Gaffey et al. (1993). A second point that arises from Fig. 5.3 is that irradiation does not change the BII/BI area ratio significantly.

A further important result concerns the suitability of using of the slope parameter to study the effects of space weathering. Figure 5.4 shows the spectral slope as a function of the BII/BI area ratio, for MBAs, NEOs, OCs, and laboratory experiments.

It turns out that space weathering acts mainly on the slope, but only marginally

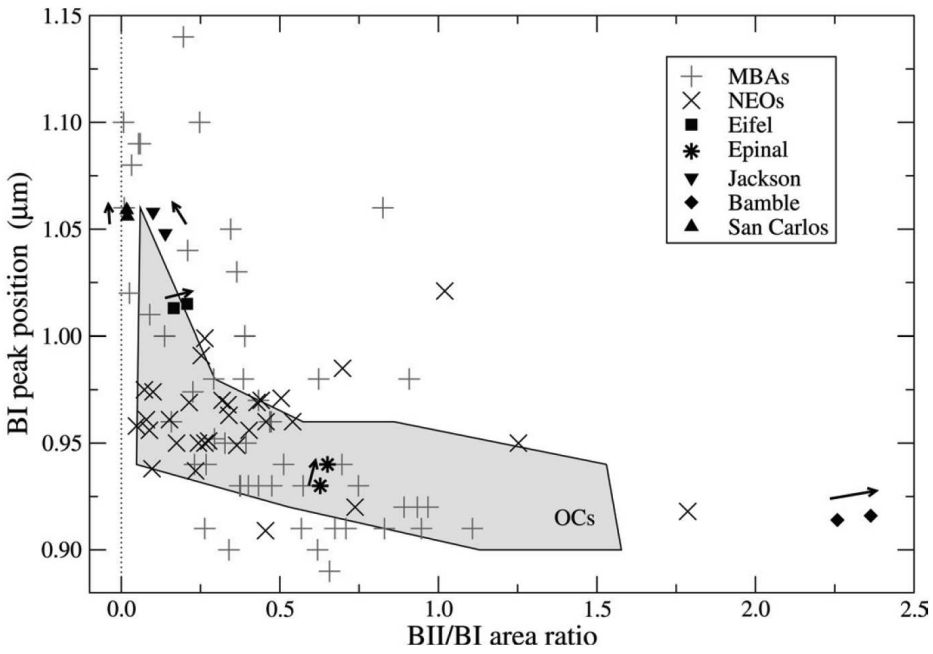

Figure 5.3: Band I peak position vs. BII/BI area ratio for MBAs and NEOs. Positions for virgin and irradiated silicate are also shown (arrows show their trend from virgin to irradiated). The shaded area corresponds to the region occupied by OCs. Symbol dimensions correspond to maximum error bars.

on the ratio BII/BI, for both pressed powder (San Carlos and Bamble) and bulk samples (Jackson, Eifel, Epinal). On the other hand, the ratio BII/BI is representative of the composition. Thus, the discrepancy between meteorites and asteroids has mainly to be ascribed to the spectral slope, and this process is reproduced well by ion irradiation experiments.

Another interesting issue related to Fig. 5.4 is that MBAs (and NEOs) have a triangle-shaped distribution, with the highest slopes achieved for low values of BII/BI, namely for high olivine contents.

From the spectra of irradiated Epinal, it has been estimated a reddening timescale of about 10^5 years at 1 AU (Astronomical Unit) from the Sun. The results reported here indicate that most of the spectral slopes of asteroids can be reproduced by damage values in the range 1-3$\times 10^{19}$ displ/cm^2 (see Fig. 5.4), in agreement with

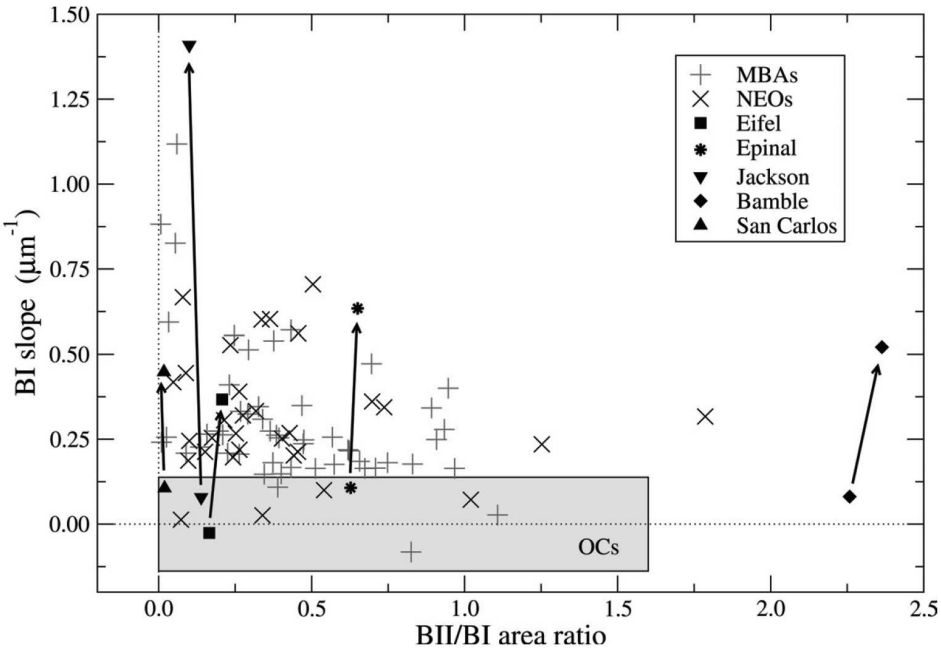

Figure 5.4: Spectral slope vs. BII/BI area ratio for MBAs and NEOs. Vertical arrows show the trend from virgin to irradiated silicates. The shaded box contains 95% of OCs as described in Fig. 5.2. Symbol dimensions correspond to maximum error bars.

what has been calculated for Epinal (see above). Therefore, it is confirmed that ion irradiation is a very efficient weathering process. Nevertheless, this is only one of the processes that can affect asteroid surfaces; in particular, the time-scale of ion-induced reddening is not expected to strictly correspond to the lifetime of the asteroid surfaces, as several rejuvenating mechanism can be present, whose efficiency could be able to partially compensate for the reddening induced by solar wind ions. Moreover, at the MB distance to the Sun, other mechanisms - such as micrometeorite impacts - could also be as efficient as ion bombardment for the weathering.

Summary

Comparing a wide set of asteroid and meteorite spectra with ion irradiation experiments, some points can be established:

1. OCs and S-type asteroids exhibit a similar mineralogy, as deduced from band parameters, more than what was previously assumed. Nevertheless, a significant mismatch was observed in the Vis-NIR spectra, which is due to very different distributions of spectral slope.

2. The continuum slope above BI band is a good parameter to quantify the degree of space weathering. Thus, a 95% OC slope limit (S_w) can be defined, beyond which an asteroid can be considered as "weathered". About 83% and 94% of the observed NEOs and MBAs, respectively, have a higher slope than this limit. Moreover, asteroid slope distributions exhibit a noticeably broader FWHM with respect to OCs distribution of about a factor of 3.

3. Ion irradiation can explain the shift of the OC distribution toward asteroid distributions. Spectra of unaltered and irradiated silicates have slopes that span a wider range than that observed in NEOs and MBAs.

4. MBA and NEO slope distributions do not differ significantly from each other. However, if compared with OCs, they exhibit an asymmetrical slope distribution, a behavior that will be a subject of further investigations.

Acknowledgements

We thank G. Strazzulla for his helpful comments, and G. A. Baratta and F. Spinella for their help during the experiments. We also thank V. Orofino for providing us with the silicate samples. We thank the anonymous referee who helped to improve the paper by means of useful comments.

5.2 S-, C-, and X-complexes: a big picture

Based on the paper: Lazzarin, M., Marchi, S., Moroz, L. V., Brunetto, R., Magrin, S., Paolicchi, P., Strazzulla, G. 2006. Space Weathering in the Main Asteroid Belt: The Big Picture. Astrophysical Journal 647, L179-L182.

S-complex asteroids are composed mainly of mafic silicates olivine and pyroxeneand possibly some spectrally featureless phases such as plagioclase, FeNi metal, and sulfides (Gaffey et al., 1993). For what concerns space weathering, laboratory experiments demonstrated that their analog materials redden under both ion bombardment (Strazzulla et al., 2005; Brunetto and Strazzulla, 2005) and laser irradiation (Moroz et al., 1996; Yamada et al., 1999; Brunetto et al., 2006a); the latter simulates micrometeorite impacts. Thus, the spectral "slope" increases with space weathering.

The reddening due to micrometeorite impacts and low-energy light ions appears to be related to the formation of nanophase metallic iron particles (SMFe; Hapke (2001); Sasaki et al. (2001)). The micrometeorite impacts may be important contributors to the reddening observed in the lunar samples (Hapke, 2001); however, note that the different space environments and surface mineralogy between the lunar samples and the MBAs do not allow for a direct extension of this statement to MBAs.

In fact, the space weathering on S-complex asteroids seems to be more related to solar ion flux rather than to micrometeorite bombardment (Marchi et al., 2006). Consistently, Brunetto and Strazzulla (2005) suggested that, in terms of the astrophysical timescale, solar wind ions (both light and heavy) are more efficient than micrometeorites.

In comparison to the S complex, our understanding of C and X complexes (together more than half of the spectrally classified asteroids) is by far less satisfactory, and their mineralogical assessment is not fully established. C and X complexes are characterized by having mostly featureless visible spectra, but with different slopes: from bluish to slightly red for the C-complex asteroids and from slightly red to moderately red for the X-complex asteroids. Due to their featureless visible spectra, the only clues to their composition can be found with the help of NIR observations and with the use of meteoritic- assumed-counterparts.

Carbonaceous chondrites (CCs) have been suggested as possible fragments of some C-complex asteroids on the basis of their spectral match and low albedo ($\sim$0.07; Johnson and Fanale (1973)). Although CC meteorites are dominated by silicates

(anhydrous and/or hydrated) by mass, their optical properties are dominated by fine-grained opaque phases (e.g., sulfides) and organics. The response of the latter phases to space weathering may be different from that of silicates (see below); thus, it is not obvious how CCs (and C-complex asteroids) would behave under space weathering.

The situation is even more complicated for the X-complex asteroids. Good spectral matches have been found with different meteorite clans like enstatite chondrites (E chondrites), aubrites, and irons (Burbine et al., 2002; Lazzarin et al., 2005, 2004). Thus, the possible composition should range from Fe-free low-Ca pyroxene, enstatite, metal, and sulfides (E chondrites and aubrites) to FeNi metal for the irons.

This is also confirmed by the wide albedo range observed. Due to recent observational work (Hardersen et al., 2005), features at 0.9 and 2 μm have been detected in the spectra of some moderate-albedo X-complex asteroids (i.e., M-type asteroids), and they have been assigned to mafic silicates (low-Fe, low- Ca pyroxene). These findings might favor a mantle-core origin, ruling out the link with undifferentiated E chondrites. However, absorption features at 3 μm have been detected and interpreted as being due to phyllosilicates (hydrated silicates), and this is inconsistent with the high-temperature scenario for a differentiated parent body (Clark et al., 2004; Lagerkvist et al., 2005).

Also, the experimental background of space weathering effects on terrestrial and meteoritic analogs relevant for C and X complexes is not well established, basically due to a lack of experimental work. The first experiments conducted on natural complex hydrocarbon materials (asphaltite and kerite) showed that materials become less red (the slope decreases) and less dark after irradiation with low-energy ions (Moroz et al., 2004a), suggesting a similar space weathering trend for organic-rich objects, opposite to that defined for silicates. Laser irradiation of a mineral mixture containing 5 percent by weight (wt.%) kerite mixed with hydrated and anhydrous silicates, metal, and calcite showed a slope decrease and darkening (Hiroi et al., 2003). The same effect was observed after laser irradiation of a unique reddish CC Tagish Lake (Hiroi et al., 2004) containing only 2.5 wt.% of organic material.

However, no ion irradiation (presumably the dominant space weathering process for asteroids; Marchi et al. (2006)) experiments have been performed on Tagish Lake, organic-poor mineral mixtures or on pure hydrated silicates and sulfides, the latter being the main darkening agents in primitive CC meteorites. The relative abundances of organics compared to silicates and other constituents, the carbonization degree of organics, as well as the texture of constituents may define which particular space weathering trend (increase or decrease of the slope) would dominate. Observations of the slope-diameter anticorrelation for dark Cybele and Hilda outer belt asteroids might suggest the dominance of the organic-like space weathering trend on these distant (3.3-4 AU) objects (Lagerkvist et al., 2005). As for the bright X-complex analog materials, no experiments have been performed yet.

5.2.1 Spectral trends in the Main Belt

With the aid of the method used for the S complex (Marchi et al., 2006), it is possible to obtain some relevant observational results concerning the above-mentioned problems. We used the largest existing MBA spectroscopic database, consisting of 559 S-complex, 418 C-complex, and 250 X-complex MBAs from the second phase of the Small Main-Belt Asteroid Spectroscopic Survey (SMASSII; Bus and Binzel (2002a)). The model takes as input a state-of-the-art estimate (Bottke et al., 2005) of the mean collisional age of the asteroids as a function of their size. Combining the ages with the asteroid's orbital configuration (namely, the semimajor axis and eccentricity), we obtain a parameter proportional to the exposure of the ion flux from the Sun. With respect to the previous model (see Marchi et al. (2006) for a detailed explanation of the definition of exposure), we improve the age estimates for the members of dynamical families, which can be set, if less than the collisional age, equal to the age of the family (we used the recent and reliable estimates of Nesvorný et al. (2006)). We also improve the exposure estimate by using the more stable proper elements (Knežević and Milani, 2003) instead of the osculating elements. We use the spectral slopes between 0.52 and 0.92 μm to characterize the degree of space weathering.

Figure 5.5 shows the slope-exposure distribution for the three major complexes. The most striking result is that for all the complexes, the trends are very clear and statistically significant (the two-tailed probability, P, is <0.01%, ∼0.7%, and ∼0.8%, for the S, X, and C complexes, respectively). The trends are, respectively, (24.9 ± 4.6), (14.6 ± 3.2), and $(8.8 \pm 5.4) \times 10^{-5}$ μm^{-1} Myr^{-1} AU^{-2}. Despite these significant statistical trends, spectral slopes of individual objects exhibit a strong scatter. This is certainly due to several parameters, like differences in composition, surface roughness/texture, and inaccurate age determination; we use a mean value and neglect possible dynamical corrections. Nevertheless, the quality of the results, in statistical terms, is also supported by the overall agreement of the linear fits with the average curves.

Notice that the trend found for the S complex is slightly reduced compared to that previously found (Marchi et al., 2006). Notice also that the trend for the C complex seems to be opposite to the only one available in the literature for family C-complex asteroids (Nesvorný et al., 2005). In order to understand the trend obtained by Nesvorný et al. (2005) using photometric rather than spectroscopic data, we selected the C-complex family members present in our database.

Within the uncertainties due to the small number of objects, we obtain that slope anticorrelates with exposure (and age), in agreement with Nesvorný et al. (2005). The discrepancy between this trend, effective only for family members, and the general, opposite, one is unclear, and it is probably due to some "sampling" effect: the listed families may not be representative of the average composition of the whole C-complex population of the main belt. The anticorrelation of family members is mainly due to five families (24 Themis, 490 Veritas, 668 Dora, 1128 Astrid, and 1726 Hoffmeister) located beyond 2.78 AU, where the abundance of organics (or other nonsilicate components) might be higher than in the inner part of the main belt. A slope-age anticorrelation within C-complex families may be due to an organic-like space weathering trend. Our conclusion is also supported by the discovery of two active Themis family asteroids (Hsieh and Jewitt, 2006), which are certainly compositionally very different from the usual C-complex asteroids; it is possible that a relevant part of the Themis family itself has similar peculiar

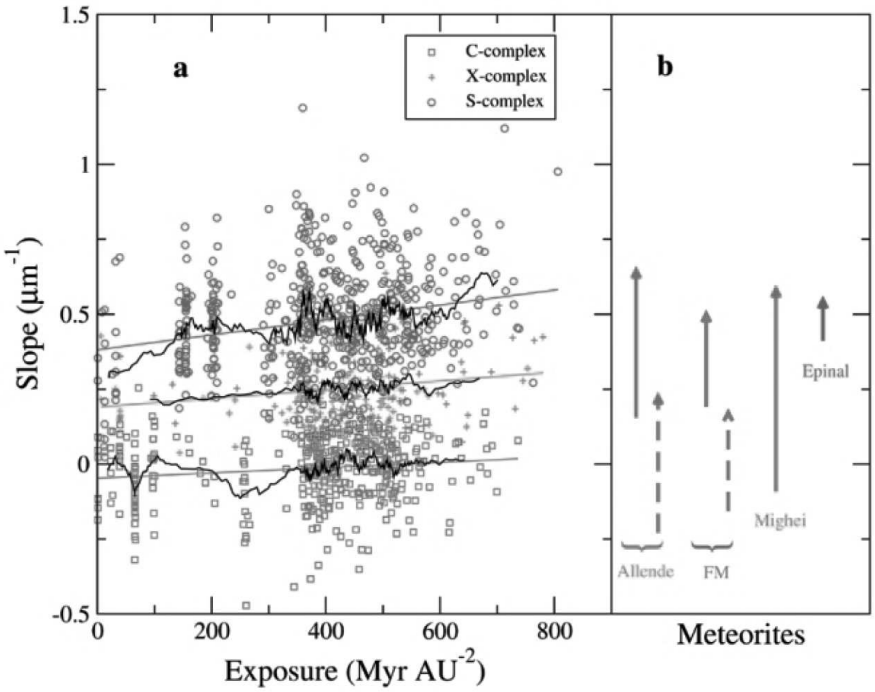

Figure 5.5: Spectral trends for MBAs and their comparison with laboratory experiments. (a) Slope-exposure trends for the three major complexes of the main belt. Average curves (20 points) are also shown (see text for further details). (b) The arrows indicate the results of the first ion-bombardment experiments performed on CC meteorites (namely, Allende and Frontier Mountain [FM] 95002); the solid arrows are for powders, while the dashed ones are for pressed samples. The results of the laser irradiation of the Mighei meteorite (dust sample) are also shown. For comparison, ion bombardment on a slab of Epinal meteorite (OC) is overplotted. In all cases, the arrow's starting point corresponds to the slope of the untreated samples, while the end of the arrow corresponds to the irradiated ones.

properties.

Although the general trends are similar, it must also be noted that the reddening rates decrease, passing from the S complex to the X complex to C complex. This may be related to an increasing content or decreasing grain size of nonsilicate components.

This new observational scenario can also be supported by new laboratory experiments, which are briefly reported here. We performed ion-bombardment experiments on two CCs, namely, CV3 Allende and CO3 Frontier Mountain 95002. Results and experimental details are presented in Fig. 5.6. Both meteorites redden under ion fluence irrespective of the sample preparation (powder vs. pressed pellet).

A similar spectral effect (see Fig. 5.6) is observed after laser irradiation of the CM2 chondrite Mighei (Moroz et al., 2004b).

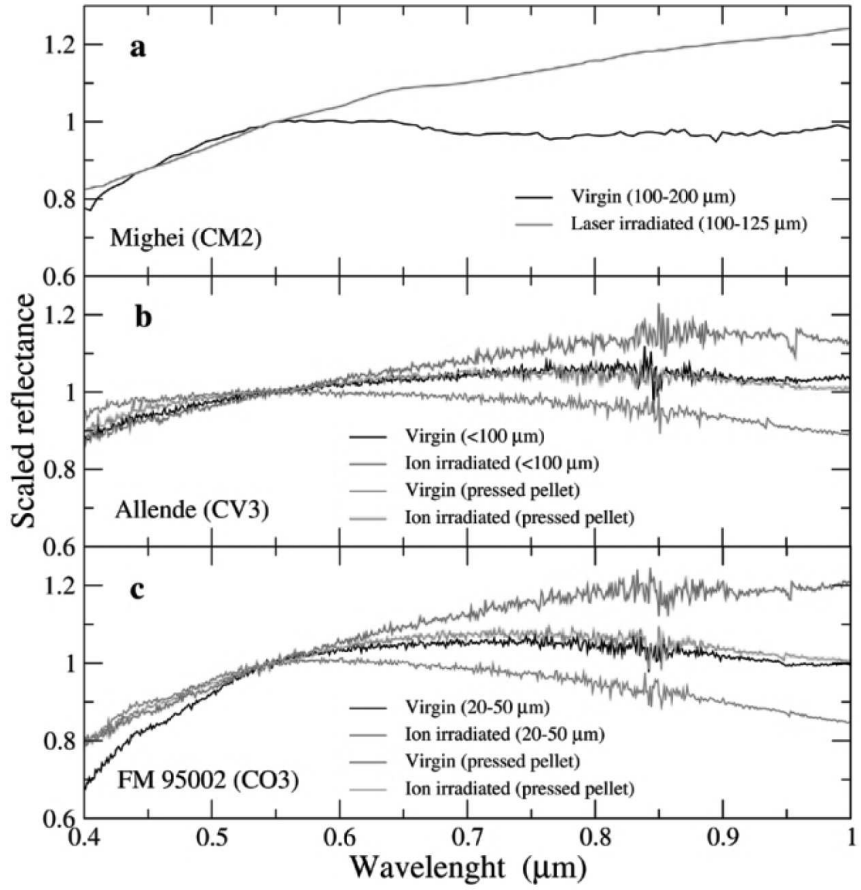

Figure 5.6: Reflectance spectra of three CC meteorites before and after laser and ion irradiation. (a) Laser irradiation experiments on CM2 Mighei samples (Moroz et al., 2004b; Shingareva et al., 2004) have been performed under vacuum using an ND-YAG multiple-pulse laser with a pulse frequency of 30-40 kHz and pulse duration of 0.5-1 ms. Bidirectional reflectance spectra of nonirradiated and laser-irradiated Mighei coarse powders were acquired at the NASA-supported RELAB facility. (b) & (c) We performed ion-bombardment experiments and in situ spectral reflectance measurements of powdered meteorites and pressed powders. Shown here are the ex situ spectra, but in situ spectra show strong reddening after ion irradiation as well. Note the significant difference in spectral slopes between powders (grain sizes are reported for each sample) and pressed samples; variations in surface roughness/texture may contribute to the scatter in spectral slopes, typical of all main-belt complexes (see text). All spectra are scaled to 1 at 0.55 μm.

Similar considerations may hold for X-complex asteroids, but so far no experi-

ments have been performed on possible analogs, such as aubrites, E chondrites, or irons. For a better comparison, Fig. 5.5 also shows the reddening rate of these experiments and the ion-irradiated H5 ordinary chondrite (OC) Epinal (Strazzulla et al., 2005). Notice that the arrow lengths do not quantify the absolute degree of reddening; they simply reflect the experimental conditions and cannot be used for a quantitative comparison.

5.2.2 The big picture

We have shown that a statistically significant slope-exposure correlation holds for all the major MBA complexes and that this result may be understood consistently in terms of the new experimental data. There are a few major implications for asteroid science. First, it entails that the response to space weathering of (nearly) all kinds of asteroids between 2 and 3.3 AU (where most of the asteroids in our sample are located) be silicate-like.

This limit corresponds to the farthest distance where the Sun-related alteration effects have been measured so far. Moreover, the existence of a reddening trend for the C complex might define an upper limit (of a few percent) to the content of organics within this region. The new space weathering simulation experiments on CCs confirm the general robustness of our scenario. In addition, the existence of slope-exposure trends indicates to us a Sun-related origin of the asteroidal space weathering, at least in this region.

The low content of organics that we are suggesting may be explained either in terms of their low original abundance in the part of the Solar Nebula from which MBAs originate or as being due to a significant contamination by inorganic materials, probably injected from the terrestrial region (e.g., within the outward migration model recently proposed Bottke et al. (2006). The existence of a slope-exposure anticorrelation among C-complex families may also be due to the existence of bodies with a different composition (as a result of the compositional gradient in the Solar Nebula or due to interlopers from the outer Solar System), perhaps with higher contents of surface organics. The case of the active Themis member asteroids may

support this conclusion.

Concerning the moderate- to high-albedo part of the X complex, if the space weathering-induced reddening is related to any change in the chemical state of Fe (e.g., SMFe formation), then E chondrites and aubrites containing only Fe-free silicates cannot be dominant components of the complex. However, additional space weathering experiments on pure Fe-free silicate targets are required. Finally, the emergence of similar reddening trends for C and X complexes may cause a severe ambiguity between the two complexes since reddened (exposed to space weathering) C-complex asteroids can be spectrally very similar to fresh X-complex asteroids, as shown by our new ion-bombardment experiments. It is also possible that space-weathered C-complex asteroids may be confused with low-albedo X-complex asteroids. On the basis of the available albedo data, this ambiguity might affect a large fraction of about 50% of X-complex asteroids.

Acknowledgements

We thank the referee B. E. Clark for useful comments. We thank D. Nesvorný for providing us with the most recent family ages and a list of family memberships. We also thank L. Folco (Museo Nazionale dell'Antartide, Italy) for providing us with samples of Allende and Programma Nazionale dell'Antartide (PNRA) meteorites. We also thank Y. Keheyan for providing us with Allende samples. M. Lazzarin, S. Marchi, S. Magrin, and P. Paolicchi have been supported by MIUR-PRIN funds. L. V. Moroz was supported by MERTIS project funds.

5.3 Irradiation mantles on centaurs and TNOs: ultra-red matter?

Based on the paper: Brunetto, R., Barucci, M. A., Dotto, E., Strazzulla, G. 2006. Ion Irradiation of Frozen Methanol, Methane, and Benzene: Linking to the Colors of Centaurs and Trans-Neptunian Objects. Astrophysical Journal 644, 646-650.

5.3.1 Observations of centaurs and TNOs

I showed in the second part of this thesis present visible and near-infrared reflectance spectra of frozen methanol, methane, and benzene, collected before and after irradiation with 200 keV H^+ and Ar^+ ions, and 400 keV Ar^{++} ions, up to a dose released to target molecule of about 350 eV per 16 amu. The results evidenced a strong reddening and darkening of the spectra, due to the formation of an organic (C-rich) refractory residue.

In this section I compare this spectral behavior with some centaurs and trans-Neptunian objects. To compare with laboratory data, I consider spectral observations of nine centaurs: (2060) Chiron (1977 UB), (8405) Asbolus (1995 GO), (10199) Chariklo (1997 CU_{26}), (32532) Thereus (2001 PT_{13}), (52872) Okyrhoe (1998 SG_{35}), (54598) Bienor (2000 QC_{243}), 55576 (2002 GB_{10}), 63252 (2001 BL_{41}), and 83982 (2002 GO_9).

I also include nine TNOs: 26181 (1996 GQ_{21}), 26375 (1999 DE_9), (28978) Ixion (2001 KX_{76}), (38628) Huya (2000 EB_{173}), 47171 (1999 TC_{36}), 47932 (2000 GN_{171}), 55565 (2002 AW_{197}), (90377) Sedna (2003 VB_{12}), and (90482) Orcus (2004 DW).

These observations are the products of the ESO Large Program (LP; PI: H. Boehnhardt), executed from 2001 April to 2003 March at the VLT and NTT ESO telescopes, covering both visible/ near-infrared photometry and spectroscopy (for details see Barucci et al. (2002); Boehnhardt et al. (2003); Barucci and Peixinho (2005)). Finally, I also consider the spectrum of centaur 5145 Pholus (after Cruikshank et al. (1998)).

To compare the experiments with the observed spectra of centaurs and TNOs, I have scaled all the spectra to 1 at 0.8 μm. A qualitative comparison with some of the observed spectra (Thereus, (83982) 2002GO_9, and Sedna) is displayed in Fig. 5.7; it indicates a general trend, i.e., the colors of the observed objects can be reproduced by progressive irradiation of simple molecules. Nevertheless, it should be stressed that the aim of the comparison in Fig. 5.7 is not to fit the observed spectra, since a scattering model of the surface would be necessary; furthermore, other species (for instance H_2O, N_2, silicates, etc.) or even a spectrally flat amorphous carbon, which

would imply low albedo, may be present. So from Fig. 5.7 it is not possible to infer the specific composition of the observed objects.

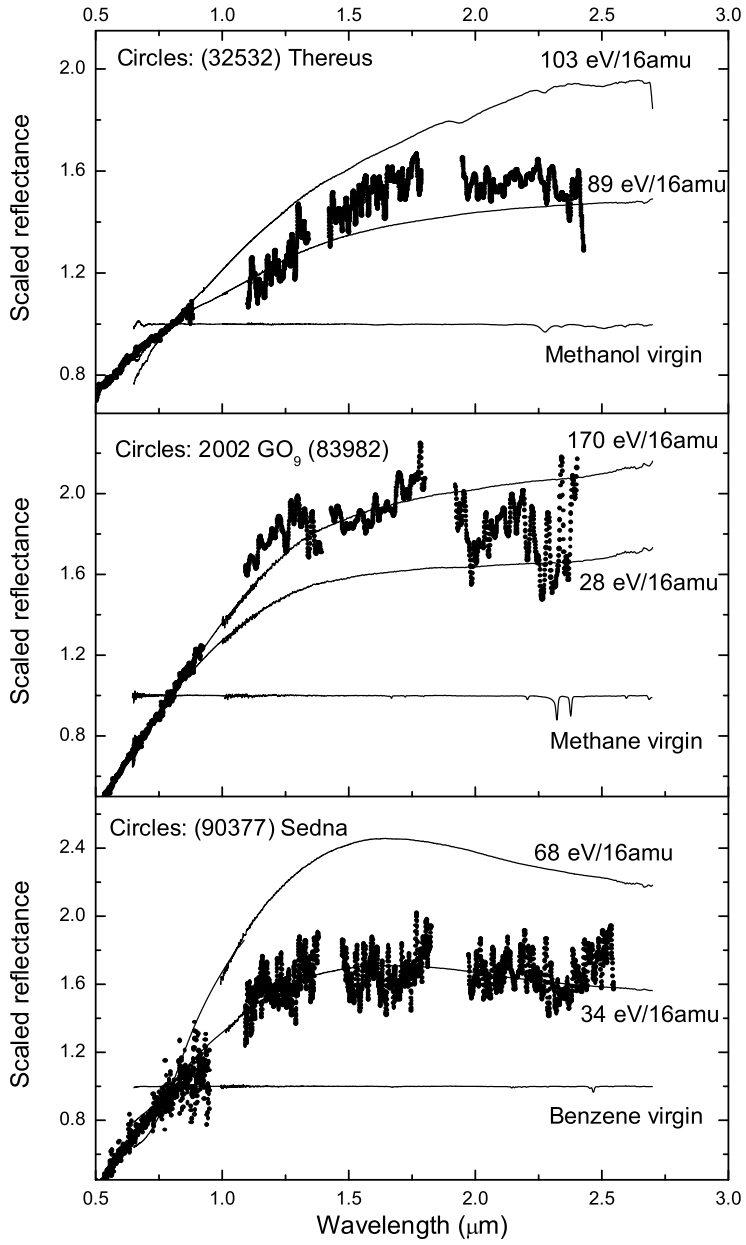

Figure 5.7: Some reflectance spectra of irradiated methanol, methane, and benzene, scaled to 1 at 0.8 μm, compared with some centaurs and TNOs. Note that the comparison is qualitative , since other species can be present (e.g., H_2O, N_2, silicates, etc.).

Object	Type	J-R slope (% per 1000 Å))	K-J slope (% per 1000 Å)
(2060) Chiron	Centaur	-1.42	0.542
(5145) Pholus	Centaur	13.2	1.86
(8405) Asbolus	Centaur	6.34	3.08
(10199) Chariklo	Centaur	9.65	0.910
(32532) Thereus	Centaur	5.52	2.39
(52872) Okyrhoe	Centaur	2.71	2.49
(54598) Bienor	Centaur	1.90	1.25
(55576) 2002 GB_{10}	Centaur	9.40	-1.12
(63252) 2001 BL_{41}	Centaur	6.36	2.22
(83982) 2002 GO_9	Centaur	14.4	-0.029
(26181) 1996 GQ_{21}	TNO	15.1	3.46
(26375) 1999 DE_9	TNO	8.41	0.194
(28978) Ixion	TNO	7.58	0.936
(38628) Huya	TNO	8.19	-1.19
(47171) 1999 TC_{36}	TNO	12.3	-0.260
(47932) 2000 GN_{171}	TNO	6.98	1.05
(55565) 2002 AW_{197}	TNO	7.28	2.08
(90377) Sedna	TNO	12.5	0.430
(90482) Orcus	TNO	-0.034	-0.611

Table 5.4: Our 10 centaurs and 9 TNOs, with their normalized reflectivity gradient.

5.3.2 The irradiation mantle

To make the comparison between observations and experiments more quantitative, I have calculated, for both experimental and observational data, the normalized reflectivity gradient, or spectral slope, S' (% per 1000 Å), as defined by Jewitt (2002). Two spectral ranges were considered, 0.68-1.25 μm (which I refer to as J-R slope) and 1.25-2.20 μm (which I refer to as K-J slope). The slopes obtained for the observed objects are given in Table 5.4.

For the experiments, it is possible to derive a sort of color-color relationship between the K-J and the J-R slopes, as shown in the top panel of Fig. 5.8. The points of each irradiated species follow a precise curve, significantly separated from one another.

In the bottom panel of Fig. 5.8, the experimental slopes are compared with

those calculated for the 9 TNOs and the 10 centaurs considered. The slopes of these objects vary from essentially flat (e.g., Chiron, Orcus) to very red (e.g., Pholus, (26181) 1996 GQ_{21}), as reported in Table 5.4; it is clear that, within the errors, most of the observed slopes can be reproduced by our ion irradiation experiments. In particular, about 70% of the observed objects have spectral slope well reproduced by irradiation of methanol, methane, and benzene. So, the surface colors of these objects are compatible with the presence of a refractory organic crust developed after prolonged irradiation by cosmic ions.

In my experiments, I used H^+ 200 keV, Ar^+ 200 keV, and Ar^{++} 400 keV ions. The energies of cosmic-ray and solar wind particles span a larger range than that used in laboratory experiments; thus, laboratory results obtained after ion irradiation experiments can be extrapolated to the astrophysical environment only if one understands the physical mechanism that causes the observed effect.

In the present case, I focus on the evidence that the total dose (elastic plus inelastic) is the most important parameter in the reddening process, confirming results obtained in the last 10 years that demonstrated that most of the modification of ices is determined by the total deposited energy, unlike what we observed for silicates and bitumens. Thus, a comparison of laboratory results is possible if cosmic particle fluxes are known, and the energy lost by elastic plus inelastic collision is estimated (see, e.g., Strazzulla et al. (2003b)). Furthermore, while it is true that in the inner Solar System the dominant energy deposition comes from 1 keV solar wind protons, in the outer Solar System the contribution from high-energy ions can be relevant, e.g., it may cause the formation of a macroscopic crust in comets (Strazzulla et al., 1991).

Thus, to give an estimation of the astrophysical timescale, I include in Fig. 5.8 the damage levels corresponding to about 10, 50, and 100 eV per 16 amu, as derived from the experiments. Note that most of the objects considered here exhibit colors that would correspond to dosages between 10 and 100 eV per 16 amu. These objects are subjected to cosmic ion bombardment for long times, which would produce an outer web consisting of a nonvolatile organic crust (Strazzulla et al., 2003b), analogous to what was previously suggested for comets in the Oort Cloud (Strazzulla et al.,

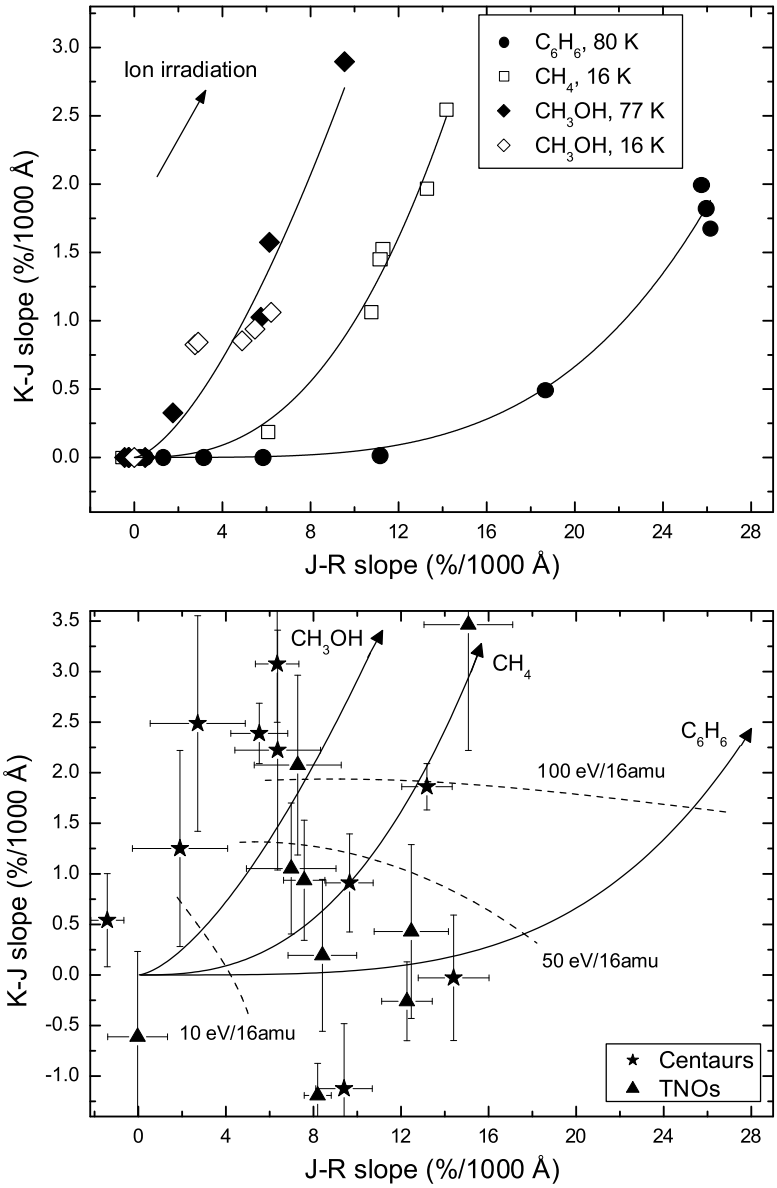

Figure 5.8: K-J slope vs. J-R slope for experimental data (methanol, methane, and benzene) and observational data (10 centaurs and 9 TNOs). In the bottom panel the corresponding dosage levels are also shown.

1991).

The thickness of the organic crust depends on many factors, such as the composition of the target and the irradiation history. Strazzulla et al. (2003b) estimated

that the surface layers (1-100 μm) of bodies between 85 AU (assumed as the solar wind termination shock) and the very local interstellar medium would accumulate 100 eV per 16 amu on timescales of 10^6-10^9 yr. At 40-50 AU, dosages are lower, and less devolatilized materials can be better preserved at the surface, as occurs on Pluto, whose spectrum is dominated by the presence of icy species (Owen et al., 1993).

Summary

I have demonstrated that icy objects in the outer Solar System may have grown an irradiation mantle, produced by cosmic ion irradiation of simple hydrocarbons and/or alcohols.

However, it is important to stress that the results shown in Fig. 5.8 cannot be used to predict whether a specific object will have an irradiation mantle of methane rather than benzene or methanol; indeed, it is known that other components are present on these objects (water ice, silicates, etc.) that would partially affect the spectral slopes. Thus, the results of Fig. 5.8 are an indication of a general behavior, i.e., simple molecules containing carbon under ion irradiation evolve toward an organic residue, whose spectral properties suggest the presence of an irradiation mantle in the objects of the outer Solar System.

Finally, I remark that two different processes have reproduced in the experiments: starting from pure C-rich frozen species, a strong reddening of the Vis-NIR spectra is induced, connected to the formation of a refractory residue (total dose); conversely, starting from a complex hydrocarbon structure such as asphaltite or kerite, a spectral flattening is induced, connected to a modification in the structure of the sample (elastic dose).

Forthcoming studies will focus on mixtures of ices and silicates, since that is probably the composition of many bodies in the outer Solar System.

Acknowledgments

We are grateful to G. A. Baratta and M. E. Palumbo for their helpful suggestions. We thank F. Spinella for precious technical assistance, and an anonymous referee

who helped us improve the paper. This research has been supported by MIUR and INAF.

Chapter 6

Peculiar objects

In the previous chapter I have shown that statistically significant correlations hold between spectral slopes and weathering effects, for the majority of NEOs and MBAs. Also, clear weathering effects are observed on TNOs and centaurs. I have also shown how these results may be understood consistently in terms of the experimental data. In this chapter I will discuss the case of a few peculiar objects, to test the space weathering models and their predictions.

6.1 Asteroid 832 Karin and its family

Based on the paper: Brunetto, R., Vernazza, P., Marchi, S., Birlan, M., Fulchignoni, M., Orofino, V., Strazzulla, G. 2006. Modeling asteroid surfaces from observations and irradiation experiments: The case of 832 Karin. Icarus 184, 327-337.

The Karin cluster is a small asteroid family that formed 5.8±0.2 Myr ago in the outer main belt. This is an exceptionally young age for an asteroid family. Thus, 832 Karin and its family give us an excellent opportunity for physical studies of a young family whose members have apparently suffered limited dynamical and collisional erosion, and to investigate the effects of a relatively short time exposition to space weathering processes.

In this section I apply a space weathering model to the observed spectra of Karin, and derive an exposure time to be compared with the age of the impact and

collisional breakup which originated the Karin asteroidal family.

In the previous sections, the spectral effects due to the solar wind and the micrometeorite bombardment have been investigated. We have seen that, when both processes are simulated in the laboratory (see, e.g., Yamada et al. (1999); Sasaki et al. (2001); Brunetto et al. (2006a); Strazzulla et al. (2005)), a lunar-style effect is observed, i.e., increased weathering results in a redder spectral slope, a lower albedo, and weaker absorption features. Thus, in this scheme, the color/slope of an asteroid spectrum is a function of exposure age and heliocentric distance; maybe this scheme cannot easily be applied to asteroids Ida and Eros, where albedo variations and spectral reddening do not seem to be strictly related (Chapman, 1996; Clark et al., 2001).

Nevertheless, it is also important to note that only reddening has been quantitatively studied to be related to the ion fluence. Qualitatively a darkening is always observed that, however, has not yet quantitatively related to the fluence. Thus, in this section I mainly focus on the reddening, also because recent results (Marchi et al., 2006) indicate that the reddening effect is also evident on MBAs, so it is at least reasonable applying this scheme to MBAs.

Asteroid spectra can be modeled by means of the Shkuratov or the Hapke scattering models (Shkuratov et al., 1999; Hapke, 1993). Nevertheless, pure silicate optical constants (olivine, pyroxene) cannot reproduce the reddening caused by space weathering processes; until now, additional components were needed, like submicroscopic metallic iron (SMFe), to get the reddening effect (Hapke, 2001).

Solar wind ions affect a very thin upper layer of the asteroid surface, so rejuvenating processes can be relevant. Old and new surfaces can even coexist on the same object and be observed at different rotational phases. In this respect, a strong evidence of space weathering may be provided by the variations of the surface properties of the same asteroid (Chapman, 1996).

Recently, Nesvorný and Bottke (2004) have integrated backward in time the known 90 members of the Karin family, a well-defined cluster of asteroids in the proper elements space, formed by a collisional breakup, and embedded within the larger Koronis family. The orbital elements of the Karin family members converge

toward a single parent-body orbit, at 5.75±0.05 Myr ago. The discovery of the Karin family offers an excellent opportunity for physical studies of a young family whose members have apparently suffered limited dynamical and collisional erosion. The most studied object of the Karin cluster is 832 Karin, a Main-Belt asteroid with a diameter of 16-20 km (Sasaki et al., 2004; Yoshida et al., 2004; Nesvorný et al., 2002; Nesvorný et al., 2005).

Here I compare the laboratory results with new spectra of 832 Karin in the visible (0.45-0.95 μm) and in the near-IR (0.8-2.4 μm), and model the surface of 832 Karin by applying a new description of space weathering.

6.1.1 Model of the continuum: the C_S parameter

To study asteroid Karin, I start from the irradiation experiments of silicates, described in the previous chapters.

The changes and modifications induced by colliding ions in the target have been monitored using in situ bi-directional reflectance spectroscopy (0.7-2.5 μm) and ex situ hemispherical reflectance spectroscopy (0.3-2.5 μm), as discussed above.

As a summary, the reflectance spectra of the samples, before and after irradiation, are shown in Fig. 6.1. All the spectra exhibit the characteristic features of silicates, with strong 1 and 2 μm bands (hereinafter band I and band II, respectively). In the case of olivine and orthopyroxene powders, we consider both in situ and ex situ experiments.

To compare different experiments (ion mass and energy) one can evaluate a damage parameter as the number d = displacements per cm^2, as demonstrated by Brunetto and Strazzulla (2005).

The effects of space weathering can be easily described by an exponential continuum. Indeed, if we compute the ratio between irradiated and unirradiated samples, the contribution of bands I and II almost disappears, and a continuum curve is left, with decreasing intensity moving from the NIR to the UV spectral range. This space weathering process does not significantly affect the position or relative intensities (areas) of the mafic silicate absorption features. This is illustrated in Fig. 6.2:

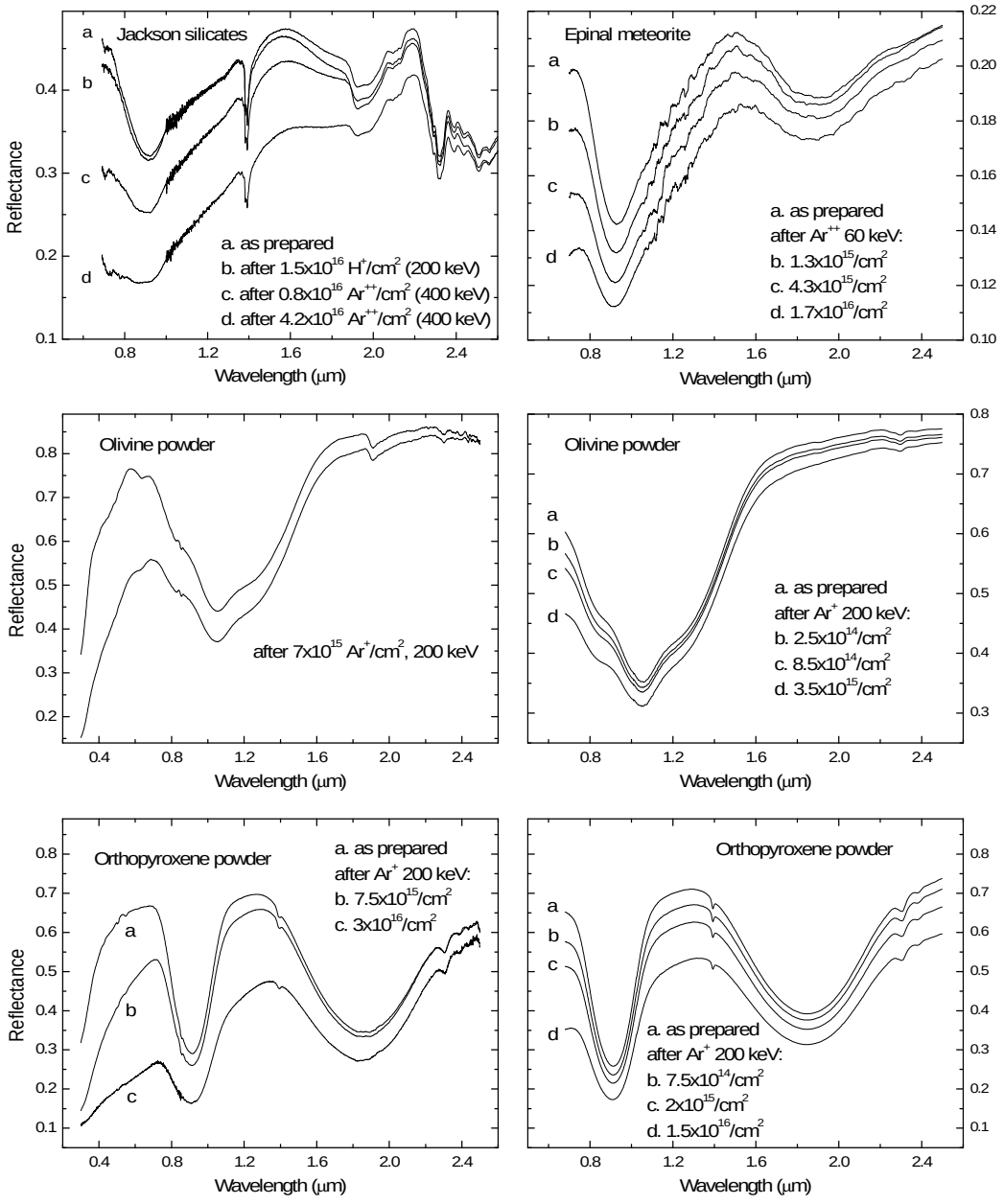

Figure 6.1: Upper panels: in situ bi-directional reflectance spectra of Epinal (right) and Jackson (left), before and after ion irradiation with various ions and fluences. Central and lower panels: in situ (right) bi-directional and ex situ (left) hemispherical reflectance spectra of olivine (central) and orthopyroxene (lower) powders, before and after ion irradiation with various fluences. Error-bars are of the order of the thickness of lines.

each panel is a ratio plot between the spectra of the corresponding irradiated and unirradiated samples, the same as in Fig. 6.1.

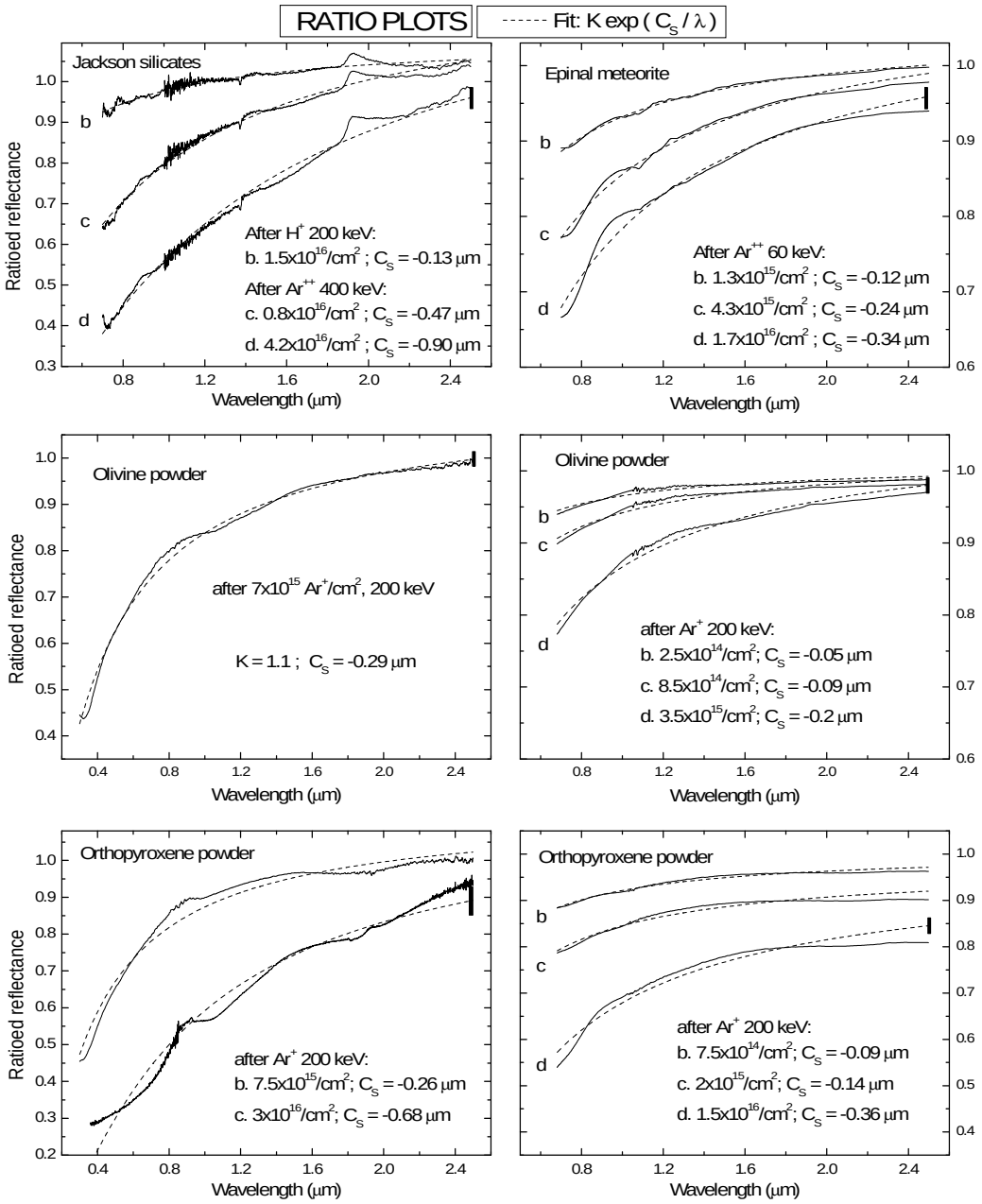

Figure 6.2: Ratio plots of the same spectra shown in Fig. 6.1; each irradiation step spectrum is divided by the corresponding unirradiated spectrum. Dashed curves are the best fit curves obtained by Eq. 6.1 and the resultant C_S values are given. In each plot, vertical black lines represent the estimated error-bars.

The ratio plots show only marginally traces of bands I and II; we consequently try to model this continuum by fitting with an exponential curve given by

$$Ratio = W(\lambda) = K \exp(C_S/\lambda) \tag{6.1}$$

where λ is the wavelength, K is a scale factor that changes according to the normalization of the spectra, and the parameter C_S rules the strength of the exponential curve, i.e., it is a measure of the effects of space weathering. The quantity $W(\lambda)$ is what we call 'weathering function'; this function is not new (see below), but for the first time it is used to fit a ratio between the spectra of irradiated and unirradiated samples. We have also tried with other functions (logarithmic, rational, etc.), but the best fit is obtained with the fitting function given by Eq. 6.1; furthermore, it describes the same continuum that is used in the so-called MGM (modified Gaussian model) of reflectance spectra. For instance, a detailed use of MGM analysis was made by Hiroi and Sasaki (2001). They modeled the natural logarithm of reflectance spectra $R(\nu)$ using the function:

$$\ln R(\nu) = C_0 + C_1\nu + \sum_i G_i(\nu) \tag{6.2}$$

where ν is the wavenumber, $G_i(\nu)$ are the superimposed Gaussian distributions that fit the reflectance bands, and C_0 and C_1 are two parameters for the background function, i.e., the continuum. Space weathering acts only marginally on the band center, strength, and width, as it has been proved by Hiroi and Sasaki (2001) for laser irradiation and by Marchi et al. (2005) for ion irradiation. For this reason, the logarithm of the ratio between irradiated and unirradiated spectra can be written as:

$$\ln[R_{IRR}(\nu)/R_{UNIRR}(\nu)] = (C_{0IRR} - C_{0UNIRR}) + (C_{1IRR} - C_{1UNIRR})\nu \tag{6.3}$$

that leads to Eq. 6.1. The parameter $C_S = C_{1IRR} - C_{1UNIRR}$ is consequently a measure of how much irradiated spectra redden with respect to their unaltered spectra.

It is important to stress out that the ratio of the irradiated spectra with the unirradiated ones does not perfectly eliminate bands I and II; this can affect the fitting of the spectral region of both bands I and II. Furthermore, in the case of Jackson silicates, ion irradiation seems to dehydrate the samples, but this marginally affects the results of the fit.

Ueda et al. (2002b) introduced a C_2 term using Hapke's space weathering model (vapor deposition of reduced iron) into the MGM scheme. The C_2 term includes also a complex z function which depends on wavelength. At the present time I do not include this C_2 term because it would complicate the model and it still has to be checked in the experimental data; it will be a subject for future studies.

Another important point is that natural logarithm of reflectance is not exactly absorbance, although it is assumed in the MGM scheme. A reflectance spectrum is a combination of volume scattering and surface scattering; as each mineral grain becomes more opaque either by increasing grain size, more Fe content, or higher degree of space weathering, the surface scattering effect becomes more significant. Taking the ratio between spectra of different degree of space weathering divides two values, each of which consists of a sum of volume and surface scattering effect. The behavior of such quantity is more complicated than what described here in terms of C_S: space weathering changes both the surface reflectance and transmittance, thus both surface and volume scattering components. Future works will try to focus on the possibility to model the experimental spectra converting the reflectance into the surface and volume component.

However, from Fig. 6.2 it is clear that the $W(\lambda)$ function [Eq. 6.1] can fit quite well the ratioed reflectance in all irradiated materials, either powder or bulk samples, either meteorite or terrestrial sample, either olivine or orthopyroxene (the obtained C_S values are reported in Fig. 6.2). This implies that a weathered spectrum can be obtained by multiplying the spectrum of the unaltered sample by a specific $W(\lambda)$ function with a precise corresponding C_S value.

From this point of view, the C_S parameter can be considered as a spectral slope; it has to be remarked that, in accordance with the definition given in Eq. 6.1, and unlike the spectral slope widely used up to now (see Gaffey et al. (1993), or Marchi et al. (2005)), the C_S parameter becomes more negative as the space weathering effect increases (as it is shown in the right panels of Fig. 6.2), and, even if not representing a real length (it is not connected with the depth of the weathered layer), it is measured in μm.

In Fig. 6.3 I plot C_S versus the number of displacements per unit area, for all

the experiments described above.

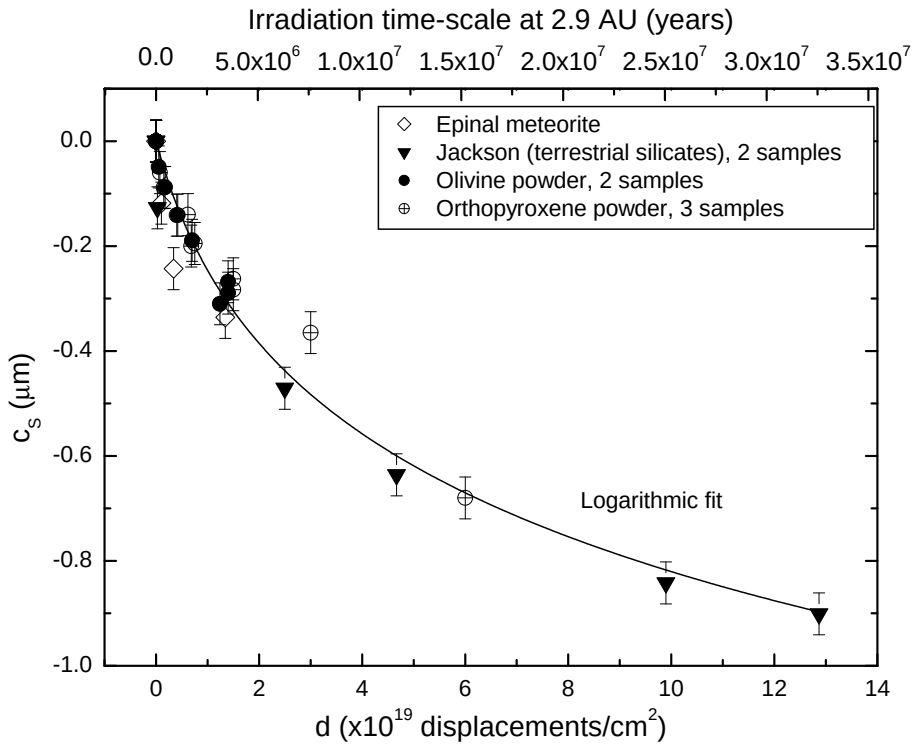

Figure 6.3: The C_S parameter as a function of the number of displacements per cm^2 (damage parameter) for ion irradiation experiments. The upper x-axis gives an estimate of the astrophysical timescale (exposure time) at 2.9 AU.

It is clear that the C_S parameter is strongly related with the number of displacements per cm^2 (damage parameter), but it seems not to depend on the composition of the target. Indeed, from our experiments we are able to draw a damage curve, which can be well fitted by

$$C_S = \alpha + \ln(\beta d + 1) \tag{6.4}$$

where α and β are two fitting coefficients: $\alpha = -0.33 \pm 0.06 \mu m$ and $\beta = (1.1 \pm 0.5) \times 10^{-19} cm^2$.

Since the C_S parameter is strongly related with the d parameter, we can estimate an astrophysical timescale for this process; indeed, each damage value d corresponds

to a given exposure time, once the ion fluxes and energies of a given astronomical environment are known. Unfortunately, such an accurate calculation is not immediate, and exceeds the goal of this work; here we just give a rough estimate of the reddening timescale, with errors of a factor of 2-3.

Solar wind ion irradiation is not the only active weathering process. However, it seems to be the most efficient one at 1 AU (see discussion above) and also in the Main Belt, as suggested by recent results on the relation between the spectral slope of silicate-rich asteroids and the exposure to space weathering (Marchi et al., 2006).

Since the solar wind flux decays about as $1/R^2$, where R is the distance from the Sun, one can use the points of irradiated Epinal meteorite to scale the estimate (discussed above) made at 1 AU considering heavy-ion fluxes of the solar wind, to the distance of 2.9 AU (about the semi-major axis of the orbit of asteroid 832 Karin). In the hypothesis of a spherical body uniformly irradiated, we have to multiply the corresponding timescale by a factor of 4, to take into account the ratio between the geometrical cross-section and the whole surface (see Baratta et al. (2004)). The upper x-axis of Fig. 6.3 gives an estimate of the timescale. At 2.9 AU, the reddest spectra should be observed roughly for timescales higher than about 3×10^7 years.

Equation 6.1 has some limitations: Fig. 6.2 shows that the exponential model works quite well between 0.3 and 2.0 μm, while it gets worse in the region of 2.0-2.5 μm. In particular, the fit is often redder than the real ratioed spectrum, with deviations of less than 5%. These discrepancies could be analyzed in future works, possibly converting the reflectance into the surface and volume component (as discussed above). However, the possibility of fitting asteroidal spectra using the C_S parameter is very important because it gives the chance of obtaining age estimates in a very simple way.

6.1.2 Observations and model of 832 Karin

Observations

Observations of the asteroid 832 Karin have been performed in the visible and in the NIR with CFHT (Canada-France- Hawaii Telescope, Mauna Kea) and IRTF

Telescope	Date	UT	$\lambda(\mu m)$	Solar phase angles
IRTF	2003 Nov. 4	06:17	0.8-2.4	21°
CFHT	2005 Mar. 3	07:29	0.45-0.92	20°

Table 6.1: Parameters of observations of 832 Karin. The time to collect a spectrum is 10 min for the visible spectra and 40 min for the NIR spectra.

(Infrared Telescope Facility, Mauna Kea) by my colleagues of the Observatory of Paris-Meudon. Since this thesis is not devoted to extensive data analysis of observations, circumstances and data reduction are briefly presented.

Visible spectra of 832 Karin with the CFTH were obtained in March 2005, using the low resolution spectrograph MOS with the R150 Grism in the 0.4-1.0 μm wavelength range with a slit width of 1.5 arcsec.

An observing run with IRTF in November 2003 was devoted to near-IR observations of the Karin family. This run was remotely conducted from the Observatory of Paris-Meudon, France. The spectrograph SpeX, combined with the 0.8×15 arcsec slit were used for spectral acquisition in the 0.8-2.4 μm wavelength range.

Table 6.1 reports the parameters of the observations. Solar phase angles were: 21° (IRTF); 20° (CFHT). The rotational period of Karin is 18.35 h (Yoshida et al., 2004). Standard techniques for visible/near-IR spectroscopy reduction have been used in order to obtain the reflectance. The software MIDAS was used to perform the data reduction of visible data. In order to perform a good correction for atmospheric extinction, spectra for different solar analog stars were collected at different airmasses during each night. We computed the ratio of these stars to estimate the difference in slope between these stars. The ratios normalized to unity at 0.55 μm were found to be almost flat, with a maximum deviation of 3% from 0.55 to 0.95 μm.

The near-IR spectroscopy reduction was performed using the software Spextool 3.2, dedicated to reducing data obtained with Spex. The technique for the data reduction is nearly identical to the one performed in the visible. In the NIR, a star was observed just after the spectrum of 832 Karin, in the same field, having a difference in airmass less than 0.03. Unfortunately the SpeX instrument is known

to introduce instrumental artifacts: Rayner et al. (2004) have noted that it can introduce spurious spectral slopes. We have observed spectral variation in the NIR of about 10%, which could probably be due to an instrumental artifact; however, these variations have a minor impact on the mineralogy of Karin as derived by the model, and they would partially affect the evaluation of the exposure age of the Karin surface (see discussion below). Further investigation shall focus on the NIR range.

Figure 6.4 illustrates a visible spectrum of 832 Karin, obtained at CFHT (see Table 6.1). The spectrum is normalized to unity at 0.55 μm. An infrared spectrum of 832 Karin is shown in Fig. 6.5, normalized to unity at 0.9 μm. Band I peak position is 0.92 μm. The water vapor absorption due to the terrestrial atmosphere does not allow to calculate precisely the center of band II.

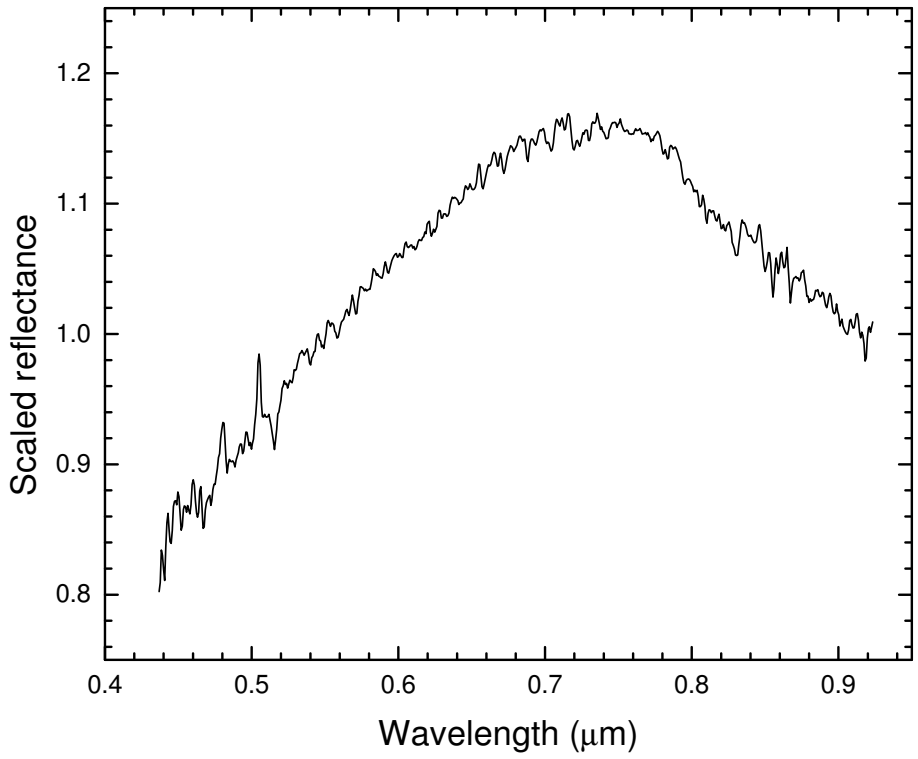

Figure 6.4: A visible spectrum of 832 Karin obtained with CFHT, normalized to unity at 0.55 μm. Error-bars are of the order of the spectral noise.

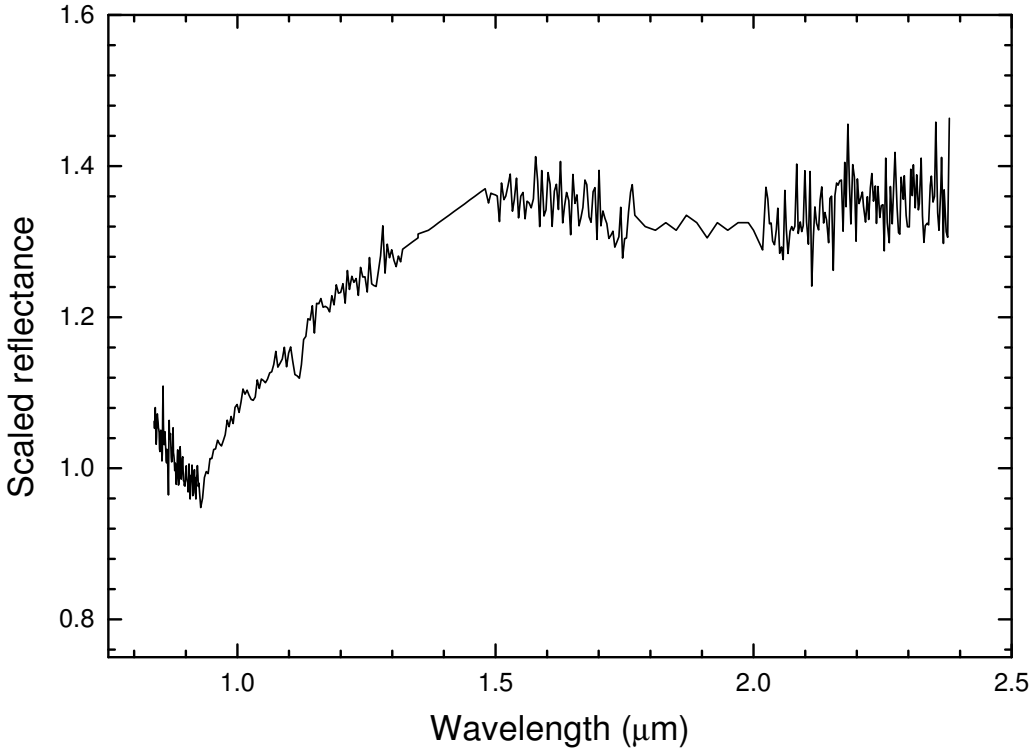

Figure 6.5: A NIR spectrum of Karin obtained with IRTF, normalized to unity at 0.9 μm. Errorbars are of the order of the spectral noise; however, spectral slope of 10% can be introduced in the NIR by instrumental artifacts of the Spex instrument.

Previous published data (Sasaki et al., 2004) showed spectral slope variations of Karin; at the present time we are not able to either confirm or confute that result. Further information will be obtained in the future by analyzing the Karin spectra over its entire rotational phase.

Model: free parameters

The spectra of 832 Karin were modeled using the Shkuratov scattering model, in order to constrain the possible surface composition of the asteroid (to compare with those of ordinary chondrites) and its space weathering degree. The space weathering was modeled with an exponential function following the experimental results (see above).

First, the model calculates the albedo of a particle of given size and composition characterized by its optical constants n, k. From this albedo it is possible to derive the reflectance of a single- or multi-component particulate surface.

The first step of the modeling was to choose reasonable endmember minerals. We decided to start with the common endmember minerals found in ordinary chondrites, namely olivine, ortho- and clinopyroxene, plagioclase feldspar, chromite, and iron metal, applying an intimate mixture.

It cannot be assumed a priori that any particular S-type asteroid has an ordinary chondrite composition. However, it is clear from the analysis of the absorption bands that Karin and the ordinary chondrites have common minerals (i.e., olivine and pyroxene) and they may be the major surface components. If there is another major component on the Karin surface it should be almost featureless because otherwise it would imply obvious signatures in the spectra. This is the reason why I refer to a composition similar to that of ordinary chondrites; nevertheless, it is true also that minor components affect the spectrum.

However, the goal is to investigate if the observed spectra of 832 Karin may be interpreted in terms of weathered surfaces. For olivine and pyroxene, the optical constants for different chemistries were considered, i.e., different Mg-number (from Lucey (1998)).

As far as the other materials are concerned, we have exploited one of the strengths of the Shkuratov model, i.e., its invertibility. The average behavior as a function of wavelength of the imaginary part k can be estimated from reflectance data.

The calculation relies on an a priori knowledge of the grain size of the particles in the sample as well as the real part of the refractive index (Shkuratov et al., 1999); a value of $n = 1.7$ was assumed (reasonable for semi-transparent minerals).

This inverted model was used to calculate the optical constants for: plagioclase (orthoclase) using the sample NMNH- 142137 Fe from USGS (Clark et al., 2003); chromite (creac11) from RELAB (http://www.planetary.brown.edu/relab/). The optical constants of iron measured by Johnson and Cristy (1974) were also used.

The free parameters of the model are the relative abundance of the components (whose sum must be equal to 1), the mineral chemistries of the various components

(variation of the Mg-number), the effective (average) optical pathlength (proportional to the grain size), and the C_S parameter.

Indeed, the space weathering contribution is included by the following expression:

$$R(\lambda) = W(\lambda)A(\lambda) = K\exp(C_S/\lambda)A(\lambda) \tag{6.5}$$

where $R(\lambda)$ is the final spectral albedo, $W(\lambda)$ is the weathering function introduced in Eq. 6.1, and $A(\lambda)$ is the albedo given by Shkuratov et al. (1999); Eq. 6.5 is assured by the experimental results, that show that a weathered spectrum can be obtained by multiplying the spectrum of the unaltered surface by a specific $W(\lambda)$ function with a precise corresponding C_S value (see above).

Since I am studying a lunar-style weathering, the porosity is assumed to be equal to 0.7 in the calculations; indeed, Shkuratov et al. (1999) used a value of 0.7 in order to model the reflectance spectra of the Moon. However, this parameter has little influence on the results (Shkuratov et al., 1999). Finally, an IDL routine using Levenberg-Marquardt algorithm was used to find the minimum root-mean-squared (RMS) residual between the measured spectrum and the computed spectrum.

Results

The model was first applied to visible and NIR spectra separately, finding that in the case of the vis spectrum the fit gives the same results as the NIR spectrum, i.e., the same composition and the same degree of space weathering (C_S value). This allows to join the two spectra to form a composite spectrum of 832 Karin (that I refer to as Karin_weathered); the NIR spectrum has been scaled to the visible spectrum using the overlap in the 0.8-0.95 μm wavelength range. Then this composite spectrum (vis-NIR) of 832 Karin was modeled, verifying that the fit for the composite spectrum gives the same results of its two components.

I illustrate in Fig. 6.6 the mixing model spectrum of Karin compared with the measured spectra. A reasonable fit for Karin_weathered was obtained in the 0.4-2.0 μm range.

Mixing ratios for each end-member are listed in Table 6.2; I do not find a specific ordinary chondrite composition. Thus, a reasonable (but not unique) interpretation

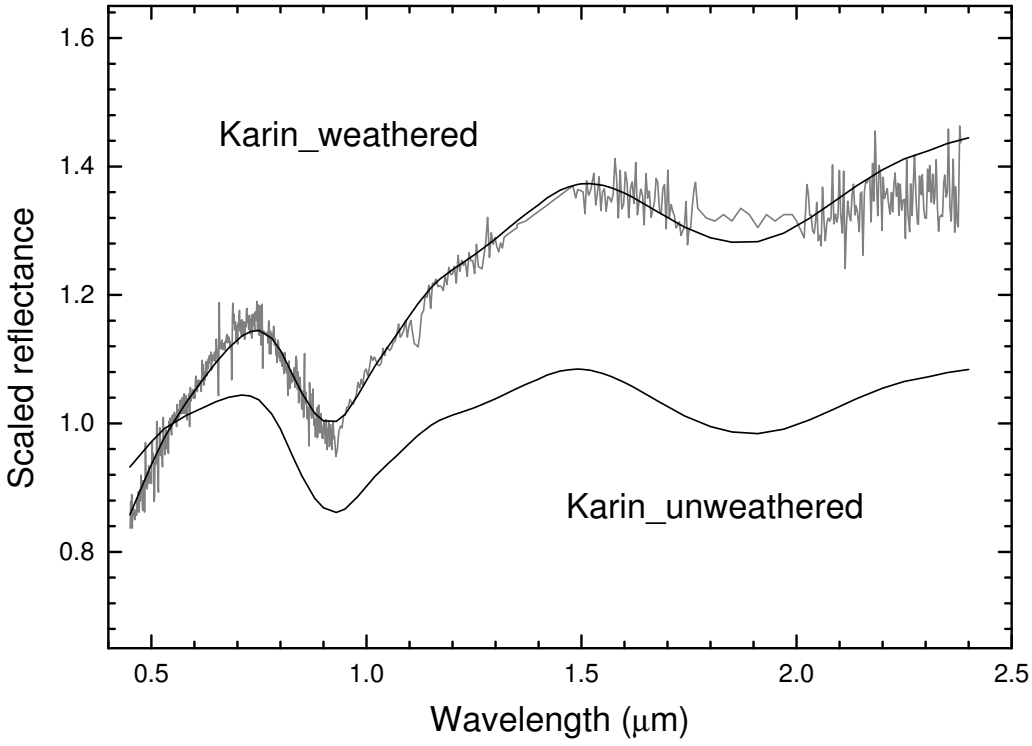

Figure 6.6: Observed Karin_weathered and the best-fit result according to the model. A synthetic spectrum is also plotted (Karin_unweathered), obtained using the same mineralogy of Karin_weathered, but fixing the C_S parameter equal to zero, i.e., Karin_unweathered is how a fresh surface of 832 Karin should look like. Error-bars are of the order of the spectral noise.

is that the surface of Karin is mainly made of olivine and orthopyroxene, in the percentage of about 58.5% and 38%, respectively (the Mg number is 77 for both olivine and orthopyroxene); clinopyroxene was not detected (the detection limit of clinopyroxene is about 3%). The resulting amount of chromite is about 2%, which is lower than what reported by Hiroi and Sasaki (2001) in the model of asteroid 446 Aeternitas, but higher than that found in recent ordinary chondrites (McSween et al., 1991; Schmitz et al., 2003). It is important to stress that this best fit is just a reasonable interpretation of the spectra rather then a unique determination of the composition of Karin.

In Fig. 6.6, a mismatch is observed in the 2-2.4 μm range, where the model is

Olivine (%)	Ortho-prx (%)	Clino-prx (%)	Chromite (%)	Iron (%)	Average opt. pathlength (μm)	Mg--number	C_S (μm)
58.5	38	0	2	1.5	8	77	-0.205

Table 6.2: Results of the fit of Karin_weathered spectrum. The optical pathlength is a free parameter; it results from the fitting routine. Different values for the optical pathlength would change the depth of the absorption bands. Errors in the percentages are of about 5% for olivine and orthopyroxene, and 0.5% for iron and chromite. Note that the iron component (native, not deposited) does not influence the spectral reddening.

redder than the observational data. This deviation may have many causes (some missing component in the model, or a problem with the optical constants or with the Shkuratov model, etc.); furthermore, another problem is that the 2 μm region suffers from the atmospheric water vapor bands (between 1.8 and 2 μm). However, the mismatch is probably due to a problem with the space weathering model: space weathering changes both surface and volume scattering components (as discussed above).

I emphasize that it is absolutely impossible to get a good fit of Karin spectra without including space weathering effect. Neither compositional nor optical pathlength variations can reproduce the spectral reddening observed in the visible and in the NIR range.

To clarify the space weathering effect on Karin, in Fig. 6.6 I also plot the synthetic spectrum of the plausible corresponding virgin surface (labeled Karin_unweathered), i.e., a spectrum constructed by the mineralogy resulting from the Karin fit but fixing the C_S parameter equal to zero[1].

This synthetic spectrum should be representative of a newly resurfaced area of the asteroid, i.e., Karin_unweathered is how a fresh surface of 832 Karin should look like. The difference between the observed spectra and Karin_unweathered is evident. This implies that observed surface of Karin, even if relatively young, has experienced an appreciable amount of space weathering.

Since the C_S parameter is strongly related with the d value, and each damage

[1]Note however that C_S may contain the native continuum curve of each mineral power sample due to a mix of volume and surface scattering components, even without space weathering.

value d corresponds to a given exposure time (as shown in Fig. 6.3), it is possible to estimate the astrophysical timescale for the fitted spectrum of 832 Karin. In Fig. 6.7, I report the C_S value obtained for Karin, in the same plot as Fig. 6.3. The corresponding timescale of about 2×10^6 years.

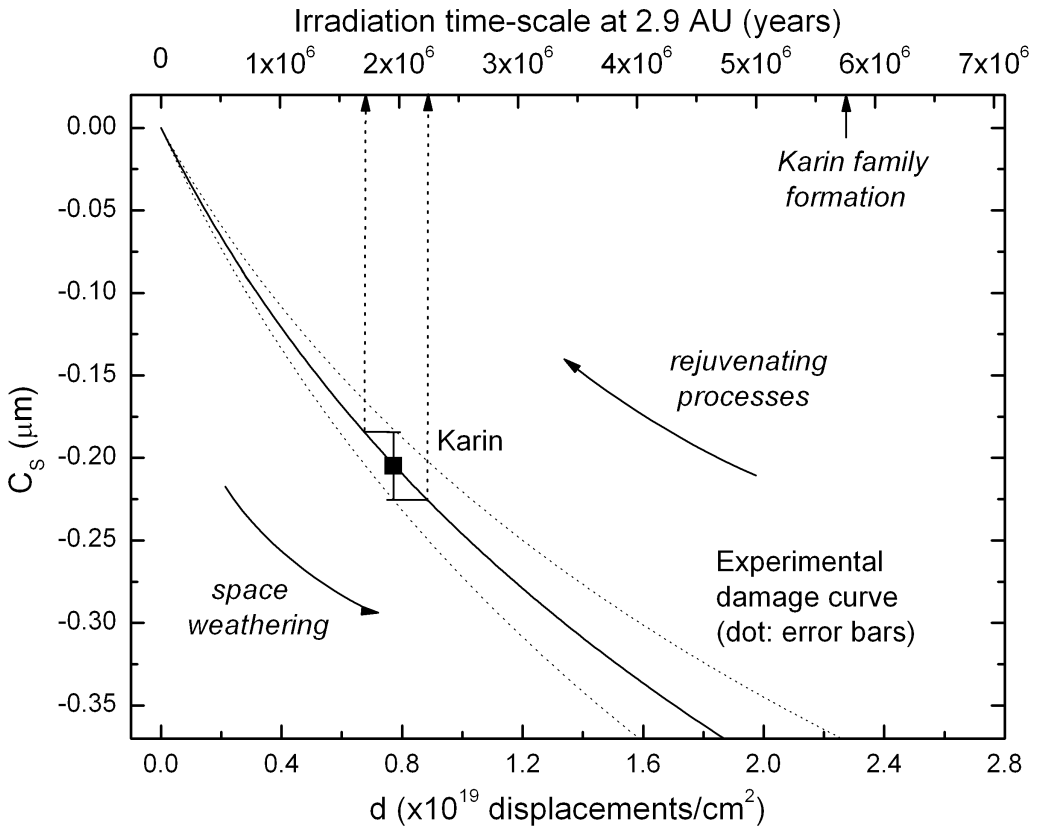

Figure 6.7: A zoom of the same plot as Fig. 6.3; the C_S value found for Karin is included, superimposed to the experimental damage curve. Upper x-axis gives the corresponding exposure times: the irradiation timescales of Karin are perfectly compatible with a surface rejuvenated 5.75×10^6 years ago by the collisional breakup which originated the Karin asteroid family. Dotted error-bars are given for the obtained curve and timescale value.

The error bars on this value (precision of the experimental curve) are shown in Fig. 6.7, but it is important to stress that the offset can be wrong by a factor of 2-3 due to the low accuracy of the estimate. The factor 2-3 refers to the indetermination in the knowledge of the fluxes of the solar wind ions over Solar System history, and to potential instrumental artifacts: indeed, as discussed above, Spex instrument

may introduce spurious spectral slopes in the NIR; we have verified that these variations do not affect the mineralogy of Karin, but they may produce slightly different timescales, for instance, in the order of 7×10^5 years. In any case, the irradiation timescale is shorter than the age of the impact, but quite close to it, which is about 5.75×10^6 years; in particular the spectrum of Karin is compatible with a surface rejuvenated 5.75×10^6 years ago and which has consequently suffered an exposure time to solar wind ions of the same order of magnitude.

6.1.3 Discussion

Results of this section suggest that a part of the surface of 832 Karin has experienced a certain degree of space weathering, but only in the last 5.75×10^6 years; this would imply that the object has been at least partially rejuvenated by the impact which originated the Karin family[2].

It is mandatory to remind that, on one hand, the timescale estimate is not very accurate, and, on the other hand, rejuvenating processes can be very relevant; actually, solar wind ions affect a very thin upper layer of the asteroid ($< 1\mu$m), so even a small impact on the surface is able to remove the weathered layer. Hence a competition between weathering and resurfacing is producing the observed reflectance spectra.

As discussed above, Sasaki et al. (2004) observed different degrees of space weathering on 832 Karin, and interpreted as the presence of a surface older than the impact. Unfortunately, we do not have a study of Karin spectra over its entire rotational phase, so it is impossible to put further constrains. However, since Karin is a small body (about 18 km), it is not clear how it could have preserved a surface older than the age of the Karin family. A number of processes support such argument.

Indeed, Nesvorný et al. (2002) discussed about the size of the parent body and the impactor: they argued about 25 and 5 km, respectively. In this case 832 Karin is

[2]It must be stressed that the space weathering modeling is independent on the scattering model; similar results are also obtained by combining Eq. 6.1 with the scattering model of Hapke (1993), rather than that of Shkuratov et al. (1999). Indeed, in Eq. 6.5, the $W(\lambda)$ function remains practically the same, and it is combined with Eq. (37) of Hapke (1981). In fact, the obtained C_S values are independent on the particular scattering theory used.

47% of the mass of the parent body (or 43% volume). According to recent results of Richardson et al. (2004), impact-induced seismic shaking can produce considerably regolith movements. This should have been quite important for the impact that formed the family and presumably affected the entire Karin surface.

Moreover, Nesvorný et al. (2002) state that it is likely that largest cluster members (i.e., fragments like Karin) accumulated small fragments. If this is true, these secondary impacts would have erased any trace of previous space weathering (keep in mind that solar wind ions affect a very thin upper layer of the surface), both by direct mixing of the regolith layer and through seismic shaking mentioned before (which is also effective for small impactors; see Richardson et al. (2004)). In these conditions, it seems hard that Karin could have retained an old surface. One would expect that after the major collision that created the family, all the parent body surface was reset. These speculations are supported by the timescales based on ion irradiation experiments.

Note that, if it is true that all the Karin parent body was rejuvenated 5.75×10^6 years ago, timescales derived from laser pulse irradiation (Sasaki et al., 2001; Brunetto et al., 2006a) are too slow (about 10^8 years) to explain the observed space weathering of Karin.

Conclusions

Spectra of asteroid 832 Karin have been obtained and analyzed in the range 0.45-0.95 and 0.8-2.4 μm. The observed vis-NIR spectra show spectral reddening that can be explained by space weathering processes.

Starting from the results of ion irradiation experiments, a simple description of space weathering given by Eq. 6.1 allows to reproduce the visible and NIR spectra of 832 Karin.

I have obtained a value for the so-called C_S parameter, related to a surface with a certain degree of space weathering by formation of displacements. Referring to the astrophysical timescale at 2.9 AU, this C_S value of Karin corresponds to irradiation timescales slightly younger than the age of the disruption which originated the Karin family. This impact rejuvenated, at least partially, Karin's surface 5.75×10^6 years

ago, and the scenario is coherent with the model of a very efficient space weathering process caused by solar wind ions, as simulated by ion irradiation experiments described in this thesis.

Acknowledgments

We are grateful to G.A. Baratta and F. Spinella for their precious support during the experiments and to M. Gaffey, T. Hiroi, and an anonymous referee, who have helped us improving the paper with their accurate reviews and useful suggestions. This research was supported by the Italian Ministero dell'Istruzione, Università e Ricerca (MIUR).

6.1.4 Appendix: the Karin family

Based on the paper: Vernazza, P., Birlan, M., Rossi, A., Dotto, E., Nesvorny, D., Brunetto, R., Fornasier, S., Fulchignoni, M., Renner, S. 2006. Physical characterization of the Karin family. Astronomy and Astrophysics 460, 945-951.

Our team observed 24 Karin asteroid members in the visible and 6 members in the near-IR. In the visible range, all the objects share the same characteristics: a maximum around $\lambda = 0.75\mu$m, and a spectral slope spanning a continuous but limited range; in the NIR, our spectra show a similar behaviour.

This indicates a similar composition and space weathering degree. None of the objects can be considered as an interloper, based on the obtained spectra, confirming the dynamical indication of a probable common origin from the fragmentation of a parent-body. Results suggest global homogeneity of the parent body.

Comparing the spectral slope of the Karin members with the slope domain of ordinary chondrites, the Karin members are found to be slightly redder than OCs. We interpret this result as an indication of a low degree of spatial alteration for the surfaces of these objects, which is in agreement with the young age of the Karin family (5.8 Myr).

This spectroscopic investigation has shown that in the case of a young family, the dynamical indentification is very reliable.

6.2 A particular case: asteroid 4 Vesta

Based on the paper: Vernazza, P., Brunetto, R., Strazzulla, G., Fulchignoni, M., Rochette, P., Meyer-Vernet, N., Zouganelis, I. 2006. Asteroid colors: a novel tool for magnetic field detection? The case of Vesta. Astronomy and Astrophysics 451, L43-L46.

6.2.1 Vesta is not red

In the previous sections, I have widely discussed how space weathering processes affect Solar System bodies that are not protected by an atmosphere or a magnetosphere, altering the optical properties of their soil. The continuous bombardment by energetic cosmic rays, solar wind ions, and interplanetary dust particles (micrometeorites) are the sources of this weathering. Such alteration processes change the spectral properties of silicate-rich objects, inducing progressive spectral darkening and reddening.

They have been studied in order to find a link between the spectral properties of meteorites and the remote sensing data of asteroids. Indeed, as discussed above, space weathering can explain the spectral mismatch between ordinary chondrites and the surface spectra of their presumed (S-type) asteroidal parent bodies (Pieters et al., 2000; Adams and McCord, 1971; Strazzulla et al., 2005; Marchi et al., 2005), while it also explain the spectral difference between lunar soils and underlying rocks.

However, this spectral mismatch is not observed in the case of 4 Vesta (Chapman, 2004), one of the three largest main belt bodies (D = 529 $\pm$ 10 km) (Thomas et al., 1997). Vesta is the only known differentiated asteroid with an intact internal structure, probably consisting of a metal core, a mantle, and a basaltic crust (McCord et al., 1970).

Strong evidence suggests that the HED meteorites, a large set of differentiated basalts (Eucrites), pyroxenites (Diogenites), and breccia mixtures of mainly these two rock types (Howardites), are impact ejecta from Vesta. The link between HED meteorites and Vesta was originally based on the good matches between the reflectance spectra and brightness of Vesta (albedo ~ 0.35) and those of HED meteorites, indicating that Vesta's surface is free of heavy space weathering (Chapman, 2004; McCord et al., 1970; Keil, 2002; Gaffey, 1983). On Vesta, the maturation effect should be $\sim$ 100-1000 times lower than that of the Moon (Gaffey, 1983).

Recent ion irradiation experiments on pyroxenes (Marchi et al., 2005) have shown significant reddening and darkening of the collected spectra with progressive irradiation, as shown in the previous sections. Since pyroxene is a major surface component of Vesta, as determined by spectroscopy, one could expect the solar wind irradiation to significantly alter the optical properties of the surface of Vesta.

To investigate this question, it is interesting to perform irradiation experiments on HED meteorites. Here I show preliminary results after irradiation of a eucrite meteorite, Bereba, chosen because its reflectance spectrum is very similar to that of Vesta. The ion irradiation experiments were performed using Ar^{++} ions with energy of 400 keV.

Powdered (10-100 μm) samples of Bereba were placed in the vacuum chamber describe above. Reflectance spectra (Fig. 6.8) were acquired using $BaSO_4$ as the reflectance standard.

The two bands in the spectra of Bereba around 0.9 and 2 μm are due to pyroxene, while the small shoulder around 1.3 μm is due to the presence of plagioclase. Irradiation of the sample produces a progressive reddening of the spectrum. The spectral slope in the region of the first band (centered around 0.9 μm) increases strongly, while the depth of both absorption bands becomes weaker. Irradiation of a virgin sample of Bereba, whose spectrum and albedo are very close to those of Vesta, yields a spectrum that is very similar to the Moon's, in terms of spectral slope and albedo (Fig. 6.8). The timescale for this process at 2.36 AU (average heliocentric distance of Vesta) is about 10^5 years.

The lunar Maria basalts and the Vesta crust are very similar in mineralogical

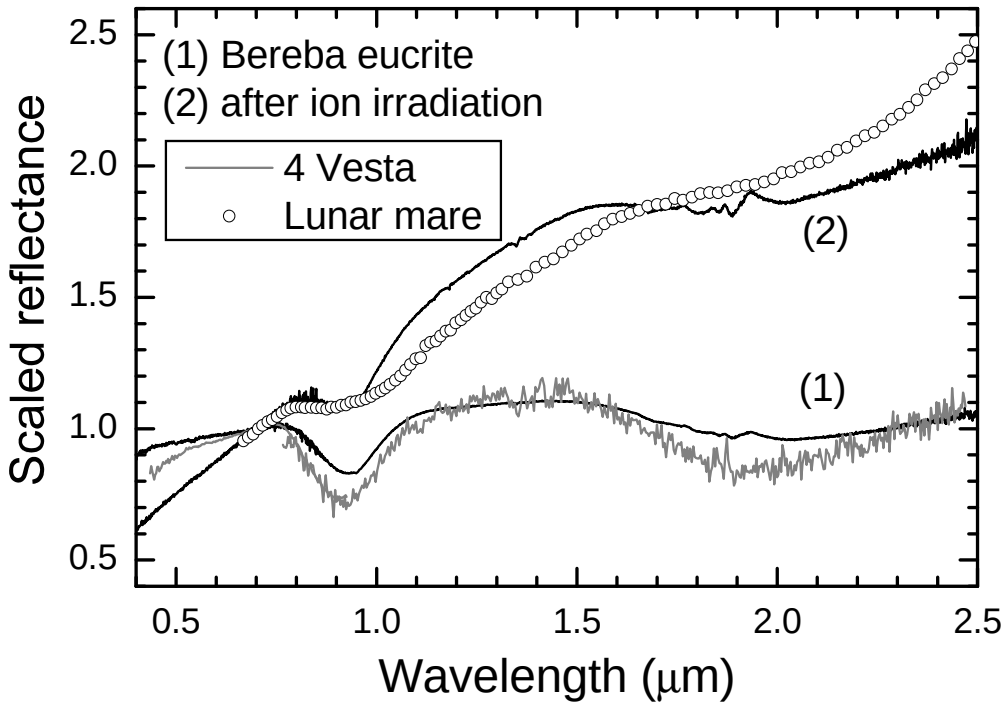

Figure 6.8: The initial reflectance spectrum of Bereba (1) and that obtained after irradiation with Ar^{++} ions, energy of 400 keV (3) are shown scaled to 1 at 0.7 μm, and compared with the spectrum of Vesta and the spectrum of a small lunar mare area.

composition (mainly pyroxene, plagioclase, and olivine). Even so, it appears that space weathering affecting the Moon surface minerals left Vesta's surface unaltered.

Particle irradiation of ordinary chondrite meteorites (Strazzulla et al., 2005) can explain the mismatch between ordinary chondrites and S-type asteroids and, most likely, solve this paradox. However, in the case of Vesta, the opposite paradox appears: if solar wind ions do reach the surface of Vesta, one should observe the same meteorite/asteroid spectral effect as for ordinary chondrites/S-type asteroids, but we did not. This implies that either Vesta is shielded from solar wind ions or some event refreshed the whole surface recently.

In the latter case, a large impact should have resurfaced the upper irradiated layers of the body about 10^5 years ago. Observations (Thomas et al., 1997) from

the Hubble Space Telescope indicate that Vesta has a 460 km basin on its surface, which was the result of an impact from a $\sim$ 35 km projectile. Furthermore, it is likely that Vesta experienced only one such impact over the Solar System history (Bottke et al., 2005). Collisional modeling results suggest that this impact took place about 1 Gyr ago and is responsible for the socalled Vestoids, a family of $D < 10$ km asteroids on Vesta-like orbits whose spectral features strongly resemble eucrites and howardites (Burbine et al., 2001; Marzari et al., 1996; Carruba et al., 2005). Considering that the Vestoids are not the result of this impact, Bottke et al. (2005) find a 19% probability that a major impact occurred on Vesta in the last 3.5 Gyr. Thus, a recent large impact (last 10^5 years) on Vesta seems unlikely.

6.2.2 A magnetic field?

There is a possibility that Vesta's interior, or crust, is a good conductor or is sufficiently magnetized, with a sufficiently coherent magnetization direction, so that it will form a barrier to the solar wind (Greenstadt, 1971). A remanent magnetic field is the most likely way of forming an obstacle to the solar wind flow resulting in its diversion. The present data do not enable us to distinguish between a global magnetic field producing a bona fide magnetosphere and a number of uniformly magnetized blocks of crustal material uniformly magnetized producing several crustal "magnetospheres". In the latter case, the solar wind particles would reach the surface via a number of "cusps".

To investigate this possibility, we estimated the fraction of Vesta's observed surface that must be unaltered, in order that Vesta's spectrum and albedo remain similar to those of HED meteorites. To make an order of magnitude estimate, we assumed that, if the solar wind ions touch the surface, the spectra of those unprotected regions would be similar to the most irradiated spectra of Bereba. By a linear combination of the most irradiated spectra of Bereba and the virgin spectra (geographical mixture), we found an upper limit of about 10% unprotected surface, over which it would be obvious that space weathering is occurring on Vesta; this limit is found when the slope of the linear combination is greater than the slope

domain of eucrites. This estimate leaves both possibilities open.

For Vesta to block the solar wind from bombarding its surface, the pressure of its magnetic field must balance the solar wind ram pressure at a distance from the surface that is greater than the proton inertial length and their gyroradii in this magnetic field. Balancing the solar wind ram pressure of about 5×10^{-10} Pa at 2.36 AU requires that the asteroid produces a magnetic field $B_0 \sim 2\times10^{-8}$ T at the stand-off distance. Since the above proton length scales ($\sim$ 200 km) are within the same order of magnitude as the radius of Vesta, the radius of the "magnetosphere" at the subsolar point should be at least twice Vesta's radius. With a dipolar globalmagnetic field, decreasing with distance as $1/r^3$, this requires a magnetic field strength of at least $2^3 B_0 \sim 0.2\mu$T at the surface of Vesta - corresponding to a magnetic dipole $\sim 3 \times 10^{16}$ A m^2. Even though such a magnetic field is expected to stand-off the solar wind (Greenstadt, 1971), this value is a lower limit since the size of the resulting magnetosphere is similar to the proton gyroradius, in which case kinetic effects are important (Omidi et al., 2002).

Alternatively, several large blocks of uniform magnetization within the crust, producing multiple crustal magnetospheres, would require higher surface magnetic fields to stand-off the solar wind and produce an irregularly shaped "magnetosphere". It is interesting to note that the Mars Global Surveyor spacecraft detected magnetic fields that imply crustal magnetized patches on Mars of magnetic moment within the same order of magnitude as the value estimated above, providing pressure responsible for localized increases in the ionopause altitude (Acuña et al., 1998). Such a mechanism has been demonstrated locally on the Moon by observed systematic coincidence between high albedo "swirls" and local magnetic field highs (Richmond et al., 2005). On the Moon, field strengths of only 10 nT at 35 km altitude are sufficient for producing this effect.

In fact, geochemical and paleomagnetic evidence from the HED meteorites strongly suggests that Vesta formed an iron core and once had an internally generated magnetic field (Cisowski, 1991; Collinson and Morden, 1994; Gattacceca and Rochette, 2004; Ruzicka et al., 1997; Righter and Drake, 1997). Eucrite and diogenite appear to have cooled in a field on the order of 10 μT, with on the average low remanence

intensities on the order of 10 mA/m, due to low metal content. However, deeper rocks may have enhanced magnetization, as may regolith rocks with a higher metal content, which is demonstrated in howardite (Rochette et al., 2004). To generate a global field from a crust or mantle magnetized within a dynamo, one needs a non uniform crustal thickness (Aharonson et al., 2004). This type of coverage is exactly the situation of Vesta, lacking its crust over a large portion, corresponding to the large crater excavated at the present South pole (Thomas et al., 1997; Drake, 2001). If the present rotation pole was the magnetic pole during remanence acquisition, this would generate a significant global remanent dipolar field.

In the case of the Moon - which has no global magnetic field or atmosphere - the average surface is exposed directly to the solar wind (except in the "swirls"), which plays an important role in the reddening and darkening of the lunar spectrum, in addition to micro-meteorite bombardment. Again, this suggests that Vesta may support a magnetic field that protects its surface from the solar wind.

In conclusion, our preliminary results suggest the presence of a magnetic field shielding a large portion of Vesta's surface from solar wind ions, with a required strength at the surface of ~ 0.2 μT. However, further experiments on a larger set of HED meteorites are needed to confirm this preliminary experiment, and a comparison with spectra of Vestoids is planned to be performed in future studies.

Acknowledgments

We thank the Muséum National d'Histoire Naturelle for providing us with the meteoritic samples. We are grateful to G. A. Baratta, D. Fulvio, and F. Spinella for their precious support during the experiments. We thank the referee J. Emery for his pertinent and constructive remarks.

Chapter 7

Optical constants

Based on the paper: Brunetto, R., Roush, T.L., Marra, A.C., Orofino, V. 2007. Optical characterization of laser ablated silicates. Icarus, submitted.

As I showed in the previous sections, silicates are a major component in the Solar System. Consequently, obtaining optical constants (real and imaginary part of the refraction index) in the laboratory has a main relevance to interpret spectral observations and remote sensing data of planetary, asteroid, TNOs' surfaces, and comets. Indeed, optical constants are the most important input parameters in surface scattering models such as the Hapke model (Hapke, 1993) or the Shkuratov model (Shkuratov et al., 1999). In this chapter I will estimate optical constants for ablated silicates, and will apply them to spectra of two interesting objects.

7.1 Optical characterization of ablated silicates

From the considerations previously exposed in this thesis about space weathering, it is clear that a detailed description of the optical properties of weathered silicates is urgent. The knowledge of optical constants for irradiated and ablated silicates helps modeling the surface spectra of an increasing number of objects.

Unfortunately, the estimation of the optical constants is not a simple task; different methods may produce different results, and several assumptions are usually

required. In the case of altered or treated samples, the situation is even more complex, since the resulting material usually retains part of the starting material characteristics, and thus it cannot be easily qualified as a specific and self-consistent species.

In the previous sections, I showed how to characterize spectra of ion irradiated samples when referred to the spectrum of the pristine material, by means of an exponential continuum related to the ion-induced damage. In this approach, the experimental curve is integrated into a classical Hapke or Shkuratov approach, to model the reflectance spectra of silicate-rich asteroids and to derive mineralogy and exposure time. Though providing useful information, this method is only applicable in the case of a surface where silicates are spatially segregated from other components. Thus, in the case of modeling intimate mixtures, optical constants are required.

The goal of this section is to provide useful tools to model space weathering effects on surfaces of asteroids and TNOs, performing an optical characterization of UV laser ablated silicates (olivine, pyroxene). In fact, successful optical characterization of weathered silicates has already been performed by other authors, in particular making use of the nanophase metallic iron model (Hapke, 2001); see e.g. Hiroi et al. (2006) for an application of this model to asteroid 25143 Itokawa. So, before I proceed, it is useful to review those results and address why it is important to perform optical characterization of my samples.

7.1.1 Nanophase metallic iron in laser ablation experiments

There is a wide consensus in the literature that spectral reddening and darkening due to space weathering is connected with the formation of metallic iron particles smaller than the wavelength, in vapor-deposited coatings on soil particle surfaces and inside agglutinates (Hapke, 2001). This is supported by the observation of the direct link between abundance of surface deposits of nanophase iron and systematic variations of optical properties of lunar soils (Pieters et al., 2000), and by several experimental results showing the formation of iron nanoparticles (see e.g. the re-

sults of laser irradiation in a simulation of lunar-like space weathering, discussed by Sasaki et al. (2001)).

The physical interpretation relies on the fact that a vapor is generated by both solar wind sputtering and micrometeorite impact, and injected preferentially downward into the porous regolith; the iron should be reduced by selective loss of oxygen during vapor deposition (Hapke, 2001).

In the second part of this thesis I have suggested that this strong and coherent scheme for space weathering needs to be enlarged, since new experiments using heavy ion irradiation (Brunetto and Strazzulla, 2005) and UV laser ablation (Brunetto et al., 2006a) have been performed, giving interesting results. In particular, I irradiated silicate samples with an UV excimer laser, below and above ablation threshold. I confirmed and extended the results for spectral alteration discussed by Sasaki et al. (2001); in particular it appeared that the most efficient experimental conditions to darken and redden the reflectance spectra are obtained performing congruent (stoichiometric) laser ablation, i.e. using an UV laser with fluence higher than ablation threshold.

In the case of UV laser a strong absorption of laser light is guaranteed by the very short wavelength. In this case it is possible to limit thermal effects onto the target and consequently a regime of stoichiometric ablation occurs. On the contrary, with IR laser sources (as the one used in previous laser ablation experiments) it is necessary to take into account the heat loading of the target, and the consequent damage occurring in the surrounding material (Brunetto et al., 2006a).

Comparing the spectral slopes after irradiation in ablating and non-ablating conditions, it was found that below ablation threshold the slope increases linearly with the dose, while in ablating conditions a saturated and very red slope is reached after a very low dose. Experiments with IR lasers (e.g. Yamada et al. (1999)) lay in between. This leads to serious concerns about which experimental regime is more suitable to this purpose.

The formation of metallic iron can be observed by different techniques. Sasaki et al. (2001) detected nanophase metallic iron on the Yamada et al. (1999) samples using transmission electron microscopy (TEM). Bentley et al. (2005), used a laser setup

similar to Yamada et al. (1999) to produce weathered olivine and performed several magnetic analyses. In particular, they observed an increase in magnetic susceptibility with laser exposure, for all irradiated samples.

Consequently, my team started to investigate variations in the magnetic susceptibility on my UV laser ablated samples. Preliminary measurements on laser ablated orthopyroxene show an increase in susceptibility with laser dose, similarly to what measured by Bentley et al. (2005). We observe an increase in magnetic susceptibility of more than a factor of 3, from 7.1×10^{-8} to 2.5×10^{-7} m^3/kg. This trend is in agreement with what was reported by Bentley (2005), and the relative increase in the magnitude is even stronger. Thus, even if a detailed microscopic surface analysis of my samples is not yet available, preliminary magnetic measurements suggest that formation of metallic iron has a major role.

Still, several open questions are arising. For instance, to explain the different experimental results between Yamada et al. (1999) and Brunetto et al. (2006a), one could wonder if the reddening effect on laser ablated silicates is only partially connected with the metallic iron production, and partially connected with some morphological and structural modification (e.g. formation of amorphous grains); also, it is possible that at least part of the metallic iron is formed inside the grains, rather than redeposited.

To try to answer those open points, I attempt to perform optical characterization to be compared with previous results, in particular with the Hapke's space weathering model.

7.1.2 Characterization of the samples

To characterize weathered silicates, I use reflectance spectra (UV-Vis-NIR range) acquired in the Astrophysics Laboratory in Lecce, Italy. The samples (San Carlos olivine, Bamble orthopyroxene, and clinopyroxene) were powdered. The grain size distribution of the powder was not characterized and sieves were not used to separate a specific size range, because the powder was pressed into a cohesive pellet to be placed in the vacuum chambers. Based upon visual inspection of the powder, it

included a wide range of dimensions with an upper limit of about 0.5 mm. How this initial distribution relates to the final grain sizes in the pressed pellet is uncertain as the pressing process could potentially fracture grains.

In the same laboratory, nanopulsed UV excimer laser (193 and 248 nm) ablation of silicates was performed in high vacuum conditions, as a simulation of micrometeorite bombardments. The experimental details and conditions are described in the previous sections. The reflectance spectra in the 0.3-2.5 μm range were studied as a function of the dose.

For the purpose of this work, the reflectance geometry plays a very important role; in these measurements, spectra are usually acquired using hemispherical geometry, by means of an integrating sphere. In the codes used to model the spectra, a bi-directional geometry is required. Thus, in the case of hemispherical geometry, I decided to apply a recent result by Shkuratov and Grynko (2005), that provides a way to estimate reflectance at 30°, R(30°), using the integral (hemispherical) albedo (A_{int}) and vice versa, through the equation:

$$logR(30^\circ) = 1.088 logA_{int} \tag{7.1}$$

Shkuratov and Grynko (2005) showed that Eq. 7.1 is valid for particulate media consisting of very irregular particles, and this seems to be quite close to our case. Note that the proportion of this correction is much smaller than the spectral variations after laser ablation (see below).

In these measurements, spectra of the altered area can sometimes refer to a position on the surface slightly different from the spectrum before treatment (shifts of hundreds of microns); since the samples have inhomogeneous grain sizes, this may lead to slightly different band areas and depths. This was noted by Brunetto et al. (2006b) in ion irradiation experiments, where spectral ratios after irradiation to before irradiation showed non-perfect compensation of the absorption bands.

In the case of laser ablation, the total dose (energy per unit area) is a critical damage parameter. Consequently, in this chapter I use the same damage parameters as before to describe variations in the optical constants.

The Hapke radiative transfer model

Hapke and Wells (1981) and Clark and Roush (1984) describe an approach to determination of the absorption coefficient, α, of a given material starting from its measured reflectance spectra. Since α is related to k via the dispersion relation, $\alpha = 4\pi k/\lambda$, this approach, that relies upon Hapke's description of radiative transfer within particulate surfaces (see Hapke (1981, 1986, 1993), and references therein), provides a useful mechanism of determining k.

Roush et al. (1990) and Lucey (1998) used the Hapke approach for determination of k for serpentine and olivines and pyroxenes, respectively. A brief summary is provided here and the interested reader is referred to Roush et al. (1990) and Lucey (1998) for more details. Beginning with the reflectance spectrum, n is assumed constant; then, an iterative change of k forces the calculated and measured reflectance to agree with one another. Additional leverage is provided in determining k if several grain sizes of the same material are used, with the assumption that the composition is not a function of grain size. Roush (2003, 2005) describes an additional iterative approach that allows determination of n as a function of wavelength using a subtractive Kramers-Kronig analysis.

The various assumptions contained within the Hapke-formalism (Hapke (1993), and references therein), used here are discussed in equations 1-6 of Roush (1994) and equations 1-4 of Cruikshank et al. (1997). Here scattering is assumed isotropic, h, the width of the opposition surge, is assumed to be 0.05, and Hapke's internal scattering parameter, s, is set at 10^{-17}. The first two of these parameters require observations at multiple viewing geometries that were not obtained. The third parameter is poorly characterized for natural materials and essentially setting it to zero effectively forces the absorption coefficient to account for all the spectral behavior.

Literature data: estimation of the grain size

The first step of the analysis was to compare the laboratory spectra obtained for pristine materials with literature data on analogue silicates, in particular to use

previously published optical constants to estimate the grain size of my samples. As a reminder, the grain size distribution was not characterized but, based upon visual examination of the powder, I estimate an upper limit of about 0.5 mm.

A widely used dataset of optical constants for olivine and pyroxene is the one by Lucey (1998), who calculated n and k in the 0.4-2.5 μm spectral range starting from reflectance measurements and using the Hapke radiative transfer theory, for different Mg/Fe content (the Mg number is the ratio between Mg and Mg+Fe). Unfortunately, attempts to fit my silicate spectra starting from the Lucey (1998) optical constants and using the Hapke radiative transfer theory were unsuccessful.

After this negative result, I decided to compare my spectra with the several spectra of San Carlos olivine and Bamble orthopyroxene (i.e. silicates of the same origin as ours) included in the RELAB spectral database (NASA RELAB facility at Brown University; http://www.planetary.brown.edu/relab/). RELAB spectra are available for different grain size ranges, so that the inverted Hapke model can be used to estimate n and k for each grain size range (here included in the 25-500 μm range); the values obtained were then averaged. The value of n was assumed to be constant and of the same value as in Lucey (1998), for the corresponding Fe content (both San Carlos olivine and Bamble orthopyroxene have FeO content <10 wt.%, see e.g. Yamada et al. (1999)); this assumption is essentially correct in the 0.3-2.5 μm spectral range, as I have verified using an iterative Kramers-Kronig analysis. I used $n = 1.654$ for olivine and $n = 1.664$ for orthopyroxene.

The values for k were obtained from RELAB data in the various intervals using the central value for the grain size in each interval (for instance using 100% of 100 μm grains for the 75-125 μm interval); values obtained in the different intervals agree quite well with each other in the 25-250 μm range; the only large deviation comes from the 250-500 μm interval, and this is probably due to a non-uniform distribution of the grain size within this interval. In fact, using a multi-component fit of the 250-500 μm RELAB spectrum, and using the optical constants derived in the 25-250 μm grain size range, an asymmetric size distribution was obtained. Following this approach, iterative steps gave final values for k in the 250-500 μm range that agree much better with the 25-250 μm grain size range.

The final averaged k values for olivine and orthopyroxene are reported in Fig. 7.1, showing also a comparison with the imaginary index in the case of olivine (Mg number 0.7), as estimated by Lucey (1998) and by Pollack et al. (1994).

The derived n and k values were used to fit my silicate spectra with a multi-component routine, whose output was the grain size distribution for the samples. In Fig. 7.2 the resulting synthetic spectra are plotted, along with the measured spectra; the fit quality is quite good, especially in the case of olivine.

Discrepancies can be attributed to the presence of a little atmospheric contamination in the ex-situ spectra. For instance, the feature at about 1.9 μm, shown by olivine, disappears in the spectra collected in high vacuum conditions Brunetto et al. (2006b). In the case of orthopyroxene, though the band depths are well reproduced, a discrepancy is present in the slope, with the synthetic spectrum having a slightly redder slope than the measured one. In the laboratory, we often observe that reflectance spectra of smooth and compact surfaces tend to produce bluer slopes, while spectra of rough and porous samples produce redder slopes. Furthermore, spectra published by Yamada et al. (1999) show the same neutral slope for Bamble orthopyroxene observed in Fig. 7.2, and both experiments used powders packed to form pellets. Thus, this discrepancy with RELAB spectral slopes can be attributed to the fact that my samples were pressed powders. However, it is important to stress that the observed discrepancies are much smaller than spectral variations induced by alteration processes (as it will be made clearer below).

The derived grain size distribution is extremely heterogeneous, and it includes dimensions from tens of microns to few millimeters (see Table 7.1); also, the resulting values are not unique, since I used a multi-component fit (a discrete number of components), while in reality the distribution is expected to be continuous; the fit usually converged using at least 3 components. Including additional components yields a more reasonable size distribution, but it does not statistically improve the quality of the fit, and it has the disadvantage of increasing the computational time.

From these considerations, the numbers here calculated should not be considered as a realistic grain size distribution, but simply as an effective grain size. This would also explain the presence of a millimeter-sized component, which was not observed in

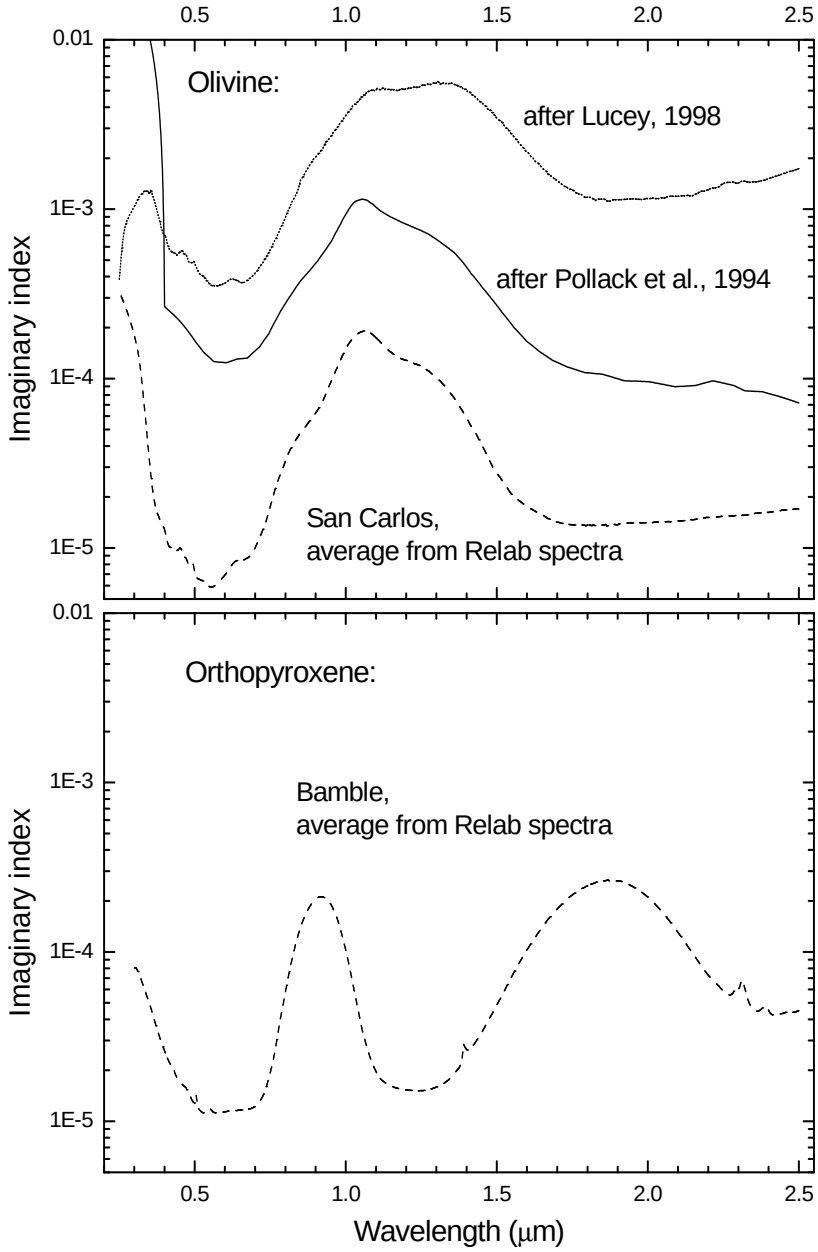

Figure 7.1: Upper panel: comparison between imaginary indices for olivine (Mg number = 0.7) after Lucey (1998) (dotted curve) and after Pollack et al. (1994) (solid curve); imaginary index of San Carlos olivine is also included (dashed curve), as calculated from inversion of RELAB data (see text). Lower panel: imaginary index of Bamble orthopyroxene, as calculated from inversion of RELAB data (see text).

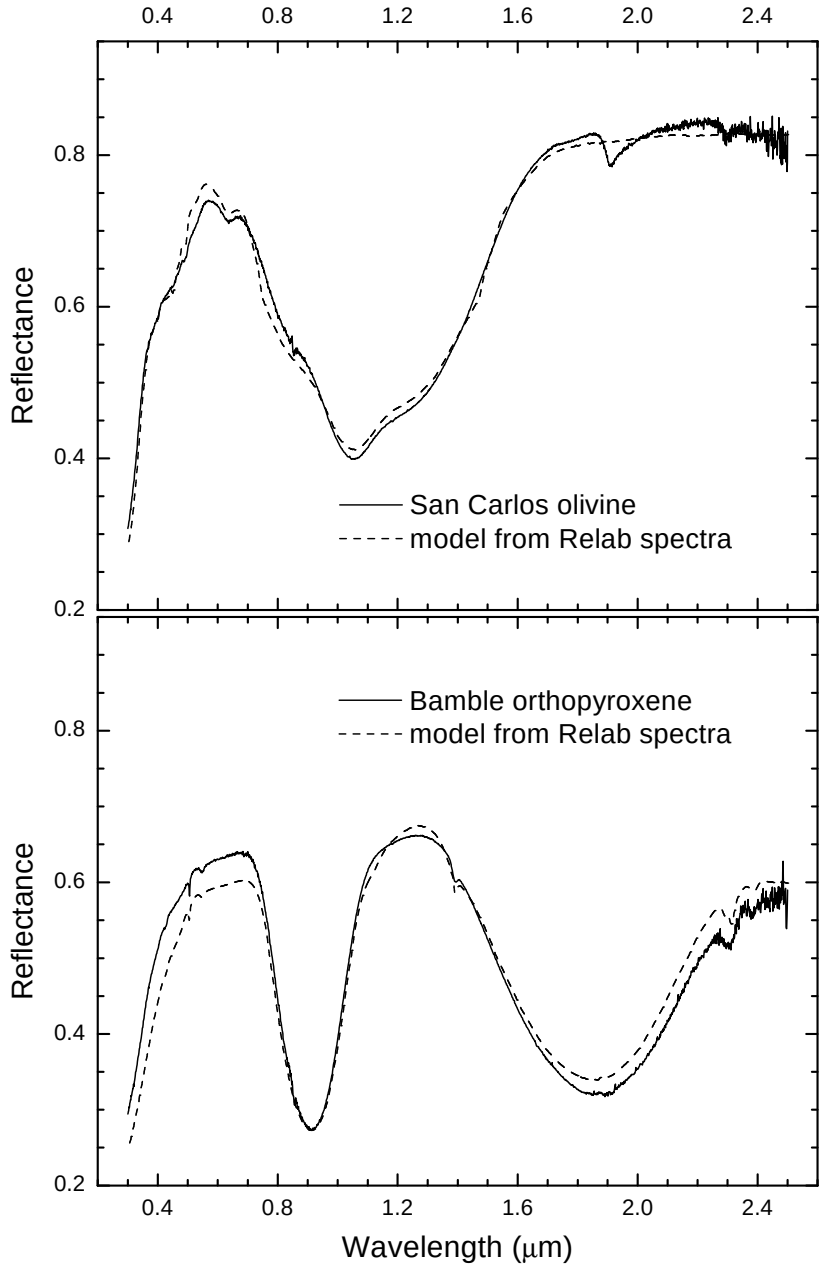

Figure 7.2: Fit curves of reflectance spectra of San Carlos olivine (upper panel) and Bamble orthopyroxene (lower panel), obtained using optical constants from RELAB data (see Fig. 7.1); corresponding grain size distributions are given in Table 7.1.

the powders before pressing, and should therefore be attributed to the preparation procedure of the pressed target.

Sample	Grain size	Relative abundance	RMS	Reduced chi squared
Olivine (whole spectrum)	7.4 μm 120 μm 2.3 mm	8.4% 14.6% 77.0%	0.0141	1.42
Olivine (only bands)	12 μm 600 μm	24.4% 75.6%	0.0138	1.34
Ortho-pyroxene (whole spectrum)	32 μm 250 μm 2.6 mm	32.1% 7.4% 60.5%	0.0286	9.25
Ortho-pyroxene (only bands)	6.6 μm 230 μm	7.7% 92.3%	0.0143	2.90

Table 7.1: Grain size distribution of olivine and orthopyroxene samples, as derived using optical constants from RELAB data; the millimeter sized component disappears when the fit is restricted to the bands. The mean optical path length is estimated to be about 450 μm for olivine, and about 210 μm for orthopyroxene. RMS here is the root mean square of the difference between measured and modeled spectral data. The reduced chi square is calculated assuming a reasonable error for the measured reflectance of 2%.

In fact, since the band depth and shape are more strictly related to the grain size distribution than the continuum, I also fitted the spectra only considering the central part of the silicate bands; in this case the millimeter sized component is eliminated, as is reported in Table 7.1. Using a weighted average of the various components, the mean optical path length (equivalent to a sort of effective grain size) is estimated to be about 450 μm for olivine, and about 210 μm for orthopyroxene. Thus, this grain size distribution obtained fitting the bands is more realistic, and gives a better estimate of the optical path-lengths of the incident UV-Vis-NIR light in the target.

All the mentioned values are input parameters for the calculations reported in the following section. In the case of clinopyroxene, unfortunately, the grain size distribution cannot be estimated since no adequate optical constants have been found for these samples. In the calculations reported below, I assume for clinopyroxene the same value of n as for orthopyroxene ($n = 1.664$).

7.1.3 Optical constants of silicates after UV laser ablation

Inversion of the Hapke scattering model

UV laser ablation affects the upper layers of the target, because silicates strongly absorb at these wavelengths (see Fig. 7.1). Thus, in a reflectance spectrum, both the contributions of the altered and underlying unaltered layers are present; of course the relative amount depends on the optical properties and on the wavelength. Yet, before I proceed with a model with iron inclusions, it is interesting to apply the inversion of the Hapke scattering model to spectra of altered samples.

In Fig. 7.3 the resulting values of k are plotted after applying such inversion to olivine (upper panel) and orthopyroxene (lower panel) spectra, assuming the same n value and grain sizes as in the previous section. The comparison is shown between samples before and after laser ablation; the imaginary index from the RELAB data is also included. As mentioned above, discrepancies with respect to RELAB data are much smaller than variations induced by weathering (note the logarithmic scale in the y-axis).

It should be stressed that the k curve for ablated olivine and orthopyroxene is just an effective curve, and cannot be regarded as a proper imaginary index, since it would imply that we are dealing with a material uniformly characterized by such k index, while a model with inclusions is by far more appropriate.

However, it is interesting to note that this curve gives an easy and useful tool to characterize a weathered surface in the Solar System, and to check if that surface is compatible with the presence of altered silicates (see below).

Hapke's space weathering model

The weathering process takes place in a very thin layer (smaller than the wavelength), so the altered layer cannot be described as a self consistent particulate medium, and a model with metallic iron inclusions in a silicate matrix is more appropriate. This model has been developed by Hapke (2001), and is widely used to describe the effects of weathering on reflectance spectra.

The Hapke's space weathering model is based on the Maxwell-Garnett effective

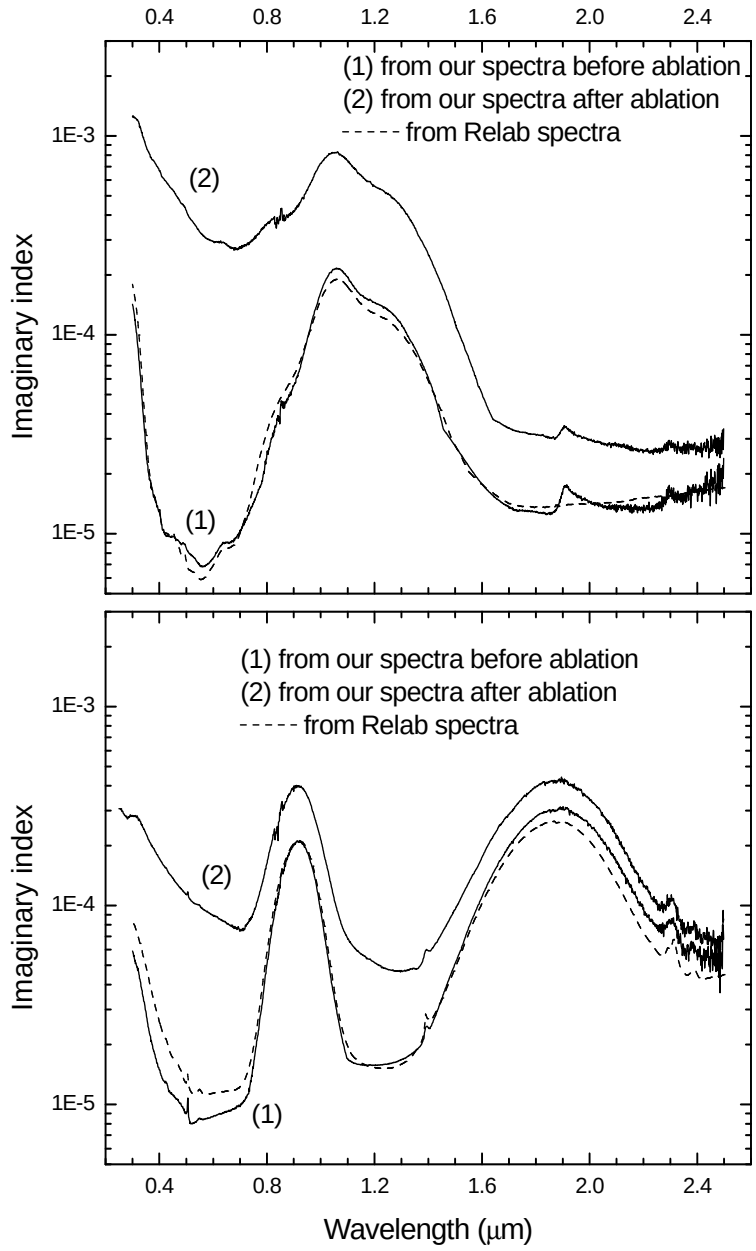

Figure 7.3: Imaginary index k of San Carlos olivine (upper panel) and Bamble orthopyroxene (lower panel) samples, before and after UV laser ablation, inverting the Hapke scattering model and using the grain size distribution of Table 1. Imaginary indices from RELAB data are also shown.

medium theory, to calculate the absorption coefficient of a silicate host medium containing inclusions of small metallic iron spheres. The resulting absorption coefficient

$\alpha(\lambda)$ of a material containing metallic iron particles is:

$$\alpha(\lambda) = \alpha_h(\lambda) + 36\pi\phi z(\lambda)/\lambda \tag{7.2}$$

where $\alpha_h(\lambda)$ is the absorption coefficient of the host silicate matrix, λ is the wavelength; ϕ is the volume fraction of metallic iron particles in the host matrix, and it is a function of the concentration of inclusions and relative densities of inclusion and host materials. The function $z(\lambda)$ is given by:

$$z(\lambda) = \frac{n_h^3 n_{Fe} k_{Fe}}{(n_{Fe}^2 - k_{Fe}^2 + 2n_h^2)^2 + (2n_{Fe}k_{Fe})^2} \tag{7.3}$$

where n_h is the real part of the refractive index of the host material, n_{Fe} and k_{Fe} are the real and imaginary parts of the refractive index of iron. In the space weathering literature, the optical constants of iron by Johnson and Cristy (1974) are commonly used in Eq. 7.3.

In the literature, a common assumption applying Hapke's space weathering model (see e.g. Hiroi et al. (2006), for asteroid 25143 Itokawa) is to assume that the absorbance spectrum of silicates can be approximated by the negative natural logarithm of their reflectance spectrum $R(\lambda)$:

$$lnR(\lambda) \approx -\{\alpha_h(\lambda) + 36\pi\phi z(\lambda)/\lambda\}d_e \tag{7.4}$$

where d_e is the above discussed mean optical path length. In the case $\phi = 0$ (no iron inclusions), Eq. 7.4 gives an estimate of $\alpha_h(\lambda)$ once we measure the reflectance spectrum and we have an estimate for the effective grain size. This is exactly the case of my samples before laser treatment (see discussion above). Consequently, Eq. 7.4 becomes:

$$R_{weath}(\lambda) \approx R_{unweath}(\lambda) exp\{-36\pi\phi z(\lambda) d_e/\lambda\} \tag{7.5}$$

This implies that the ratio between spectra of weathered to unweathered samples is described by an exponential curve. The use of Eq. 7.5 is reasonable in the present case because the Fe-bearing coatings are expected to be present only on the upper sides of the powder grains seen by the spectrometer. Eq. 7.4 and Eq. 7.5 are easy

to use, but they represent relatively poor approximation. Note that, in Eq. 7.5, an underestimate of the d_e parameter implies an overestimate in the volume fraction of metallic iron, and vice versa. Note also that applying Eq. 7.5 to ratioed spectra, one needs an estimate of n_{Fe}, k_{Fe}, and n_h, but not of k_h.

I applied Eq. 7.5 to spectra after laser ablation, to check if they are compatible with the presence of metallic iron particles. In Fig. 7.4 the results are plotted for olivine; the upper panels show spectra before and after laser ablation with two different doses, and the fit curves according to Hapke's space weathering model; the lower panels are ratio plots, once again proving how the alteration process mainly affects the continuum and does not affect the band position and relative intensity.

The fit quality is poor for wavelengths below 0.45 μm, probably because that is a region of strong absorptions, that cannot be described by the simple model used here. The fit quality is better in the 0.45-2.5 μm range, which is the range of main interest for Solar System studies. Though discrepancies are present, they could be partially attributed to a non-perfect compensation of the silicate bands, as discussed above; discrepancies can also be attributed to the relatively poor approximation of Eq. 7.5. The fit curve seems to deviate at lower dose case more than higher dose: this may indicate that saturation and uniformity of the surface has been reached; in fact, in the ablation regime, the difference between lower dose (e.g. 27 J/cm^2) and higher dose (e.g. 52 J/cm^2) is given by the number of pulses, and some saturation effect is achieved at the higher doses.

The volume fraction of nanophase iron is $\sim 0.01\%$ for doses of 27- and 52-J/cm^2, using a reasonable mean optical path length of about 450 μm, as calculated from the previous fitting of the silicate bands. This would reassert that the nanophase iron scenario described above is correct, and it would remain consistent with the magnetic susceptibility measurements.

The case of orthopyroxene is depicted in Fig. 7.5; the quality of the fit curves is better than the case of olivine.

It results $\phi \sim 0.01$ vol. % for doses of 43- and 86-J/cm^2, using a reasonable mean optical path length of about 210 μm, as calculated from the previous fitting the silicate bands. Note that the amount of nanophase iron in the two cases is

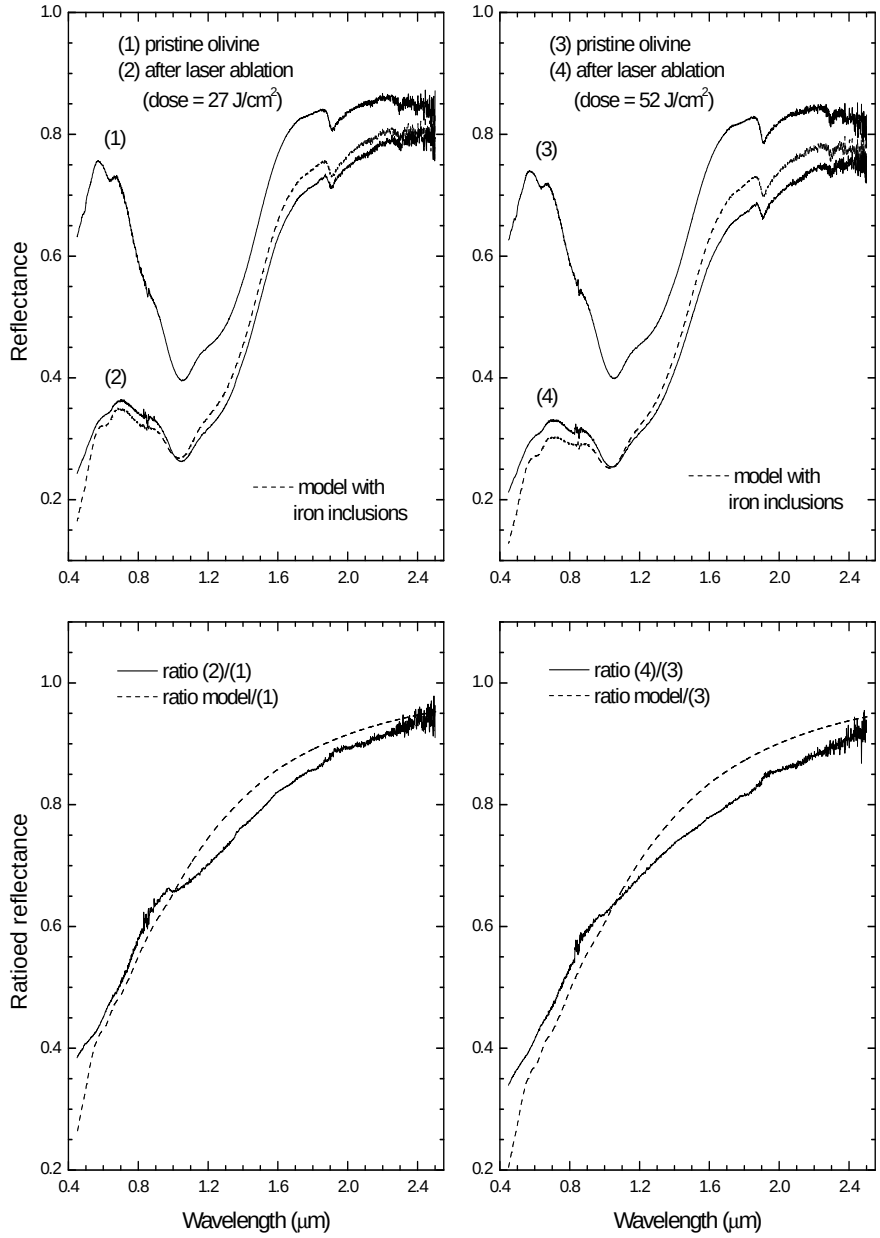

Figure 7.4: Upper panels: reflectance spectra of San Carlos olivine, before and after ablation with nanopulsed UV laser (193 nm), with two different doses; the dashed curves are the resulting fit using metallic iron inclusions in the Hapke's space weathering model as incorporated into Eq. 7.5 (see text). Lower panels: ratio plots of the spectra shown in the upper panels; the spectra after ablation and the corresponding fit curves are divided by the spectra before treatment.

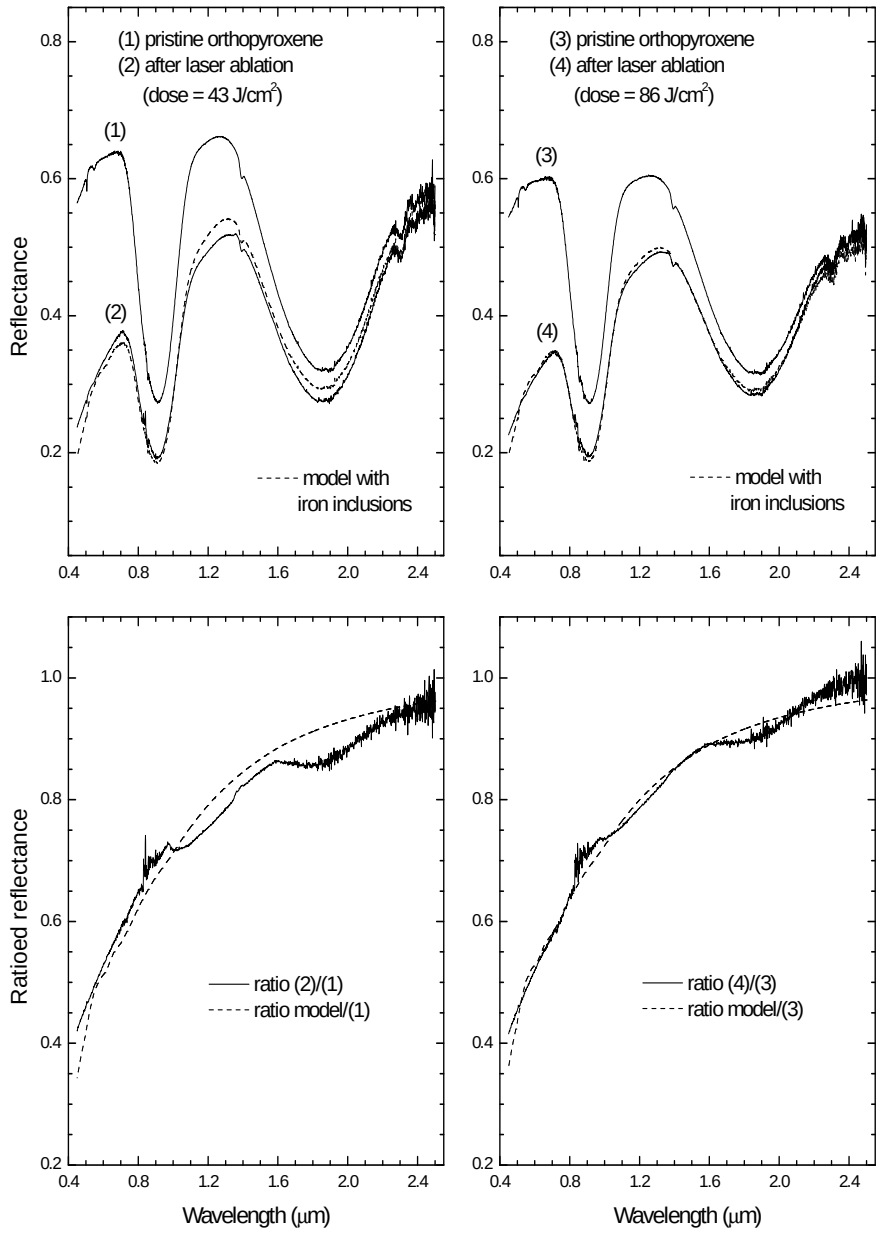

Figure 7.5: Same as Fig. 7.4, for ablated orthopyroxene.

practically the same, even if the laser dose is doubled. Again, this suggests that a sort of saturation is reached in the damaged layer, both for olivine and orthopyroxene.

We stress that the values found for ϕ are affected by large errors (on the order

of a factor of 2), that essentially come from the error of the estimated mean optical path length. Hence, a comparison between ϕ values for olivine and orthopyroxene implies that the amount of nanophase iron formed in the process is of the same order of magnitude, and one cannot discriminate whether the process is more effective for olivine or orthopyroxene. Probably the spectral changes depend more on the ferrous content than on the crystal structure, and thus a comparison between olivine and orthopyroxene could be done only using materials with the same Fe content. In any case, laser ablated olivine produces NIR spectral slopes that are redder than pyroxene (Hiroi and Sasaki, 2001; Brunetto et al., 2006a).

Using Hapke's space weathering model on ablated clinopyroxene (Fig. 7.6) gives a better fit than ablated orthopyroxene; here a value of $n_h = 1.664$ is assumed for clinopyroxene, i.e. the same value estimated for orthopyroxene. One can use Eq. 7.5 because it does not require the knowledge of k_h. Unfortunately in this case the metallic iron content cannot be calculated since we do not have a precise estimate of the grain size; however, one can calculate the product $\phi d_e = 0.02\mu$m, and assuming a mean optical path length of about 210 μm (as the one of orthopyroxene) again it results about $\sim$ 0.01 vol.%. These results are not strongly sensitive to the range of n-values of clinopyroxene. Using an n_h value of 1.84, near the upper bounds of clinopyroxene, produces $\phi = 0.007$ vol.%, and this is consistent with the interpretation that $\phi \sim 0.01$ vol.%.

It is interesting to note that the product ϕd_e obtained for ortho- and clinopyroxene (about 0.02 μm) is nearly identical to what Hiroi et al. (2006) found for the dark and red areas on asteroid 25143 Itokawa.

7.1.4 Other possible scenarios

Metallic iron particles without ablation process

A few experiments have been performed in our laboratory, investigating the laser effect below the ablation threshold. In Fig. 7.7 the results of the model described above are plotted for clinopyroxene laser processed below the ablation threshold (using the same assumptions as above). It comes out that the Hapke's space weathering

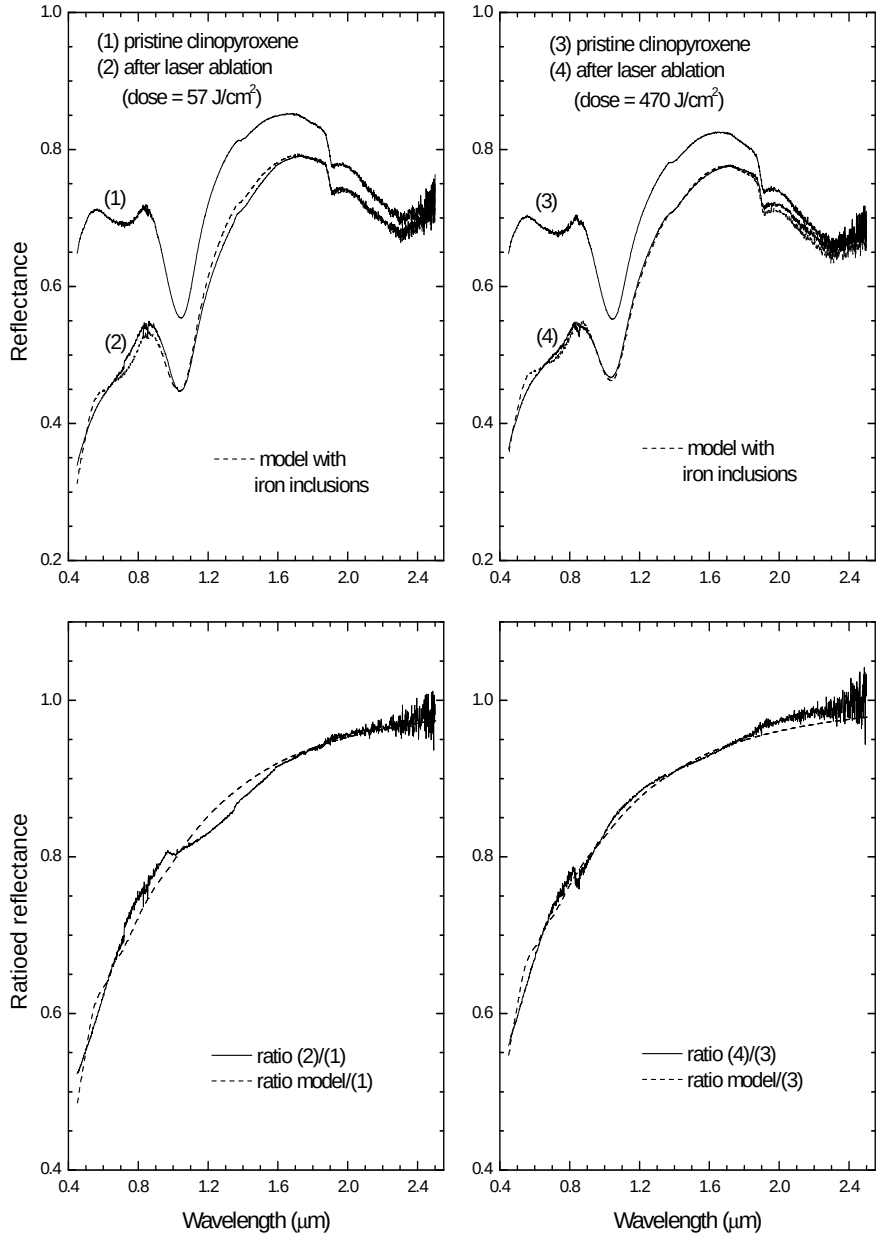

Figure 7.6: Same as Fig. 7.4, for ablated clinopyroxene, with the assumption that $n = 1.664$, as estimated for orthopyroxene.

model with metallic iron inclusions can fit the spectra of the irradiated samples, even when there is no vapor plume formed in the process.

Usually, laser irradiation of a solid below the ablation threshold induces changes

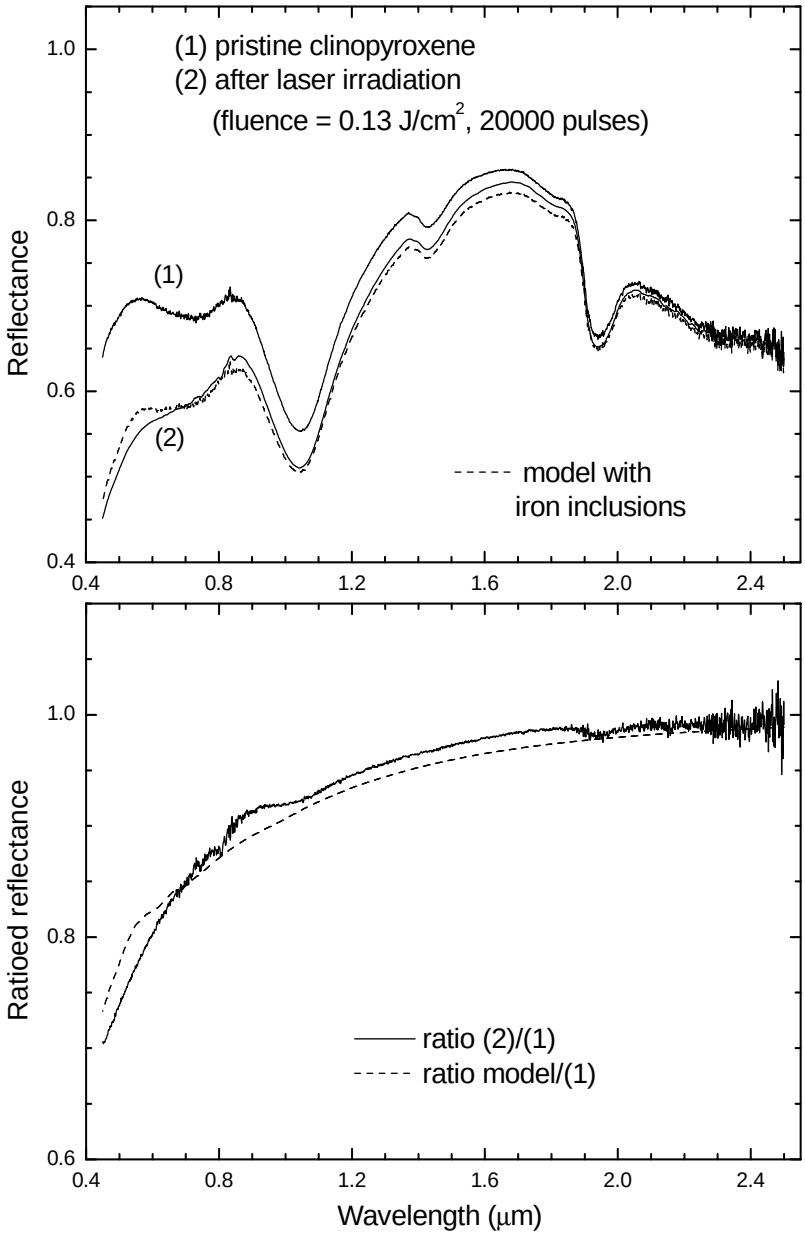

Figure 7.7: Same as Fig. 7.4, for clinopyroxene irradiated below the ablation threshold (no vapor plume); in this case, irradiation was performed with a 248 nm laser, with a relatively low fluence, but 20000 pulses on the target, which means a total dose of about 2600 J/cm2. Again, it is assumed $n = 1.664$, as in Fig. 7.6.

in the morphology and microstructure of the surface, generating defects and deplet-

ing one or several components of the target. Such processes can also play a role in a micrometeorite impact. Thus, the results from these tests cannot rule out whether the iron inclusions are formed from the vapor phase or not.

Experiments below the ablation threshold indicate that a weathering effect is present also when there is no plasma ejected from the target. From this comparison, and also with respect to the experiments by Yamada et al. (1999) in ablating conditions, one can speculate that below the ablation threshold some other materials are produced and/or inclusions are formed inside the grains.

The possibility of photo-sputtering is not very probable since, assuming a photo-sputtering yield of 5×10^{-7} atom per photon Walmsley et al. (1999), I find an upper limit of 0.2 nanometers for the thickness of the photo-sputtered material. Thus, thermal effects are likely to prevail, even if a photo-sputtered component cannot be excluded.

These suppositions cannot be verified in this work, and require different experimental and theoretical approaches that are beyond the scope of this thesis.

Formation of amorphous structures

Another scenario that can be investigated is the formation of amorphous silicate structures in the grains after laser treatment. In fact, a comparison between the values for $z(\lambda)$ in the Hapke's space weathering model (see Eq. 7.3) and the imaginary part of the refractive index for olivine and pyroxene glass (after Dorschner et al. (1995)) shows very similar trends. The melting process of Dorschner et al. (1995) was not performed in inert conditions, and part of the Fe^{2+} in contact with the air oxidized to Fe^{3+}, producing an absorption from UV to NIR.

As a test, a spectrum of ablated orthopyroxene was fitted using Eq. 7.5, but replacing the iron contribution (i.e., n_{Fe} and k_{Fe}) with the optical constants of orthopyroxene glass in Eq. 7.3; the result is reported in Fig. 7.8.

A good fit is found in the range 0.45-2.5 μm; again, the mismatch in the region below 0.45 μm is probably due to the strong absorption towards the UV. Because of the experimental conditions of Dorschner et al. (1995) the reddening and darkening produced by these optical constants is probably due to broad Fe^{3+} absorptions. In

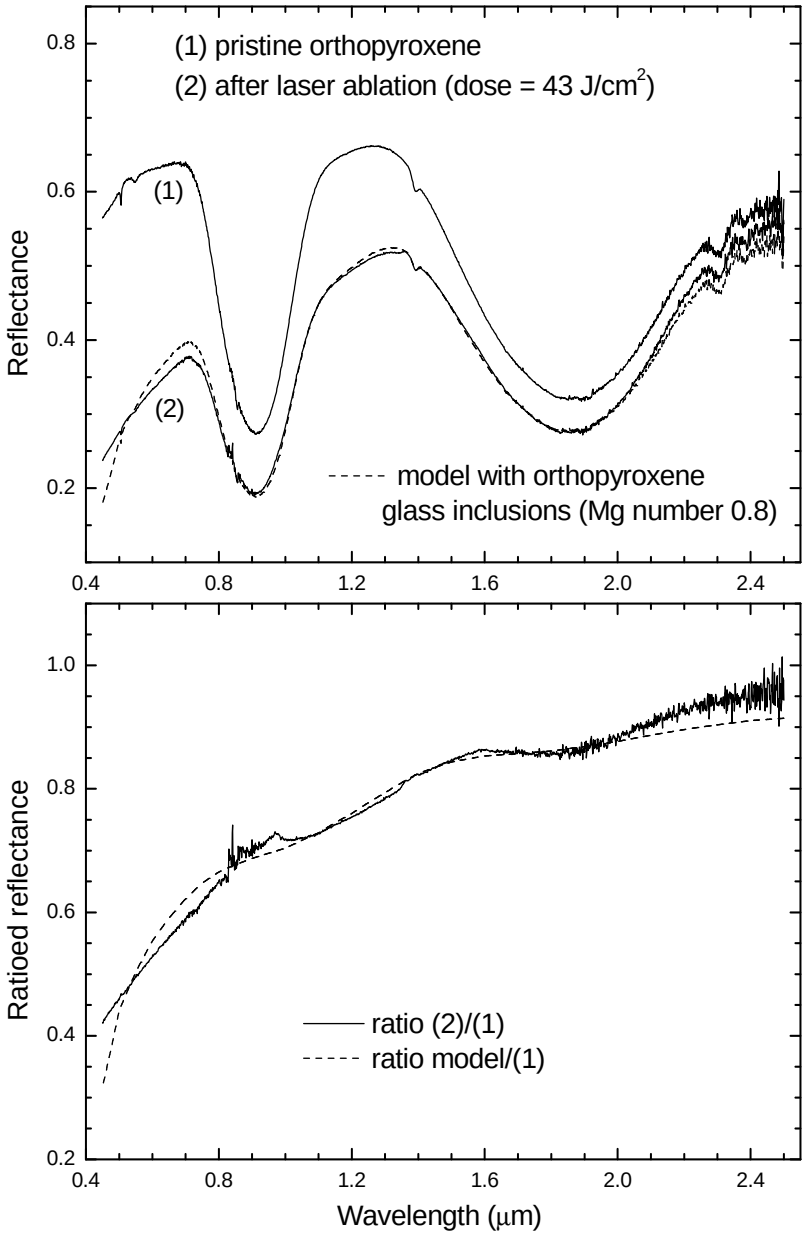

Figure 7.8: Same as left panels of Fig. 7.5, but using orthopyroxene glass (Mg number = 0.8) inclusions instead of metallic iron.

fact, it is interesting to note that the values of k for the amorphous pyroxene used here range between 10^{-3} and 10^{-2} in the visible, while the values of k for Fe-free pyroxene glass are between 10^{-5} and 10^{-4} in the same spectral range. This indicates

that the use of effective medium theory is reasonable, while it would not probably be so for Fe-free glass particles, as scattering would become important. In fact, effective medium theory does not take into account scattering by individual particles (as reported above, the contaminants are assumed to be very small spheres).

I use orthopyroxene glass with Mg number of 0.8 and a volume fraction for the inclusions of $\phi = 8.6$ vol.%; this last value is quite large, suggesting that second order effects should be probably included in Eq. 7.3.

Furthermore, the data from Dorschner et al. (1995) closest to the Bamble orthopyroxene composition are for Mg number of 0.8 and 0.95; a Mg number in between would be probably more appropriate for Bamble orthopyroxene, but since optical constants for that are not currently available, this scenario cannot be investigated in more detail. However, these results indicate that the presence of contributions by amorphous or glassy silicates containing iron, after the weathering process cannot be excluded a priori, and indeed it deserves further experimental investigation.

Conclusions

Performing an optical characterization of samples before and after UV laser ablation, it results that the weathering trend (reddening and darkening of the reflectance spectra) is compatible with the Hapke's space weathering model, using the optical constants of metallic iron in a silicate matrix. The formation of nanophase iron inclusions in the targets is also supported by new magnetic susceptibility measurements of the laser ablated orthopyroxene. Both results agree with previous studies using IR lasers (Yamada et al., 1999; Bentley et al., 2005).

I also investigated the potential formation of amorphous silicates (enriched in Fe^{3+}) in the process and preliminary results indicate that additional spectral contributions from such materials may well be present. Also, from experiments below ablation threshold, I suggest that a small part of the metallic iron or the iron-bearing glassy inclusions may form independent of a vapor plume. It must be stressed that a deeper analysis of the micrometeorite bombardment process should be investigated looking at real micro-impact experiments.

Acknowledgments

We thank B. Hapke and an anonymous reviewer for their comments and suggestions in the reviewing process, and warmly thank L. Sagnotti for his magnetic measurements. We are also grateful to A. Blanco, L. Folco, M. Martino, L. Moroz, F. Romano, and G. Strazzulla for their precious help and suggestions. This research was supported by the Italian Ministero dell'Istruzione, Università e Ricerca (MIUR), and TLR acknowledges support enabling this research from NASA's Planetary Geology and Geophysics Program.

7.2 Application to minor bodies

7.2.1 Centaur 5145 Pholus: a mixture of silicates and organics

The surfaces of objects in the outer Solar System are dominated by ices and organic refractories, but silicates have been tentatively identified on a few objects, for instance on the centaur Pholus (Cruikshank et al., 1998) and the Uranian moon, Miranda (Bauer et al., 2002). Since the red organic compounds observed on TNOs and centaurs have very likely been produced by irradiation of simpler molecules (Brunetto et al., 2006c), it is reasonable to ask if weathered silicates are present also in the outer Solar System.

Many authors have already applied the Hapke's space weathering model to interpret the spectra of minor and airless bodies in the Solar System (see e.g. Hiroi et al. (2006), and references therein). In space weathering studies, a high number of efforts have been focusing on the connection between Main-Belt and Near-Earth asteroids and meteorites (see e.g. Chapman (1996), and Clark et al. (2002)). The weathering process has been shown to be highly efficient.

Here, I want to investigate if the darkening and reddening spectral effect of altered silicates can be observed also on outer Solar System objects, where silicates are probably mixed with icy species (H_2O, N_2, CH_4, CH_3OH, etc.) and complex organics. Resurfacing processes may bring pristine silicate grains close to the sur-

Spatial mixture:	Carbon black	Intimate mixture	RMS	Pearson coefficient
Original fit	61.5%	38.5%	0.0102	0.991
New fit	63%	37%	0.0097	0.992

Table 7.2: Relative abundances of carbon black and the intimate mixture given in Table 7.3, used to fit the reflectance spectrum of Pholus, by Cruikshank et al. (1998) (original fit) and in the present work (new fit). The RMS and the Pearson correlation coefficient are very similar in the two cases, but slightly better in the new fit.

face; there, they would suffer the exposure to solar wind ions and micrometeorite bombardment.

Let us take the case of centaur 5145 Pholus: Cruikshank et al. (1998) found a good fit of the spectrum using two spatially segregated components: dark amorphous carbon and an intimate mixture of water ice, methanol ice, olivine grains, and complex organic compounds (tholins). The carbon black component was used in the fit to match the low albedo of the object. The presence of tholins is probably due to processing of simple ices containing carbon, since it has been shown that weathering processes can produce an organic and refractory crust on many centaurs and TNOs Brunetto et al. (2006c). In fact, the surface of Pholus is probably a mix of altered and pristine materials; thus, it is reasonable to ask if its spectrum is compatible with the presence of a weathered olivine component.

Following the approach of Cruikshank et al. (1998), I apply the Hapke scattering model.

The upper panel of Fig. 7.9 shows the result of a fit of Pholus' spectrum, using the same materials as Cruikshank et al. (1998).

Relative abundance in the spatially segregated mixture are given in Table 7.2, while relative abundance and grain size of the four components (water ice, methanol ice, olivine, and tholins) in the intimate mixture are reported in Table 7.3.

The central panel of Fig. 7.9 plots results of a new fit, substituting the pristine olivine component with a weathered olivine component. A rigorous model would require a rather long calculation, putting metallic iron inclusions in a complex matrix made of water and methanol ices, and pristine olivine grains; a much simpler

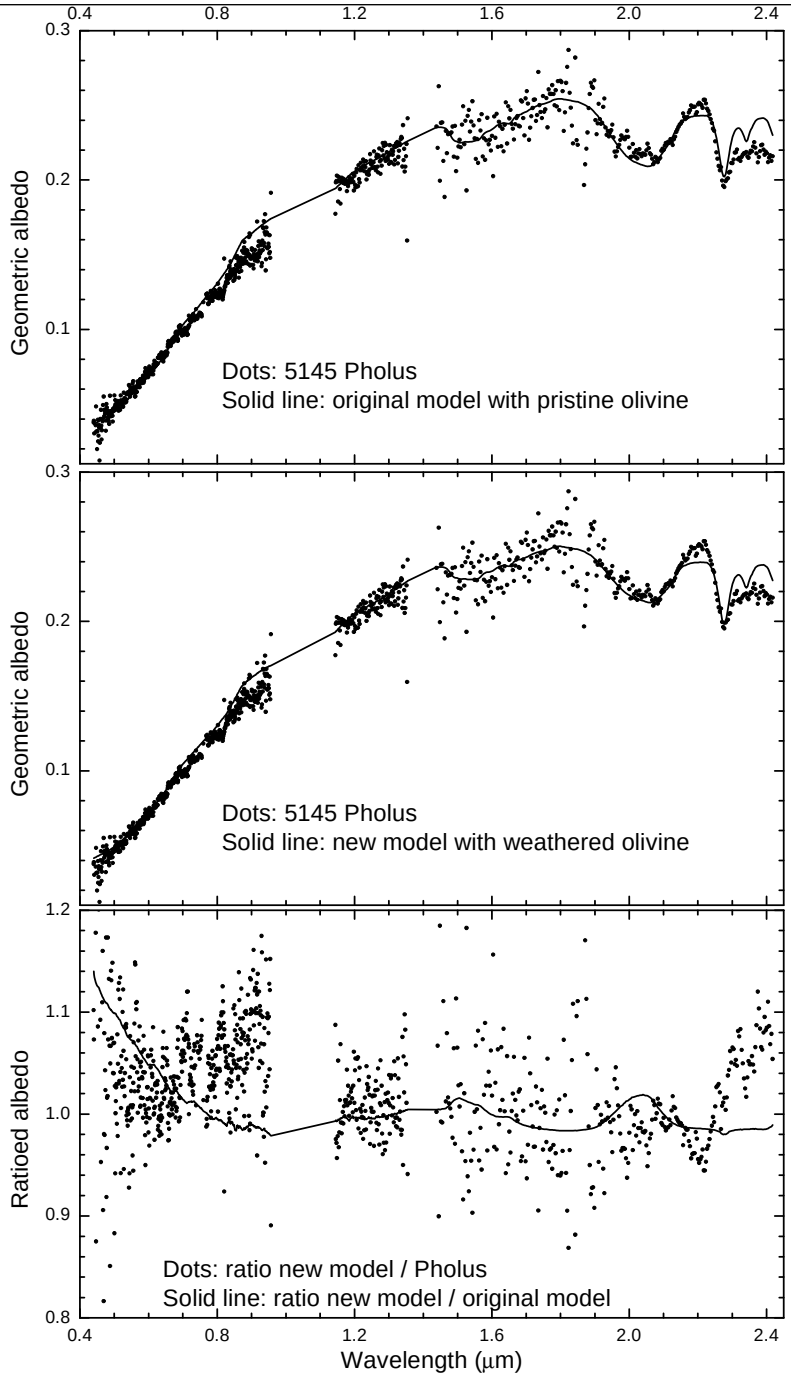

Figure 7.9: Upper panel: the spectrum of Pholus (dots) fitted by a spatial mixture of carbon black and an intimate mixture of water ice, methanol ice, tholins, and pristine olivine, using the Hapke scattering model (solid line), after Cruikshank et al. (1998). Central panel: a new fit (solid line) performed using weathered olivine instead of pristine olivine. Abundances and grain sizes are given in Table 7.2. Lower panel: the ratio between the new model and the spectrum of Pholus (dots), and the ratio between the new model and the original model (solid line) are plotted.

Intimate mixture:	Water ice	Methanol ice	Tholins	Pristine olivine	Weathered olivine
Original fit	15%	15%	15%	55%	0%
	10 μm	10 μm	1 μm	20 μm	-
New fit	13%	15%	13%	0%	59%
	23 μm	7 μm	1 μm	-	7 μm

Table 7.3: Abundance and grain size for the intimate mixtures of water ice, methanol ice, olivine grains, and complex organic compounds (tholins), used to fit the reflectance spectrum of Pholus (see Table 7.2), by Cruikshank et al. (1998) (original fit) and the present work (new fit).

calculation can be performed using the effective optical constants as derived from ablated olivine spectra inverting the Hapke's scattering model (see previous sections). Again, abundances and grain sizes of the various components are given in Table 7.2 and Table 7.3.

The two fit curves (using pristine and weathered olivine) are nearly identical. The Pearson correlation coefficient was 0.991 for the original fit, and it slightly increases to 0.992 for the new fit. To make the comparison clearer, the lower panel of Fig. 7.9 includes the ratio between the new model and the spectrum of Pholus, and the ratio between the new model and the original model; as it is indicated in Table 7.3, the new fit uses slightly lower amount of water ice and tholins, and higher amount of silicates. Discrepancies between the two models are well within the spectral noise of Pholus, except for a noticeable discrepancy already noted by Cruikshank et al. (1998) between the model and the observation that is present in the region 2.3-2.4 μm. Weathered olivine cannot help to improve the fit in that spectral region, while a better fit could be probably achieved using weathered instead of pristine methanol Brunetto et al. (2005a).

It must be remarked that the red color of Pholus is mainly determined by organics and only marginally by weathered silicates. In particular, in the intimate mixture used in the central panel of Fig. 7.9, a ratio (tholins / weathered olivine) of about 1/5 is already enough to let the tholin component determine the visible slope. In fact, I attempted to fit Pholus' spectrum using the same materials, including the weathered olivine, but eliminating the tholins component. The results are unrealistic as they produce negative values for grain size and relative abundances. I also produced a

synthetic spectrum of the new fit shown in the central panel of Fig. 7.9, by removing tholins and rescaling the abundance of the other components. No result can match the slope in the visible and very near-infrared region of the Pholus spectrum. Other silicate components, such as pyroxenes, cannot help improving the fit quality. It must be concluded that a tholin-like component is necessary to reproduce the red slope of Pholus.

The amount of olivine used in the model increases when using the weathered component, and the amount of tholins required decreases. However the presence of weathered olivine is not significantly improving the quality of the fit, so it cannot be ruled out if such a component is really present on the surface. In any case, this result is an indication that optical characterization of weathered silicates may help in interpreting the surface spectra also of bodies in the outer Solar System.

In conclusion, using the effective optical constants of weathered silicates to fit the spectrum of centaur 5145 Pholus indicates that its surface spectrum does not exclude the presence of weathered olivine, but such component cannot be clearly detected when mixed with complex organics.

7.2.2 Asteroid 1951 Lick: space weathering to the highest level

Asteroid (1951) Lick is a Near-Earth object that orbits in the limit that separates Amor objects from Mars Crossers[1]. It has been classified as an A-type asteroid by Bus and Binzel (2002b). A-type asteroids, usually found in the main asteroid belt between Mars and Jupiter, have spectra that are very similar to spectra of olivine (Cruikshank and Hartmann, 1984).

Lick has a very red spectrum (de León et al., 2004), and it is probably one of the most weathered Near-Earth asteroids. Thus, it is interesting to apply the space weathering models that I have described in the previous sections to Lick's spectrum. This can be a test for space weathering to its highest levels, and to investigate the

[1]The Amor asteroids are a group of near-Earth asteroids named after the asteroid 1221 Amor. They approach the orbit of the Earth from beyond, but do not cross it. A Mars-crosser asteroid is an asteroid whose orbit crosses that of Mars.

saturation regime.

If the models are correct, we should be able to reproduce the spectrum in terms of space weathering parameters, such as the abundance of nanophase iron particles.

In the experiments described in this thesis, the highest spectral slope produced was the one after laser ablation of San Carlos olivine. In Fig. 7.10 I plot a qualitative comparison of San Carlos olivine before and after laser ablation, with Lick's spectrum obtained by de León et al. (2004).

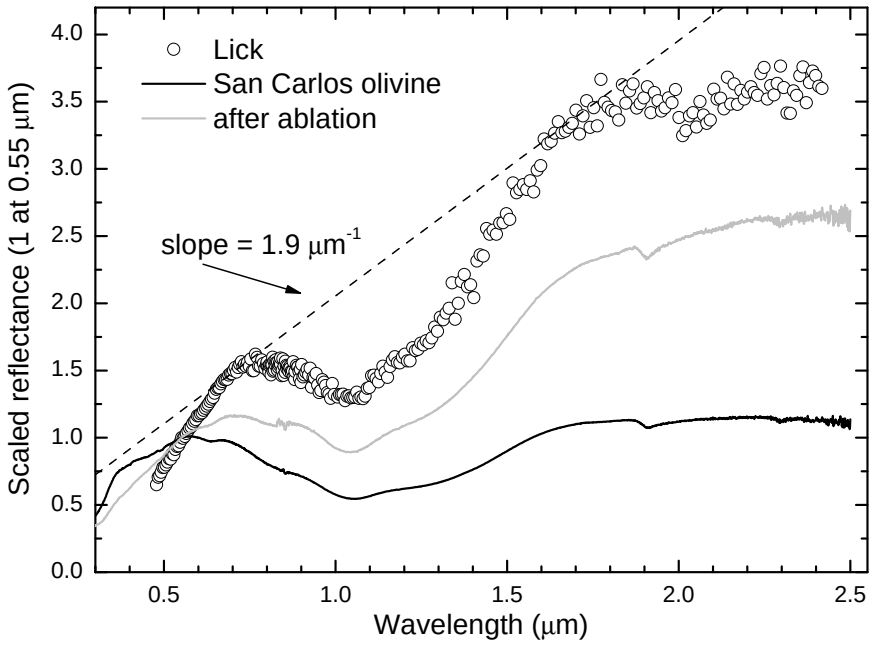

Figure 7.10: The spectrum of Lick (circles) compared with the spectra of San Carlos olivine, before and after UV laser ablation. Spectra are scaled at 0.55 μm. The dashed line represents the spectral slope.

Lick is distinctly redder than the ablated sample of olivine. The slope above the 1 μm band is about 1.9 μm^{-1}. This high value of spectral slope puts Lick among the reddest Near-Earth asteroids (see Fig. 5.4), so it is a good test to check if the laboratory experiments can simulate space weathering at such a high level.

Since the highest slope variations are in the visible, it is more convenient to scale the spectra at 1.04 μm, i.e. close to the olivine band center. This is shown in

Fig. 7.11. In this way one can force any model to reproduce the depth of the band, and eventually understand what is causing the spectral mismatch in the continuum.

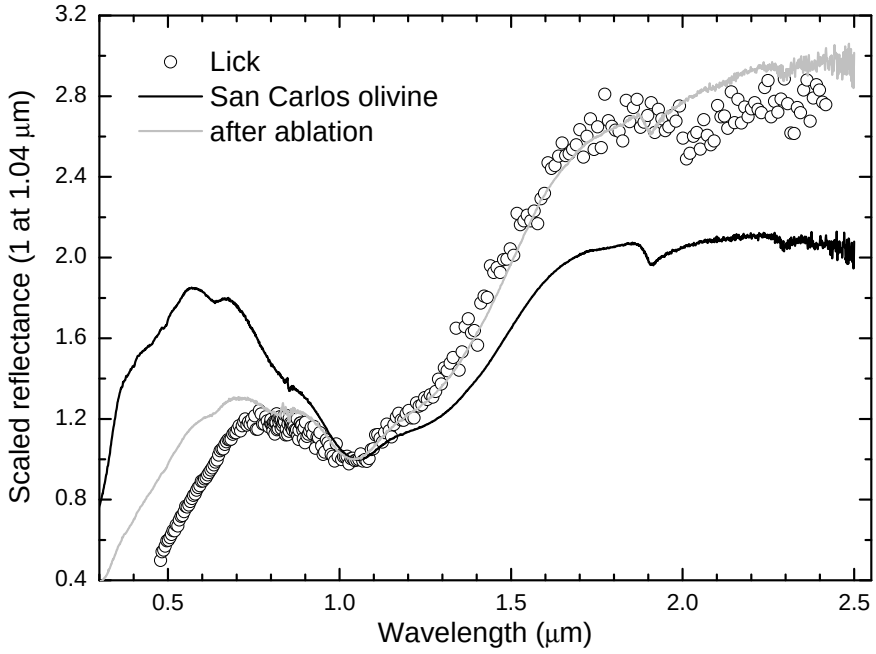

Figure 7.11: Same as Fig. 7.10, but with spectra scaled at 1.04 μm.

Thus, from Fig. 7.11 it is clear that the spectrum of weathered olivine can reproduce the Lick spectrum only for wavelength greater than about 0.8 μm. In fact, there is a large discrepancy in the visible.

To make the comparison between Lick spectrum and laboratory data more quantitative, one can use the Hapke scattering model, as described in the previous sections. In Fig. 7.12 it is shown a result from a scattering model, using only pure and ablated olivine (optical constants estimated above, Brunetto et al. (2007)). Also in this case, the model can fit the 0.8-2.5 μm range, but it cannot reproduce the visible range.

It is interesting to note that the model restricted to the NIR gives a dominant percentage of weathered olivine with respect to the pristine one. This, again, tells us that Lick is very weathered, but also that the NIR range can give interesting

indications about weathering.

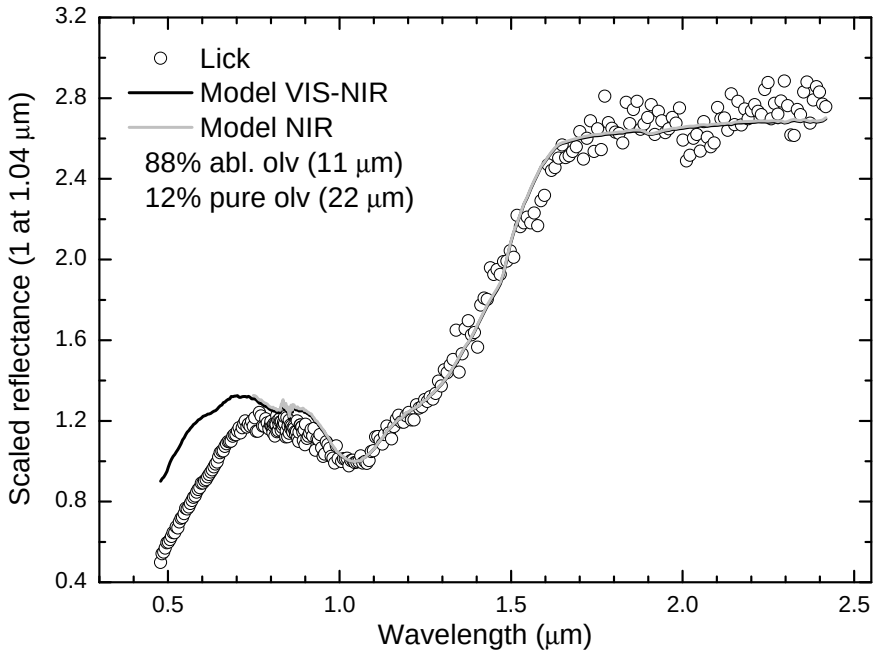

Figure 7.12: Fit of Lick spectrum using optical constants of pristine and ablated olivine estimated in this thesis. We consider intimate mixtures, using the Hapke scattering model. The gray line represents the best fit considering only the NIR range. Abundances and grain size for the mixture are similar for both models.

Discrepancies in the visible range could be caused by two different factors: (1) a space weathering effect; (2) a compositional effect.

I first consider the space weathering effect; this means that the optical constants of ablated olivine are not adequate, because they do not represent the saturation regime. If this is the case, then one might be able to reproduce the visible spectrum of Lick using the Hapke space weathering model (small metallic iron inclusions in a silicate matrix) described in the previous sections, to check a level of space weathering higher than the experimental one.

Using Eq. 7.4 one can apply this model to an asteroid, starting from the spectrum of a compound that is similar to the asteroid's one. Applying the metallic iron model, and using San Carlos olivine as starting composition, yields to the results shown in Fig. 7.13.

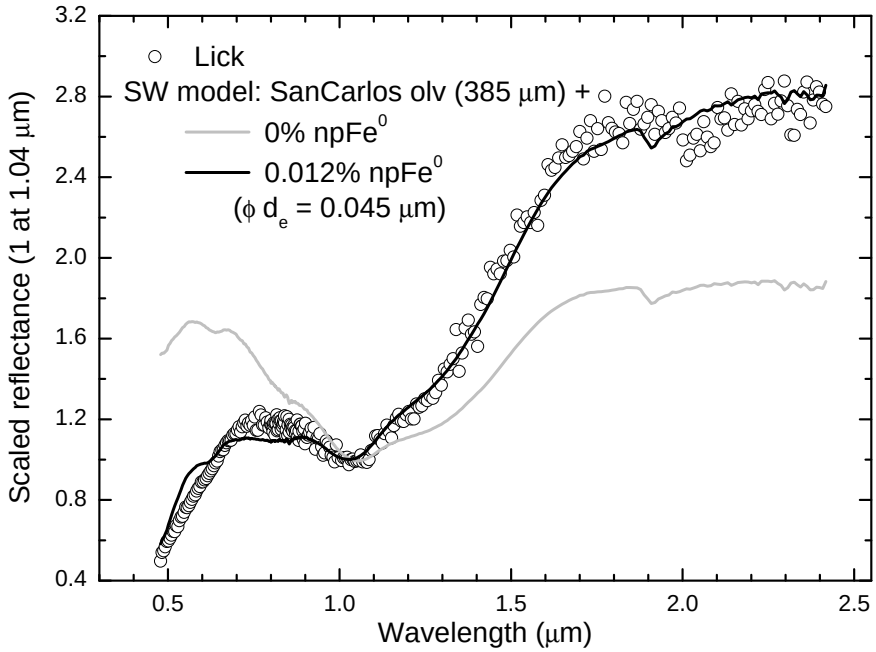

Figure 7.13: Fit of Lick spectrum using Hapke space weathering model (small metallic iron inclusions) and San Carlos olivine as starting composition. The volume fraction of nanophase iron is also given.

The fit (black curve) is improving, but some discrepancies are still present. Note, however, that the ϕd_e product is close to what what found in the UV laser ablation experiments, i.e. about 0.045 μm (note that ϕd_e gives a measure of how red is the spectrum). Thus, the improvement probably comes from the peculiar combination of grain size and volume fraction of metallic iron inclusions.

Since discrepancies between observed and fit curves are only partially explained by a space weathering effect, we need to explore the possibility of a compositional effect. Spectral mismatch could be explained by the presence of other components, such as clinopyroxene. However, putting clinopyroxene in the scattering models does not help improving the fit. The same thing holds for orthopyroxene.

The mineralogy of Lick has been shown to be pretty close to the one of the Brachina meteorite (de León et al., 2004). This meteorite, that gives the name to the Brachinites group, is very rich in olivine (about 80%) but it also includes plagioclase,

clinopyroxene, chromite, Fe-sulfide, etc. (Mittlefehldt et al., 2003). Thus, if Lick's composition is similar to Brachina's, to get a good fit of the spectrum one should use all the main components, not only olivine. Unfortunately, optical constants for all those materials are difficult to be found, and often uncertain.

A solution may come from the use of Brachina's spectrum itself. From two RELAB spectra at different grain size, I estimated the absorption coefficient (as discussed above), and then put it in the model (Eq. 7.4), obtaining an effective grain size d_e for the asteroid (mean optical path-length) and the volume fraction ϕ of nanophase iron. The result is shown in Fig. 7.14.

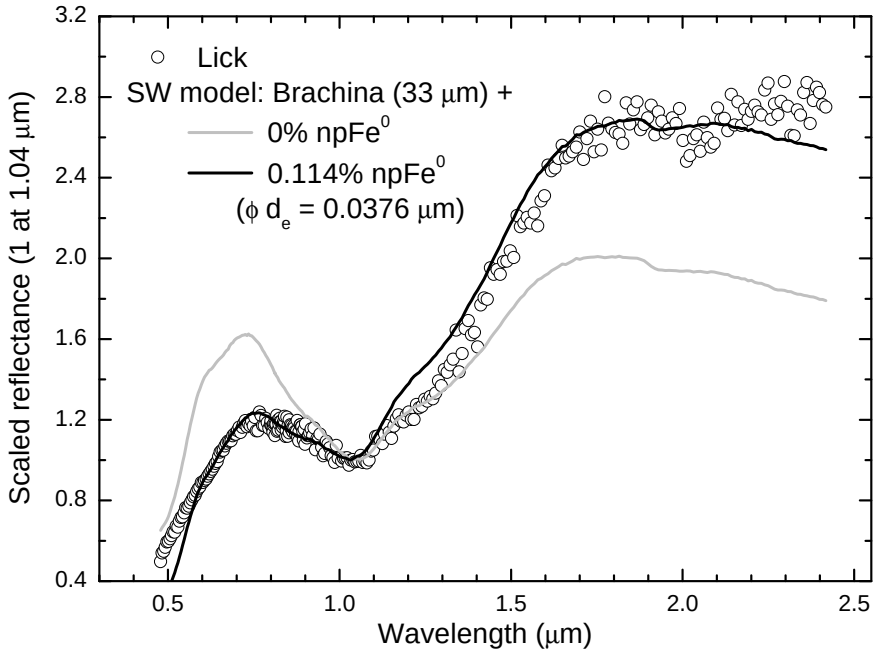

Figure 7.14: Fit of Lick spectrum using Hapke space weathering model (small metallic iron inclusions) and Brachina meteorite as starting composition. The volume fraction of nanophase iron is also given.

Although a mismatch is still present at around 0.5, 1.2, and 2.4 μm, the fit curve has an interesting trend, in particular in the visible range. The value $\phi d_e = 0.0376\mu$m is close to the experimental saturation value, and again this tells us that Lick is probably an object with a saturated space weathering effect. Discrepancies

are present because probably the mineralogy of Brachina is not exactly the same of Lick.

From Fig. 7.13 and Fig. 7.14 it seems that San Carlos olivine can help in the spectral regions where the Brachina fit has discrepancies. Thus, performing a linear combination of the reflectance spectra shown in Fig. 7.13 and Fig. 7.14, we obtain the spectrum plotted in Fig. 7.15.

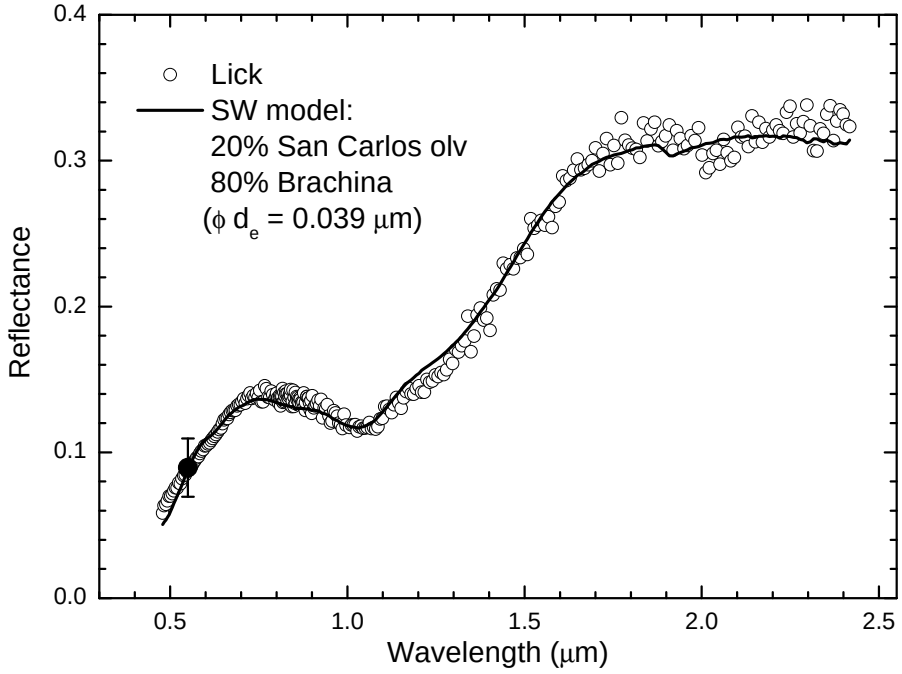

Figure 7.15: Best fit of Lick spectrum obtained by a linear combination of the spectra plotted in Fig. 7.13 and Fig. 7.14. The final ϕd_e product is about 0.039 μm. The IRAS albedo of this body is used to obtain a scale of absolute reflectance (Tedesco et al., 2004).

Note that in this case the spectra are not scaled. Thus, a combination of 20% of San Carlos olivine and 80% of Brachina, with a nanophase iron model that produces $\phi d_e = 0.039\mu$m (saturation regime), is able to well reproduce the spectrum and the albedo of Lick.

The surface composition of Lick is probably close to Brachina's, but with some more Mg-rich olivine. In fact, San Carlos olivine has an Mg number of about 0.9, which is closer to the value that de León et al. (2004) found with the Modified Gaussian Model for Lick (Brachina has Mg number of about 0.66). This is probably

the reason why using a combination of San Carlos olivine and Brachina gives a good fit. Thus, the mismatch shown in the previous figures was due to a compositional effect.

The nanophase iron model for Lick produces $\phi d_e = 0.039\mu$m, similar to what Brunetto et al. (2007) found for laser ablated olivine. It is interesting to note that, on the contrary, the product ϕd_e obtained for ortho- and clinopyroxene by Brunetto et al. (2007) was about 0.02 μm. This is actually nearly identical to what Hiroi et al. (2006) found for the dark and red areas on asteroid Itokawa, whose composition is much more pyroxene-rich than Lick. This indicates that the laboratory experiments are a good simulation of the asteroidal space weathering, at any regime.

An additional confirmation of the saturation regime comes from the comparison with the results of Brunetto et al. (2006b); in the previous chapter it was shown that computing the ratio between spectra of weathered and unweathered materials, the contribution of silicate bands almost disappears, and a continuum curve is left, that is related to the exposure to space weathering. This continuum is parameterized by a C_S coefficient, related to the exposure time. Since we estimated the composition of Lick, from the results shown in Fig. 7.15 one can derive a value of $C_S \sim -0.7\mu$m for Lick. From the results of Brunetto et al. (2006b), this value is close to the saturation regime. As a comparison, the recently rejuvenated asteroid 832 Karin has a value of $C_S \sim -0.2\mu$m (as discussed above).

The surface of Lick is extremely weathered; this may give information about surface age and history, in particular about the lack of resurfacing events. Further investigation is required in terms of collisional evolution and impact events.

In conclusion, the value $\phi d_e = 0.039\mu$m found in the best fit of Lick indicates that the weathering process active on silicate-rich asteroids is properly simulated by experiments described in this thesis, and that the presence of a saturation regime (observed in the laboratory) is the correct interpretation for an asteroid surface probably older than about 10^7-10^8 years (as discussed in the previous chapters about space weathering timescales).

Acknowledgments

J. de León, J. Licandro, and T. Roush are warmly acknowledged for help and suggestions. This research was supported by Istituto Nazionale di Astrofisica (INAF) and by Isaac Newton Group of Telescopes (ING).

Conclusions

In this PhD Thesis, I focused on the space weathering processes on Solar System minor bodies, using mainly laboratory results, and applying them to observations through spectral models.

To simulate space weathering, I have used nano-pulsed UV laser irradiation and ablation to simulate micro-meteorite impacts, and ion irradiation to simulate cosmic ion irradiation, in the Lecce and Catania Laboratories. Weathered silicates, ices, and carbons, have been studied mainly using transmission and reflection spectroscopy in the UV-Vis-IR range.

The main experimental results are:

1. laser and ion processing of a large number of silicate-rich samples (terrestrial and meteoritic) induce a substantial decrease of the spectral reflectance (darkening), mainly in the UV-Vis range (reddening); this process is highly efficient, and is probably caused by the formation of nanophase metallic iron inclusions in the surface grains;

2. ion irradiation of carbon-rich ices (such as CH_3OH, CH_4, C_6H_6) causes a strong variation of the chemical composition, with a preferential loss of H and O that drives the carbonization of the samples; this induces spectral reddening and darkening, related to the destruction of the original molecules and consequent production of a stable carbonaceous residue, even when these ices are mixed with H_2O;

3. optical constants of some of these processed materials have been estimated; they have been and will be used in the spectral models.

From the comparison between laboratory data and observations of minor bodies, the following results have been obtained:

4. the spectral reddening of silicates is able to reproduce the observed spectral slopes for Near-Earth and Main Belt asteroids; consequently, it is possible to explain the spectral mismatch between the most abundant meteorites (ordinary chondrites) and their presumed parent bodies (S-type asteroids);

5. the astrophysical timescales (between the Earth orbit and the Main Belt) for the reddening of S-type asteroids has been estimated to be about 10^5-10^6 years; this also suggests a relatively high efficiency for the rejuvenating processes (e.g. impacts) that oppose to the spectral reddening;

6. the spectra of residues (produced after irradiation of ices) explain the spectral variety of minor bodies in the outer Solar System (centaurs, Kuiper Belt or Trans-Neptunian objects, comets) and indicate the presence of a surface mantle composed of organic refractory materials in the majority of these bodies;

In addition, for some peculiar bodies I have performed a more detailed analysis (thanks to several collaborations), with the following results:

7. I have developed a space weathering model that, using the optical constants of silicates, allows to estimate the surface composition of asteroids and their weathering level; application of this model to asteroid 832 Karin showed that the irradiation timescales that we estimate for this body are in agreement with the age of the impact that rejuvenated the surface about 5.8×10^6 years ago.

8. I have applied the space weathering models to two peculiar objects, i.e. asteroid 1951 Lick and centaur 5145 Pholus, showing that the experimental results correctly simulate the reddening of silicates, even in a saturation regime or when silicates are mixed with ices and organic materials.

Finally, it must be stressed that this thesis provides useful laboratory and theoretical tools as a support for new observations collected with modern telescopes and space missions, that help us to understand the origin and evolution of the Solar System.

Bibliography

Acuña, M.H., and 19 colleagues, 1998. Magnetic Field and Plasma Observations at Mars: Initial Results of the Mars Global Surveyor Mission. Science 279, 1676-1680.

Adams, J.B., and McCord, T.B., 1971. Alteration of Lunar Optical Properties: Age and Composition Effects. Science 171, 567-571.

Adams, J.B., 1975. Interpretation of visible and near-infrared diffuse reflectance spectra of pyroxenes and other rock-forming minerals. In: Karr, C. (Ed.), Infrared and Raman Spectroscopy of Lunar and Terrestrial Minerals. Academic Press, San Diego, pp. 91-116.

Aharonson, O., Zuber, M.T., Solomon, S.C., 2004. Crustal remanence in an internally magnetized non-uniform shell: a possible source for Mercury's magnetic field?. Earth and Planetary Science Letters 218, 261-268.

Andronico, G., Baratta, G.A., Spinella, F., Strazzulla, G., 1987. Optical evolution of laboratory-produced organics: applications to Phoebe, Iapetus and outer belt asteroids. Astron. Astrophys. 184, 333-336.

Baratta, G.A., Leto, G., Palumbo, M.E., 2002. A comparison of ion irradiation and UV photolysis of CH_4 and CH_3OH. Astron. Astrophys. 384, 343-349.

Baratta, G.A., Mennella, V., Brucato, J.R., Colangeli, L., Leto, G., Palumbo, M.E., Strazzulla, G., 2004. Raman spectroscopy of ion-irradiated interplanetary carbon dust analogues. J. Raman Spectrosc. 35, 487-496.

Barucci, M.A., Fulchignoni, M., Birlan, M., Doressoundiram, A., Romon, J., Boehnhardt, H., 2001. Analysis of trans-neptunian and Centaur colours: continuous trend or grouping? Astron. Astrophys. 371, 1150-1154.

Barucci, M.A., and 19 colleagues, 2002. Visible and near-infrared spectroscopy of the Centaur 32532 (2001 PT_{13}). ESO Large Program on TNOs and Centaurs: First spectroscopy results. Astron. Astrophys. 392, 335-339.

Barucci, M.A., Cruikshank, D.P., Dotto, E., Merlin, F., Poulet, F., Dalle Ore, C., Fornasier, S., de Bergh, C., 2005. Is Sedna another Triton? Astron. Astrophys. 439, L1-L4.

Barucci, M. A., and Peixinho, N., 2005. TransNeptunian objects' surface properties. In Proc. IAU Symp. 229, Asteroids, Comets, Meteors, ed. D. Lazzaro, S. Ferraz-Mello, & J. A. Fernandez (Cambridge: Cambridge Univ. Press), 171-190.

Bauer, J.M., Roush, T.L. T.R. Geballe, T.C. Owen, K.J. Meech, W.D. Vacca, and J.T. Rayner, 2002. The near infrared spectrum of Miranda: Evidence for crystalline water ice. Icarus 158, 178-190.

Bauerle, D., 2000. Laser Processing and Chemistry. Third ed. Springer-Verlag, Berlin.

Bell, J.F., Hawke, B.R., Owensby, P.D., Gaffey, M.J., 1985. The 52-Color Asteroid Survey: Results and Interpretation. Bulletin of the American Astronomical Society 17, 729.

Bentley, M.S., 2005. Space weathering on Mercury: Laboratory studies and modelling. Ph.D. Thesis.

Bentley, M.S., Ball, A.J., Dyar, M.D., Pieters, C.M., Wright, I.P., Zarnecki, J.C., 2005. Space Weathering: Laboratory Analyses and In-Situ Instrumentation. 36th Annual Lunar and Planetary Science Conference 36, 2255.

Binzel, R.P., Bus, S.J., Burbine, T.H., Sunshine, J.M., 1996. Spectral properties of near Earth asteroids: evidence for sources of ordinary chondrite meteorites. Science 273, 946-948.

Binzel, R.P., Birlan, M., Bus, S.J., Harris, A.W., Rivkin, A.S., Fornasier, S., 2004. Spectral observations for near-Earth objects including potential target 4660 Nereus: Results from Meudon remote observations at the NASA Infrared Telescope Facility (IRTF). Planet. Space Sci. 52, 291-296.

Binzel, R.P., Rivkin, A.S., Stuart, J.S., Harris, A.W., Bus, S.J., Burbine, T.H., 2004. Observed spectral properties of near-Earth objects: results for population distribution, source regions, and space weathering processes. Icarus 170, 259-294.

Boehnhardt, H., and 21 colleagues, 2003. Results from the Eso Large Program on Transneptunian Objects and Centaurs. Earth Moon and Planets 92, 145-156.

Bohn, R.B., Sandford, S.A., Allamandola, L.J., Cruikshank, D.P., 1994. Infrared spectroscopy of Triton and Pluto ice analogs: the case for saturated hydrocarbons. Icarus 111, 151-173.

Boogert, A.C.A., Schutte, W.A., Tielens, A.G.G.M., Whittet, D.C.B., Helmich, F.P., Ehrenfreund, P., Wesselius, P.R., de Graauw, T., Prusti, T., 1996. Solid methane toward deeply embedded protostars. Astron. Astrophys. 315, L377-L380.

Boogert, A.C.A., Helmich, F.P., Schutte, W.A., Tielens, A.G.G.M., Wooden, D.H., 1997. Infrared observations and laboratory simulations of interstellar CH_4 and SO_2. Astron. Astrophys. 317, 929-941.

Bottke, W.F., Durda, D.D., Nesvorný, D., Jedicke, R., Morbidelli, A., Vokrouhlický, D., Levison, H., 2005. The fossilized size distribution of the main asteroid belt. Icarus 175, 111-140.

Bottke, W.F., Nesvorný, D., Grimm, R.E., Morbidelli, A., O'Brien, D.P., 2006. Iron meteorites as remnants of planetesimals formed in the terrestrial planet region. Nature 439, 821-824.

Brucato, J.R., Palumbo, M.E., Strazzulla, G., 1997. Carbonic Acid by Ion Implantation in Water/Carbon Dioxide Ice Mixtures. Icarus 125, 135-144.

Brucato, J.R., Strazzulla, G., Baratta, G., Colangeli, L., 2004. Forsterite amorphization by ion irradiation: Monitoring by infrared spectroscopy. Astron. Astrophys. 413, 395-401.

Brunetto, R., Baratta, G.A., Strazzulla, G., 2004. Raman spectroscopy of ion irradiated diamond. J. Appl. Phys. 96, 380-386.

Brunetto, R., Baratta, G.A., Domingo, M., Strazzulla, G., 2005a. Reflectance and transmittance spectra (2.2-2.4 μm) of ion irradiated frozen methanol. Icarus 175, 226-232.

Brunetto, R., Baratta, G.A., Strazzulla, G., 2005b. Amorphization of diamond by ion irradiation: A Raman study. J. Phys. Conf. Ser. 6, 120-125.

Brunetto, R., and Strazzulla, G., 2005. Elastic collisions in ion irradiation experiments: a mechanism for space weathering of silicates. Icarus 179, 265-273.

Brunetto, R., Romano, F., Blanco, A., Fonti, S., Martino, M., Orofino, V., Verrienti, C., 2006a. Space weathering of silicates simulated by nanosecond pulse UV excimer laser. Icarus 180, 546-554.

Brunetto, R., Vernazza, P., Marchi, S., Birlan, M., Fulchignoni, M., Orofino, V., Strazzulla, G., 2006b. Modeling asteroid surfaces from observations and irradiation experiments: The case of 832 Karin. Icarus 184, 327-337.

Brunetto, R., Barucci, M.A., Dotto, E., Strazzulla, G., 2006c. Ion Irradiation of Frozen Methanol, Methane, and Benzene: Linking to the Colors of Centaurs and Trans-Neptunian Objects. Astrophys. J. 644, 646-650.

Brunetto, R., Roush, T.L., Marra, A.C., Orofino, V., 2007. Optical characterization of laser ablated silicates. Icarus, submitted.

Burbine, T. H., 2000. Forging Asteroid-Meteorite Relationships Through Reflectance Spectroscopy. Ph.D. Thesis, Massachusetts Institute of Technology.

Burbine, T.H., Buchanan, P.C., Binzel, R.P., Bus, S.J., Hiroi, T., Hinrichs, J.L., Meibom, A., McCoy, T.J., 2001. Vesta, Vestoids, and the howardite, eucrite, diogenite group: Relationships and the origin of spectral differences. Meteor. Planet. Sci. 36, 761-781.

Burbine, T.H., McCoy, T.J., Meibom, A., Gladman, B., Keil, K., 2002. Meteoritic Parent Bodies: Their Number and Identification. In Asteroids III, ed. W. F. Bottke Jr. et al. (Tucson: Univ. Arizona Press), 653-667.

Burns, R.G., 1993. Mineralogical Applications of Crystal Field Theory, 2nd edition. Cambridge Univ. Press, Cambridge.

Bus, S.J., 1999. Compositional Structure in the Asteroid Belt: Results of a Spectroscopic Survey. Ph.D. Thesis, Massachusetts Institute of Technology.

Bus, S.J., and Binzel, R.P., 2002a. Phase II of the Small Main-Belt Asteroid Spectroscopic Survey The Observations. Icarus 158, 106-145.

Bus, S.J., and Binzel, R.P., 2002b. Phase II of the Small Main-Belt Asteroid Spectroscopic Survey A Feature-Based Taxonomy. Icarus 158, 146-177.

Carruba, V., Michtchenko, T.A., Roig, F., Ferraz-Mello, S., Nesvorný, D., 2005. On the V-type asteroids outside the Vesta family. I. Interplay of nonlinear secular resonances and the Yarkovsky effect: the cases of 956 Elisa and 809 Lundia. Astron. Astrophys. 441, 819-829.

Cassidy, W., Hapke, B., 1975. Effects of darkening processes on surfaces of airless bodies. Icarus 25, 371-383.

Chapman, C.R., 1996. S-type asteroids, ordinary chondrites, and space weathering: The evidence from Galileo's fly-by of Gaspra and Ida. Meteorit. Planet. Sci. 31, 699-725.

Chapman, C.R., 2004. Space Weathering of Asteroid Surfaces. Annual Review of Earth and Planetary Sciences 32, 539-567.

Chrisey, D.B., and Hubler, C.K. (Eds.), 1994. Pulsed Laser Deposition of Thin Films. Wiley, New York.

Cisowski, S.M., 1991. Remanent magnetic properties of unbrecciated eucrites. Earth and Planetary Science Letters 107, 173-181.

Clark, B.E., and 11 colleagues, 2001. Space weathering on Eros: Constraints from albedo and spectral measurements of Psyche crater. Meteorit. Planet. Sci. 36, 1617-1637.

Clark, B.E., Hapke, B., Pieters, C., Britt, D., 2002. Asteroid space weathering and regolith evolution. Asteroids III, W. F. Bottke Jr., A. Cellino, P. Paolicchi, and R. P. Binzel (eds), University of Arizona Press, Tucson, 585-599.

Clark, B.E., Bus, S.J., Rivkin, A.S., Shepard, M.K., Shah, S., 2004. Spectroscopy of X-Type Asteroids. Astron. J. 128, 3070-3081.

Clark, R.N., and Roush, T. L. 1984. Reflectance spectroscopy: Quantitative analysis techniques for remote sensing applications, J. Geophys. Res. 89, 6329-6340.

Clark, R.N., Swayze, G.A., Wise, R., Livo, K.E., Hoefen, T.M., Kokaly, R.F., Sutley, S.J., 2003. USGS Digital Spectral Library splib05a. USGS Open File Report, 03-395.

Collinson, D.W., and Morden, S.J., 1994. Magnetic properties of howardite, eucrite and diogenite (HED) meteorites: Ancient magnetizing fields and meteorite evolution. Earth and Planetary Science Letters 126, 421-434.

Conel, J.E., and Nash, D.B., 1970. Spectral reflectance and albedo of Apollo 11 lunar samples: Effects of irradiation and vitrification and comparison with telescopic observations. Geochimica et Cosmochimica Acta Supplement 1, 2013.

Coustenis, A., Schmitt, B., Khanna, R.K., Trotta, F., 1999. Plausible condensates in Titan's stratosphere from Voyager infrared spectra. Planet. Space Sci. 47, 1305-1329.

Cruikshank, D.P., and Hartmann, W.K., 1984. The meteorite-asteroid connection - Two olivine-rich asteroids. Science 223, 281-283.

Cruikshank, D.P., Roush, T.L., Owen, T.C., Geballe, T.R., de Berg, C., Schmitt, B., Brown, R.H., Bartholomew, M.J., 1993. Ices on the surface of Triton. Science 261, 742-745.

Cruikshank, D.P., Roush, T.L., Moore, J.M., Sykes, M.V., Owen, T.C., Bartholomew, M.J., Brown, R.H., and Tryka, K.A., 1997. The Surfaces of Pluto and Charon, in Pluto and Charon, S.A. Stern, and D.J. Tholen (Eds.), Univ. Arizona Press, Tucson, AZ, 221-267.

Cruikshank, D.P., and 14 colleagues, 1998. The Composition of Centaur 5145 Pholus. Icarus 135, 389-407.

Cruikshank, D.P., Roush, T.L., Poulet, F., 2003. Quantitative modeling of the spectral reflectance of Kuiper belt objects and Centaurs. C. R. Phys. 4, 783-789.

Cruikshank, D.P., Owen, T.C., Ore, C.D., Geballe, T.R., Roush, T.L., de Bergh, C., Sandford, S.A., Poulet, F., Benedix, G.K., Emery, J.P., 2005. A spectroscopic study of the surfaces of Saturn's large satellites: H_2O ice, tholins, and minor constituents. Icarus 175, 268-283.

Dartois, E., Schutte, W.A., Geballe, T.R., Demyk, K., Ehrenfreund, P., D'Hendecourt, L., 1999. Methanol: the second most abundant ice species towards the high mass protostars RAFGL7009S and W 33A. Astron. Astrophys. 342, L32-L35.

de Bergh, C., Delsanti, A., Tozzi, G.P., Dotto, E., Doressoundiram, A., Barucci, M.A., 2005. The surface of the transneptunian object 90482 Orcus. Astron. Astrophys. 437, 1115-1120.

de León, J., Duffard, R., Licandro, J., Lazzaro, D., 2004. Mineralogical characterization of A-type asteroid (1951) Lick. Astron. Astrophys. 422, L59-L62.

Demyk, K., Carrez, Ph., Leroux, H., Cordier, P., Jones, A.P., Borg, J., Quirico, E., Raynal, P.I., d'Hendecourt, L., 2001. Structural and chemical alteration of crystalline olivine under low energy He^+ irradiation. Astron. Astrophys. 368, L38-L41.

Doressoundiram, A., Barucci, M.A., Fulchignoni, M., Florczak, M., 1998. EOS family: a spectroscopic study. Icarus 131, 15-31.

Doressoundiram, A., Peixinho, N., de Bergh, C., Fornasier, S., Thbault, P., Barucci, M.A., Veillet, C., 2002. The color distribution in the Edgeworth-Kuiper Belt. Astron. J. 124, 2279-2296.

Dorschner, J., Begemann, B., Henning, T., Jaeger, C., Mutschke, H., 1995. Steps toward interstellar silicate mineralogy. II. Study of Mg-Fe-silicate glasses of variable composition. Astron. Astrophys. 300, 503.

Douté, S., Schmitt, B., Quirico, E., Owen, T.C., Cruikshank, D.P., de Berg, C., Geballe, T.R., Roush, T.L., 1999. Evidence for methane segregation at the surface of Pluto. Icarus 142, 421-444.

Drake, M.J., 2001. The eucrite/Vesta story. Meteor. Planet. Sci. 36, 501-513.

Dukes, C.A., Baragiola, R.A., McFadden, L.A., 1999. Surface modification of olivine by H^+ and He^+ bombardment. J. Geophys. Res. 104, 1865-1872.

Ferini, G., Baratta, G.A., Palumbo, M.E., 2004. A Raman study of ion irradiated icy mixtures. Astron. Astrophys. 414, 757-766.

Florczak, M., Barucci, M.A., Doressoundiram, A., Lazzaro, D., Angeli, C.A., Dotto, E., 1998. A visible spectroscopic survey of the Flora Clan. Icarus 133, 233-246.

Fornasier, S., Dotto, E., Barucci, M.A., Barbieri, C., 2004. Water ice on the surface of the large TNO 2004 DW. Astron. Astrophys. 422, L43-L46.

Foti, G., Calcagno, L., Sheng, K.L., Strazzulla, G., 1984. Micrometre-sized polymer layers synthesized by MeV ions impinging on frozen methane. Nature 310, 126-128.

Gaffey, M.J., 1983. The Asteroid (4) Vesta: Rotational Spectral Variations, Surface Material Heterogeneity, and Implications for the Origin of the Basaltic Achondrites. Lunar and Planetary Institute Conference Abstracts 14, 231-232.

Gaffey, M.J., Bell, J.F., Cruikshank, D.P., 1989. Reflectance spectroscopy and asteroid surface mineralogy. In: Binzel, R.P., Gehrels, T., Matthews, M.S. (Eds.), Asteroids II. Univ. of Arizona Press, Tucson, AZ, pp. 98-127.

Gaffey, M.J., Burbine, T.H., Piatek, J.L., Reed, K.L., Chaky, D.A., Bell, J.F., Brown, R.H., 1993. Mineralogical variations within the S-type asteroid class. Icarus 106, 573-602.

Gattacceca, J., and Rochette, P., 2004. Toward a robust normalized magnetic paleointensity method applied to meteorites. Earth and Planetary Science Letters 227, 377-393.

Gilabert, E., and Lavielle, B., 2001. Noble gas exposure ages of the French chondrite falls. In: 64th Ann. Metor. Soc. Meeting. Abstract #5358.

Gilabert, E., Lavielle, B., 2002. Collisional history of the French chondrite falls. In: 65th Ann. Metor. Soc. Meeting. Abstract #5217.

Greenstadt, E.W., 1971. Conditions for Magnetic Interaction of Asteroids with the Solar Wind. Icarus 14, 374.

Guyot, F., Boyer, H., Madon, M., Velde, B., Poirier, J.P., 1986. Comparison of the Raman microprobe spectra of (Mg, Fe)$_2$SiO$_4$ and Mg$_2$GeO$_4$ with olivine and spinel structures. Phys. Chem. Miner. 13, 91-95.

Hapke, B., 1981. Bidirectional reflectance spectroscopy. 1. Theory. J. Geophys. Res. 86, 3039-3054.

Hapke, B., 1986. Bidirectional reflectance spectroscopy 4: Extinction and the opposition effect, Icarus 67, 264-280.

Hapke, B., 1993. Combined theory of reflectance and emittance spectroscopy. In: Pieters, C.M., Englert, P.A.J. (Eds.), Remote Geochemical Analysis: Elemental and Mineralogical Composition. Cambridge Univ. Press, New York, pp. 31-42.

Hapke, B., 2001. Space weathering from Mercury to the asteroid belt. J. Geophys. Res. 106 (E5), 10039-10073.

Hapke, B., and Wells, E., 1981. Bidirectional reflectance spectroscopy 2: Experiments and observations, J. Geophys. Res. 96, 3055-3060.

Hardersen, P.S., Gaffey, M.J., Abell, P.A., 2005. Near-IR spectral evidence for the presence of iron-poor orthopyroxenes on the surfaces of six M-type asteroids. Icarus 175, 141-158.

Hiroi, T., and Sasaki, S., 2001. Importance of space weathering simulation products in compositional modeling of asteroids: 349 Dembowska and 446 Aeternitas as examples. Meteorit. Planet. Sci. 36, 1587-1596.

Hiroi, T., Moroz, L.V., Shingareva, T.V., Basilevsky, A.T., Pieters, C.M., 2003. Effects of Microsecond Pulse Laser Irradiation on Vis-NIR Reflectance Spectrum of Carbonaceous Chondrite Simulant: Implications for Martian Moons and Primitive Asteroids. Lunar and Planetary Institute Conference Abstracts 34, 1324.

Hiroi, T., Pieters, C.M., Rutherford, M.J., Zolensky, M.E., Sasaki, S., Ueda, Y., Miyamoto, M., 2004. What are the P-type Asteroids Made Of? Lunar and Planetary Institute Conference Abstracts 35, 1616.

Hiroi, T., Abe, M., Kitazato, K., Abe, S., Clark, B.E., Sasaki, S., Ishiguro, M., Barnouin-Jha, O.S., 2006. Developing space weathering on the asteroid 25143 Itokawa. Nature 443, 56-58.

Hsieh, H.H., and Jewitt, D., 2006. A Population of Comets in the Main Asteroid Belt. Science 312, 561-563.

Huang, E., Chen, C.H., Huang, T., Lin, E.H., Xu, J., 2000. Raman spectroscopic characteristics of Mg-Fe-Ca pyroxenes. Am. Mineral. 85, 473-479.

Hudson, R.L., and Moore, M.H., 2000. IR spectra of irradiated cometary ice analogues containing methanol: a new assignment, a reassignment, and a nonassignment. Icarus 145, 661-663.

IAU 2006 General Assembly: Resolutions 5 (Definition of a Planet in the Solar System) and 6 (Pluto), IAU, 24 August 2006.

Jäger, C., Fabian, D., Schrempel, F., Dorschner, J., Henning, Th., Wesch, W., 2003. Structural processing of enstatite by ion bombardment. Astron. Astrophys. 401, 57-65.

Jedicke, R., Nesvorný, D., Whiteley, R., Ivezic, Z., Juric, M., 2004. An age-color relationship for Main-Belt S-complex asteroids. Nature 429, 275-277.

Jewitt, D.C., 2002. From Kuiper Belt Object to Cometary Nucleus: The Missing Ultrared Matter. Astron. J. 123, 1039-1049.

Jewitt, D.C., and Luu, J., 2004. Crystalline water ice on the Kuiper belt object (50000) Quaoar. Nature 432, 731-733.

Johnson, P.B., and Cristy, R.W., 1974. Optical constants of metals: Ti, V, Cr, Mn, Fe, Co, Ni, and Pd. Phys. Rev. B. 9, 5056-5070.

Johnson, R.E., Cooper, J.F., Lanzerotti, L.J., Strazzulla, G., 1987. Radiation Formation of a Non-Volatile Comet Crust. Astron. Astrophys. 187, 889.

Johnson, R.E., 1998. Sputtering and Desorption from Icy Surfaces. In: B. Schmitt, C. de Bergh (Eds.), Solar System Ices, Kluwer Netherlands, Dordrecht, p. 303.

Johnson, T.V., and Fanale, F.P., 1973. Optical properties of carbonaceous chondrites and their relationship to asteroids. J. Geophys. Res. 78, 8507-8518.

Jull, A.J.T., Wilson, G.C., Long, J.V.P., Reed, S.J.B., Pillinger, C.T., 1980. Sputtering rates of minerals and implications for abundances of solar elements in lunar samples. Nucl. Instrum. Methods 168, 357-365.

Kachurin, G.A., Tyschenko, I.E., Zhuravlev, K.S., Pazdnikov, N.A., Volodin, V.A., Gutakovsky, A.K., Leier, A.F., Skorupa, W., Yankov, R.A., 1997. Visible and near-infrared luminescence from silicon nanostructures formed by ion implantation and pulse annealing. Nucl. Instrum. Methods Phys. Res. B 122, 571-574.

Keane, J.V., Tielens, A.G.G.M., Boogert, A.C.A., Schutte, W.A., Whittet, D.C.B., 2001. Ice absorption features in the 5-8 μm region toward embedded protostars. Astron. Astrophys. 376, 254-270.

Keil, K., 2002. Geological History of Asteroid 4 Vesta: The "Smallest Terrestrial Planet". Asteroids III 573-584.

Khare, B.N., Sagan, C., Arakawa, E.T., Suits, F., Callcott, T.A., Williams, M.W., 1984a. Optical constants of organic tholins produced in a simulated Titanian atmosphere - From soft X-ray to microwave frequencies. Icarus 60, 127-137.

Khare, B.N., and 10 colleagues, 1984b. The organic aerosols of Titan. Advances in Space Research 4, 59-68.

Khomenkova, L., Korsunska, N., Torchynska, T., Yukhimchuk, V., Jumayev, B., Many, A., Goldstein, Y., Savir, E., Jedrzejewski, J., 2002. Defect-related luminescence of Si/SiO_2 layers. J. Phys. Condens. Matter 14, 13217-13221.

Killen, R.M., Potter, A.E., Reiff, P., Sarantos, M., Jackson, B.V., Hick, P., Giles, B., 2001. Evidence for space weather at Mercury. J. Geophys. Res. 106 (E9), 20509-20526.

Knežević, Z., and Milani, A., 2003. Proper element catalogs and asteroid families. Astron. Astrophys. 403, 1165-1173.

Lacy, J.H., Carr, J.S., Evans Neal II, J., Baas, F., Achtermann, J.M., Arens, J.F., 1991. Discovery of interstellar methane. Observations of gaseous and solid CH_4 absorption toward young stars in molecular clouds. Astrophys. J. 376, 556-560.

Lagerkvist, C.I., Moroz, L., Nathues, A., Erikson, A., Lahulla, F., Karlsson, O., Dahlgren, M., 2005. A study of Cybele asteroids. Astron. Astrophys. 432, 349-354.

Lazzarin, M., di Martino, M., Barucci, M.A., Doressoundiram, A., Florczak, M., 1997. Compositional properties of Near-Earth Asteroids: spectroscopic comparison with Ordinary Chondrite Meteorites. Astron. Astrophys. 327, 388-391.

Lazzarin, M., Marchi, S., Barucci, M.A., Di Martino, M., Barbieri, C., 2004. Visible and near-infrared spectroscopic investigation of near-Earth objects at ESO: First results. Icarus 169, 373-384.

Lazzarin, M., Marchi, S., Magrin, S., Licandro, J., 2005. Spectroscopic investigation of near-Earth objects at Telescopio Nazionale Galileo. Monthly Notices of the Royal Astronomical Society 359, 1575-1582.

Lazzarin, M., Marchi, S., Moroz, L.V., Brunetto, R., Magrin, S., Paolicchi, P., Strazzulla, G., 2006. Space Weathering in the Main Asteroid Belt: The Big Picture. Astrophys. J. 647, L179-L182.

Lazzaro, D., Moth-Diniz, T., Carvano, J.M., Angeli, C.A., Betzler, A.S., Florczak, M., Cellino, A., Di Martino, M., Doressoundiram, A., Barucci, M.A., Dotto, E., Bendjoya, P., 1999. The Eunomia family: a visible spectroscopic survey. Icarus 142, 445-453.

Leto, G., and Baratta, G.A., 2003. Ly-alpha photon induced amorphization of Ic water ice at 16 Kelvin. Effects and quantitative comparison with ion irradiation. Astron. Astrophys. 397, 7-13.

Licandro, J., and Pinilla-Alonso, N., 2005. The Inhomogeneous Surface of Centaur 32522 Thereus (2001 PT_{13}). Astrophys. J. 630, L93-L96.

Licandro, J., Pinilla-Alonso, N., Pedani, M., Oliva, E., Tozzi, G.P., Grundy, W.M., 2006. The methane ice rich surface of large TNO 2005 FY_9: a Pluto-twin in the trans-neptunian belt?. Astron. Astrophys. 445, L35-L38.

Lucey, P.G., 1998. Model near-infrared optical constants of olivine and pyroxene as a function of iron content. J. Geophys. Res. 103 (E1), 1703-1714.

Luu, J., and Jewitt, D., 1996. Color Diversity Among the Centaurs and Kuiper Belt Objects. Astron. J. 112, 2310.

Luu, J.X., Jewitt, D.C., Trujillo, C., 2000. Water Ice in 2060 Chiron and Its Implications for Centaurs and Kuiper Belt Objects. Astrophys. J. 531, L151-L154.

Marchi, S., Brunetto, R., Magrin, S., Lazzarin, M., Gandolfi, D., 2005. Space weathering of near-Earth and Main-Belt silicate-rich asteroids: Observations and ion irradiation experiments. Astron. Astrophys. 443, 769-775.

Marchi, S., Paolicchi, P., Lazzarin, M., Magrin, S., 2006. A general spectral slope-exposure relation for S-type Main Belt and near-Earth asteroids. Astron. J. 131, 1138-1141.

Marzari, F., Cellino, A., Davis, D.R., Farinella, P., Zappala, V., Vanzani, V., 1996. Origin and evolution of the Vesta asteroid family. Astron. Astrophys. 316, 248-262.

McCord, T.B., Adams, J.B., Johnson, T.V., 1970. Asteroid Vesta: Spectral Reflectivity and Compositional Implications. Science 168, 1445-1447.

McSween, H.Y., Bennett, M.E., Jarosewich, E., 1991. The mineralogy of ordinary chondrites and implications for asteroid spectrophotometry. Icarus 90, 107-116.

Mittlefehldt, D.W., Bogard, D.D., Berkley, J.L., Garrison, D.H., 2003. Brachinites: Igneous rocks from a differentiated asteroid. Meteor. Planet. Sci. 38, 1601-1625.

Moore, M.H., 1999. The physics and chemistry of ices in the interstellar medium. In: d'Hendecourt, L., Joblin, C., Jones, A. (Eds.), Solid Interstellar Matter: The ISO Revolution. EDP Sciences, Springer-Verlag, Berlin, pp. 199-218.

Moore, M.H., Hudson, R.L., Ferrante, R.F., 2003. Radiation Products in Processed Ices Relevant to Edgeworth-Kuiper-Belt Objects. Earth Moon and Planets 92, 291-306.

Moretti, P.F., Maras, A., Palomba, E., Colangeli, L., Girasole, M., Pompeo, G., Longo, G., Cricenti, A., Somma, F., Serracino, M., 2005. Detection of Nanostructured Metal in Meteorites: Implications for the Reddening of Asteroids. Astrophys. J. 634, L117-L120.

Moroz, L.V., Fisenko, A.V., Semjonova, L.F., Pieters, C.M., Korotaeva, N.N., 1996. Optical Effects of Regolith Processes on S-Asteroids as Simulated by Laser Shots on Ordinary Chondrite and Other Mafic Materials. Icarus 122, 366-382.

Moroz, L.V., Arnold, G., Korochantsev, A.V., Wasch, R., 1998. Natural solid bitumens as possible analogs for cometary and asteroid organics. 1. Reflectance spectroscopy of pure bitumens. Icarus 134, 253-268.

Moroz, L., Schade, U., Wäsch, R., 2000. Reflectance Spectra of Olivine-Orthopyroxene-Bearing Assemblages at Decreased Temperatures: Implications for Remote Sensing of Asteroids. Icarus 147, 79-93.

Moroz, L., Baratta, G., Strazzulla, G., Starukhina, L., Dotto, E., Barucci, M.A., Arnold, G., Distefano, E., 2004a. Optical alteration of complex organics induced by ion irradiation: 1. Laboratory experiments suggest unusual space weathering trend. Icarus 170, 214-228.

Moroz, L.V., Hiroi, T., Shingareva, T.V., Basilevsky, A.T., Fisenko, A.V., Semjonova, L.F., Pieters, C.M., 2004b. Reflectance Spectra of CM2 Chondrite Mighei Irradiated with Pulsed Laser and Implications for Low-Albedo Asteroids and Martian Moons. Lunar and Planetary Institute Conference Abstracts 35, 1279.

Mumma, M.J., Weissman, P.R., Stern, S.A., 1993. Comets and the origin of the Solar System: reading the Rosetta stone. In: Levy, E.H., Lunine, J.I., Matthews, M.S. (Eds.), Protostars and Planets III. Univ. of Arizona Press, Tucson, pp. 1177-1252.

Mumma, M.J., DiSanti, M.A., Dello Russo, N., Fomenkova, M., Magee-Sauer, K., Kaminski, C.D., Xie, D.X., 1996. Detection of abundant ethane and methane, along with carbon monoxide and water, in Comet C/1996 B2 Hyakutake: evidence for interstellar origin. Science 272, 1310-1314.

Mumma, M.J., DiSanti, M.A., Dello Russo, N., Magee-Sauer, K., Rettig, T.W., 2000. Detection of CO and ethane in Comet 21P/Giacobini-Zinner: evidence for variable chemistry in the outer solar nebula. Astrophys. J. 531, L155-L159.

Mumma, M.J., Dello Russo, N., DiSanti, M.A., Magee-Sauer, K., Novak, R.E., Brittain, S.T., Rettig, T.W., Mc Lean, I.S., Reuter, D.C., Xu, Li.-H., 2001. Organic composition of C/1999 S4 (LINEAR): a comet formed near Jupiter? Science 292, 1334-1339.

Nesvorný, D., and Bottke, W.F., 2004. Detection of the Yarkovsky effect for mainbelt asteroids. Icarus 170, 324-342.

Nesvorný, D., Bottke,W.F., Dones, L., Levison, H.F., 2002. The recent breakup of an asteroid in the main-belt region. Nature 417, 720-771.

Nesvorný, D., Jedicke, R., Whiteley, R.J., Ivezić, Ž., 2005. Evidence for asteroid space weathering from the Sloan Digital Sky Survey. Icarus 173, 132-152. (corrigendum 177, 291)

Nesvorný, D., Bottke, W.F., Vokrouhlický, D., Morbidelli, A., Jedicke, R., 2006. Asteroid families. In IAU Colloq. 229, Asteroids, Comets, Meteors, ed. L. Daniela, M. Sylvio Ferraz, & F. J. Angel (Cambridge: Cambridge Univ. Press), 289-299.

Omidi, N., Blanco-Cano, X., Russell, C.T., Karimabadi, H., Acuna, M., 2002. Hybrid simulations of solar wind interaction with magnetized asteroids: General characteristics. J. Geophys. Res. (Space Physics) 107, 12-1.

Orofino, V., Politi, R., Blanco, A., Fonti, S., 2006. Diffuse reflectance of altered olivine grains: Remote sensing detection and implications for Mars studies. Planet. Space Sci. 54, 784-793.

Owen, T.C., Roush, T.L., Cruikshank, D.P., Elliot, J.L., Young, L.A., de Berg, C., Schmitt, B., Geballe, T.R., Brown, R.H., Bartholomew, M.J., 1993. Surface ices and atmospheric composition of Pluto. Science 261, 745-749.

Palumbo, M.E., Castorina, A.C., Strazzulla, G., 1999. Ion irradiation effects on frozen methanol. Astron. Astrophys. 342, 551-562.

Palumbo, M.E., and Strazzulla, G., 2003. Nitrogen condensation on water ice. Canadian Journal of Physics 81, 217-224.

Palumbo, M.E., Ferini, G., Baratta, G.A., 2004. Infrared and Raman spectroscopies of refractory residues left over after ion irradiation of nitrogen-bearing icy mixtures. Advances in Space Research 33, 49-56.

Peixinho, N., Boehnhardt, H., Belskaya, I., Doressoundiram, A., Barucci, M.A., Delsanti, A., 2004. ESO large program on Centaurs and TNOs: visible colors-final results. Icarus 170, 153-166.

Pieters, C.M., Fischer, E.M., Rode, O.D., Basu, A., 1993. Optical effects of space weathering on lunar soils and the role of the finest fraction. J. Geophys. Res. 98, 20817-20824.

Pieters, C.M., Taylor, L.A., Noble, S.K., Keller, L.P., Hapke, B., Morris, R.V., Allen, C.C., McKay, D.S.,Wentworth, S., 2000. Space weathering on airless bodies: Resolving a mystery with lunar samples. Meteorit. Planet. Sci. 35, 1101-1107.

Pollack, J.B., Hollenbach, D., Beckwith, S., Simonelli, D.P., Roush, T., Fong, W., 1994. Composition and radiative properties of grains in molecular clouds and accretion disks. Astrophys. J. 421, 615-639.

Poulet, F., Cuzzi, J.N., Cruikshank, D.P., Roush, T., Dalle Ore, C.M. 2002. Comparison between the Shkuratov and Hapke Scattering Theories for Solid Planetary Surfaces: Application to the Surface Composition of Two Centaurs. Icarus 160, 313-324.

Quirico, E., and Schmitt, B., 1997. Near-infrared spectroscopy of simple hydrocarbons and carbon oxides diluted in solid N2 and as pure ices: implications for Triton and Pluto. Icarus 127, 354-378.

Rayner, J.T., Onaka, P.M., Cushing, M.C., Vacca, W.D., 2004. Four years of good SpeX. In: Moorwood, A.F.M., Masanori, I. (Eds.), Ground Based Instrumentation for Astronomy. In: Proc. SPIE, vol. 5492. SPIE, Bellingham, WA, pp. 1498-1509.

Richardson, J.E., Melosh, H.J., Greenberg, R., 2004. Impact-induced seismic activity on Asteroid 433 Eros: A surface modification process. Science 306, 1526-1529.

Richmond, N.C., Hood, L.L., Mitchell, D.L., Lin, R.P., Acuña, M.H., Binder, A.B., 2005. Correlations between magnetic anomalies and surface geology antipodal to lunar impact basins. J. Geophys. Res. (Planets) 110, 5011.

Righter, K., Drake, M.J., 1997. A magma ocean on Vesta: Core formation and petrogenesis of eucrites and diogenites. Meteor. Planet. Sci. 32, 929-944.

Rivkin, A.S., Binzel, R.P., Sunshine, J., Bus, S.J., Burbine, T.H., Saxena, A., 2004. Infrared spectroscopic observations of 69230 Hermes (1937 UB): possible unweathered endmember among ordinary chondrite analogs. Icarus 172, 408-414.

Rochette, P., Gattacceca, J., Menvielle, M., Eisenlohr, P., Chevrier, V., 2004. Interest and design of magnetic properties measurements on planetary and asteroidal landers. Planet. Space Sci. 52, 987-995.

Roush, T.L., 1994. Charon: More than water ice? Icarus 108, 243-254.

Roush, T.L., 2003. Estimated optical constants of the Tagish Lake meteorite, Meteor. Planet. Sci. 38, 419-426.

Roush, T.L., 2005. Near-infrared (0.67-4.7 μm) optical constants estimated for montmorillonite, Icarus 179, 259-264.

Roush, T.L., Pollack, J. B., Witteborn, F. C., Bregman, J. D., and Simpson. J. P. 1990. Ice and minerals on Callisto: A reassessment of the reflectance spectra, Icarus 86, 355-382.

Ruzicka, A., Snyder, G.A., Taylor, L.A., 1997. Vesta as the HED Parent Body: Implications for the Size of a Core and for Large-Scale Differentiation. Meteor. Planet. Sci. 32, 825-840.

Sasaki, S., Nakamura, K., Hamabe, Y., Kurahashi, E., Hiroi, T., 2001. Production of iron nanoparticles by laser irradiation in a simulation of lunar-like space weathering. Nature 410, 555-557.

Sasaki, T., Sasaki, S., Watanabe, J., Sekiguchi, T., Yoshida, F., Kawakita, H., Fuse, T., Takato, N., Dermawan, B., Ito, T., 2004. Mature and fresh surfaces on the newborn Asteroid Karin. Astrophys. J. 615 (2), L161-L164.

Schmitz, B., Häggström, T., Tassinari, M., 2003. Sediment-dispersed extraterrestrial chromite traces a major asteroid disruption event. Science 300 (5621), 961-964.

Shingareva, T.V., Basilevsky, A.T., Fisenko, A.V., Semjonova, L.F., Korotaeva, N.N., 2004. Mineralogy and Petrology of Laser Irradiated Carbonaceous Chondrite Mighei. Lunar and Planetary Institute Conference Abstracts 35, 1137.

Shkuratov, Y., Starukhina, L., Hoffmann, H., Arnold, G., 1999. A model of spectral albedo of particulate surfaces: implications for optical properties of the Moon. Icarus 137, 235-246.

Shkuratov, Y.G., and Grynko, Y.S., 2005. Light scattering by media composed of semitransparent particles of different shapes in ray optics approximation: consequences for spectroscopy, photometry, and polarimetry of planetary regoliths. Icarus 173, 16-28.

Strazzulla, G., and Johnson, R.E., 1991. Irradiation effects on comets and cometary debris. In: Newburn Jr., R., Neugebauer, M., Rahe, J. (Eds.), Comets in the Post-Halley Era. Kluwer, Dordrecht, pp. 243-275.

Strazzulla, G., and Baratta, G.A., 1991. Laboratory study of the IR spectrum of ion-irradiated frozen benzene. Astron. Astrophys. 241, 310-316.

Strazzulla, G., Baratta, G.A., Johnson, R.E., Donn, B., 1991. Primordial comet mantle - Irradiation production of a stable, organic crust. Icarus 91, 101-104.

Strazzulla, G., 1997. Ion bombardment of comets. In: Pendleton, Y.J., Tielens, A.G.G.M. (Eds.), From Stardust to Planetesimals. In: ASP Conf. Series, vol. 122. ASP, San Francisco, pp. 423-433.

Strazzulla, G., Baratta, G.A., Palumbo, M.E., 2001. Vibrational spectroscopy of ion-irradiated ices. Spectrochim. Acta A 57 (4), 825-842.

Strazzulla, G., Leto, G., Gomis, O., Satorre, M.A., 2003a. Implantation of carbon and nitrogen ions in water ice. Icarus 164, 163-169.

Strazzulla, G., Cooper, J.F., Christian, E.R., Johnson, R.E., 2003b. Ion irradiation of TNOs: from the fluxes measured in space to the laboratory experiments. C. R. Phys. 4, 791-801.

Strazzulla, G., Dotto, E., Binzel, R., Brunetto, R., Barucci, M.A., Blanco, A., Orofino, V., 2005. Spectral alteration of the meteorite Epinal (H5) induced by heavy ion irradiation: a simulation of space weathering effects on Near-Earth Asteroids. Icarus 174, 31-35.

Tedesco, E.F., Noah, P.V., Noah, M., Price, S.D., 2004. IRAS Minor Planet Survey V6.0. NASA Planetary Data System, IRAS-A-FPA-3-RDR-IMPS-V6.0 12.

Thomas, P.C., Binzel, R.P., Gaffey, M.J., Storrs, A.D., Wells, E.N., Zellner, B.H., 1997. Impact excavation on asteroid 4 Vesta: Hubble Space Telescope results. Science 277, 1492-1495.

Ueda, Y., Hiroi, T., Pieters, C.M., Miyamoto, M., 2002a. Changes of Band I center and Band II/Band I area ratio in reflectance spectra of olivine-pyroxene mixtures due to the space weathering and grain size effects. Lunar Planet. Sci. XXXIII. Abstract 2023.

Ueda, Y., Hiroi, T., Pieters, C.M., Miyamoto, M., 2002b. Expanding the modified Gaussian model to include the space weathering effects: Estimation of the weathering degrees of Pulse-Laser treated olivine samples. Lunar Planet. Sci. XXXIII. Abstract 1950.

Vernazza, P., Brunetto, R., Strazzulla, G., Fulchignoni, M., Rochette, P., Meyer-Vernet, N., Zouganelis, I., 2006. Asteroid colors: a novel tool for magnetic field detection? The case of Vesta. Astron. Astrophys. 451, L43-L46.

Walmsley, C.M., Pineau des Forêts, G., Flower, D.R., 1999. Silicon chemistry in PDRs. Astron. Astrophys. 342, 542-550.

Xu, S., 1994. CCD Photometry and Spectroscopy of Small Main-Belt Asteroids. Ph.D. Thesis, Massachusetts Institute of Technology

Yamada, M., Sasaki, S., Nagahara, H., Fujiwara, A., Hasegawa, S., Yano, H., Hiroi, T., Ohashi, H., Otake, H., 1999. Simulation of space weathering of planet-forming materials: Nanosecond pulse laser irradiation and proton implantation on olivine and pyroxene samples. Earth Planets Space 51, 1255-1265.

Yoshida, F., and 10 colleagues, 2004. Photometric observations of a very young family-member Asteroid (832) Karin. Astron. Soc. Jpn. 56, 1105-1113.

Ziegler, J.F., Biersack, J.P., Littmark, U., 1985. The Stopping and Range of Ions in Solids. Pergamon, Elmsford, NY.